

Towards the near-infrared detection of exoplanets

Jason James Neal

Tese de doutoramento apresentada à
Faculdade de Ciências da Universidade do Porto
Astronomia

2019

TOWARDS THE NIR DETECTION OF EXOPLANETS

by

Jason James Neal

A thesis submitted in conformity with the requirements
for the degree of Doctor of Philosophy
Graduate Department of Departamento de Física e Astronomia
University of Porto

To Jessica, Timothy, and Amelia

Acknowledgements

First I would like to thank my supportive wife Jessica, and darling children Timothy and Amelia for bearing with and supporting me through this journey to a distant land. For all the late nights and trips away, and a mentally exhausted presence; it is now finally over.

I would also like to thank my supervisors, Pedro, Claudio and team leader Nuno for their patience, wisdom, support and guidance throughout these last four years.

I acknowledge support from Fundação para a Ciência e a Tecnologia (FCT) though the PhD::Space fellowship PD/BD/52700/2014. I was also supported by the short term contract with reference CIAAUP-20/2018-BIM. Without this funding we could not have moved halfway around the world to undertake this research in Portugal.

This work was undertaken within the Exoplanet team in the Instituto de Astrofísica e Ciências do Espaço and Centro de Astrofísica da Universidade do Porto. This team was supported by Fundação para a Ciência e a Tecnologia (FCT) (Portugal) research grants through Portuguese funds and from FEDER - Fundo Europeu de Desenvolvimento Regional, through COMPETE2020 - Programa Operacional Competitividade e Internacionalização (POCI) by the following grants:

UID/FIS/04434/2013 & POCI-01-0145-FEDER-007672; PTDC/FIS-AST/1526/2014 & POCI-01-0145-FEDER-016886; PTDC/FIS-AST/7073/2014 & POCI-01-0145-FEDER-016880; PTDC/FIS-AST/28953/2017 & POCI-01-0145-FEDER-028953; FCT: PTDC/FIS-AST/32113/2017 & POCI-01-0145-FEDER-032113.

Abstract

With a vast number of exoplanets discovered in the last decades, the field has pushed towards detecting their atmospheres, particularly in the near-infrared (nIR) where flux ratios are favourable for detecting exoplanetary emission. The contents of this work focuses specifically on high resolution nIR spectra with the aim to separate the blended spectra of FGK stars with suspected Brown Dwarf companions. This has two main purposes, to develop nIR spectral separation techniques on larger companions with the intent to move towards planetary atmospheres, and to constrain the mass of the Brown Dwarf companions in the process. Two different techniques are explored to analyse the available CRIRES observations: a differential subtraction method between two separate observations, and a χ^2 fitting of the observations to a binary model comprised of synthetic spectra. Both techniques were unsuccessful in recovering useful information about the Brown Dwarf companions mainly due to observational issues, the small flux ratios of the companions and discrepancies to synthetic models.

Remaining in the nIR, effort was diverted to extend the understanding of radial velocity precision of M-dwarf spectra, a focus of new nIR instrumentation. Software to calculate the radial velocity precision is improved to provide the radial velocity precision estimates for the exposure time calculators of two new nIR spectrographs, NIRPS and SPIRou. Finally a preliminary analysis is performed on the radial velocity precision attainable from the CARMENES spectrograph, comparing synthetic models to observed M-dwarf spectra.

Chapter 1 presents an introduction to detecting exoplanets and their atmospheres along with some exoplanet properties. Chapters 2 and 3 give further descriptions of detecting exoplanet via the radial velocity method and basic concepts of nIR spectroscopy respectively. Chapter 4 presents the affect of Earth's atmosphere on observations and the models used to correct it, as well as detailing the synthetic stellar libraries used. The data reduction steps applied to nIR spectra are given in Chapter 5 followed by the post reduction wavelength calibration and telluric correction steps. The differential subtraction technique is presented in Chapter 6, identifying the insufficient separation between observations. Chapter 7 presents the χ^2 method with binary synthetic models followed by a discussion on the results observed. Finally the nIR information content and radial velocity precision of M-dwarf CARMENES spectra are investigated in Chapter 8. The theoretical precision of stellar spectra is calculated for the latest generation of near-infrared spectrographs to help detect planets around M-dwarf stars.

Resumo

Com o vasto número de exoplanetas descobertos nas últimas décadas, este campo avançou na detecção das suas atmosferas, em particular no infravermelho próximo (nIR), onde a razão entre o fluxo do planeta e da estrela é favorável à detecção da emissão exoplanetária. O conteúdo deste trabalho foca-se na utilização de espectroscopia de alta resolução no infravermelho próximo para separar os espectros combinados de estrelas FGK com possíveis anãs castanhas companheiras. Este trabalho tem dois objectivos principais. O primeiro consiste em desenvolver técnicas de separação espectral no infravermelho próximo para companheiros de maior massa, com a intenção de avançar para atmosferas planetárias. O segundo consiste em restringir a massa das anãs castanhas companheiras detectadas. Duas técnicas diferentes são exploradas para analisar observações obtidas com o espectroógrafo CRIRES. A primeira consiste num método de subtração diferencial entre duas observações independentes. A segunda num ajuste χ^2 das observações a um modelo binário composto por espectros sintéticos. Nenhuma das técnicas propostas teve sucesso na recuperar ação de qualquer tipo de informação útil sobre as anãs castanhas companheiras. Esta falta de resultados deve-se principalmente a questões observacionais, à diminuta razão entre o fluxo da estrela e companheira e discrepâncias relativamente aos modelos sintéticos. O fóco do trabalho foi então desviado para o estudo da precisão na recuperação da velocidade radial de estrelas anãs do tipo M a partir dos seus espectros no infravermelho próximo, um dos objectivos dos novos instrumentos planeados para observar nessa banda do espectro electromagnético. Com esse objectivo em vista, foram melhoradas as aplicações desenvolvidas para estimar a precisão na velocidade radial obtida pelos calculadores de tempo de exposição de dois novos nIR espectrógrafos: NIRPS e SPIRou. Finalmente, uma análise preliminar é realizada sobre a precisão da velocidade radial obtida a partir do espectroógrafo CARMENES, comparando modelos sintéticos com os espectros reais de estrelas anãs do tipo M.

No Capítulo 1 apresentamos e introduzimos a detecção de exoplanetas e suas atmosferas, juntamente com algumas propriedades de exoplanetas. Nos Capítulos 2 e 3 fornecemos descrições adicionais da detecção de exoplaneta através do método de velocidade radial e conceitos básicos de espectroscopia no infravermelho próximo. No Capítulo 4 apresentamos o impacto da atmosfera da Terra nas observações e nos modelos usados para corrigi-la, assim como apresentamos em detalhe as bibliotecas estelares sintéticas usadas. As etapas de redução de dados aplicadas aos espectros de infravermelho próximo são descritas no Capítulo 5, seguidas pelas etapas de calibração de comprimento de onda pós-redução e correção telúrica. A técnica de subtração diferencial é apresentada em Capítulo 6, identificando a separação insuficiente entre observações. No Capítulo 7 apresentamos o método χ^2 com modelos sintéticos binários seguidos de uma discussão sobre os resultados observados. Finalmente o conteúdo de informação presente no

infravermelho próximo e a precisão na medição da velocidade radial a partir de espectros no infravermelho próximo de estrelas anãs do tipo M com o CARMENES são investigados no Capítulo 8, assim com o cálculo da precisão teórica dos espectros estelares para a última geração de espetrógrafos de infravermelho próximo para detectar planetas em redor de estrelas anãs do tipo M.

Contents

List of Tables	x
List of Figures	xi
1 Introduction	1
1.1 Towards the characterization of exoplanets	1
1.2 Exoplanet detection methods	2
1.2.1 Radial Velocimetry	2
1.2.2 Transit method	4
1.2.3 Direct Imaging	7
1.2.4 Astrometry	8
1.2.5 Microlensing	8
1.2.6 Pulsar timing	10
1.3 Detecting atmospheres	10
1.3.1 Occultation and phase variations	11
1.3.2 Transmission spectroscopy	12
1.3.3 High resolution spectroscopy	14
1.4 The diversity of exoplanets	15
1.4.1 Brown Dwarfs: bridging the gap	17
1.5 Motivation for this thesis	18
2 Radial Velocity	20
2.1 Keplerian Orbits	20
2.1.1 Mass function	22
2.1.2 Binary mass ratio	23
2.2 Measuring the RV	24
2.3 RV precision	25
3 Near-infrared spectroscopy	27
3.1 Spectrograph basics	27
3.2 The detectors	29
3.2.1 Spectrograph cooling	31

3.3	CRIRES	32
3.4	The new generation	32
3.4.1	CRIRES+	33
3.4.2	CARMENES	34
3.4.3	NIRPS	34
3.4.4	SPIRou	34
4	Atmospheres and Models	35
4.1	Earth’s atmosphere, in the nIR	35
4.1.1	Telluric correction	37
4.1.1.1	TAPAS web service	39
4.1.1.2	Requests for this work	39
4.1.1.3	Issues with TAPAS	39
4.1.1.4	Telluric masking	41
4.2	Synthetic Stellar models of cool stars	41
4.2.1	PHOENIX-ACES models	42
4.2.2	BT-Settl	43
4.2.3	Model access	44
4.2.4	Comparing models	44
4.3	Evolutionary models	46
4.3.1	Estimating Companion-host Flux ratio	47
4.3.2	Baraffe tables	48
5	Spectroscopic reduction	49
5.1	nIR reduction concepts	49
5.1.1	Dark Current	50
5.1.2	Flat-field	50
5.1.3	Nodding and Jitter	51
5.1.4	Th-Ar lamp calibration	52
5.1.5	Extraction	52
5.2	Pipeline Comparison	53
5.2.1	ESO CRIRES pipeline	53
5.2.2	DRACS	54
5.2.3	Pipeline comparison and selection	55
5.2.3.1	Reduction issues	57
5.2.4	Reduction experience	60
5.3	Post reduction stages	61
5.3.1	Wavelength calibration	61
5.3.2	Telluric correction	65
5.3.2.1	Separate H ₂ O scaling	66
5.3.3	Wavelength masking	66
5.3.4	Barycentric RV correction	67

6 Separating the spectra of faint companions	68
6.1 Spectral separation techniques	68
6.2 Motivation and target selection	70
6.2.1 The CRIRES data	73
6.3 Direct Subtraction Method	73
6.3.1 Calculation of expected RV	75
6.4 Results of spectral differential analysis	76
6.4.1 Relative differential amplitude	78
6.5 Orbital Solutions	79
6.5.0.1 Differential scheduling challenges	81
6.6 Contrast to other works	85
6.7 Direct recovery in the mIR	86
6.8 Summary	86
7 Synthetic companion recovery	87
7.1 Binary χ^2 spectral recovery	87
7.1.1 The χ^2 method	87
7.1.2 Computed model spectra	88
7.1.2.1 Single component model	89
7.1.2.2 Binary model	90
7.1.2.3 Effective radius	90
7.1.3 Re-normalization	91
7.1.4 Reducing dimensionality	91
7.2 Simulation and results	95
7.2.1 Simulated binaries	95
7.2.2 HD211847 observation	96
7.2.3 Companion injection-recovery	98
7.3 Discussion	100
7.3.1 Mismatch in synthetic models	102
7.3.2 Line contribution of faint companions	102
7.3.3 χ^2 asymmetry	103
7.3.4 Component RV separation	106
7.3.5 Wavelength range	107
7.3.6 The BT-Settl models	107
7.3.7 Impact of $\log g$	108
7.3.8 Interpolation	109
7.3.9 Comparisons to other works	109
8 Information content in the nIR	111
8.1 Overview	111
8.1.1 Fundamental photon noise limitation	112
8.2 Deriving RV precision of synthetic spectra	116
8.2.1 Prepare PHOENIX-ACES models	116
8.2.2 Convolution	116

8.2.3	Interpolation	118
8.2.4	SNR scaling	119
8.2.5	Bands	119
8.2.6	Precision calculations	119
8.3	<i>eniric</i> : Extended nIR information content	119
8.3.1	Automated testing	120
8.3.2	Performance	120
8.3.3	Model extension	121
8.4	Numerical Gradient	122
8.4.1	Masking Function	126
8.4.1.1	Masking order	127
8.4.2	SNR scaling	128
8.4.3	Atmospheric masking bug	129
8.5	RV precision update	130
8.6	Metallicity and $\log g$	132
8.7	SPIRou and NIRPS ETC	136
8.8	Application to CARMENES spectra	137
8.8.1	Target selection	137
8.8.1.1	Spectral preparation and Telluric correction	139
8.8.2	Impact of telluric correction	141
8.8.3	Barnard’s star	141
8.8.3.1	Future tasks	142
8.9	Summary	145
9	Conclusions	146
9.1	Future prospects	147
A	RV Precision Tables	149
B	Artefacts in Optimal Extraction	172
C	Multi-detector wavelength calibration	178
D	Vacuum wavelengths	182
E	PhD output	183
Bibliography		204

List of Tables

2.1	Induced radial velocity semi-amplitudes.	23
3.1	Properties of popular optical/IR detector materials.	29
3.2	Summary of high-resolution nIR spectrographs.	33
4.1	Standard infrared pass-bands.	37
4.2	PHOENIX-ACES parameter space.	42
4.3	BT-Settl parameter space.	44
4.4	Companion/host flux ratios.	47
6.1	Stellar parameters of host stars.	71
6.2	Orbital parameters of companions.	71
6.3	List of CRIRES observations.	72
6.4	Semi-amplitude and RV separation of companions.	76
7.1	χ^2 simulation results.	94
7.2	Upper mass limits from χ^2 simulations.	101
7.3	Analysis of spectral line depths.	104
8.1	Affect of numerical gradient.	123
8.2	RV precision with different splitting.	128
8.3	CARMENES targets for RV precision analysis.	138
8.4	Properties of Barnard’s star from (Artigau et al., 2018). T _{eff} , [Fe/H] and log g values are only the adopted (closest) model parameters.	142
A.1	RV precisions for the PHOENIX-ACES and BT-Settl spectral libraries.	150
A.2	RV precisions calculated for the SPIRou ETC.	156
A.3	RV precisions calculated for the NIRPS ETC.	159
B.1	Identification of nod spectra artefacts.	173
B.2	Nod position tally of artefacts.	173
C.1	Example of multi-detector fitting parameters and correlation.	180

List of Figures

1.1	Number of exoplanet detections per year separated by method.	2
1.2	The RV method.	3
1.3	Exoplanet discovery year verses exoplanet mass.	4
1.4	Transit of Venus and successive transit corssings.	6
1.5	Direct detection of four exoplanets around HR 8799.	7
1.6	Modelled astrometric path on the sky.	9
1.7	Microlensing magnification of OGLE2005-BLG-390.	10
1.8	Flux contribution from a star and planet in a transiting exoplanet system.	11
1.9	Exoplanet phase variations and temperature map.	11
1.10	Transmission spectroscopy diagram.	13
1.11	Transmission spectra for several Hot-Jupiter exoplanets.	13
1.12	Cross-correlation signal from CRIRES observations of HD 209458 b.	14
1.13	Mass-Radius diagram for rocky planets with composition contours.	16
1.14	Mass-Radius relationship with probabilistic fit.	17
2.1	The basic elements of the Keplerian orbit.	21
2.2	Elements of an elliptical orbit.	22
3.1	Basic components of a spectrograph.	27
3.2	Dispersion mechanisms.	28
3.3	Schema differentiating CCD and CMOS detectors.	30
3.4	Side by side comparison of the NIRPS and SPIRou spectrographs.	31
3.5	CRIRES layout schematic.	32
3.6	CRIRES/CRIRES+ detector focal plane arrays.	34
4.1	Telluric absorption map from 0.3–30 μm at $R \sim 10\,000$	36
4.2	Telluric correction applied using the Molecfit, TelFit and TAPAS.	38
4.3	Telluric spectra for the H ₂ O and non-H ₂ O species.	40
4.4	Difference in successive PHOENIX-ACES spectra around 5000 K.	43
4.5	Large scale comparison between the PHEONIX-ACES and BT-Settl spectra.	45
4.6	Comparision of the spectrum of Arcturus to synthetic spectra.	45
4.7	Comparision of the spectrum of 10 Leo to synthetic PHOENIX-ACES spectum.	46

5.1	Example dark frames for different exposure times.	49
5.2	Example of flat-field correction.	50
5.3	Illustration of the nodding technique.	51
5.4	Example Th-Ar calibration lamp frames for each detector.	52
5.5	Comparision between DRACS and ESOs reduction pipeline output.	56
5.6	Example of DRACS artefacts in the optimally extracted spectra HD 162020.	58
5.7	Artefacts comparision with and altered pipeline parameter.	59
5.8	Example of telluric corrected spectrum of HR 7329-B using TAPAS.	61
5.9	Example of the wavelength calibration using the synthetic telluric spectra.	63
5.10	Example reduced CRIRES spectra for each target.	65
6.1	Example of the spectral differential technique.	77
6.2	Simulated relative amplitude of differntial spectrum.	80
6.3–6.11	RV curves for the host and companion of each target.	82
7.1	χ^2 contour for companion recovery of a simulated Sun - M-dwarf binary.	93
7.2	χ^2 contour for companion recovery of a simulated observation of HD 211847.	94
7.3	χ^2 contour for an observation HD 211847.	98
7.4	Comparison between observation of HD 211847 and the best fit synthetic binary model. .	99
7.5	Result of simulated injection-recovery of synthetic companions on HD 30501.	101
7.6	Shape of simulated χ^2 with different injected companion temperatures.	105
7.7	PHOENIX-ACES spectra for temperatures between 2500 and 5000 K, corresponding to the same lines in Figure 7.6. The flux units are the native units of the PHOENIX-ACES spectrum, ($\text{erg s}^{-1} \text{cm}^2 \text{cm}^{-1}$), and have not been scaled by the stellar radii. All spectra have a $\log g=5.0$ and $[\text{Fe}/\text{H}]=0.0$. The vertical dotted lines indicate the edges of the CRIRES detectors.	106
7.8	Detector #1 spectrum for HD 211847 (blue) alongside the PHOENIX-ACES (orange dash-dot) and BT-Settl (green dashed) synthetic spectra for the host star only, with parameters $T_{\text{eff}}=5700$ K, $\log g=4.5$ and $[\text{Fe}/\text{H}]=0.0$. Both synthetic models have been normalized and convolved to $R = 50\,000$. There is a 0.05 off-set between each spectrum. .	108
8.1	Demonstration of a shifted arbitrary spectral line.	112
8.2	Left: Apparent disk of the star, thought of as a series of strips parallel to the projected rotation axis, each with the Doppler shift proportional to x . The amount of light at each Doppler shift varies with the length of the strip, from $-y_1$ to $+y_1$, where $y_1 = \sqrt{R^2 - x^2}$ for a circular disk. Right: The rotation profile, Equation 8.20, is shown by the solid black line for a limb darkening coefficient $\varepsilon = 0.6$ and labelled “total”. It is the sum of the “1st term” and “2nd term” curves. These are reproductions of Figures 18.3 and 18.5 from Gray (2005).	117
8.3	Comparing of numerical gradient alogithms.	124
8.4	Comparision of RV precision results to Figueira et al. (2016).	131
8.5	Quality factor verse $[\text{Fe}/\text{H}]$ and $\log g$ for different spectral types and wavelength bands. .	133

8.6 Flux as a function of wavelength in the Z -band (top) and J -band (bottom) for the $v \sin i = 1.0 \text{ km s}^{-1}$ and spectral types M0, M3, M6, and M9 (<i>top to bottom</i> panels), when seen at a resolution at 100 000. Flux units are arbitrary. Reproduced from Figueira et al. (2016).	135
8.8 Bad pixel removal in CARMENES.	140
8.9 Barnard's star spectral quality.	141
8.10 Telluic correction of the CARMENES nIR spectrum.	143
8.11 Barnard's star spectral quality compared to CARMENES	143
8.12 Measured RV content of Barnard's star over the optical and near-infrared domain.	144
B.1–B.7 Extra examples of reduced spectra with artefacts. One for each target.	174
C.1 Multi-detector fit and difference to individual fits.	179
C.2 Difference of multi-detector combined fit to the individual calibration mappings.	179
C.3 Multi-detector calibration parameter correlations.	181

Chapter 1

Introduction

1.1 Towards the characterization of exoplanets

The field of exoplanetary science is rapidly accelerating. Large scientific and instrumental investments have been undertaken, with the ultimate goal of detecting and characterizing an Earth-like planet that has the potential for life (as we know it). Since the very first exoplanet detection around a Sun-like star (Mayor et al., 1995) the number of confirmed exoplanets has grown to over 3872 with another 2898 candidates awaiting confirmation as of January 2019¹. A planet transitions from a candidate to confirmed when the probability of false positives is very low, is usually achieved using advanced analysis or a detection with a complementary method. However, simply detecting the presence of exoplanets is not nearly enough to satisfy our quest for knowledge. There is an exorbitant amount of insight to be gained through the full characterization of these known exoplanets, such as: density, composition, internal structure, atmosphere properties, and surface temperature.

When a new extra-solar planet is suspected, follow-up observation and analysis is required to confirm its existence, and its properties. In particular for the highly sought after Earth-twin, a full characterization is required to determine their habitability. Notably, here have been several small planets, which have had early claims of Earth-twin status, later determined to be false (or fall below a 99% probability level) after follow up investigation (e.g. Mullally et al., 2018; Burke et al., 2019), and the presence of some have been heavily debated in literature such as Gliese 581g (Vogt et al., 2010; Gregory, 2011; Robertson et al., 2014). Detecting and analysing exoplanet atmospheres aid in the characterization of exoplanets by allowing their temperature, atmospheric structure, the presence of any scattering aerosols, and the chemical composition to be determined (e.g. Kreidberg, 2018, and references therein). All providing clues towards a full exoplanet characterization.

There are several new developments for detecting and characterisation of new exoplanetary systems. For instance, the new space-based transit missions such as TESS, PLATO and CHEOPS. One of the more promising ground-based approaches is high-resolution near-infrared (nIR) spectroscopy. Several new nIR spectrographs are in development (e.g. Wright et al., 2017) primarily to detect and characterize exoplanets around cooler M-dwarf stars. The nIR wavelengths are closer to the peak emissions of cooler stars and exoplanets, while the smaller mass and radius of M-dwarfs allow exoplanets to induce larger

¹ <https://exoplanets.nasa.gov>

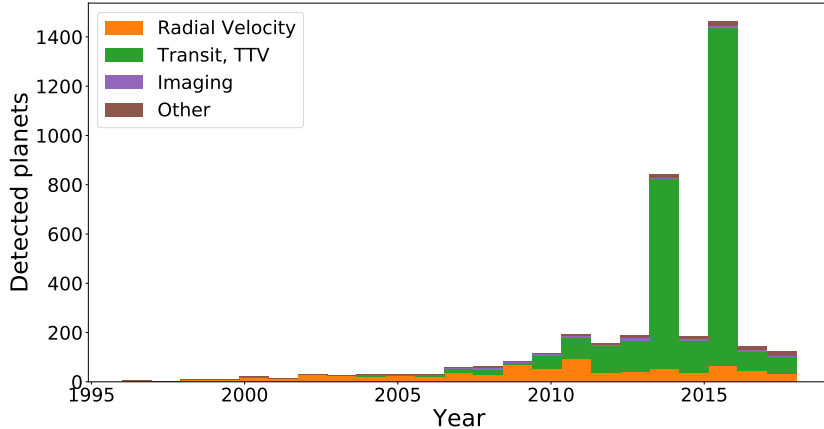


Figure 1.1: Number of exoplanet detections per year separated by method (data from exoplanet.eu October 2018).

relative signals that are relatively easier to detect.

In this chapter the common exoplanet and atmospheric detection methods will be introduced, followed by some exoplanet property distributions and the motivation for the work performed in this thesis.

1.2 Exoplanet detection methods

There are several detection methods used to build up the picture of the current understanding of exoplanet candidates. The different detection methods are often complementary, in that they are sensitive to different parameter spaces and are able to contribute different exoplanet properties, or detect different classes of exoplanet. The simplest example is that planetary mass and radius are obtained from the radial velocity and transit methods separately. Also the transit and radial velocity methods are both sensitive to large planets close to the star however, the direct imaging technique cannot see planets too close to the star, as the planets image is contaminated by the stellar image and speckles.

The exoplanet detection rates for different methods since 1995 are shown in Figure 1.1. The detection rates among different methods are not uniform, with the transit method having the majority of detections due to the use of the Kepler space telescope (Borucki et al., 2008). The radial velocity method has a fairly consistent detection rate, while direct imaging and other methods have only made a small contribution to the total number of detections so far. Details about the various main detection methods are provided in the following sections.

1.2.1 Radial Velocimetry

This technique measures the radial velocity² (RV) of the star by analysing the relative Doppler shift of its spectral lines due to the gravitational interaction with a companion. As the star and companion orbit around their common centre of mass (barycentre) the spectrum of the star periodically oscillates, with the orbital period of the planet, due to the change in relative motion to the observer as depicted in Figure 1.2 (left).

² Velocity projected along line of sight.

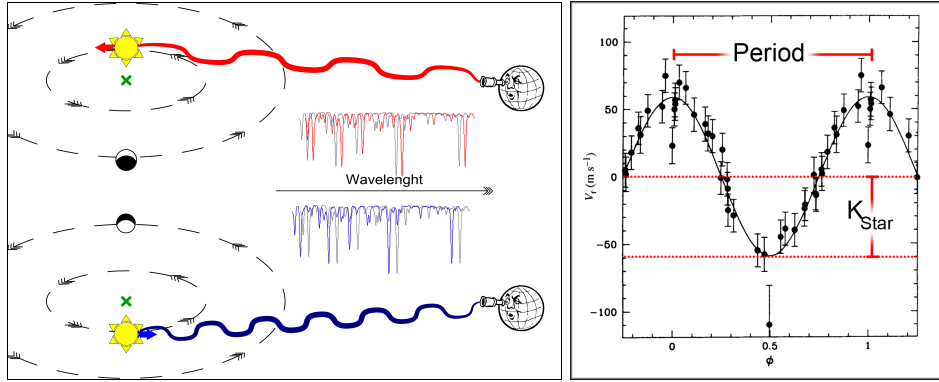


Figure 1.2: Left: Diagram of RV method. Right: RV variation for the detection of 51 Pegasi.
Credit: Mayor et al. (1995)

The radial velocity variation, directed along the line of sight, is given by:

$$RV = \gamma + K[\cos(\nu(t, P, T_0, e) + \omega) + e \cos(\omega)] \quad (1.1)$$

where γ is constant barycentre velocity of the system relative to the Sun³, K is the velocity semi-amplitude, e the eccentricity, and ω is the argument of periastron. The true anomaly ν , is a function of time t , orbital period P , and the time of periastron passage T_0 , and eccentricity.

The velocity amplitude K of a star of mass M_\star due to a companion with mass M_p with orbital period P , eccentricity e , and inclination⁴ i is (e.g. Cumming et al., 1999):

$$K = \left(\frac{2\pi G}{P} \right)^{1/3} \frac{M_p \sin i}{(M_p + M_\star)^{2/3}} \frac{1}{\sqrt{1 - e^2}}, \quad (1.2)$$

where G is the gravitational constant.

The key exoplanet property determined by the amplitude RV technique is the companion mass, relative to the orbital inclination $M_p \sin i$. As the companion mass is in the numerator of Equation 1.2 the RV technique is more sensitive to larger mass planets. Also since $K \propto P^{-1/3}$ the amplitude is greater for short period close in orbits⁵.

The RV method kick-started the exoplanet discipline by detecting the first exoplanet around a solar-type star 51 Pegasi (Mayor et al., 1995). The RV curve for 51 Pegasi is shown on the right side of Figure 1.2. The first discoveries were surprising as Jupiter mass planets in short period orbits⁶ were unlike anything in our Solar System and not predicted by standard planet formation theories. Several exoplanet discoveries followed in quick succession (e.g. Butler et al., 1996b; Marcy et al., 1996) with many confirming the existence of the type of planets now referred to as “hot-Jupiters” (Butler et al., 1997; Charbonneau et al., 2000).

The radial velocity amplitudes of the first exoplanets detected were around 60 m s^{-1} while the radial velocity signal of the Earth in a one year orbit around a solar-type star however is 8.9 cm s^{-1} (e.g. Figueira et al., 2010). Dedicated spectrographs, such as HARPS (Mayor et al., 2003) along with improved

³ Earth’s barycentre motion is well known and removed.

⁴ Relative to a plane that is tangential to the celestial sphere, $i = 90$ is edge on.

⁵ From Kepler’s Law $P^2 \propto a^3$

⁶ $M_p \sin i = 0.47 \text{ M}_{\text{Jup}}$ orbiting at 0.05 au for 51 Pegasi

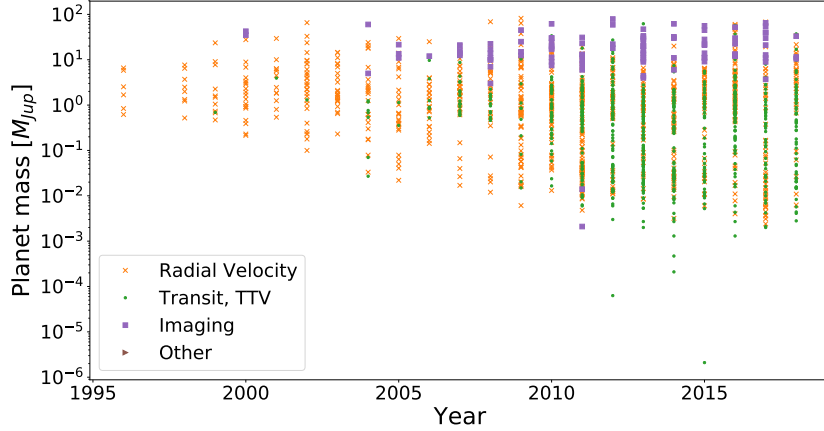


Figure 1.3: Exoplanet discovery year versus exoplanet mass showing a trend towards detecting lower mass planets. Exoplanets without a measured mass are not shown. The colours indicate the initial detection method.

reduction techniques (Lovis et al., 2007) pushed this mass detection limit down to the m s^{-1} level. ESPRESSO (Pepe et al., 2014a; Mégevand et al., 2014) is the next generation high precision optical spectrograph aiming to push the detection limits to 10 cm s^{-1} , to detect an Earth twin. The gradual decrease in measured mass of exoplanets over time is shown in Figure 1.3. The different symbols indicate the detection method, not necessarily the method used to measure the exoplanet mass.

Most RV detection has been performed using optical spectrographs. However, as the amplitude of RV signal is inversely proportional to the mass of the star ($\text{RV} \propto M_{\star}^{-2/3}$), there are dedicated surveys focusing on smaller mass M-dwarf stars (e.g. Reiners et al., 2018). M-dwarfs are inherently cooler and thus emit a majority of their stellar output in the near-infrared. New dedicated high-resolution nIR spectrographs have and are being designed and implemented to meet this demand e.g. CARMENES, NIRPS, SPIRou, CRIRES+.

1.2.2 Transit method

The transit method detects the presence of an exoplanet by observing the periodic dimming of the star due to the passage of the exoplanet between the star and observer, partially blocking the star. Geometry requires the orbit of the exoplanet to be aligned edge-on to the line of sight (low inclinations) for a transit to occur. The geometric probability, P , that a exoplanet transits is estimated by

$$P \approx \frac{R_{\star}}{a(1 - e^2)}, \quad (1.3)$$

where e is the eccentricity of the orbit, R_{\star} is the star radii and a is the semi-major axis of the orbit (star-planet distance) (e.g. J. W. Barnes, 2007). The probability of transit increases with the size of the star but decreases with distance to the star.

The drop in stellar brightness during the transit allows the measurement of the planet/star radius ratio:

$$\frac{\Delta L}{L} \sim \left(\frac{R_p}{R_{\star}}\right)^2 \quad (1.4)$$

where L is the luminosity of the star, ΔL is the maximum luminosity variation (transit depth), and R_\star and R_p are the radius of the star and planet respectively.

The transit method complements RV measurements as the inclination, i , of the orbit can be determined from the transit. This removes the $\sin i$ ambiguity found in the $M_p \sin i$ of RV detections so the true mass, M_p , of the exoplanet can be revealed. The true mass along with the planet's radius provides a value for the exoplanets average density⁷, hinting at the possible composition.

There are several other astrophysical phenomena which can mimic transiting exoplanet signals, created by configurations of two or more stars which may not involve an exoplanet. For example a transiting low-mass or white-dwarf star, grazing binary stars, or a transit in a multi-star system (see e.g. Cameron, 2012; Santerne et al., 2013). Follow-up RV observations (e.g. Santerne et al., 2011) are usually required to confirm the planets existence. Statistical validation techniques are also possible, such as the PASTIS software (Díaz et al., 2014), when follow-up can not be performed. These techniques assess the likelihood of the planet being a true planet against the different false positive scenarios, validating or confirming the planet if the likelihood is high enough.

The transit method has the highest false positive rate among the detection methods presented here. With RV follow-up, Santerne et al. (2012) found a false positive rate as high as 35% for short period giant planets, while Santerne et al. (2016b) found a 54.6% false positive rate of 129 giant planets with periods less than 400 days. These sub-sample false positive rates are however higher than the global false positive rate of 9.4% (Fressin et al., 2013)/11.3% (Santerne et al., 2013) found for Kepler.

The identification of unresolved multiple stars, such as a binary or an unrelated background star, can be achieved through high-resolution spectroscopy in which the spectral lines of individual stars can be separated (Kolbl et al., 2015). This is important to measure the correct radii of exoplanets as the extra light contribution from an unresolved secondary star will reduce the transit depth, mimicking a smaller transiting planet.

Due to the mass-radius degeneracy the transit of a single planet can not directly determine the planetary mass. However, in multiple planet systems, the masses and sometimes the presence of other planets in the system can be determined from perturbations in the transit time and duration (e.g. Holman et al., 2005; Holman et al., 2010). A large number of systems have been detected that show transit timing variations (TTV) and transit duration variations (TDV) (e.g. Holczer et al., 2016) due to the gravitational interaction between planets. The statistical validity of multi-transiting planets is more straightforward than single planets as the probability of having multiple false positives, being the product of the individual probabilities, is lower than having multiple planets in the system (Lissauer et al., 2012), making multiple planet systems easier to validate.

Stellar activity can affect the measurements determined by the transit method as it introduces variability in the luminosity of the star. For instance a star spot is a cooler region on the stellar surface due to concentrated magnetic fields which reduce convection. These cooler region have a lower luminosity appearing dark, and rotate with the star, creating a quasi periodic brightness variations near the stellar rotation period as they evolve. Examples of spots can be seen in the middle of the Sun from an image of the 2012 transit of Venus in Figure 1.4 (left). It shows several dark sunspots alongside Venus, although Venus did not cross them. Unlike for other stars, sunspots are spatially resolved. star-spots can influence the precision of the planet radius measured through the transit. An unidentified spot will appear to create a deeper transit, leading to a larger planetary radius determined. The presence of star spots on the

⁷ $\rho \equiv \frac{\text{Mass}}{\text{Volume}} = \frac{3}{4\pi} \frac{M_p}{R_p^3}$

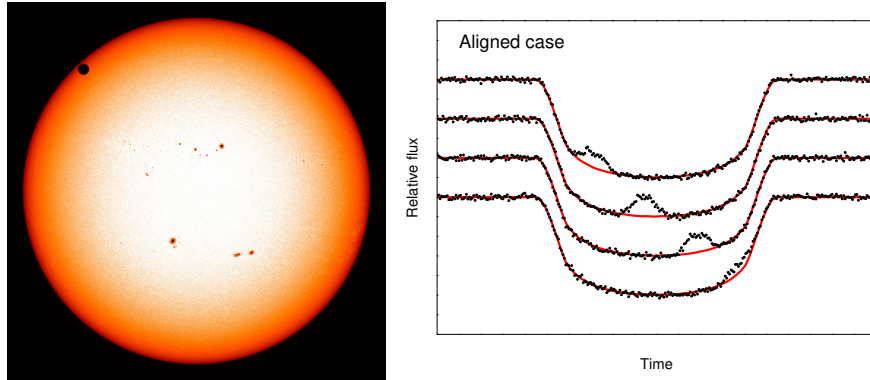


Figure 1.4: Left: Image from the 2012 transit of Venus obtained from the Solar Dynamics Observatory satellite. Venus is the dark circle in the top left of the Sun. Limb darkening is observed as the change in colour/brightness from white to red near the edge. Several sunspots are also observed on the surface of the Sun. Credit: NASA/SDO, HMIR. Right: Simulation of 4 successive transits crossing a star spot with the orbit aligned with the stellar rotation. The stellar rotation is 1/10 the orbital period. Adapted from Sanchis-Ojeda et al. (2013, Figure 1).

surface of a star can be observed during transit. If an exoplanet passes in front of a spot, the luminosity decrease from the spot is temporarily hidden and a small bump occurs in the transit shape. The presence of spots in successive transits (see Figure 1.4 (right)) can indicate the alignment of the stellar rotation to the planet orbital plane (Sanchis-Ojeda et al., 2013). In this simulation an orbit aligned with the stellar rotation and the transit crosses the spot in four successive orbits. In a misaligned case a spot would only be observed in one transit.

Some of the currently known exoplanet systems with the smallest radii and lightest mass have been detected through transit and later confirmed with high-precision RV follow-up (e.g. Queloz et al., 2009; Pepe et al., 2013; López-Morales et al., 2016; Ment et al., 2018). The vast majority of transit detections have come from Kepler (Borucki et al., 2011), which focused on a small patch of sky (0.25%) for four years continuously. Kepler’s impressive sensitivity compared to previous surveys, allowed it to detect planets down to around $2 R_{\oplus}$. However, CoRoT (Barge et al., 2008) and ground-based surveys, such as WASP (Pollacco et al., 2006), OGLE (Udalski et al., 2002), TreS (Alonso et al., 2004) have also had successful transit detections.

Following in Kepler’s footsteps the next generation transit hunter TESS (Ricker et al., 2015) has already announced discoveries of new transiting planets only months after launch (Vanderspek et al., 2018; Gandolfi et al., 2018; Huang et al., 2018a). It will eventually cover more than 90% of the sky with an impressive planetary yield expected of $\sim 10\,000$ exoplanets, with around 3500 the size of Neptune or smaller (Barclay et al., 2018; Huang et al., 2018b). However, the observation coverage is not uniform, with the majority of the ecliptic plane receiving only one month of observations, limiting the detection sensitivity to short period transiting planets. On the other hand, the ecliptic poles will receive almost one year continuous observation.

PLATO (Rauer et al., 2014) is another transit survey mission planned for launch in 2026. In contrast to Kepler it will focus on brighter nearby stars, with the goal to detect and accurately determine the planetary parameters of Earth-like planets in the habitable zone.

A smaller transiting mission, CHEOPS (Broeg et al., 2013), is also scheduled for launch at the end of

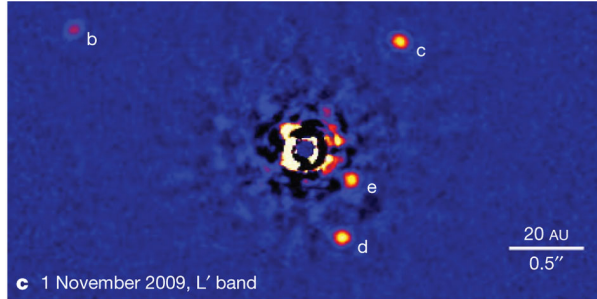


Figure 1.5: Direct detection of four exoplanets around HR 8799 (Marois et al., 2010).

2019. Unlike the transiting surveys mentioned above, CHEOPS will perform dedicated transit follow-up of bright stars with known planets, such as those found with RV surveys. It will provide high precision transit photometry, if the geometry allows, to obtain precise planetary radii.

1.2.3 Direct Imaging

The direct imaging technique involves directly imaging an exoplanet in orbit around a star. The first planets directly imaged were 2MASSWJ 1207334–393254 b using adaptive optics with NACO on the VLT (Chauvin et al., 2004), three planets around HR 8799 using angular differential imaging on the Keck and Gemini telescopes (Marois et al., 2008), and Fomalhaut b using chronography on the HST (Kalas et al., 2008). As an example, the direct image of HR 8799 is shown in Figure 1.5, where a fourth planet was revealed (Marois et al., 2010).

Direct imaging requires resolving the angular separation between the star and planet and is best suited to detect giant planets in wide orbits (>10 au) around nearby stars. This is shown by the clustering of direct image detections shown in Figure 1.3. Extremely young giants observed in the infrared are favoured as they have higher thermal emissions (while they are still cooling) and larger surface area resulting in a higher contrast ratio to the host.

High-contrast adaptive optics instruments, such as SPHERE@VLT (Beuzit et al., 2008) and GPI (Macintosh et al., 2008), are being used with several different techniques to observe targets closer to the star and with smaller contrasts, usually involving blocking or cancelling out the light from the star while retaining the signal of the planet (e.g. Marois et al., 2005; Mawet et al., 2005; Schmid et al., 2005; Sirbu et al., 2017b; Sirbu et al., 2017a; Wang et al., 2017). Ground based direct imaging requires adaptive optics to reduce the turbulence induced by the atmosphere, increasing the angular resolution down to the telescope diffraction limit.

On top of hardware based solution to the stellar contamination, clever observing strategies and cancelling algorithms. Angular differential imaging (ADI) (eg. Marois et al., 2005) is one such technique. ADI, disables the field de-rotator component in the telescope so that the viewing field rotates relative to the plane of the detector during the night. Several images taken at different angles are rotated to a reference position and stacked. The stacking of images from different angles cancels out the pseudo-static speckle caused by the telescope and optics while increasing the contrast of any faint object in the star's vicinity, i.e. a planetary companion.

The direct imaging technique is also used to observe circumstellar and protoplanetary disks, and has even captured images of planets during formation (e.g. Sallum et al., 2015). Combining direct images

from different photometric bands can allow for the creation of low-resolution exoplanet spectra (e.g. Kuzuhara et al., 2013; Zurlo et al., 2015).

1.2.4 Astrometry

Astrometry measures the precise position of the stars on the plane of the sky. The motion of a star with an exoplanet about its centre of mass can be observed in the periodic oscillating of position from its proper motion in the sky.

For a circular orbit the angle of the semi-major axis of the apparent orbital ellipse, the amplitude of the astrometric signature (θ), is given by

$$\theta = \frac{M_p}{M_{star} + M_p} \frac{a}{d} \quad (1.5)$$

where, M_p and M_\star are the planet and stellar mass, a is the semi-major axis (in au) and d is the distance from the observer to the system (in parsec) (M. Perryman, 2011).

This shows that the astrometric signal is proportional to the companion/star mass ratio and to the orbital radius, a . The amplitude of the astrometric signal also decreases inversely with distance from the observer, as the angles become smaller. This is unlike the RV and transit methods for which the amplitude is not affected by distance. Astrometry is complementary to the RV method as it measures the orbital motion perpendicularly to the line of sight, allowing the three-dimensional orbit to be determined. A modelled astrometric signal is shown in Figure 1.6, for a star at a distance of $d = 50$ pc, with a proper motion of 50 mas yr^{-1} , and orbited by a planet of $M_p = 15 M_{\text{Jup}}$, $e = 0.2$, and $a = 0.6$ au (M. A. C. Perryman, 2000). The straight dashed line shows the path of the system's barycentric motion viewed from the Solar System barycentre. The dotted line shows the effect of parallax (the Earth's orbital motion around the Sun, with a period of 1 year). The solid line shows the apparent motion of the star as a result of the planet, the additional perturbation being magnified by $\times 30$ for visibility.

Although astrometry has detected many binary stars (e.g. Gontcharov et al., 2000) and found several brown-dwarf companions (e.g. Sahlmann et al., 2011), the exoplanet discovery's are few. A $1.5 M_{\text{Jup}}$ mass planet in a roughly 1000 day orbit around HD 176051 was reported by Muterspaugh et al. (2010), and recently the astrometric perturbation of a known planet, Beta Pictoris b, was performed utilizing measurements from GAIA (GAIA Collaboration et al., 2016) and HIPPARCOS (ESA, 1997) to determine a mass of $11 M_{\text{Jup}}$ (Snellen et al., 2018).

The predicted astrometric variations for an exoplanet are at the level of sub-milliarcseconds and therefore are not achievable from the ground due to atmospheric turbulence. The most precise astrometric measurements come from spacecraft. These are currently being performed using GAIA with the recent release of astrometric parameters for 1332 million sources (GAIA Collaboration et al., 2018) and reaching a precision of 0.04 mas for the brightest stars (<14 magnitude). Simulations predict that more than 21 000 large mass planets ($1-15 M_{\text{Jup}}$) in long-period orbits should be discovered during the 5 year nominal GAIA mission (M. Perryman et al., 2014).

1.2.5 Microlensing

Microlensing is an astronomical effect predicted by Einstein's General Theory of Relativity. The mass of an object bends space-time which causes light to be visibly deflected around large mass objects. As a

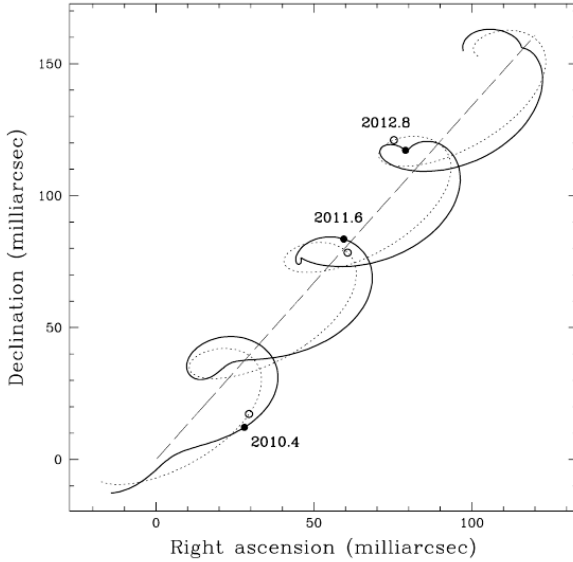


Figure 1.6: The modelled astrometric path on the sky from M. A. C. Perryman (2000). Showing a star at a distance of 50 pc, with a proper motion of 50 mas yr^{-1} , and orbited by a planet of $M_p = 15 M_{\text{Jup}}$, $e = 0.2$, and $a = 0.6 \text{ au}$. The straight dashed line shows the path of the system's barycentric motion viewed from the Solar System barycentre. The dotted line shows the effect of parallax (the Earth's orbital motion around the Sun, with a period of 1 year). The solid line shows the apparent motion of the star as a result of the planet, the additional perturbation being magnified by $\times 30$ for visibility.

star passes between Earth and a distant star it acts like a lens, bending and magnifying the light from the background star. The gravitation of a planet orbiting the lens star (if it exists) creates a distortion in the lens, leading to small caustics, deviations in the microlensing light curve for a single lens event (star without a planet).

An example is shown in Figure 1.7 where a lensing magnification of up to $\times 3$ is observed for OGLE2005-BLG-390 (Beaulieu et al., 2006). On the falling edge of the lensing event (and inset top right) there is a bump due to the presence of a $5.5 M_{\text{Jup}}$ companion.

The difficulties of microlensing is that they require the chance alignment between Earth, a nearby lens star, and a distance source star, which is unrepeatable. Some caustics are often difficult to fit and yield degenerate results, making characterization of the planet difficult. Follow-up measurements of a handful of microlensing events have been performed (e.g. Kubas et al., 2012; Batista et al., 2015; Santerne et al., 2016a) to break degeneracies. However, follow-up can be difficult as microlensing is sensitive to distant host stars, which are outside the ability of current spectrographs. It is also sensitive to planets with a wider orbital separation compared to transits and RV. Currently there are 87 planets in 82 systems detected by microlensing, as listed in the exoplanet.eu database.

The microlensing technique has been efficient in detecting Neptune analogue planets, distant planets similar in size to Neptune. Showing that cold Neptune planets are likely most common type of planet outside of the snow line (Suzuki et al., 2016), the distance from a star at which point it is cold enough for volatile compounds (e.g. H_2O , NH_3 , CO_2) to condense into solid ice grains.

Microlensing events are detected and monitored using dedicated global telescope networks such as OGLE, MOA, microFUN and PLANET. They focus their viewing towards the galactic bulge where there

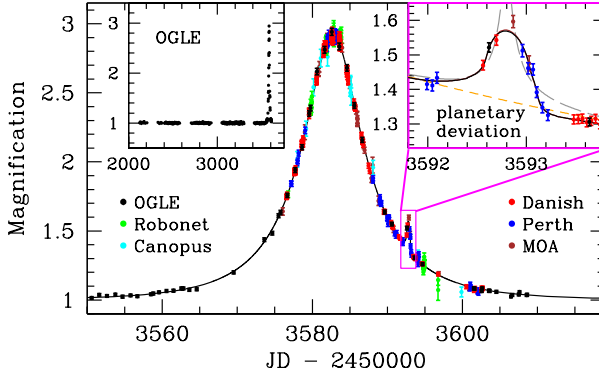


Figure 1.7: Microlensing magnification of OGLE2005-BLG-390 from (Beaulieu et al., 2006). The presence of the $5.5 M_{\text{Jup}}$ planet causes the small bump shown in the upper right inset plot.

are more stars and a higher chance for microlensing events to occur.

The precise stellar proper motions from the GAIA mission are being used to predict possible future alignments that could produce microlensing events (Klüter et al., 2018)

1.2.6 Pulsar timing

Pulsars are rapidly rotating neutron stars or white dwarfs formed after the death of a giant star, that radiate an intense electromagnetic beam. The timing variations of the millisecond pulsar⁸ PSR1257+12 led to the detection of the first planetary mass object orbiting another star (Wolszczan et al., 1992). There are two models of planet formation around pulsars: either they were present before the supernova explosion and survived it, or they formed from the remnants of the supernova afterwards (Starovoit et al., 2017). There is still a rarity of less than 10 pulsars with known orbiting planets.

The rarity of these events is partially associated to the technique which requires very precise instrumentation on high cadence (< milliseconds) to precisely measure the electromagnetic radiation from the pulsar. For example the first pulsar was detected with the Arecibo radio telescope. With the primary dish fixed into the mountain, its pointing is limited and achieved by moving the receiver. It has a limited number of stars that can be observed with a sufficient time coverage to detect planets around pulsars.

1.3 Detecting atmospheres

To help characterize an exoplanet, a detection of its atmosphere can provide useful information. After the detection of exoplanets and the measurement of their bulk properties, detecting their atmospheres is the next step. The detection of planetary atmosphere is difficult due to the low planet-to-star flux ratio. This requires high precision instrumentation to detect. For example the planet-to-star flux ratio in the optical is $\approx 10^{-4}$ for a hot Jupiter with a 3 day orbit, in which the main component is reflected star light. In the infrared the thermal emission of the planet dominates and the flux ratio rises to $\approx 10^{-3}$. These flux ratios require observations with signal-to-noise ratios of 10^4 and 10^3 in the optical and infrared respectively to achieve a planetary signal at the same level as the noise level. These detections are only just at the capabilities of the current generation of technology, and with very long observation cost.

⁸ Rotating at 9650 revolutions per minute

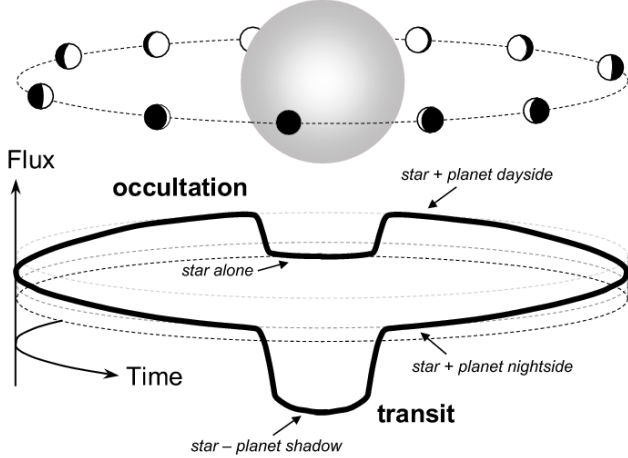


Figure 1.8: Illustration of the flux contribution from a star and planet in a transiting exoplanet system throughout its orbit. Credit Winn (2010).

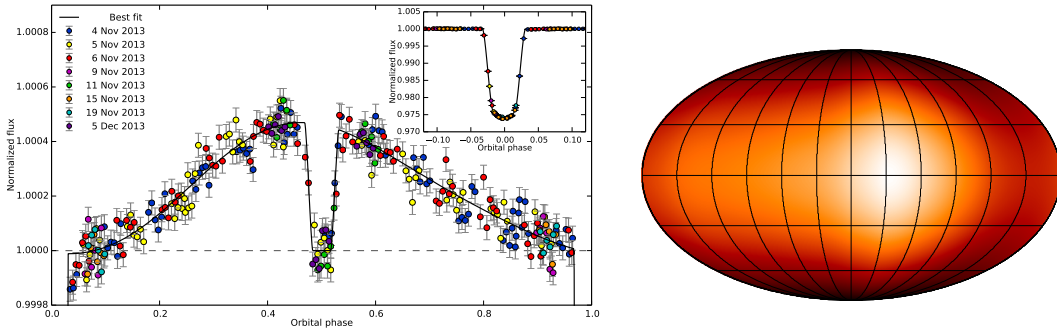


Figure 1.9: Left: Band integrated phase variation of WASP-43b from the HST (Stevenson et al., 2014). The primary transit is inset top right. The peak of brightness occurs before the secondary transit. Right: Global temperature map of the hot Jupiter HD 189733b obtained with Spitzer Space Telescope (Knutson et al., 2007a). The hottest point is offset from the sub-stellar point with the day side and night side temperatures around 930 K and 650 K respectively.

Several photometric and high-resolution spectroscopic techniques are showing promising results; these are detailed in the following sections.

1.3.1 Occultation and phase variations

Secondary transit and phase variations are an extension of the transit method, requiring higher precision to detect the reflection and thermal emission of the exoplanet. The observed light curve is analysed considering it has two components, not only light emitted from the star but also light from the planet, albeit at a much lower flux level. To help visualize and discuss the components of exoplanet atmospheres Figure 1.8 is provided showing a transiting planet in orbit around a star, in which the planet also passes behind the star causing an occultation. The planet is shown at several positions of the orbit indicating the proportion of day side and night side observed. Below the star and planet is a diagram showing the changing flux variation (solid black line) over time, following the orbit. If the orbital alignment is such that the planet will pass behind the star it will cause an occultation of the planet. At this point the only

light received is from the star alone, creating a baseline stellar measurement. While during the primary transit there is also a small thermal emission contribution from the night side of the planet, as well as it partially blocking the star.

Throughout the orbit of the planet there is a variation in the planetary flux due to the alternating day/night side of the planet observed. There are multiple components of the planetary flux, reflection and emission, that can be analysed with multi-band phase curves (e.g. Knutson, 2009; Esteves et al., 2013). Optical phase curves will mostly show the reflected light from the day side of the planet, allowing modelling of the atmospheric albedo (fraction of light reflected by the atmosphere), and can provide details on the atmospheric scattering (Madhusudhan et al., 2012) and aerosol composition (Oreshenko et al., 2016) through the optical phase function (day/night fraction). Thermal emission of the planet will provide stronger modulation of infrared phase curves and can provide insights into the atmospheres thermal structure and heat circulation (Goodman, 2009; Koll et al., 2016).

An example of phase variations in the infrared spectra of WASP-43b obtained with the Hubble Space telescope is given in Figure 1.9 (left). The large amplitude of phase variation between the day and night side indicates that the night side is much cooler and there is an inefficient heat circularity from the day to night side. A planet with an efficient day/night heat distribution mechanism would quickly equalize and have smaller phase variation. One key observable from Figure 1.9 is that the peak of the phase variation is offset from the location of the secondary transit. The hottest part of the atmosphere does not correspond to the sub-stellar point i.e. the point of the planet's surface closest to the star. This is also observed in surface temperature mapping of the hot Jupiter HD 189733b obtained with the Spitzer Space Telescope (Knutson et al., 2007a) shown in the right of Figure 1.9. Simulations of atmospheric circulation models find that this offset is caused by super-rotating equatorial jets which move the location of the hottest point of the planet (e.g. Heng et al., 2015, and references therein).

The point of occultation, at which the planet is completely blocked by the star, enables a baseline measurements for the star to be obtained without the planet. The depth of the occultation, gives a direct measurement of the relative brightness of the planetary disk if the star-planet radius ratio is known (Winn, 2010). It is a measure of the flux from the day side of the planet which can indicate the atmospheric reflection and thermal emission of the planet's atmosphere.

Spectra obtained during the occultation will have no planetary signal and can be used remove the stellar component from spectra obtained at other phases to obtain the planetary spectrum.

Detecting lingering molecular absorption post-transit has even been thought to indicate an extended atmosphere, torn away from and trailing the planet in its orbit as a comet-like tail. This is observed in Nortmann et al. (2018) which detect an extended Helium atmosphere around the Saturn-mass planet WASP-69b in the nIR at 1089 nm.

1.3.2 Transmission spectroscopy

When a transiting planet crosses in front of the host star it blocks out light from the star. However, a small portion of light passes through the atmosphere of the planet as shown in Figure 1.10. The light that passes through the exoplanet atmosphere is partially absorbed, and is faintly imprinted with absorption lines.

In planetary transits, usually defined by their duration and depth, there are degeneracies of the system properties from the transit shape in a single band, for example systems with differently sized planets and stars can have the same $\frac{R_p}{R_*}$ ratio. Observing transits in multiple band-passes (i.e. by splitting the

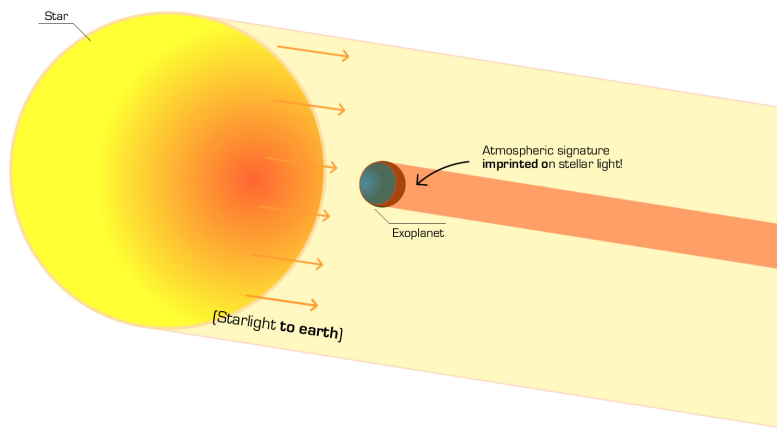


Figure 1.10: Diagram of transmission spectroscopy imprinting the atmosphere of the exoplanet. Sourced from <http://www.sc.eso.org/ esedagha/research.html>

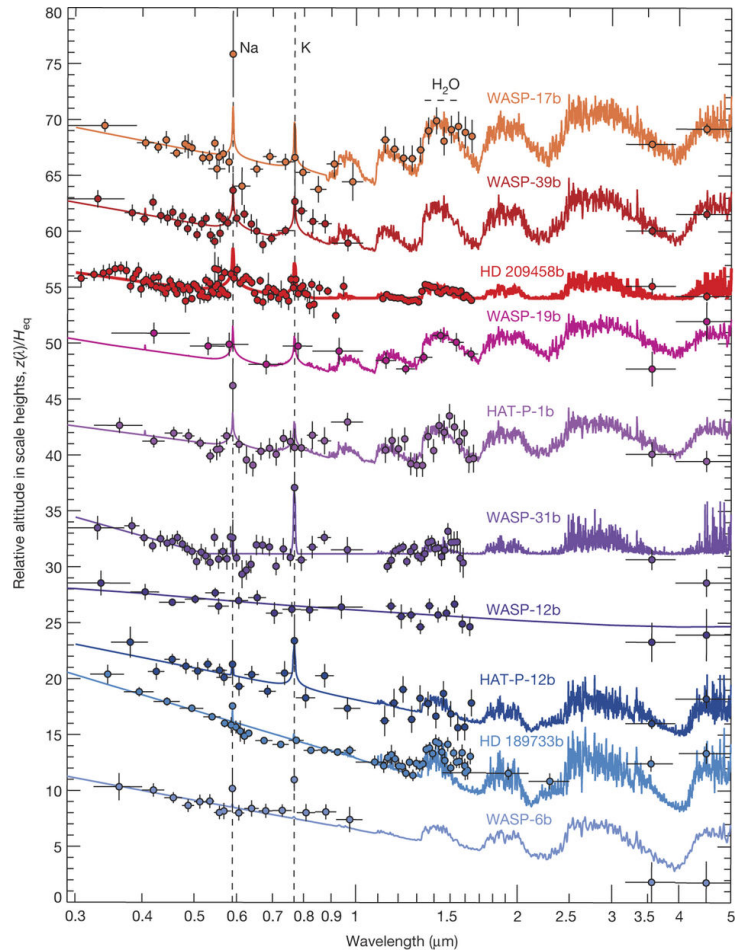


Figure 1.11: Transmission spectra (dots) for several Hot-Jupiter type exoplanets which increase in the amount of haze and clouds from top to bottom. The solid lines indicate the best fit atmospheric models. Credit Sing et al. (2016).

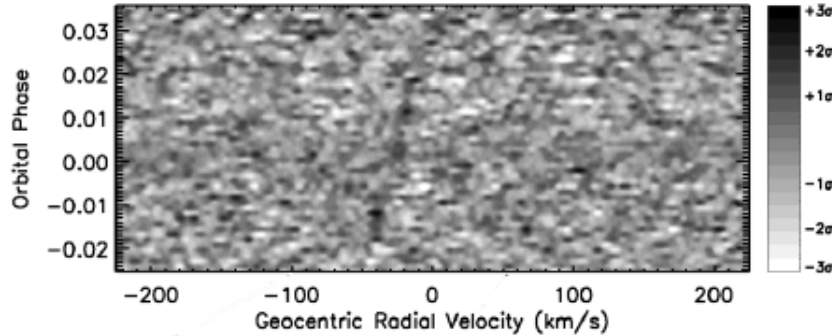


Figure 1.12: Cross-correlation signal of CRIRES observations during the transit of HD 209458 b with a CO template. Credit Snellen et al. (2010).

spectra observed during transits into several bands) has been shown to break the degeneracies between the stellar radius and the orbital inclination as well as determine the stellar limb darkening (Jha et al., 2000; Knutson et al., 2007b).

The radius of the transiting exoplanet can also appear to change size when observed at wavelengths where there is strong opacity in the atmosphere (e.g. Burrows et al., 2000; Seager et al., 2000). Transits in different wavelength bands will have varying depths, dependant on the opacity of the atmosphere to each band.

The transmission spectra observed with space observatories and ground based high resolution spectrographs has been used to detect several elements and molecules in the atmosphere. For example Na (Charbonneau et al., 2002; Redfield et al., 2008; Wyttenbach et al., 2015; Nikolov et al., 2016), H₂O (Tinetti et al., 2007; Brogi et al., 2014), CO (Brogi et al., 2014; Snellen et al., 2018), CH₄ (Redfield, 2010), Fe and Ti (Hoeijmakers et al., 2018). The presence of clouds in the atmosphere have also been detected, as they mask the atmospheric constituents as they produce wavelength-independent fluxes (e.g. Barman et al., 2011; Kreidberg et al., 2014; Sing et al., 2016).

Transmission spectra for several transiting Hot-Jupiter exoplanets from Sing et al. (2016) is shown in Figure 1.11. The amount of haze and clouds present in the atmospheres increases in the spectra shown from the top to bottom. Hazes are particles produced from chemistry in the atmosphere that results in the formation of involatile solids, while clouds form through the process of condensation and comprise of liquid droplets or ice crystals suspended in the atmosphere. Sing et al. (2016) defines hazes as having a Rayleigh-scattering-like opacity, which could be due to sub- μm sized particles, while they define clouds as having a grey opacity, for simplicity. The spectra near the top have clearer atmospheres, with little or no haze and clouds, show large alkali (Na and K) and H₂O absorption. Hazier and cloudier planets lower down the figure have strong optical scattering slopes with narrow alkali lines and have a partially or completely obscured H₂O absorption. This shows how the transmission spectra can reveal properties of the planetary atmospheres.

1.3.3 High resolution spectroscopy

Precise high resolution spectrographs that are able to spectrally resolve individual absorption lines, are key to analysing the atmospheres of exoplanets. Unfortunately, these are too large and bulky to fly in space, and they would be near impossible to keep in precise alignment during a rocket launch. The large collecting area of current and future ground based telescopes make high resolution spectroscopy

a great contender for obtained high-resolution observations for detecting and exploring exoplanetary atmospheres. Transmission spectroscopy is one beneficiary of high-resolution spectroscopy, although it is not the only technique to utilize high-resolution. Typically high-resolution and high SNR spectra are cross correlated with modelled stellar and/or planetary templates to recover the faint signal of the companion (e.g. Piskorz et al., 2016).

The development of new high resolution spectrographs operating in the nIR opens a whole new window to the study of exoplanets. The larger planet-to-star flux ratio in the nIR along with the richness of molecular lines have achieved some impressive detections. Notably with CRIRES there has been detections of the orbital motion, atmospheric constituents and exoplanetary winds through the detection of nIR molecular lines in the planetary atmosphere (e.g. Snellen et al., 2010; de Kok et al., 2013; Brogi et al., 2014; Brogi et al., 2016; H. Schwarz et al., 2015). The rotation rate of exoplanets has been achieved by measuring the spectral line broadening of lines in the nIR (Snellen et al., 2014; Brogi et al., 2016). As an example Figure 1.12 shows the result from Snellen et al. (2010). A series of sequential nIR spectra were taken during a planetary transit. A spectral template of CO lines is cross correlated against the series of spectra, resulting in a visible shift the CO lines during the transit due to the orbital motion of the exoplanet.

The spectrum of the star and planet usually cannot be spatially resolved so methods to identify and remove the stellar component are required. This usually involves constructing a high SNR stellar mask from observations, possibly at different phases (e.g. Rodler et al., 2012), to subtract from the observed spectra leaving behind the planetary signal. If the planet is able to be spatially resolved, then a spectrum of the planet could be obtained without stellar contamination (e.g. Snellen et al., 2015).

High resolution spectroscopy of atmospheres is not limited to transit spectroscopy with detections also possible for non-transiting exoplanets (e.g. Brogi et al., 2012; Brogi et al., 2014; Lockwood et al., 2014; Piskorz et al., 2016). It has been shown that the albedo of the exoplanet can also be measured by directly detected the reflected light off the planets atmosphere Martins et al. (2015) and Martins et al. (2016).

An advantage of high-resolution spectra is that it allows the molecular absorption lines of Earth's atmosphere to be resolved. This way they can be identified and corrected/removed to avoid contamination with the atmosphere of the exoplanet. Lower resolution and photometric methods are unable to fully resolve and remove Earth's atmosphere from ground based observations.

1.4 The diversity of exoplanets

Exoplanetary detections have challenged the theoretical formation models with their variety and distribution of sizes and, locations. For instance, the discovery of the hot-Jupiter class (large mass planets on close in orbits) challenged the accepted planet formation theories at the time (e.g Pollack et al., 1996; Boss, 1997) in which our Solar System was thought to be typical with small rocky planets close to the Sun and large giant planets further away.

The precise characterization of more exoplanets with the detection of exoplanetary atmospheres will allow for the constraints of exoplanetary composition and formation mechanisms to be improved. For instance, the core accretion model has been able to reproduce the large number of super-Earths, the correlation between star metallicity and planet frequency (e.g. Santos et al., 2004; Fischer et al., 2005), and the presence of many Hot-Jupiter and Neptune like planets in close-in orbits, with the help of

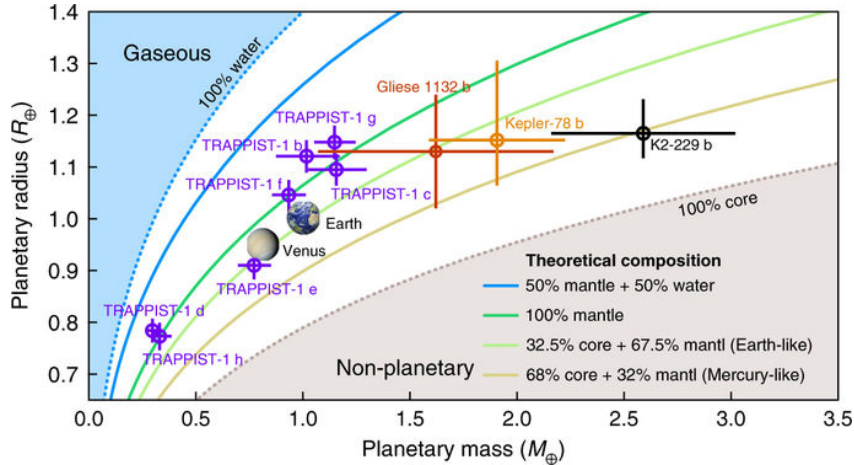


Figure 1.13: Mass-Radius diagram for rocky planets with composition contours. Adapted from Santerne et al. (2018)

migration mechanisms (e.g. Triaud, 2016). Recent models also combine both planetary formation and evolution to describe the observed exoplanets (e.g. Mordasini et al., 2012) and can reproduce general population properties in a statistically significant way (Mordasini et al., 2009).

A proxy for the composition and structure of an exoplanet is the average density, computed from the mass and radius. A mass-radius diagram is shown in Figure 1.13 for Earth-like rocky planets. The tracks show contours of mass-radius for different theoretical compositions (Brugger et al., 2017), while the circles indicate a number of detected small mass exoplanets, with K2-229 b being a super-Earth with a Mercury-like density (Santerne et al., 2018). The density can give an approximate composition but for a given mass there are an infinite number of combinations of metal/silicate/ice and gas that can produce the same radii (e.g. Seager et al., 2007). Low mass planets tend to be rocky and tend to have small or no atmosphere. With rock being in-compressible, to first order, it is relatively insensitive to the incident flux. The radii of solid exoplanets are sensitive to gas content of the atmosphere as a small increase in H and/or He can cause a large increase in radius (Adams et al., 2008).

When the gas component becomes dominate, planets begin to have radii independent of their mass (e.g. Lopez et al., 2014). The atmospheres of gas giants are also susceptible to stellar irradiation, with close-in Hot-Jupiters having inflated atmospheres and larger radii (e.g Fortney et al., 2010). Evaporation has also been used to explain exoplanet properties, such as the Fulton gap. A gap between super-earths and mini-neptunes with radii between 1.5–2.0 R_{\oplus} (Fulton et al., 2017).

Models of the mass-radius relation are important as they enable insight into the likely planetary properties when only either mass or radius can or has been measured. For example Chen et al. (2016) developed a probabilistic model over 9 orders-of-magnitude in mass and 3 orders-of-magnitude in radius, with the result shown in Figure 1.14. There are four separate power laws and three different transition regions fitted by the model. This breaks the mass radius relation into different regions classified after a representative example from our solar system. The lowest mass range is the rocky "Terran" worlds up to $2.0 M_{\oplus}$ and inclusive of dwarf planets, "Neptunian" worlds between $2.0 M_{\oplus}$ and $0.41 M_{Jup}$ and, "Jovain" worlds between $0.41 M_{Jup}$ and $0.08 M_{\odot}$. The transitions regions are indicative of a changing composition or physical processes (such as the hydrogen burning limit in stars) and consistent with other works (e.g. Weiss et al., 2013; Dieterich et al., 2014; Hatzes et al., 2015; Rogers, 2015).

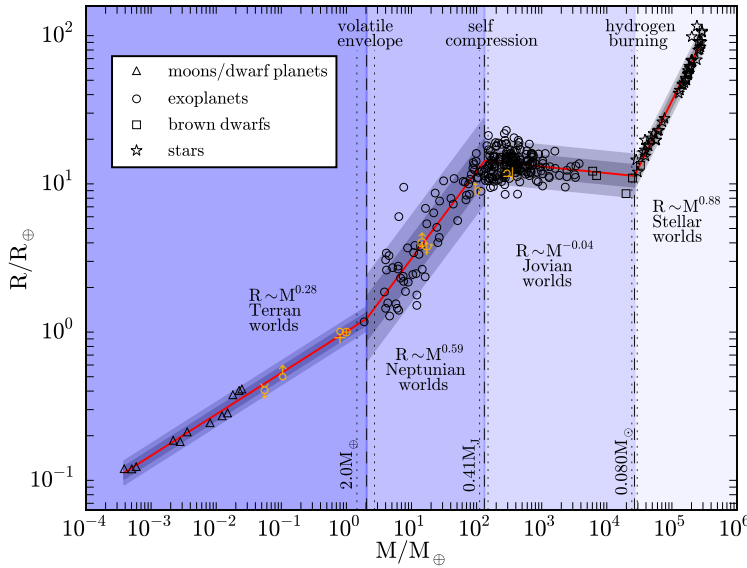


Figure 1.14: Mass-Radius relationship with probabilistic fit from dwarf planets to late-type stars from Chen et al. (2016). The black symbols represent the objects used to fit the model, with the key in the top-left, while the orange symbols represent the solar system planets. The red line indicates the average value, while the light and dark grey regions indicate the 65% and 95% confidence intervals.

1.4.1 Brown Dwarfs: bridging the gap

Recently, there has been a renewed interest in Brown Dwarf (BD) candidates triggered by exoplanetary searches as they bridge the gap between giant planets and low-mass stars. It is difficult to distinguish between giant planets and BDs with a loosely suggested definition of mass between 13–80 M_{Jup} ⁹ for Brown Dwarfs as this is between the Deuterium fusion mass of around 13 M_{Jup} (e.g. Spiegel et al., 2011) and the Hydrogen fusion limit of 80 M_{Jup} (Chabrier et al., 2000; Dieterich et al., 2014). Several works found similar properties on the two populations, like a similar density (Hatzes et al., 2015; Chen et al., 2016) seen in Figure 1.14 by the same power law spanning giant planets and BDs, while others have found intriguing differences. When classified using just mass and size Chen et al. (2016) find no difference between giant planets and Brown Dwarfs, with Brown Dwarfs just being large giant planets.

There is a paucity of BD companions in short period orbits around Sun-like stars ($\lesssim 5 \text{ au}$), compared to stellar or planetary companions, termed the *brown dwarf desert* (Halbwachs et al., 2000; Zucker et al., 2001; Sahlmann et al., 2011; Ranc et al., 2015) which can be seen as the gap in the "Jovian" worlds section of Figure 1.14. There are observed differences in the host star metallicity (Maldonado et al., 2017; Santos et al., 2017; Schlaufman, 2018) and orbital eccentricity distribution (Ma et al., 2014) either side of the period/mass gap with the lower mass BDs having properties similar to giant planets and high mass BDs having properties more like stars. There is a very strong hint of different formation mechanisms as BDs below the gap may primarily form via gravitational instability in protoplanetary disks, while above this gap BDs may form more like stellar binary from molecular cloud fragmentation (Ma et al., 2014).

As the number of known BDs orbiting solar type stars is low, the characterization of benchmark

⁹ $0.01\text{--}0.08 M_{\odot}$

BDs in the brown dwarf desert (e.g. Crepp et al., 2016) is beneficial in understanding this sub-stellar population and to help constrain formation and evolution theories (Whitworth et al., 2007). There is an inherent degeneracy between the mass, age and luminosity of a given BD (Burrows et al., 1997) because without sustained fusion, BDs cool down over time with an age-dependent cooling rate.

BDs in binary systems, unlike free-floating BDs (e.g Gagné et al., 2017), allow for the determination of their masses, when complemented with radial velocity (RV) and astrometry measurements. The RV technique provides the mass lower-limit ($M_2 \sin i$) of binary and planetary companions, while complementary astrometry measurements can often provide mass upper-limits (e.g. Sahlmann et al., 2011). Measuring or tightening the constraints of BD masses improves the understanding of mass dependence on BD formation processes. Photometry along with stellar evolution models (e.g. Baraffe et al., 2003; Allard, 2013) can also be used to estimate the mass of BD companions (e.g. Moutou et al., 2017) if there is sufficient orbital separation, and a precise determination of the age (Soderblom, 2010).

Without sustained fusion, brown dwarfs are relatively cool, and cool down over time, with temperatures below around 3000 K with a few BDs discovered with effective temperatures around 600 K (Leggett et al., 2009). At temperatures below 2600 K BD atmospheres become cool enough for condensation and the formation of molecular clouds and hazes (Allard et al., 2012b; Helling et al., 2014). Their spectra are rich with broad molecular bands as well as narrow neutral atomic species. They are dim and emit a majority of their light at infrared wavelengths, thus can be difficult to detect with optical instrumentation. However, they are a prime target for nIR instrumentation, such as CRIRES (e.g. Guenther, 2005; Crossfield et al., 2014).

1.5 Motivation for this thesis

As shown here there is a vast field of exoplanet research, with one of the current challenges being the detection of planetary atmospheres. The purpose of this thesis was to develop methodologies and tools to extract the minute signals of planetary spectra from nIR spectra. With access to nIR spectra of stars with suspected Brown Dwarf companions¹⁰ the higher temperature and relatively larger size of BDs compared to giant-planets makes the development of spectral recovery techniques for BD companions a logical step towards the spectroscopic detection of planetary atmospheres. For one, the spectrum of the BD companion will have a higher flux ratio than an exoplanet, and hence should be easier to detect. Secondly, being able to recover the spectra of these BD companions would help to constrain their mass and differentiate them from low-mass stars, helping to complete the puzzle regarding BD companions and their formation.

The original plan was to use the methodologies developed as a stepping stone to request observational time and apply the techniques on giant exoplanets in the nIR with the state-of-the-art detectors that are *still* in development (i.e. CRIRES+). In Chapters 2 and 3 the fundamental concepts of the radial velocity method and nIR spectroscopy are presented. In Chapter 4 models of the atmosphere are presented along with the stellar atmosphere and evolutionary models used in this work. The process of reducing nIR CRIRES spectra, with a comparison between two different reduction software is given in Chapter 5, followed by the post reduction calibration and atmosphere correction techniques required.

Chapter 6 presents spectral disentanglement techniques, focusing on the application of a differential subtraction technique to the nIR spectra of BD companions, as well as analysing the phase of the

¹⁰ Only the minimum mass $M_2 \sin i$ known

observations obtained. A second technique is developed in Chapter 7 which performs a fit to the observations with a model comprised of two synthetic spectral components.

The RV precision achievable in stellar spectra are important for the detection and characterization of extrasolar planets through the RV technique. Chapter 8 focuses on computing the fundamental RV precision of M-dwarf spectra in the nIR wavelength band. M-dwarfs are the best candidates for detecting small mass planets in their habitable zone, and are a major focus for the new and upcoming nIR RV spectrographs. A focus was shifted towards updating the tools to compute the RV precision to prepare for the release of the CARMENES nIR spectral library. With available CARMENES spectra a test of the spectral precision of synthetic models to reality can be performed.

Chapter 2

Radial Velocity

The radial velocity method, has been a consistent power-horse for the measurement of the orbital motion of binary stars and stars hosting exoplanets. In this chapter some of the key properties of Keplerian orbits and the RV signal will be presented along with an introduction to the notion of RV precision.

2.1 Keplerian Orbits

When two bodies are in orbit (two stars or a star and a planet) they orbit about their common centre of mass. Their 3-dimensional motion can be derived with a combination of Newton's universal law of gravitation, and represented through Kepler's laws. The full derivation is quite long and can be commonly found in several celestial mechanics texts (e.g. Moulton, 1914; M. Perryman, 2011; Fitzpatrick, 2012). The notes given here mainly follow Bozza et al. (2016).

Figure 2.1 shows the basic elements of the Keplerian orbit. There are several parameters required to situate the orbit in space. When dealing with exoplanetary systems, there is a *reference plane*, usually considered as tangential to the celestial sphere, that cuts the orbital plane with a *line of nodes*. The *ascending node* is the point on the plane at which the body crosses the reference plane moving away from the observer, and is defined relative to the vernal reference point, Υ , with the *longitude of the ascending node*, Ω , setting the orientation.

To fully parametrize a Keplerian orbit requires seven parameters. These are: a the semi-major axis of the elliptical orbit, e the orbital eccentricity, P orbital period, T_0 the *time of periastron passage*, i orbital inclination relative to the line of sight, ω the *argument of periastron*, and Ω . From RV measurements alone all of these parameters except for i and Ω can be determined. Ω is irrelevant for determining the orbital mass, but the inclination i is very important as it affects the projection of the velocity towards the observer, and as such affects the mass one ultimately aims to measure.

With a two body system with masses M_1 and M_2 , under the force of gravity, their orbits are elliptical orbits about their barycentre mass, as seen in Figure 2.2. In polar coordinates the ellipse of an orbit about the centre of mass (located at the focus F_1) is described by:

$$r = \frac{a(1 - e^2)}{1 + e \cos \nu(t)}, \quad (2.1)$$

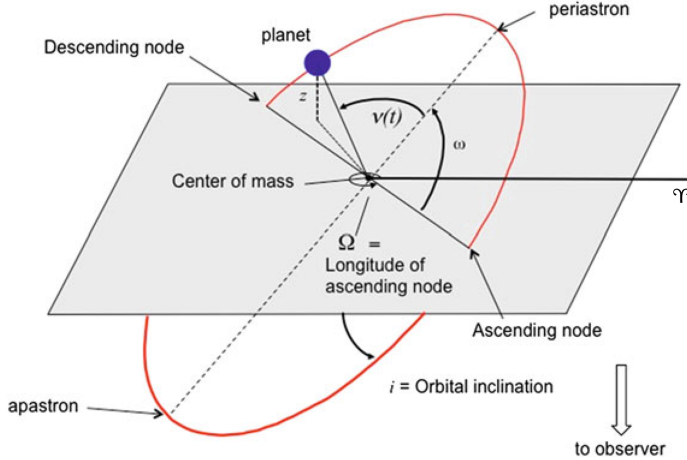


Figure 2.1: The basic elements of the Keplerian orbit. Adapted from Bozza et al. (2016).

where a is the length of the semi-major axis for the body, e is the eccentricity, ν is the *true anomaly* the angle between the current position of the orbiting body and periastron, as seen from the main focus of the orbital ellipse.

The true anomaly is not only a function time, t , but also the orbital period P , the *time of periastron passage*, T_0 , and eccentricity. It is geometrically related to the eccentric anomaly:

$$\cos \nu(t) = \frac{\cos E(t)}{1 - e \cos E(t)} \quad (2.2)$$

which can be numerically determined from the mean anomaly $M(t)$:

$$M(t) = \frac{2\pi}{P}(t - T_0) = E(t) - e \sin E(t) \quad (2.3)$$

The mean anomaly is the angle for the average orbital motion of the body at a time after periastron passage $t - T_0$.

From Kepler's second law¹ $\frac{1}{2}r^2 d\nu/dt = \text{constant}$, while in one full period P , the total area of the ellipse $\pi a^2(1 - e^2)^{1/2}$ will be covered, leading to:

$$r^2 \frac{d\nu}{dt} = \frac{2\pi a^2(1 - e^2)^{1/2}}{P} \quad (2.4)$$

The radial velocity is the change in r along the line of sight z . The component of r along the line of sight (from Figure 2.1) is:

$$r_z = r_1 \sin(\nu_1(t) + \omega) \sin i + \gamma \quad (2.5)$$

where γ is the mean velocity of the barycentre, and the subscripts '1' refers to the star. Differentiating

¹ Orbit sweeps out equal areas in equal times

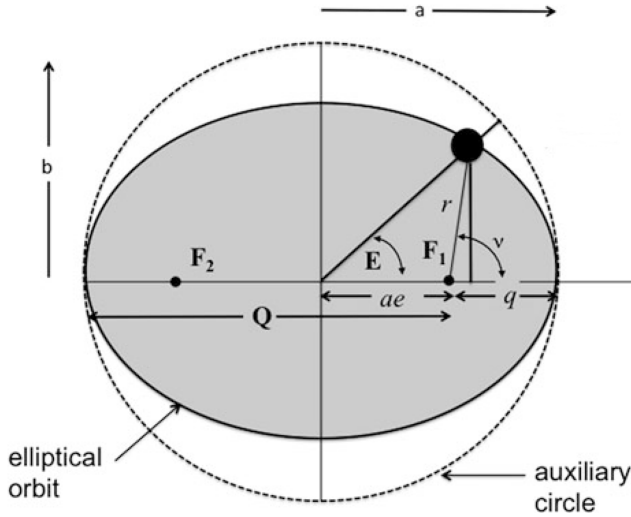


Figure 2.2: Elements of an elliptical orbit about the common centre of mass F_1 . ν is the angle to the position of the orbiting body from the perihelion (closest point to barycentre). The auxiliary circle has a radius equal to the semi-major axis of the ellipse. Adapted from Bozza et al. (2016).

Equation 2.5 and substituting in Equation 2.4 leaves the common RV equation:

$$RV = \dot{r}_z = \frac{2\pi a_1 \sin i}{P(1 - e^2)^{1/2}} [\cos(\nu(t) + \omega) + e \cos \omega] + \gamma \quad (2.6)$$

$$= K_1 [\cos(\nu(t) + \omega) + e \cos \omega] + \gamma, \quad (2.7)$$

where several parameters and constants have been condensed into K , referred to as the *semi amplitude*. In this case K_1 is the semi amplitude for the star. From the above equation it can be seen that a fit to the RV time series allow for the parameters K_1 , P , T_0 , ω , e , and γ to be derived.

2.1.1 Mass function

Once the orbital parameters have been determined then it is possible to determine the mass function of the system. From the centre of mass the distance between the two bodies is $a = a_1 + a_2$ where a_1 and a_2 are the respective distances to the barycentre with the subscripts ‘1’ and ‘2’ refer to the star and planet (or companion star), respectively. The value $M_1 a_1 = M_2 a_2$ can allow these re-arrangements:

$$a = a_1 \left(1 + \frac{a_2}{a_1}\right) = a_1 \left(1 + \frac{M_1}{M_2}\right) = \frac{a_1}{M_2} (M_1 + M_2) \quad (2.8)$$

Kepler’s third law ($G(M_1 + M_2)/4\pi^2 = a^3/P^2$) can be written as:

$$\frac{G(M_1 + M_2)}{4\pi^2} = \frac{a_1^3}{P^2} \left(\frac{M_1 + M_2}{M_2}\right)^3 \quad (2.9)$$

Table 2.1: The RV semi-amplitude induced by the planets with different masses and periods around a $1 M_{\odot}$ -mass star.

M_2	$K_1(P = 3 \text{ d})$	$K_1(P = 1 \text{ yr})$	$K_1(P = 5 \text{ yr})$	
M_{Jup}	140.8	28.4	16.6	m s^{-1}
M_{Nep}	7.60	1.53	0.90	m s^{-1}
M_{\odot}	44.3	8.9	5.2	cm s^{-1}

replacing a_1 with K_1 from Equation 2.6 results in the *mass function*, $f(M)$:

$$f(M) = \frac{(M_2 \sin i)^3}{(M_1 + M_2)^2} = \frac{K_1^3 P (1 - e^2)^{3/2}}{2\pi G} \quad (2.10)$$

This function can be determined directly from the measurable parameters P , e and K_1 . It shows that to determine the planet mass, M_2 , knowledge of the stellar mass, M_1 , must also be known. It can be seen from Equation 2.10 that the true mass of the planet M_2 is not obtained but only the projected mass $M_2 \sin i$.

For a planetary companion the approximation $M_2 \ll M_1$ can be made and for circular orbits ($e = 0$) the radial velocity semi-amplitude can be re-written as:

$$K_1 = \frac{28.4}{\sqrt{1 - e^2}} \frac{M_2 \sin i}{M_{\text{Jup}}} \left(\frac{M_1}{M_{\odot}} \right)^{-2/3} \left(\frac{P}{1 \text{ yr}} \right)^{-1/3} [\text{m s}^{-1}] \quad (2.11)$$

This can be used to calculate the RV amplitude created by different mass planets in various circular orbits as given in Table 2.1. The recently commissioned ESPRESSO optical spectrograph is designed with the goal of achieving 10 cm s^{-1} , which is the level of precision required to detect an Earth mass planet in a one year orbit round a Sun-like star.

If there is more than one companion/planet then there will be a gravitational influence between each other and their orbits become non-Keplerian, i.e. an N-body problem (e.g. Chenciner, 2007; Correia, 2018; Gao et al., 2018; Lillo-Box et al., 2018; Leleu et al., 2019). Assuming that the gravitational influence between companions is negligible, the RV signal observed in the host star can be treated as just a sum of tugs from each companion. For the two instances in this work where the target star has two companions, the companions will be treated separately, as if they were alone.

2.1.2 Binary mass ratio

In the above equation RV of the companion has not yet been addressed. Equation 2.6 above is the RV of the star in an elliptical orbit around the centre of mass between it and its companion. Similarly the elliptical orbit of the planet around the centre of mass is given by:

$$RV_2 = K_2 [\cos(\nu(t) + \omega_2) + e \cos(\omega_2)] + \gamma, \quad (2.12)$$

where $\omega_2 = \omega + 180^\circ$ due to the phase difference between the two components, resulting in the relative velocity (ignoring γ) of the companion being opposite the star and:

$$K_2 = \left(\frac{2\pi G}{P(1-e^2)^{3/2}} \right)^{1/3} \frac{M_1 \sin i}{(M_1 + M_2)^{2/3}} = \frac{2\pi a_2 \sin i}{P(1-e^2)^{1/2}} \quad (2.13)$$

The orbits of the host and companion are directly related through the mass ratio of the star and companion:

$$q = \frac{M_2}{M_1} = \frac{K_1}{K_2} = \frac{RV_1}{RV_2}. \quad (2.14)$$

Typically in exoplanet detections the companion (planet) is too faint to measure the planetary velocity. In fact exoplanet field originates from, and is the lower limit of, the study of binary stars, revolutionized by works such as Duquennoy et al. (1991). In double lined spectroscopic binary the spectrum of both stars can be identified in the blended spectra and the RV of both star and companion can be measured and monitored over the orbit. With both velocities the mass ratio of the binary can be found. The individual masses however are still not determinable due to the inclination $\sin i$ of the orbit.

In Chapter 6 the detection of the faint spectra of known companions is attempted, in order to determine the velocity change of the companion and hence the mass ratio. To help with the analysis and simulations the known orbital parameters (see Tables 6.1 and 6.2) are used along with the companion mass (M_2 or $M_2 \sin i$) to predict or estimate the RV of the companion using Equations 2.12 and 2.14. Note, that for the targets in which only the minimum mass ($M_2 \sin i$) is known and used in the mass ratio, this will result in the maximum RV semi amplitude for the companion. The estimated K_2 for each companion is provided in Table 6.4 while the RV for both components at the time of each observation is provided in Table 6.3.

2.2 Measuring the RV

So how does one measure the RV from an observed spectrum? The relative motion of the star towards and away from the Earth shifts the lines of its spectra through the Doppler Effect. In the non-relativistic limit this can be written as:

$$\frac{\Delta\lambda}{\lambda} = \frac{v}{c}, \quad (2.15)$$

where $\Delta\lambda$ is the wavelength shift of wavelength λ with a velocity relative to the observer of v , and the constant c is the *speed of light*. To measure the RV the relative positions of the stellar lines need to be measured over time. Typically this is done via the cross-correlation (CCF) of the observed spectrum with a template mask (e.g. a binary mask (Baranne et al., 1996) or weighted mask (Pepe et al., 2002)) suitable for the spectral type of the observed star. The CCF stacks together the spectral lines creating an “average” line, reducing the random noise on the individual N spectral lines by a factor of the order of \sqrt{N} . The CCF collapses the RV from all the lines into one number with higher precision than individual lines.

2.3 RV precision

To achieve a high-level RV precision, two types of noise must be controlled: systematic errors induced by the spectrograph and statistical error from the photon noise of the obtained spectrum.

Instrumental errors can occur through thermal or mechanical changes in the spectrograph. This causes variations in the instrumental profile which affects the line shape and position of lines in the spectrum, introducing fictitious RV shifts. These systematic errors can be reduced by using thermally and mechanically stabilized spectrographs, precisely calibrated in wavelength, along with the combination of thousands of lines (e.g. Pepe et al., 2014b).

The fundamental source of noise is photon noise, which follows a Poisson distribution. In the high flux case the number of counted photons N has a standard deviation \sqrt{N} .

A very general formula for the RV precision achievable of a given non-resolved spectrum, in terms of general spectral parameters is given by Hatzes et al. (1992) as:

$$\sigma \propto \frac{1}{\sqrt{F} \sqrt{\Delta\lambda} R^{1.5}}. \quad (2.16)$$

where F is the average flux level, $\Delta\lambda$ is the wavelength coverage (bandwidth) and R the resolution. \sqrt{F} represents the photon noise error (SNR) of the spectrum in the Poisson-dominated noise regime. While $\sqrt{\Delta\lambda}$ represents the increase in statistics from including independent measurements of lines. That is if σ_{RV} is measured on one line then after combining N lines the measured error becomes $\frac{\sigma_{RV}}{\sqrt{N}}$. This assumes that the spectrum contains a homogeneous distribution of uniform lines, per unit wavelength, and that the only noise present is photon noise. The precision depends more steeply on the spectral resolution with $R^{-1.5}$. At a higher resolution the slope of the spectral lines will be steeper as the spectral lines will have a higher contrast and a reduced line width, also narrower. The sharper spectral lines allow smaller pixels shifts on the detector to be measured, improving the RV precision.

As a star rotates its lines become broadened by an area preserving rotation kernel (see Section 8.2.2). In a similar way to the resolution, R , the RV precision is dependent on rotational velocity of the star ($v \sin i$) to the power 1.5, $\sigma_{RV} \propto v \sin i^{1.5}$.

An alternate derivation comes from Bouchy et al. (2001), based off Connes (1985), in which an optimal weight, $W(i)$, for each pixel, i , is calculated for a spectrum A_0 via:

$$W(i) = \frac{\lambda^2(i)(\partial A_0(i)/\partial\lambda)^2}{A_0(i) + \sigma_D}. \quad (2.17)$$

where λ is the wavelength and σ_D the detector noise. Here, $\partial A_0(i)/\partial\lambda$ is the slope of the spectral at each pixel so the edges of sharp spectral lines carry more weight.

The RV precision is calculated over all pixels as

$$\delta V_{RMS} = \frac{c}{\sqrt{\sum_i W(i)}}. \quad (2.18)$$

where c is the speed of light.

Both formulations have some key properties to achieve high RV precision: a high stellar flux F to achieve a high SNR, observed at high resolution to have sharp spectral lines. With steeper gradients $\partial A_0(i)/\partial\lambda$, the better defined the position of the line will be, allowing for a higher precision measurement

of the RV. The flux F or SNR of an observation increases with the number of photons collected which depends on the stellar brightness as well as distance², coupled with the telescope size and with the exposure time. In practice, this limits the highest precision RV measurements to relatively nearby stars. Cross-dispersed echelle spectrographs mounted on the largest telescopes are capable of delivering the high-resolution, high SNR and high bandwidth requirements necessary to achieve high precision RV measurements.

These formula have recently been used to assess the theoretical RV precision of synthetic spectra for the development of instrument designs of new nIR spectrographs (e.g. Figueira et al., 2016) as well as compare precision of real and synthetic spectra (e.g. Artigau et al., 2018). The RV precision will be analysed further in Chapter 8 with a detailed derivation of the Bouchy et al. (2001) method given and implemented to analyse the precision of nIR spectra.

² Basically the stars apparent magnitude.

Chapter 3

Near-infrared spectroscopy

In this chapter the basics of spectroscopy will be laid out, with the difference between optical and infrared spectroscopy given. A summary of several high-resolution nIR spectrographs relevant to this thesis will end this chapter.

3.1 Spectrograph basics

A spectrograph is a instrument of measuring the electromagnetic flux as a function of wavelength. All spectrographs have a few basic components common to all. A simple diagram with the basic components is shown in Figure 3.1. The left hand side is the telescope which is used to collect light and focus the image of the sky onto its focal plane. The spectrograph begins at a slit (or an optical fibre¹) placed on the telescopes focal plane used to block all but the light from the desired target. The light passing through the slit is diverging so a collimator is used to turn the diverging light into a parallel beam. The dispersing element is next and is responsible for dispersing the light into its separate components. This can be either a prism, grating or even both. The final elements are the optics for the camera, used to focus the dispersed (but still fairly collimated) light onto the detector, commonly a two-dimensional array of light sensitive pixels situated at the focal plane. Usually several optical elements, both lenses and mirrors, are used in combination to meet the constraints of the design specifications.

Figure Figure 3.2 shows the schematic for three different dispersion mechanisms: Snells law, a

¹ Fibres allow for the spectrograph to be situated far from the telescope, in a stabilized environment, and for a better isolation of the light from a specific source of interest.

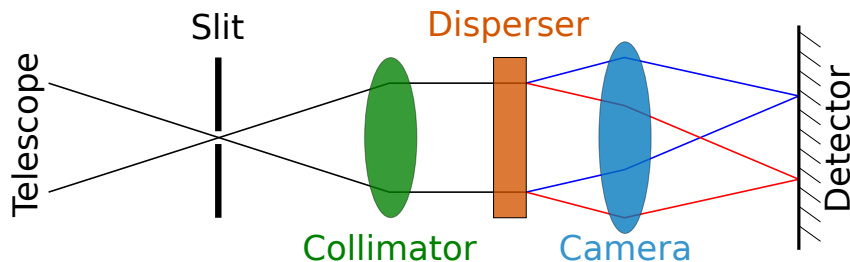


Figure 3.1: Diagram of the basic components of a spectrograph.

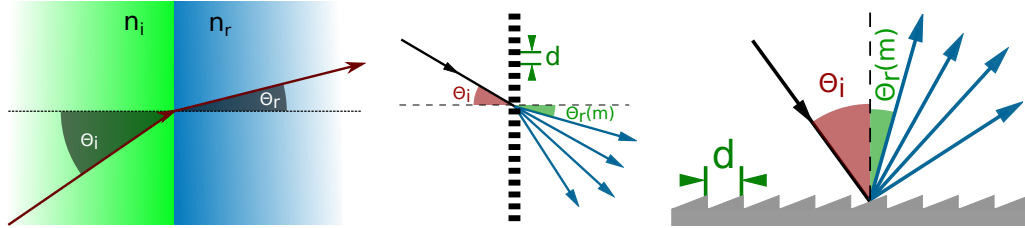


Figure 3.2: Left: Dispersion at an optical boundary due to Snell’s law. Middle: Dispersion from a transmission grating. Right: Dispersion from reflection grating.

transmission grating and, a reflection grating.

The left hand picture is a depiction of the refraction of light when passing between two materials with a different refraction index, n_i , and n_r . The angle of incidence θ_i and angle of refraction θ_r relative to the normal (perpendicular) of the surface are related through Snell’s law:

$$n_i \sin(\theta_i) = n_r(\lambda) \sin(\theta_r).$$

The index of refraction of a material is wavelength dependant so the angle of refraction will be different for each wavelength, causing dispersion, like a prism.

The two dispersion gratings in Figure 3.2 are comprised of parallel narrow slits (transmission) or grooves (reflection), very close together. Diffraction from these slits/grooves constructively and destructively interfere to create spectral orders that obey the grating equation:

$$m\lambda = d [\sin(\theta_i) \pm \sin(\theta_r)]. \quad (3.1)$$

Here m is the order number, λ the wavelength, d the spacing between the slits/grooves, and again θ_i and θ_r the incident and reflection angles respectively, relative to the normal.

This equation has degeneracy as different combinations of $m\lambda$ will be dispersed at the same angles. For instance the value $m\lambda$ for order $m = 54$ at $\lambda = 2100 \text{ nm}$ is that same as the order $m = 55$ at $\lambda = 2061.8 \text{ nm}$. This degeneracy can be overcome in two ways, either by applying a wavelength filter to specifically select only one order or by adding a cross-disperser.

A *cross-disperser* is a second dispersive element oriented to disperse the orders perpendicular to the grating dispersion direction. This allows for multiple orders to recorded simultaneously on a two-dimensional detector, dramatically increasing the wavelength coverage. Echelle spectrographs are a special type of spectrograph, with a groove shape and orientation specifically for high reflection angles. They are able to observe at a high spectral order (high m) to achieve a high dispersion and high resolution. At higher orders the range of wavelengths of a given order that fall within a fixed angle, corresponding to the angular size of detector, decreases.

Some important concepts for discussing spectrographs are the spectral resolution, resolving power, spectral coverage and spectral sampling. The spectral resolution, $\delta\lambda$, is the smallest difference in wavelength able to be identified. It is related to resolving power which is defined as $R = \frac{\lambda}{\delta\lambda}$. The resolving power, R , is colloquially also referred to as the resolution, although not quite the same. The higher the resolution (resolving power), R , the smaller the $\delta\lambda$ that can be measured on a spectrum, leading to highly sampled spectral lines and more precise measurement. The resolution $\delta\lambda$ corresponds to the

Table 3.1: Properties of popular optical/IR detector materials. ε_g is the material band gap, the minimum excitation energy. λ_c is the cut-off wavelength corresponding to the maximum wavelength for each material. Common values for the detector operating temperature for the materials are given as T_{op} .

Material	Symbol	ε_g [eV]	λ_c [μm]	T_{op} [K]
Silicon	Si	1.12	1.1	163–300
Mer-Cad-Tel	HgCdTe	0.09–1.00	1.24–14	20–80
Indium Antimonide	InSb	0.23	5.5	30
Arsenic doped Silicon	Si:As	0.05	25	4

full-width-at-half maximum (FWHM) of a non-resolved spectral line. As the name states the FWHM is the width of the line at half of the maximum height.

To be considered high-resolution, spectrographs typically have $R > 20\,000$, but the definition of “high” can differ between sub-fields of astronomy. The spectral coverage is the range of wavelengths able to be covered by the spectrograph, while the spectral sampling is the number of pixels required to sample the FWHM of the spectral lines. Nyquist sampling states that to avoid a loss of spectral information, the sampling must be performed at a rate at-least twice that of the spectral feature (\geq two pixels per resolution element). Most spectrographs aim to achieve a higher than this Nyquist sampling rate, for example HARPS has a sampling rate of 3.2 pixels per resolution element (Mayor et al., 2003).

3.2 The detectors

Optical and infrared spectrographs both follow the basic principles of spectroscopy however one major difference is in the design of their detectors. Nowadays the most common type of detector are focal plane arrays, a two-dimensional array of pixels located at the focal plane of the spectrographs camera. The purpose of the detector is to count the number of photons hitting each pixel in the array. This is achieved via the photoelectric effect on a crystalline structure, in which incident photons are transformed into electrons which can be recorded electronically. Silicon is the best material for the detection of optical light (0.3–1.1 μm), while in the near-infrared (1–5 μm) two materials are used: Mercury-Cadmium-Telluride (HgCdTe) and Indium Antimonide (InSb). In the mid-infrared (5–20 μm) arsenic doped Silicon is used (Si:As). A summary of values for different material properties is given in Table 3.1.

Since photon energy is inversely proportional to wavelength², longer wavelengths must have smaller band gaps³. However, smaller band gaps are also more susceptible to electrons excited by thermal energy, known as the dark current. The dark current is dependant on detector temperature, the pixel size, quality of material and the materials cut-off wavelength λ_c .

The technologies for optical and IR detectors are very different. Figure 3.3 shows the main architectural difference between CCD and CMOS with a very brief comparison between them given below. Charge-Coupled Devices (CCDs) are used in the visible. Their use of silicon allows for the photo-induced electrons to methodically transfer the charge from pixel to pixel along to one end. The electrons from each pixel pass into an amplifier to increase the signal, and are then measured as a voltage difference with an analogue-to-digital converter (ADC). As the charge is shifted between pixels, CCDs require high charge

² $E_{photon} = \frac{hc}{\lambda}$, where c is the speed of light, h is Plank’s constant and λ wavelength.

³ Energy level needed to excite an electron in the pixel material.

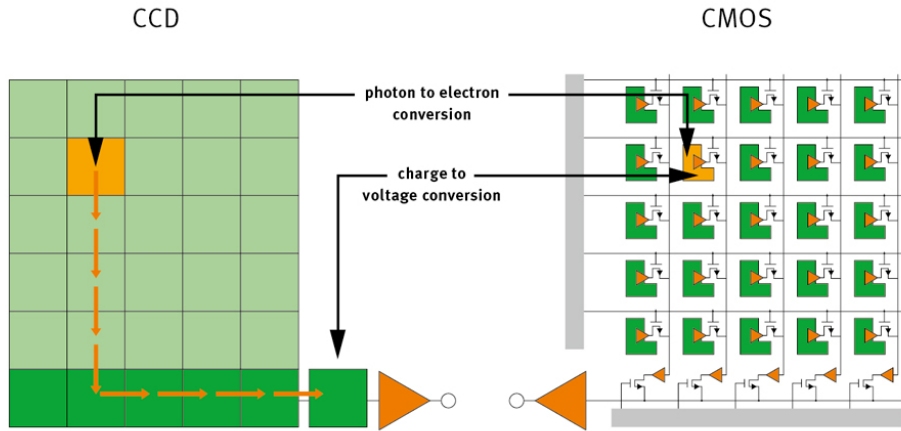


Figure 3.3: Schema differentiating CCD and CMOS detectors. In CCDs the charge is transferred to a specific pixel for measurement while in CMOS the charge is measured at the location of each pixel by individual amplifiers and ADCs. Credit <https://automatie-pma.com>.

transfer efficiency (CTE) to not leave charge behind, which would be assigned to the incorrect pixels. CCDs have an almost 100% filling of photosensitive material. However the λ_c cut-off of silicon makes them unsuitable for the IR. More information on CCDs can be found in Howell (2000).

For IR the technology of choice is CMOS (Complementary Metal Oxide Semiconductor). Unlike CCDs, each individual pixel contains the electronic circuitry to read, amplify and, measure the collected charge. Since the charge is read and amplified at each pixel there is no charge transfer between pixels and the readout is non-destructive. As a consequence, the same pixel can be read several times, averaging and thus reducing the effective readout noise of each pixel. In theory, if one averages N measurements before an observation (of a freshly reset detector), and N measurements of the observed charge after the observation, the readout noise can be reduced by a factor of $\sqrt{(N)}$, referred to as *Fowler Sampling* (Fowler et al., 1990). Reading a CMOS detector is very versatile as it can be read in multiple ways, with the ability to randomly read any pixel at any time, allowing for windowing⁴ or guiding on the detector. The filling area of the photosensitive material is reduced in CMOS due to the presence of support architecture that is required for the circuitry on the top surface, partially blocking some of the incident light, reducing their efficiency.

As it is impossible to have every individual amplifier perfectly identical, there is a small sensitivity and gain difference between CMOS pixels, which are exposed by calibrating with a uniform light source. This contrasts with the one or few amplifiers used in CCDs, which lead to extremely homogeneous amplification (as all pixels are amplified by the same amplifier). The CMOS circuitry is also intrinsically non-linear due to the changing capacitance as charge is collected. Irrespective if the charge is photo-induced or dark current, the circuitry measurement changes with the pixel charge level. This requires careful characterization of the non-linearities in the detector by calibrating its response to a uniform light source for a large range of integration times. For CRIRES there are a set of non-linearity coefficients that are applied while performing the flat-field corrections (see Section 5.1.2).

Other benefits of CMOS detectors are that they use lower power, and do not need a mechanical shutter as they can be reset electronically. While CCDs have been manufactured almost the same way

⁴ Reading only a specific area.

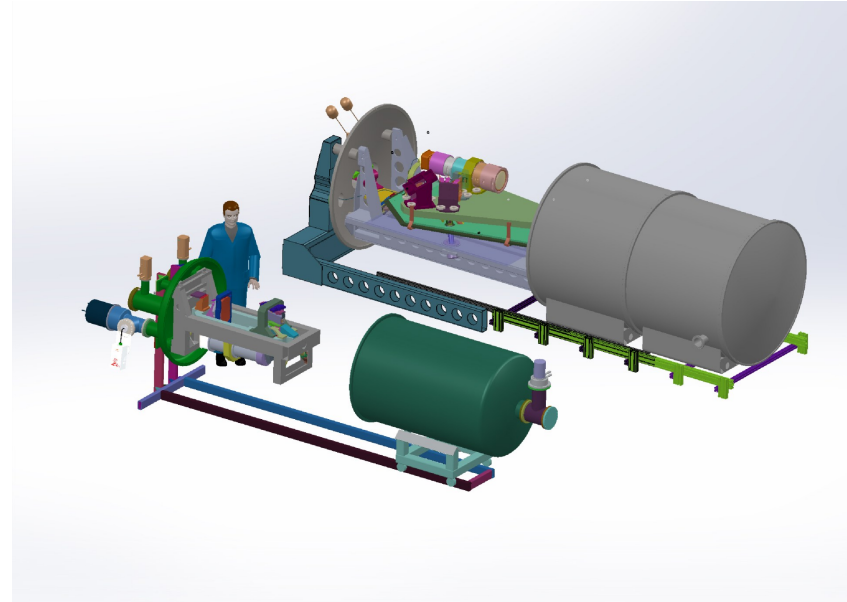


Figure 3.4: Side by side comparison of the NIRPS and SPIRou spectrographs. NIRPS is the smaller spectrograph. The cryostat's are shown in the open position and slide to enclose the instruments. Credit <http://www.astro.umontreal.ca/nirps/>.

for the last 40 years, CMOS technology is still advancing, partially driven by the consumer electronics market. Nowadays, most cellphone and laptop cameras use CMOS chips, helping to push investment in this technology. After the charge has been digitized into a number, the processes are once again similar for both technologies.

3.2.1 Spectrograph cooling

Spectrographs must be cooled down for their detectors operate effectively as seen in Table 3.1. This is achieved by placing spectrographs and their supporting components inside a vacuum chamber, away from all warm (radiating) components and precisely cooled⁵ to a low temperature. These are often referred to as cryostat's. Modern instruments use closed-cycle refrigerators, with for example, helium as the working fluid to achieve very stable low temperatures inside the cyrostat. Providing an isolated, temperature controlled, and stable environment for the spectrograph allows spectra science to be performed with the highest precision possible, essential for detecting and characterizing exoplanets.

Cooling plays two important roles for IR astronomy. Firstly, the thermal infrared emission from the components of the spectrograph surrounding the detector is reduced, diminishing the local background. Secondly, the detectors own thermally-generated background (dark current) is greatly reduced at low temperatures, leading to a gain in sensitivity.

Examples of two cryostat housings surrounding the spectrograph (but shown open) can be seen in Figure 3.4.

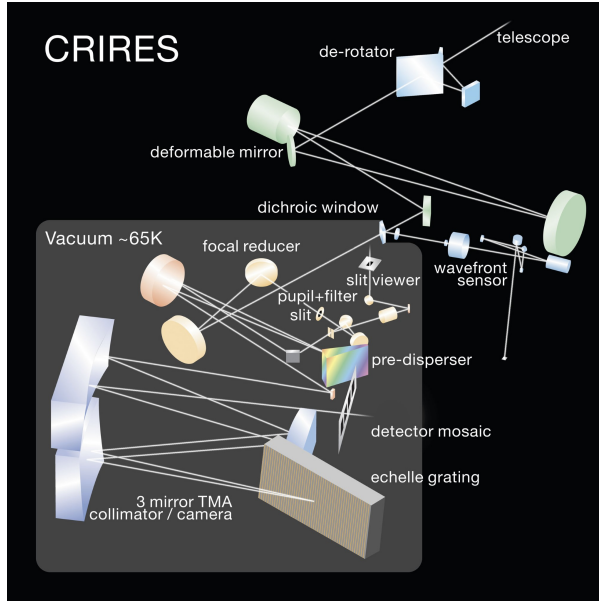


Figure 3.5: CRIRES layout schematic, taken from the CRIRES manual v93.

3.3 CRIRES

CRIRES (Cryogenic InfraRed Echelle Spectrograph) is an ESO IR spectrograph that was mounted on the Unit Telescope (UT1, Autu) of the European Southern Observatory's Very Large Telescope (VLT) (Kaeufl et al., 2004) and available from April 2007 through July 2014⁶. The main optical elements consist of a prism pre-disperser and an echelle grating with 31.6 lines/mm. The instrument provides resolutions up to 100 000 when used with a 0.2'' slit⁷. The wavelength range is 960–5200 nm with an instantaneous wavelength coverage of $\sim \lambda/50$. The spectra are imaged on a detector mosaic, consisting of four Aladdin III detectors (4096×512 pixel) in a row, with a gap of ~ 250 pixels between each chip. Adaptive optics (MACAO - Multi-Applications Curvature Adaptive Optics) can be used to optimize the signal-to-noise ratio and the spatial resolution. Figure 3.5 displays the schematic representation of the CRIRES optical layout.

CRIRES lead the way for high-resolution spectrograph in the IR with a resolution higher than any of its predecessors, and unique capabilities, like adaptive optics. As with any new instrument there were several problems that affected CRIRES during its science operations. For instance there were several mechanical issues with the slit: the slit edges were not parallel and there were issues with precise and reproducible positioning. Other issues that require post observation correction such as detector glow, the odd even effect, and the wavelength calibration are detailed in Sections 5.1.1, 5.1.2 and 5.3.1.

3.4 The new generation

Building off the success of CRIRES several other nIR spectrograph have and are being developed for different telescopes.

⁵ Temperature stability in the milli-Kelvin range.

⁶ Note this PhD research began in October 2014.

⁷ The rule of thumb for the resolution of CRIRES is $R = 100\,000 \times \frac{\text{slit width}}{0.2''}$, with the slit width in arcseconds.

Table 3.2: A comparison between the properties of some high-resolution nIR spectrographs.

	CRIRES+	CARMENES (red)	NIRPS	SPIRou
Location	Paranal, Chile	Calar Alto, Spain	La Silla, Chile	Mauna Kea, Hawaii
Latitude	24°40' S	37°13' N	29°15' S	19°49' N
Available (* expected)	2019*	2016	2019*	2019*
Telescope diameter (m)	8.2	3.5	3.6	3.6
Wavelength Range (nm)	920–5200	960–1710	970–1810	980–2350
Resolution	50 000/100 000	80 400	75 000/100 000	70 000
RV precision (m s ⁻¹)	2–3	~1	1	1
Operating Temperature (K)	70	140	80	77

Their science goals for these instruments involve some or all of the following:

- Detecting low-mass planets in the habitable zone around late-type stars (M-dwarfs).
- Detecting and characterising the atmospheres of exoplanets.
- Observe and monitor weather patterns, clouds, and hazes on brown dwarfs.
- Analysing the spectra and atmospheres of cool stars.
- The origin and evolution of stellar magnetic fields (through spectropolarimetry).

These goals are better tackled in the nIR as the targets (cool stars and exoplanets) are cooler and emit more of their light at infrared wavelengths.

A few points about some of the nIR instruments used in this work are detailed below with a summary also provided in Table 3.2. These are but a few of the almost two-dozen next-generation instruments extremely precise Doppler velocimeters being designed, built, or commissioned today tabulated in Wright et al. (2017).

3.4.1 CRIRES+

CRIRES was removed from operation in 2014 to undergo significant upgrades (Dorn et al., 2014). These include adding a cross-disperser to increase the simultaneous wavelength coverage by up to a factor of 10, improving the wavelength calibration by replacing the Th-Ar calibration lamp with a U-Ne lamp which has a richer set lines in the IR, and developing new multi-species gas absorption cells for the IR. The new upgrade adds the capability for spectropolarimetry using a polarization selective beam-splitter, in which the polarization of light in the spectrum can be analysed. The current detector mosaic will be replaced by 3 Hawaii 2RG detectors (6144×2048 pixels) at a pixel size of $18\text{ }\mu\text{m}$. A comparison between the new and old detector size is shown in Figure 3.6. The new detector mosaic will not only provide a larger area but also have a lower noise, higher quantum efficiency, better cosmetic quality and, a lower dark current⁸. CRIRES+ will operate with resolutions of $R=50\,000$ and $100\,000$ between 1000–5300 nm but requires 17 individual observations to cover this whole spectral range. The current estimate for the first light of CRIRES+ is late 2019.

⁸ https://www.eso.org/sci/facilities/develop/instruments/crires_up.html

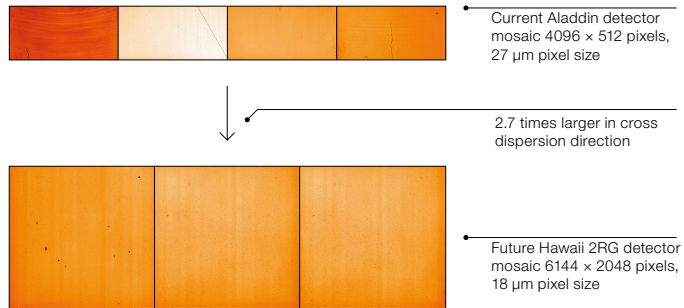


Figure 3.6: CRIRES detector focal plane array comparison with the new detectors. Credit Dorn et al. (2014).

3.4.2 CARMENES

CARMENES (Calar Alto high-Resolution search for M-dwarfs with Exoearths with Near-infrared an optical Échelle Spectrographs) (Quirrenbach et al., 2014) has been operating since 2016, performing a dedicated RV survey of ~ 300 late-type main-sequence stars with the goal of detecting low-mass planets in the habitable zone. It is mounted on the 3.5 m telescope at the Calar Alto Observatory in Spain, the light from the telescope passes through a beam splitter and enters into two separate spectrographs, one in the optical between 520–960 nm with a resolution of $R=94\,600$ and the other in the infrared between 960–1710 nm with $R=80\,400$. A library of single spectra of the M-dwarf targets CARMENES is monitoring was recently released in Reiners et al. (2018).

3.4.3 NIRPS

NIRPS (Near-InfraRed Planet Searcher) (Bouchy et al., 2017), on the 3.6 m telescope at La Silla, Chile, is a nIR extension to the HARPS spectrograph, one of the most prominent spectrographs detecting exoplanets via the RV method. It will operate in the wavelength range 950–1800 nm at a resolution between 75 000 and 100 000. A replacement for the HARPS telescope adapter will be used to split the light and send the optical and IR wavelengths via fibres simultaneously to HARPS and NIRPS respectively. The adaptor also includes adaptive optics and a new calibration unit.

3.4.4 SPRIou

SPRIou (SPectroplorimètre InfraROUge) (Artigau et al., 2014) is another high-resolution nIR spectrograph that will be installed at the CFHT (Canada-France-Hawaii Telescope) in Hawaii. It will provide a spectrum covering from 950–2340 nm in a single exposure at a resolution of around 75 000. Like the other spectrographs detailed here it is built to obtain very high radial velocity accuracy, of the order of meters per second over several years. It also includes spectropolarimetry, being able to derive the linear and circularly polarized state of the observed target.

A physical side-by-side comparison of the NIRPS and SPRIou spectrographs is shown in Figure 3.4, with NIRPS being the smaller of the two spectrographs.

Chapter 4

Atmospheres and Models

This chapter focuses on atmospheres, primarily the atmosphere of the Earth, through which stellar light passes, and the atmospheres of stars which produce the spectral lines observed. Both of these influence the spectra of the stellar light observed. In this work synthetic models of both the Earth's atmosphere and stellar atmospheres are used to correct and analyse the observed spectra. Details of each are included below.

4.1 Earth's atmosphere, in the nIR

While the Earth's atmosphere is important for life on Earth, it can be a nuisance for ground-based astronomical observations. The atmosphere is mostly transparent in the visible, with only minor transmission and emission features, but it is not uniformly transparent in the infrared.

As light from astronomical sources passes through Earth's atmosphere, the molecular species absorb specific wavelengths (corresponding to molecular rotational and vibrational energy levels) densely populating the nIR with absorption lines, commonly referred to as telluric absorption. Figure 4.1 contains the model telluric absorption spectrum for the atmosphere from 0.3–30 μm at $R \sim 10\,000$ from Smette et al. (2015). It clearly shows that there are regions where the atmosphere is mostly transparent (transmission of 1), with other wavelength regions (e.g. at 4.5 μm) that are completely opaque. Molecules which are the main contributors to the absorption are labelled.

The windows of transmission define the location of photometric bands in the infrared, with the common ones listed in Table 4.1 (see e.g. Sterken et al., 1992; Binney et al., 1998). These photometric bands are chosen for high average photometric¹ throughput, and do not consider the variable spectroscopic content inside the individual bands that becomes evident when observing at high resolution.

The most prominent absorber in the infrared is water vapour (H_2O) which is a strong absorber and defines the photometric bands as seen in Table 4.1. Water vapour is mostly concentrated in the lower 5 km, so infrared observatories are situated in dry places at high altitude. Even under ideal conditions the absorption of water vapour defines the IR bands. Other molecular species in the atmosphere such as: CO, CO₂, CH₄, are also important at various wavelengths.

When performing spectroscopy from the ground, the absorption spectrum of Earth's atmosphere

¹ Considering all photons in the band equally, regardless of wavelength (Very low resolution)

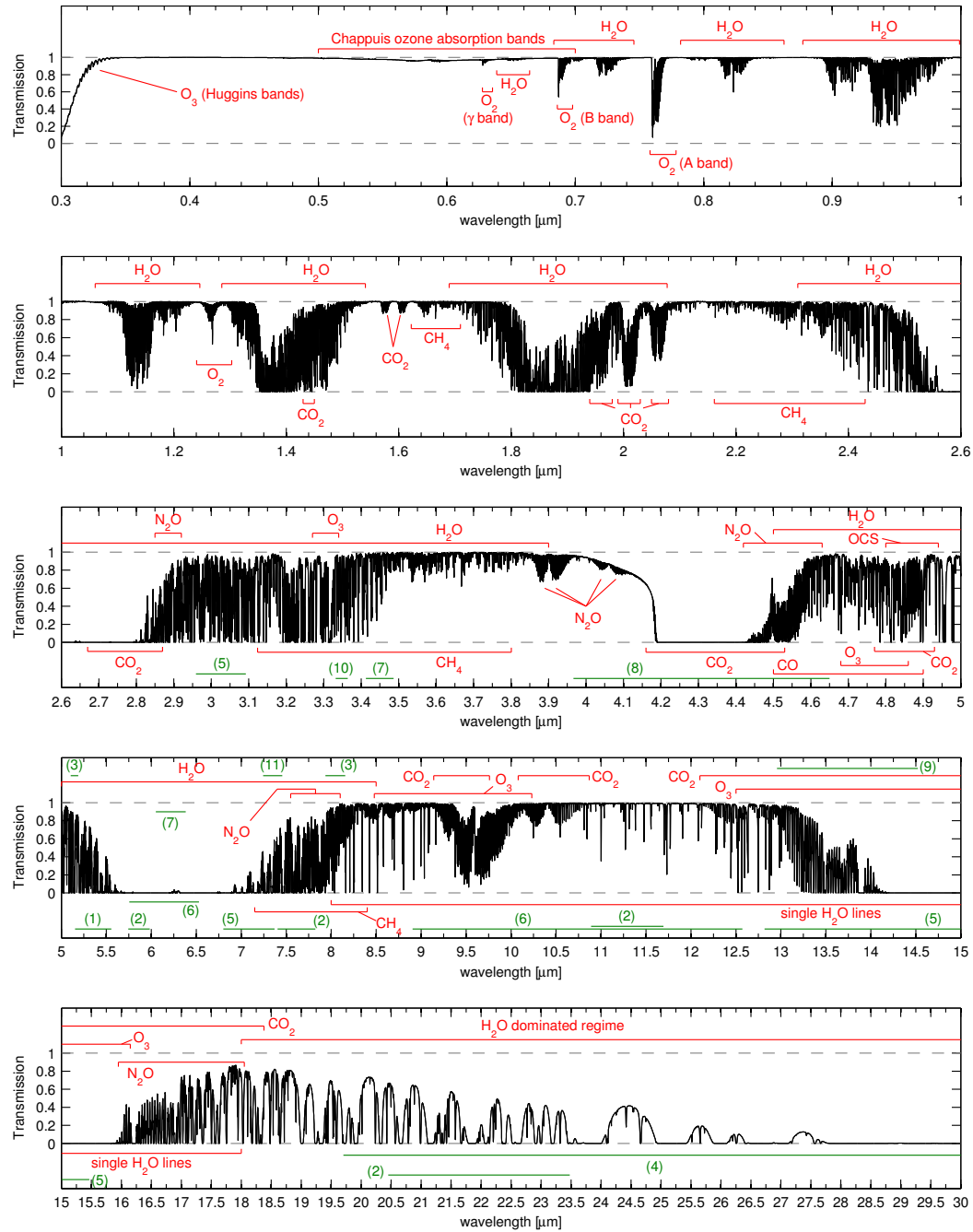


Figure 4.1: Telluric absorption map from 0.3–30 μm at $R \sim 10\,000$. The eight main molecules O₂, O₃, H₂O, CO, CO₂, CH₄, OCS, and N₂O contribute more than 5% to the absorption in some wavelength regimes. The red regions mark the ranges where they mainly affect the transmission, minor contributions of these molecules are not shown. The green regions denote minor contributions from the following molecules: (1) NO; (2) HNO₃; (3) COF₂; (4) H₂O₂; (5) HCN; (6) NH₃; (7) NO₂; (8) N₂; (9) C₂H₂; (10) C₂H₆; and (11) SO₂. Credit Smette et al. (2015, Figure 1).

Table 4.1: Standard infrared pass-bands.

Band	Central wavelength [μm]	Bandwidth [μm]
Z	0.9	0.06
Y	1.05	0.12
J	1.25	0.38
H	1.65	0.48
K	2.2	0.4
L	3.5	1.2
M	4.8	0.6
N	10.6	2.5
Q	21	5.8

contaminates the spectrum of the intended target. In high-resolution spectroscopy the stellar and atmospheric lines in principle can be resolved allowing for the identification and separation of the spectra. The removal or correction for the telluric lines is very important for accurate science, especially for detecting exoplanet atmospheres in which the species trying to be detected also reside in the atmosphere (Snellen et al., 2010; Brogi et al., 2014; de Kok et al., 2013).

The absorption of atmosphere is highly variable on many different time scales. The change in water vapour can occur rapidly over the course of the night while the concentrations of atmospheric constituents vary seasonally and even longer².

On top of this is the observational dependence on the airmass of the target. The airmass, defined as $m = \sec(\theta)$ with zenith angle θ , is the relative path length through the atmosphere compared to the zenith. Light from an object at a higher airmass passes through more atmosphere, and is subject higher attenuation due to the atmosphere constituents, following Beer's Law (Beer, 1852), and is contaminated with deeper telluric lines.

Works such as Snellen et al. (2010), fit and remove the telluric variation during a series of continuous observations³, to accurately remove the varying strength telluric lines and detect the absorption lines of exoplanet atmospheres. The telluric lines, being Earth based are stationary with respect to the instrument, where as stellar lines change their position due to the relative motion between Earth and the scientific target.

4.1.1 Telluric correction

Typically the absorption of the Earth's atmosphere (telluric lines) is corrected with the standard star method (e.g. Vacca et al., 2003). This method relies on the observation of a “standard star”, a very hot (O or A-type), fast rotating star. These stars have minimal spectral features themselves so allow the spectrum of the telluric lines to be revealed. The fast rotation is desired as it broadens the few remaining stellar lines, essentially diluting their impact. The telluric lines present in a spectrum of the science target can be corrected/removed by dividing it by the spectrum of the standard star.

The standard star needs to be observed close in the sky and in time to the science observation to have a similar atmospheric absorption to the science target. Airmass and molecular composition

² For instance the increase in atmospheric CO₂ caused by anthropomorphic climate change has caused a 6% change to CO₂ line depths since 2000 (Smette et al., 2015).

³ 51 spectra of the same target in 180 minutes for Snellen et al. (2010)

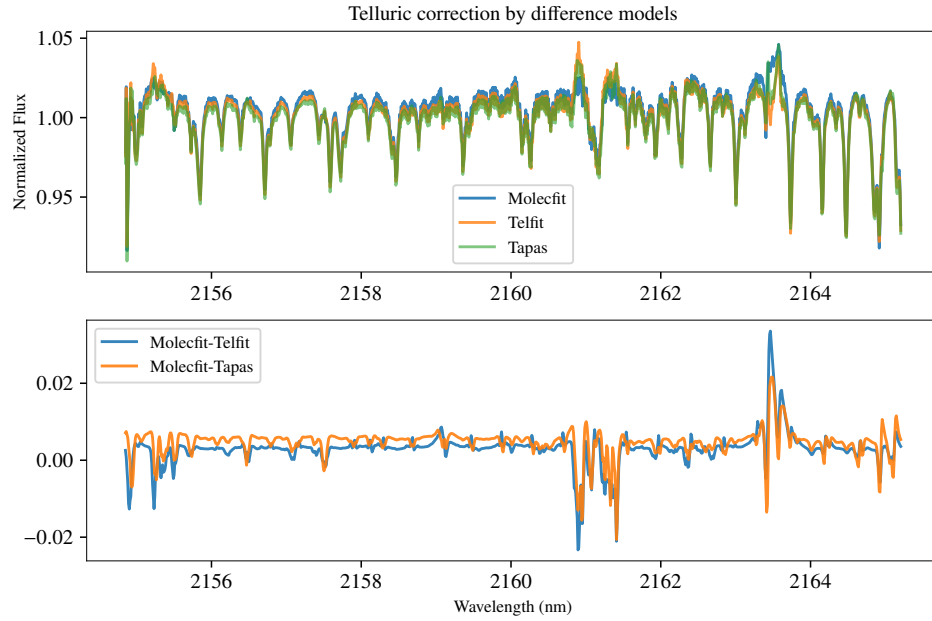


Figure 4.2: CRIRES spectra with telluric correction applied using the Molecfit, TelFit and TAPAS. Top: The telluric corrected spectra. Bottom: Difference between the corrected spectra from the different methods.

differences along the different paths to the target and standard will however cause variations in the line strengths (Bailey et al., 2007).

Recently synthetic modelling of telluric absorption has gained popularity with several works focusing on correcting telluric absorption with synthetic models (e.g. Bailey et al., 2007; Cotton et al., 2014; Seifahrt et al., 2010) and achieving better correction than the standard star method. There are several different software packages available which usually build upon the standard line-by-line radiative transfer model code LBLRTM (Clough et al., 1995). Some examples are TelFit (Gullikson et al., 2014), and ESO’s Molecfit (Smette et al., 2015) which both model and fit a synthetic absorption spectra to observations, whereas TAPAS (Bertaux et al., 2014) just creates synthetic models based on atmospheric data for an observation (without fitting). The synthetic models at high resolution are very sensitive to atmospheric constituents, especially water vapour, and observing conditions such as the airmass.

Recently Ulmer-Moll et al. (2018) compared the telluric correction efficiency between TelFit, Molecfit, TAPAS, and the standard star method. They found that Molecfit and TelFit synthetic corrections lead to smaller residuals for lines arising from H₂O, while the standard star method corrects for O₂ lines best. All methods (synthetic and standard star) resulted in a scatter of 3–7% inside the telluric lines (Ulmer-Moll et al., 2018). They also find that an observatory tailored atmospheric profile leads to reduced scatter inside telluric lines and that the correction performed better with lower precipitable water vapour.

As an example Figure 4.2 shows the telluric correction using the three different methods, Molecfit, TelFit and TAPAS⁴, of a spectrum extracted for this work, detector #4 of observation HD 4747-1 (see Table 6.3). There are differences between the models of around 2% level, with the largest difference near the deep telluric line around 2163 nm.

Since sufficient telluric correction can be achieved through synthetic modelling, the observational

⁴ Performed here by Solène Ulmer-moll.

requirement is halved as the standard star is not required, allowing more observing time for science. This is the case with the CRIRES observations analysed in this work. This work utilizes the synthetic telluric spectra produced from TAPAS to used correct the telluric lines in CRIRES spectra. This is detailed further below.

4.1.1.1 TAPAS web service

In this work the telluric correction is performed using the TAPAS models. Telluric absorption spectra can be obtained with the TAPAS (Transmissions of the AtmosPHERE for AStromonical data) web service⁵ (Bertaux et al., 2014). TAPAS uses the standard line-by-line radiative transfer model code LBLRTM (Clough et al., 1995) along with the 2008 HITRAN spectroscopic database (Rothman et al., 2009) and ARLETTY atmospheric profiles derived using meteorological measurements from the ESPRI data centre⁶ to create telluric line models.

The ARLETTY atmospheric profiles have a 6 hour resolution. However, differences to the actual profile at the time of observation are likely to exist as there are seasonal, daily, and even hourly variations in the volume mixing ratio of atmospheric constituents (e.g. Ramanathan et al., 1953; Thoning et al., 1989; Schneising et al., 2009). The most prominent being water vapour, which is directly related to the local weather conditions.

There are several parameters that can be submitted to the web service to define the requested telluric spectra, such as: target coordinates, date and time, location, spectral resolution, wavelength range and units choice observations, as well as the atmospheric profile and the choice of several atmospheric constituents to be included in the model spectra. TAPAS produces the telluric spectrum and sends a link to the results via email.

4.1.1.2 Requests for this work

Synthetic telluric absorption were requested from the TAPAS web service for this work. These were to match the CRIRES observations which are presented in Table 6.3.

The mid-observation time for each observation was used to request a synthetic spectrum individually for each observation, with the ARLETTY atmospheric profiles and vacuum wavelengths selected. The telluric models were retrieved without barycentric correction to keep the telluric lines at a radial velocity of zero with respect to the instrument. For each observation one model was requested with all available atmospheric species present, convolved to a resolution of $R = 50\,000$ corresponding to the resolution of the CRIRES data, and a further two models without the instrumental profile convolution applied. For these two extra models, one contained only the transmission spectra of H_2O while the other contained contributions from the all other constituents except H_2O . This was to explore a known issue with the depth of H_2O absorption lines in the TAPAS models (Bertaux et al., 2014) (see Section 5.3.2). An example of the telluric spectrum for the H_2O and the non- H_2O species is given in Figure 4.3. To obtain a combined model of all species these two can be multiplied together.

4.1.1.3 Issues with TAPAS

There are a number of issues encountered when using the TAPAS web service, mainly due to interaction with the website. Often their service was down for weeks at a time without any warning or notification.

⁵ <http://cds-espri.ipsl.fr/tapas>

⁶ <https://cds-espri.ipsl.upmc.fr>

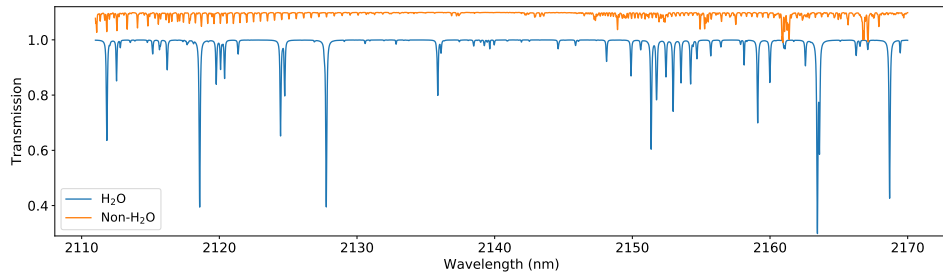


Figure 4.3: Telluric absorption spectrum for H₂O and the non-H₂O species available from TAPAS. In the wavelength range 2110–2170 nm and both at a resolution of 50 000. A vertical offset of 0.1 has been added to the non-H₂O spectrum.

With this, time was wasted filling out and submitting requests via the the web form without a response, or a returned spectra. There was also a variable level of success between different web browsers. A number of bug reports were submitted to the owners of the webpage without any acknowledgement.

The webpage is useful for quickly obtaining a small number of spectra but can be tedious for many spectra. For this work this was around upwards of 50 telluric spectra, (3 for each of the 17 observations). TAPAS offers the ability to request multiple spectra at a time but this was found to be unreliable when attempting to request more than four spectra in a single request.

A script⁷ was created to automatically generate the data necessary to fill out a TAPAS request for each CRIRES observations. The script scanned the CRIRES header for information such as the mid-time of observations, target coordinates, slit width etc. and populated the XML request form provided by TAPAS. The script output is copied and pasted into the web browser for submission.

Trial and error was needed to understand all the XML form entries, such as the molecules requested and the atmospheric model to use (ARLETTY) to achieve a valid TAPAS request. The main issue was with the TAPAS ID number. Each TAPAS request has an ID number (which is provided with the email response). This ID number needs to be correctly set in the XML form before submission. This number is incremented by 1 with each submission made to the server; as such, the absolute request ID is unknown to the requester. If a submission is made via the XML request with the incorrect ID number a response will be returned with the currently correct ID number, but a failed request will be returned due to the incorrectly submitted ID number. This can then be used to increment the ID number by 1 and hopefully make a valid request. Unfortunately, if another user makes a TAPAS request between submissions the ID number will again be invalid. It is unknown if multiple transmission spectra could have been requested at the same time with the XML form.

There is another issue with a one hour time offset between the requested and the time returned by TAPAS. For instance if the requested time was for an observation at 0200h UTC then the transmission spectrum returned by TAPAS is for 0100h UTC. This changes the position of the target, the airmass and potentially the ARLETTY model used (6 hour time steps), affecting the strength of the telluric lines. It is tedious to remember to offset your input time by one hour to obtain the correct time, and slightly more work when you also have to adjust the date when going backwards past 0000h. When submitting the XML script the time that is returned is the time requested. Attempts were made to bring this issue to the attention of the TAPAS team in 2016 but as of August 2018 this issue is still present.

⁷ Available at <https://github.com/jason-neal/equanimous-octo-tribble/blob/master/octotribble/Tapas/>

These issues need to be considered when requesting TAPAS spectra, adding unnecessary difficulty to the relatively simple process.

4.1.1.4 Telluric masking

The telluric spectra from TAPAS can not only be used for correcting individual spectra but are also easily used to create a wavelength mask. For instance Figueira et al. (2016) and Artigau et al. (2018) use TAPAS spectra to mask out atmospheric lines deeper than 2% for computing the photon noise limited radial velocity precision. A telluric wavelength mask is similarly used in Chapter 8 when extending the analysis of Figueira et al. (2016). The telluric model used for this is an average of 52 TAPAS spectra (one per week in 2014), simulated at La Silla Observatory at an airmass of 1.2 ($z = 33.5^\circ$). This is to incorporate long-term variations of absorption over the year. Masking is applied by defining a cut-off line depth, typically 2%, at which to mask out any deeper lines.

4.2 Synthetic Stellar models of cool stars

The understanding of stellar physics is strongly built upon modelling, incorporating stellar structure, atmospheres and evolution, pieced together with several physical, chemical and hydrodynamical models. One particular model output of importance for this work are the synthetic stellar spectra. These spectra can be compared to observed spectra to attempt to classify and understand the stellar populations, as well as test the models fit to reality. There is an ever evolving effort to improve these stellar models and synthetic spectra to better match the observations; incorporating more physics, chemical reactions, line lists, and using the latest element abundances. This work extensively uses the PHOENIX-ACES synthetic spectra, with a little experimentation with the BT-Settl models. A collection of several theoretical stellar spectral libraries can be found at the Spanish Virtual Observatory Theoretical Spectra Web Server⁸.

The Kurucz (1979), among others, models are popular synthetic models for stars ranging between G-O type with effective temperatures between 5500–50 000 K. For cooler stars, M-dwarfs and even Brown Dwarfs the stellar models are based on the PHOENIX code (e.g. Hauschildt et al., 1997). Initially created for studying the ejecta of Novae it was *Extended* to low mass stars and Brown Dwarfs (Allard et al., 1995). The PHOENIX modelling code has evolved over time incorporating new physical models to better explain the atmospheres. The *NextGen* models (Hauschildt et al., 1999) treat the stellar atmosphere as a gas in chemical equilibrium, but the resulting spectra for very low mass stars was poor due to no treatment of dust in the stellar atmospheres.

The Allard et al. (2001) *COND* and *DUSTY* models both investigate the extreme limits of clouds in the atmospheres of cool stars. They include condensation physics (Gibbs free energy, gas partial pressures etc.) into the chemical equilibrium model, as well as the optical interaction of light with the dust/condensates (dust opacities and scattering). The *DUSTY* models simulate ‘inefficient/no settling’ where condensation/dust forms and stays in the atmosphere and it affects the spectrum through the dust opacities. At the other extreme the *COND* models ignore the dust opacities and simulate ‘efficient settling’, in which all the condensates and dust clouds fall below the spectrum forming region.

The treatment of clouds and dust is important for the modelling of low mass stars and Brown Dwarfs. The *DUSTY/COND* models are similar above 2600 K but below this temperature they diverge due to the crystallization of silicates in the atmosphere (Allard et al., 2001). These are only a few of the

⁸ <http://svo2.cab.inta-csic.es/theory/newov/index.php>

Table 4.2: Full parameter space of the PHOENIX-ACES spectral grid. Reproduced from Husser et al. (2013).

	Range	Step size
T_{eff} [K]	2 300 – 7 000	100
	7 000 – 12 000	200
$\log g$	0.0 – 6.0	0.5
[Fe/H]	-4.0 – -2.0	1.0
	-2.0 – +1.0	0.5
$[\alpha/\text{Fe}]$	-0.2 – +1.2	0.2

physical considerations implemented in the synthetic models. The other notable changes are due to use of specific line lists used. The models prefixed by the word AMES use the NASA-AMES H₂O and TiO line lists, while the BT models use the Barber et al. (2006) H₂O line list. Between model versions the use of improved solar abundance measurements is also included (Asplund et al., 2009).

In this work synthetic spectral from the PHOENIX-ACES and to a lesser extent the BT-Settl stellar models are used. These are further evolutions of the *DUSTY/COND* models and are detailed below.

Both sets of synthetic models do not handle the affects of radiation from a neighbouring star, which may have an affect on the BD companions studied here.

4.2.1 PHOENIX-ACES models

The PHOENIX-ACES models (Husser et al., 2013) are a descendant of the *COND* models. They include condensation in equilibrium with the gas phase while ignoring dust opacity and any mixing or settling which is important for cooler atmospheres. As such the PHOENIX-ACES models are restricted to $T_{\text{eff}} > 2300$ K as the treatment of dust/clouds is not handled. It uses the most recent version (16) of the PHOENIX code and is suitable for the spectra of cool stars. THE PHOENIX-ACES models uses the Astrophysical Chemical Equilibrium Solver (ACES, Barman 2012) new in version 16 of PHOENIX to perform state-of-the-art treatment of the chemical equilibrium. It also adds parametrisations for the mass and mixing-length, and uses the solar abundances of Asplund et al. (2009).

As noted in Husser et al. (2013) there are significant differences between the spectra from PHOENIX-ACES and previous PHOENIX model spectra. For instance the equation of state solver ACES strongly affects the stellar structure and different line and molecular band strengths. Unfortunately there are several changes introduced with PHOENIX-ACES making it difficult to distinguish and quantify the different effects.

The full parameter grid space of the pre-computed PHOENIX-ACES spectra is given in Table 4.2 although this full range is not utilized in this work. This work uses models below 7000 K with no α variation⁹. This means the models are likely to be more adequate to thin-disk stars close to solar metallicity (Adibekyan et al., 2012). The spectral sampling of the grid are $R \approx 50\,000$ for 300–2500 nm, covering the wavelengths used here.

The lower temperature limits of this library limits the stellar mass to the high mass BDs. For example a $T_{\text{eff}} = 2300$ K corresponds to a BD/low-mass star¹⁰ with $M \sim 84 M_{\text{Jup}}$ at 5 Gyr from the Baraffe et al.

⁹ α elements are created during nuclear fusion by the successive addition of helium nuclei (alpha particles), thus have atomic numbers with an integer multiple of 4.

¹⁰ With the transition between 80–90 M_{Jup} .

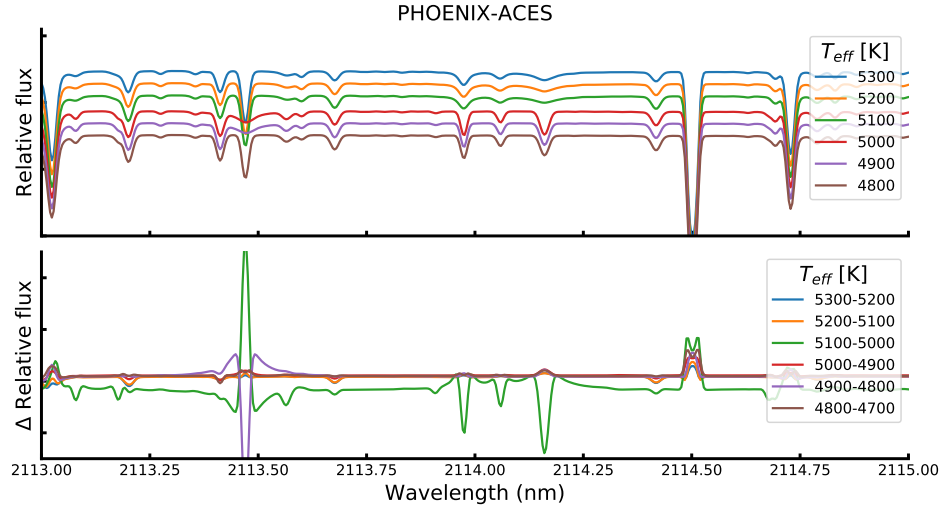


Figure 4.4: Top: Incremental PHOENIX-ACES model spectra between 4800–5300 K with $\log g=4.5$ and $[\text{Fe}/\text{H}]=0.0$ fixed. Bottom: Difference in flux between successive models separated by 100 K. Apart from near absorption lines there is a discontinuity in the flux of the PHOENIX-ACES models between 5000 and 5100 K.

(2003) evolutionary models, (see Section 4.3).

While using the PHOENIX-ACES models a discontinuity in the stellar flux is observed between 5000 K and 5100 K. In Figure 4.4 several PHOENIX-ACES spectra in incremental steps are shown in a small wavelength range of 2113–2115 nm. The line profile seems to change suddenly between the model with 5000 K and 5100 K, causing a slight discontinuity in the models. This slightly impacts the use of these models while attempting χ^2 fitting in Chapter 7. The bottom panel shows the flux difference between models separated in temperatures of 100 K (one grid step). The difference between 5000 and 5100 K (green) is offset from the other model differences. This is potentially caused by the change in treatment of the model atmospheres at 5000 K. For instance Husser et al. (2013) mention that the reference wavelength defining the mean optical depth grid, is fixed to $\lambda_{\tau} = 1200$ nm for $T_{\text{eff}} > 5000$ K and $\lambda_{\tau} = 500$ nm for hotter stars in the PHOENIX-ACES modelling.

4.2.2 BT-Settl

The BT-Settl models (Allard et al., 2012a; Allard et al., 2012b; Rajpurohit et al., 2013; Baraffe et al., 2015), are an evolution of both the *DUSTY* and *COND* models. They are better suited for the entire range of BD temperatures down to 400 K, through hydrodynamical modelling of the mixing and settling of dust/clouds in the atmosphere of cool dwarfs (Freytag et al., 2010). The BT-Settl models now also include 3-D radiation transfer (Seelmann et al., 2010).

The BT-Settl are generally more difficult to work with because of their file format (in comparison to PHOENIX-ACES). The most recent BT-Settl spectral library, using version 15.5 of the PHOENIX code, is designated CIFIST2011_2015¹¹ (Baraffe et al., 2015) and includes newer Caffau et al. (2011) solar abundances and is combined with evolutionary modelling. It is available in a fits format which is easier to use. The parameter range available from the pre-computed library is given in Table 4.3.

¹¹ https://phoenix.ens-lyon.fr/Grids/{BT-Settl}/CIFIST2011_2015/

Table 4.3: Full parameter space of the BT-Settl (CIFIST2011_2015) spectral grid (Baraffe et al., 2015).

	Range	Step size
T_{eff} [K]	1 200 – 7 000	100
$\log g$	2.5 – 5.5	0.5
[Fe/H]	0 – 0	-
[α /Fe]	0 – 0	-

In this work the BT-Settl models below the PHOENIX-ACES limit of 2300 K were not used. Above this temperature there are some difference observed in the line strengths between the two models but their spectra are similar in the nIR (see Section 4.2.4).

4.2.3 Model access

The pre-computed synthetic spectral libraries for the PHOENIX-ACES models (Table 4.2) are easily obtainable from <http://phoenix.astro.physik.uni-goettingen.de/> while pre-computed models for the BT-Settl (Table 4.3) and other PHOENIX spectra can be found at <https://phoenix.ens-lyon.fr/Grids/>. A simulator is also available to generate BT-Settl spectra or other PHOENIX spectra from Allard France at phoenix.ens-lyon.fr, for specific parameters or abundances.

The spectral model libraries were downloaded using the above links and accessed using the “grid tools” interface provided in the *Starfish*¹² Python package (Czekala et al., 2015). The “grid tools” enables the fast, efficient, and simple loading of stellar spectra for use in the simulation performed in this work. For instance a spectra from a given model can be loaded simply using the four values of identifying parameter values [T_{eff} , $\log g$, [Fe/H], [α /Fe]]¹³.

4.2.4 Comparing models

Here a comparison between the PHOENIX-ACES and BT-Settl spectra is briefly given. Figure 4.5 shows the model spectral flux in the nIR range of 0.9–3 μm for three different stellar temperatures: 5500, 4000, and 2300 K. At this large scale the spectra look fairly similar.

On closer inspection though, the spectra are slightly different with the PHOENIX-ACES spectra having deeper absorption lines compared to the BT-Settl models; however they do appear to have most of the same absorption lines. This can be seen in Figure 4.6 which contains the PHOENIX-ACES and BT-Settl at two different regions in the nIR, 1013 nm and 2110 nm. Temperature of both models is 4300 K while the $\log g$ is 1.5 for PHOENIX-ACES and 2.5 for BT-Settl and the models are convolved to $R=100,000$. These $\log g$ values were the closest available to the target in the respective model libraries. A comparison using the same $\log g=2.5$ should also have been performed, but was not done here. This is in an attempt to match the parameters to the observations of Arcturus at $R=100\,000$ shown blue. Cross-correlation and a Doppler shift has been used to align the model spectra to the observations. There is a striking difference between the models and observations with several lines present in the models that are not seen in the real observation, while a few lines observed that are not seen in the models. When

¹² <https://github.com/iancze/Starfish>

¹³ [Fe/H] and [α /Fe] are abundances of Fe and α elements relative to those in the Sun. The definition of the scale is $[X/H] = \log_{10} \left(\frac{n_X}{n_H} \right)_* - \log_{10} \left(\frac{n_X}{n_H} \right)_\odot$, where n_X is the number of atoms of element X and n_H is the number of atoms of Hydrogen.

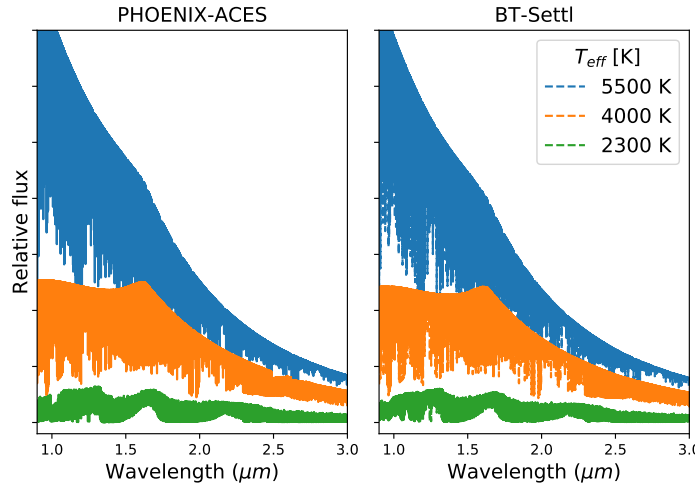


Figure 4.5: PHOENIX-ACES (left) and BT-Settl (right) spectra in the nIR wavelength region for three different temperature stars, $\log g=4.5$, $[Fe/H]=0$.

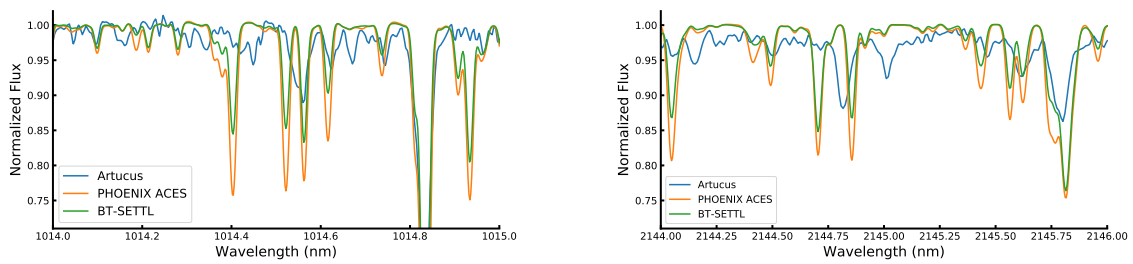


Figure 4.6: Spectrum of Arcturus compared to synthetic spectra with the closest spectral parameters at wavelengths around 1014 nm (left) and 2145 nm (right).

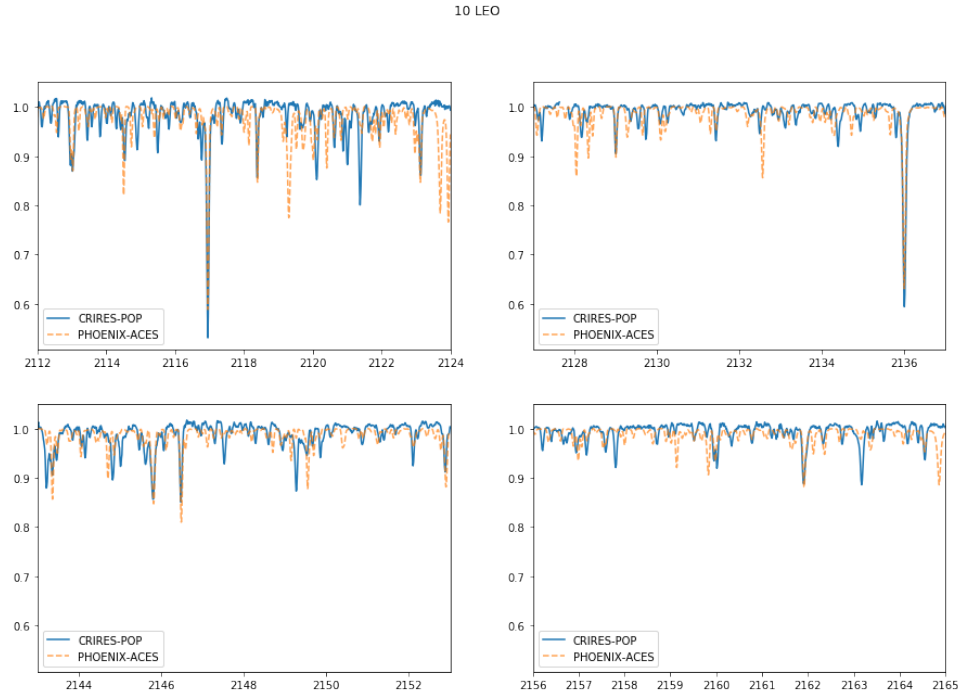


Figure 4.7: CRIRES-POP spectra of 10 Leo compared with a PHOENIX-ACES model for a CRIRES observation between 2112-2165 nm.

the observed absorption lines do align with the models there is a difference in the depth of the lines. These differences are primarily not from the differences between the model parameters actual stellar parameters which are small. These differences are shown at two different wavelengths and reveal that there is still room for improvement in the synthetic models to match observed spectra in the nIR and at high resolution. Spectral discrepancies in the BT-Settl models are noted by Rajpurohit et al. (2013).

A further example of this is shown in Figure 7.4 in which an observed CRIRES spectra is fitted with a binary model. The flux ratio $F_2/F_1=0.066$ so the model is dominated by a single PHOENIX-ACES model, and shows several line discrepancies. This caused issues with the fitting procedure in Chapter 7. Figure 4.7 is a further example of the spectral differences at the nIR wavelengths specifically used in this work, in a spectra from (in reduced form) the CRIRES-POP library (Lebzelter et al., 2012; Nicholls et al., 2017). It shows differences between the CRIRES-POP K -band spectra of 10 Leo and the PHOENIX-ACES spectrum with corresponding parameters ($T_{\text{eff}}=4800$, $\log g=3.00$, $[\text{Fe}/\text{H}]=0.0$).

4.3 Evolutionary models

Modelling of the evolution of a star, from birth thorough its journey on the main sequence until its death as it slowly cools as a dwarf or explodes as a super-novae, is important for understanding how the observable properties (temperature/photometric colours) change over time. The main factor for the fate and evolution rate is a stars mass, with large stars evolving quickly and dying explosive deaths while low mass stars sustain fusion for several orders of magnitudes longer. Brown Dwarfs do not have enough mass to achieve stable hydrogen fusion and slowly cool down over their lifetime.

This work uses stellar evolutionary models of Baraffe et al. (2003) and Baraffe et al. (2015) to

Table 4.4: Estimated companion/host flux ratios given the companion mass (M_2 or $M_2 \sin i$) from Table 6.2.

Companion	Host m_K	Host π mas	Companion M_K	Estimated F_2/F_1 K -band	Estimated N_2/N_1 (noise ratio)
HD 4747	5.305	53.184	3.82	7×10^{-5}	76
HD 162020	6.539	32.410	4.10	2×10^{-8}	1615
HD 167665	5.038	32.014	2.60	6×10^{-5}	105
HD 168443b	5.211	25.208	2.35	1×10^{-16}	1×10^8
HD 168443c	5.211	25.208	2.35	1×10^{-11}	4×10^5
HD 202206B	6.485 ^a	21.726	3.04	4×10^{-8}	1586
HD 202206c	6.485 ^a	21.726	3.04	9×10^{-18}	2×10^7
HD 211847B	7.018	20.489	3.50	0.011	14
HD 30501	5.525	49.081	3.96	0.003	27

^a Magnitude from 2MASS catalogue instead of SIMBAD.

estimate the properties of the giant planets, brown dwarfs and low-mass stars given the mass and age. The models range in mass between $0.0005\text{--}1.4 M_\odot$ and ages $0.001\text{--}10.0$ Gyr of which span temperatures $sim100\text{--}6000$ K. Stellar or BD properties such as T_{eff} , $\log g$, radius, and absolute magnitudes in different photometric bands can be determined from the tables given by the evolution models.

4.3.1 Estimating Companion-host Flux ratio

In order to visually or spectroscopically detect binary or planetary companions it is helpful to calculate the flux/contrast ratio between the host and companion.

The companion-host flux or contrast ratio of the system can be estimated using:

$$\frac{F_2}{F_1} \approx 2.512^{m_1 - m_2}, \quad (4.1)$$

where m_1 and m_2 are the magnitude of the host and companion respectively.

The photometric apparent magnitudes for the host stars, m_1 , in several wavelength bands are easily obtained through online catalogues such as SIMBAD (Wenger et al., 2000) or 2MASS (Skrutskie et al., 2006). However, the magnitudes of the companions, m_2 , are not readily available as they have not been directly measured. The stellar evolution models of Baraffe et al. (2003) and Baraffe et al. (2015) are used to estimate the absolute magnitude in different bands of the companion. A given companion mass, and a stellar age will uniquely identify a point in the Baraffe models which corresponds to a specific set of magnitudes for the companion. The evolution tables are also interpolated to reach companion masses and stellar ages between the models provided.

In Table 4.4 the host-companion flux ratio estimates for the targets analysed in this work are presented. The K -band magnitudes to calculate the K -band flux ratios to match the observed CRIRES spectra at $2.1\mu\text{m}$. The stellar ages used for each system are given in Table 6.1 while the companion masses are given from Table 6.2. The age and companion mass are both used to obtain the absolute magnitude for the companions. For the companions in which only the minimum mass ($M_2 \sin i$) is known then the flux-ratio given will be the lower limit, or worst case scenario.

The magnitudes provided by SIMBAD are given in apparent magnitude, m , while the magnitudes

in the evolutionary models are absolute magnitudes M . That is, the apparent magnitude that the star would have if it was observed at a distance of 10 parsecs (32.6 light-years). The apparent magnitudes of the hosts are converted to absolute magnitudes using $M = m - \mu$ where μ is the distance modulus:

$$\mu = 5 \log_{10}(d_{pc}) - 5. \quad (4.2)$$

Here d_{pc} is the distance to the object in parsec. The distance is obtained from the trigonometric parallax π using the formula $d(pc) = 1/\pi(\text{arcsec})$, with the parallax in arcseconds¹⁴. In this work the recent high-precision parallax measurements from GAIA (GAIA Collaboration et al., 2018) are used.

The noise ratio between the host and companion can also be calculated in a similar way using the equation $N_2/N_1 = \sqrt{2} \times \sqrt{F_1/F_2}$. This equation takes into account the difference between two stellar spectra and assumes the stellar noise of the sum is represented by the stellar noise of the host, see Appendix E.7 for more details. The factor of two appears due to the difference between the two spectra, with their errors adding. If $\sigma_A \approx \sigma_B$ then the error on the difference is $\sigma_{A-B} = \sigma_A + \sigma_B \approx 2\sigma_A$.

4.3.2 Baraffe tables

A simple tool¹⁵ was created to calculate/estimate the host-companion flux ratio using the Baraffe et al. (2003) and Baraffe et al. (2015) evolution tables. Given the name of the target star, the mass of a companion and the stellar/system age the tool determines the flux ratios in the available spectral bands. The tool uses the targets name and the *astroquery* package to obtain the stellar properties from SIMBAD, specifically the flux magnitudes and parallax. It then interpolates the Baraffe tables to the desired companion mass and age, calculating and returning values for all parameters of the companion given in the tables (e.g. T_{eff} , $\log g$, R/R_{\odot}). The stellar magnitudes are converted to absolute values using Equation 4.2 and the flux ratios computed using Equation 4.1.

An extension of this tool is that can be used to perform the reverse calculation also. That is, given the target name, age and flux ratio in a given band it can estimate the mass of the companion mass using the evolution tables.

¹⁴ Most parallax values e.g. GAIA are tabulated in milliarcseconds (mas). Therefore it is important to remember to convert the parallax to arcseconds first, to avoid embarrassing calculation errors!

¹⁵ Available at https://github.com/jason-neal/baraffe_tables

Chapter 5

Spectroscopic reduction

The work of this thesis relies on the use of nIR spectra obtained by the CRIRES instrument. Specifically 17 observations around 2110–2160 nm which are detailed in Table 6.3. This chapter contains an overview of the steps undertaken to extract astronomical spectra, focusing on the CRIRES instrument specifically. A comparison between two different reduction pipelines for CRIRES is performed with the chosen pipeline used. Details of the issues encountered with the reduction output are presented. This chapter also includes the post reduction steps performed, specifically wavelength calibration and telluric correction. The reduced spectra produced in this chapter will be analysed in Chapter 6 and Chapter 7.

5.1 nIR reduction concepts

In reducing nIR spectra, or any spectrum in general, a number of calibration steps are performed to removed the imprint of the spectrograph and detector's signature on the spectra as much as possible. The main calibration steps required for nIR spectra are given below with examples from CRIRES. More information about the different effects with regards to CRIRES can be found in the CRIRES user manual and reduction cookbook.



Figure 5.1: Master dark frames for exposure times of 3 and 180 seconds. Each master is created by averaging 3 images in which the detector received no incident light. Both frames are on the same scale and show dark current grows with exposure time. The colour has been inverted so that black is the recorded measurement.

5.1.1 Dark Current

The dark current is a form of instrumental noise, in which the detector measures photons while not being illuminated. It is the detection of thermal electrons moving inside the detector, creating spurious photon counts. Calibration and removal of the dark current is performed by taking exposures in which the detector is not illuminated. The detectors in the CRIRES instrument are cryogenically cooled to a temperature of $\sim 27\text{ K}$ (within 0.1 K) to significantly reduce the dark current, and to maintain consistency. The electrical components of the CRIRES detectors create thermal energy while operational which impacts the dark current. A strong “glow” is observed in the bottom corners of the CRIRES detector in Figure 5.1 due to nearby amplifiers. As per the CRIRES calibration plan, “dark frames” need to be taken at the exact same exposure as the science frame. This is necessary because the detectors are non-linear and cannot be appropriately scaled to different times. Figure 5.1 shows the master dark frame created from averaging three dark frames for exposure times of 3 seconds (for the flats) and 180 seconds (for the science), both on the same amplitude scale. For the CRIRES detectors the dark current per pixel is around $0.2\text{--}0.4\text{ }e^{-\text{s}^{-1}}$, while the glow at the two corners of the 180 second exposure shown here is $\sim 9000/180 \approx 50\text{ }e^{-\text{s}^{-1}}$.

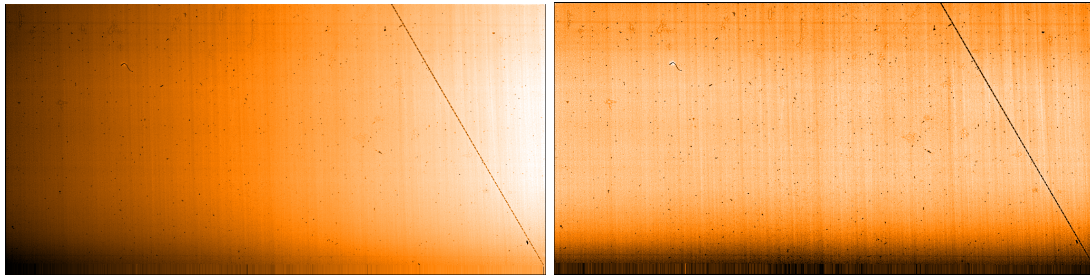


Figure 5.2: A flat-field image for detector #2 before (left) and after (right) the non-linearity corrections are performed.

5.1.2 Flat-field

Due to the architecture of CMOS, in which pixels are read independently and each pixel has an independent amplifier with a different gain. To correct for pixel-to-pixel variations in gains and photon sensitivity across the detector and for any distortions in the optical path, a flat-field correction is needed. Exposures of a uniform¹ light source are taken, allowing the individual pixel-to-pixel sensitivity to be measured and corrected. The flat-field frames are corrected for dark current by subtraction of the master dark frame with the appropriate exposure time.

The CRIRES detector suffers from non-linearities in sensitivity across the detector. This can be seen in the flat-field image on the left of Figure 5.2 where there is an intensity gradient from dark to light across the detector. A set of coefficients for each pixel is provided by ESO² to apply the correction for the non-linearity of the detectors. This also corrects for a slight difference in sensitivity between the pixels from the odd and even columns in the CRIRES detectors, commonly called the “odd-even effect”. This occurs because the odd and even columns are read separately by different large amplifiers that have a different gains. The frame on the right of Figure 5.2 has been corrected for the non-linearities.

¹ Ideally uniform intensity and spectral distribution

² Available at <https://www.eso.org/sci/facilities/paranal/instruments/cires/tools.html>

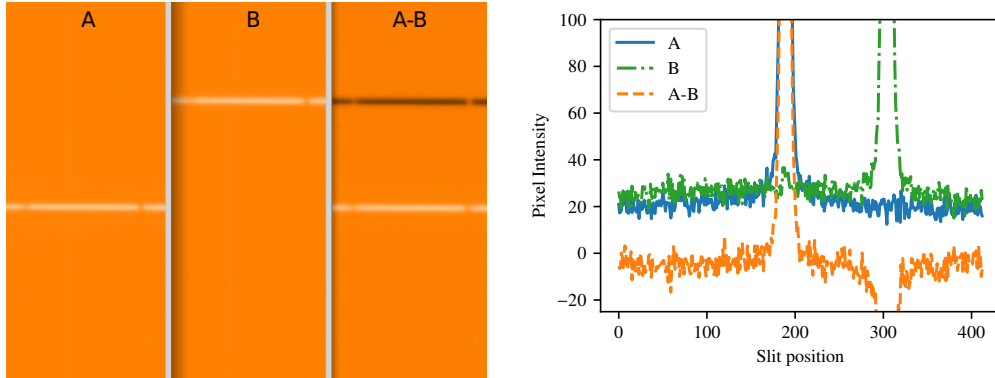


Figure 5.3: Illustration of the nodding technique. Left: Sample slice of successive images at nod positions A and B, and their difference A minus B for detector #1. Right: A vertical slice along the slit at column 512 (middle of detector). The background level observed in A and B is effectively removed by the subtraction.

The flat-field can also reveal defects in the detector e.g. dead pixels, dust and scratches: a large scratch is clearly visible in Figure 5.2. The flat-field and non-linearity correction are performed in the same reduction step.

5.1.3 Nodding and Jitter

The technique of *nodding* is used to remove sky emission, detector dark current, and glow. First, an observation is divided into multiple separate exposures. Between each exposure the telescope is moved to change the vertical position of the target in the slit. The light from the star travels through a slightly different optical path and is recorded on a different part of the detector. The frames from the two nod positions, A and B, are then subtracted ($A - B$) to remove the background measurement from each spectra.

A visual example of the nodding is shown in Figure 5.3. On the left are slices of 150 pixel columns from successive nod positions A and B as well as the difference A minus B. On the right is a single pixel column from each image on the left. The background signal at the level of 20–30 counts in the image is almost cancelled out by the opposite nod. This efficiently removes the background signal/noise from the observed spectra target.

Observations of faint targets, that need long exposure times to achieve a sufficient SNR, are also broken up into multiple images so that the instrument glow from Figure 5.1 does not saturate the detector. A small random vertical offset is applied to each observation which ensures that all spectra at the same nod position do not consistently land on the same pixels each time. This is known as the *jitter* and allows for the correction of bad pixels and decreases the effect from any systematics of the detector. As an example, the CRIRES observations analysed for the work performed in Chapters 6 and 7 were performed with an ABBAABBA nod cycle pattern (including jitter) with an exposure time of 180 s each, totalling 24 minutes when combined.

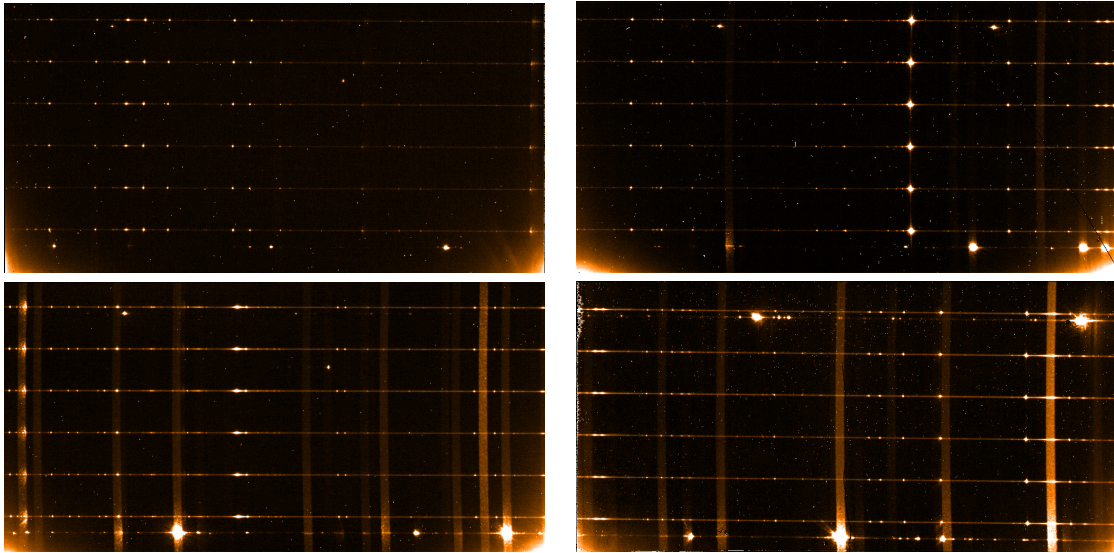


Figure 5.4: Example Th-Ar calibration lamp frames for each detector. These are the raw frames in which dark current correction has not been performed (i.e the dark current is still visible on the bottom corners).

5.1.4 Th-Ar lamp calibration

As part of the CRIRES calibration procedure, spectra are taken of Th-Ar lamps. The Th-Ar spectra are placed into the instrument using 6 optical fibres, creating six uniformly spaced spectra across the detector. Figure 5.4 contains the Th-Ar spectra for all four detectors. There are ~ 50 Th-Ar lines that fall across the four detectors for the wavelength setting here, although most of them are faint.

The purpose of the Th-Ar fibres is to perform cross-correlation against a Th-Ar template to obtain a wavelength solution for each detector. Optical defects (e.g. scratches on the detector) interfere with the performance of the correlation between Th-Ar lines and the spectral template in ESO pipeline. This can be resolved by first applying a pixel mask (although this was not attempted in this work). At the top and bottom there are also two meteorological fibres that can not be used for wavelength calibration as they pass through a different optical pathway. The brightest one at the bottom has strong features that seem to overwhelm or washout many columns in detector #2–4 (vertical stripes). This information is included here for completeness, as the Th-Ar were not used in the chosen data reduction method, see Section 5.3.1. The very uneven distribution of Th-Ar line make their use difficult in many cases, not just this work.

5.1.5 Extraction

The process of extraction is, in brief, turning the two-dimensional image of the spectrum into a one-dimensional representation. This is done by summing the photon counts along the spatial direction, for each column in the dispersion direction in a small window around the spectrum. To do this one needs to identify the position of the spectrum across the detector, referred to as order tracing. For CRIRES there is only one spectral order dispersed across the detector, selected using wavelength filters, but for a cross-dispersed configuration there will be several parallel orders to trace. A rectangular box, with a specified aperture width, is centred along the traced spectrum.

There are two types of extraction commonly used. The *rectangular* extraction performs a simple

aperture sum in the spatial direction, counting all photon counts that fall within the aperture. Basically, summing the rows that contain the spectrum. The *optimal* extraction (Horne, 1986) is an improved technique to reduce the affect of noise and deviant pixels on the extracted spectrum. Instead of simply summing the rows, the optimal extraction fits a spatial profile to each column of the detector spectrum, perpendicular to the spectral dispersion. The spatial profiles are used as weighting functions so that the pixels furthest from the centre of the spectrum, which have lower signal and are hence noisier, contribute less to the extracted spectrum. This achieves a extracted spectrum with a better SNR than the rectangular method. Optimal extraction can increase the effective exposure time by up to 1.69 times at 3σ (Horne, 1986). Both rectangular and optimal extraction methods are available from both the ESO CRIRES and DRACS pipeline, compared below.

5.2 Pipeline Comparison

To transform the observed 2-D image from the telescope into an extracted 1-D spectrum of the target a number of steps (some outlined above in Section 5.1) have to be performed in sequence. The series of steps, performed by various software tools, is referred to as a *pipeline*. Each stage in the pipeline performs a specific task, for example creating the master dark frame, or performing the nod subtraction. The result of one stage is passed to the next (either automatically or manually). Two different pipelines were available to reduce the CRIRES observations used in this work. The first is the standard CRIRES pipeline³, available from ESO. The second is an in-house pipeline previously used in Figueira et al. (2010) called DRACS (Data Reduction Algorithm for CRIRES Spectra) This was created due to a lack of a reduction pipeline for CRIRES at the time. In these next sections the experience gained using both pipelines, comparing the extracted spectra and user experience is documented.

5.2.1 ESO CRIRES pipeline

The ESO CRIRES pipeline was used to reduce CRIRES nodding spectra following direction from the CRIRES pipeline user manual⁴ and the CRIRES reduction cookbook⁵.

The GASGANO⁶ graphical user interface (GUI) was used to interact with the pipeline with guidance from the GASGANO manual⁷. This pipeline provides a number of *recipes* which perform the required extraction steps. From the GUI each recipe is manually selected, then the correct calibration and observation files need to be selected to use with each recipe. The final output from the ESO pipeline is a table in a fits format with the combined extracted spectra (both *rectangular* and *optimal* extractions), pixel errors and a wavelength solution.

For a novice of spectral extraction this pipeline and the available documentation was very helpful to get started and perform the extraction. However, to reduce many spectra it soon became a long tedious process.

Constant revision of the documentation was necessary to ensure all the correct image and calibration files were added to each recipe. The ESO pipeline makes all the recipe parameters easily accessible to modify via a window of the recipe interface, but the recipe parameter defaults get restored for each

³ <https://www.eso.org/sci/software/pipelines/>

⁴ <ftp://ftp.eso.org/pub/dfs/pipelines/cires/cires-pipeline-manual-1.13.pdf>

⁵ https://www.eso.org/sci/facilities/paranal/instruments/cires/doc/VLT-MAN-ESO-14200-4032_v91.pdf

⁶ <https://www.eso.org/sci/software/gasgano.html>

⁷ <https://www.eso.org/sci/software/gasgano/VLT-PRO-ESO-19000-1932-V4.pdf>

observation, making it difficult to reduce all of the observations in a consistent manner. Having the parameters adjustment on the recipe interface is great for adjusting the parameters and for identifying which parameters are relevant to each recipe. Unfortunately, when trying to experiment with the recipe parameters to achieve a high quality spectral extraction it was repetitive to change the same parameters for each observation, and it was also difficult to keep track of all the changes while assessing their effect on the final output.

The parameters for the wavelength calibration were the most tedious. To try and improve the wavelength calibration, the y-positions of the 6 Th-Ar fibres were manually found from the images for each detector and every observation and then entered as input parameters for the calibration recipe. This helped the wavelength calibration recipe to correctly identify/fit more of the Th-Ar spectra in most cases, but this took time. Because of this, it was chosen to use the other pipeline and these calibration were not used.

ESO has a new reduction “workflow” called ESO Reflex (Freudling et al., 2013)⁸. This enables automated reduction with the ability to chain together the extraction recipes in the specific order desired, repeat steps to optimize the reduction, and automatically handle the data organization (no need to manually select the files for each recipe). This would likely have enabled a quicker and more consistent reduction of the spectra. Unfortunately ESO Reflex was not, and is still not, available for the CRIRES pipeline.

5.2.2 DRACS

DRACS (Data Reduction Algorithm for CRIRES Spectra) is a custom reduction pipeline (Figueira et al., 2010) written in IRAF’s CL⁹ (Tody, 1993). It provides for automated dark and nonlinearity corrections (using the nonlinearity coefficients provided by ESO), as well as the flagging and replacement of bad pixels. Sensitivity variations are corrected by dividing by a flat-field which was corrected from the blaze function effect. The nodding pairs are mutually subtracted and the order tracing is accomplished by fitting cubic splines. Order tracing allows the extraction algorithm to follow the shape for the dispersion across the detector¹⁰. By default the pipeline returns the *optimal* extraction (Horne, 1986), but the *rectangular* extraction can also be obtained. The extracted spectra from each nod is continuum normalized by dividing by a polynomial fitted to the continuum, with the polynomial degree selected individually for each spectrum and detector. Finally, the normalized nod-cycle spectra are averaged together to give a single reduced spectrum, normalized to 1.

The DRACS pipeline was originally developed to work with *H*-band spectra. Because of this, some of the parameters were adjusted in an attempt to achieve a better reduction on the *K*-band spectra analysed here. The parameters adjusted were the tracing and normalization polynomial functions and their specific order on the detector. Also, there was initially no reduction parameters present for the third detector as it was not reduced in previous works using this pipeline. Therefore, the pipeline was extended to be able to reduce detector #3 of CRIRES, by adjusting the pipeline code and finding suitable parameters for detector #3.

When using the DRACS pipeline on a new target, the tedious part is initially creating the lists of

⁸ <https://www.eso.org/sci/software/esoreflex/>

⁹ IRAF is distributed by the National Optical Astronomy Observatories, which are operated by the Association of Universities for Research in Astronomy, Inc., under cooperative agreement with the National Science Foundation.

¹⁰ The spectra do not fall perfectly horizontally on the detector and usually contain some curvature due to the optics of the instruments.

files identifying which files are the dark, flat, and the science frames¹¹. After these lists are created, the reduction pipeline can be run and re-run easily, making the effort worth it.

The first time through is interactive with a number of manual checks and decisions to be made (e.g. confirming the order tracing position, and fit is good). DRACS remembers choices in a database, allowing for a reduced level of user interaction a second or third time through the pipeline. This was useful to experiment with and iterate the reduction parameters of the pipeline. When changing the parameters which affect the order tracing, the database with the order tracing results needed to be deleted so that it would not influence the new fits. These parameters were therefore slower to iterate on.

This semi-autonomous nature of the DRACS pipeline means that all the spectra can be reduced in a simple and consistent way, relatively quickly, and does not require manual spectra selection for each individual recipe as was done with the ESO pipeline.

There are a couple of drawbacks with using the DRACS pipeline. The first is the lack of documentation on how to use it. This required looking through the source code to find which functions and scripts do which part of the extraction. DRACS makes use of many IRAF packages which have documentation available online¹². Searching through this documentation was difficult, but required, to understand how to use and modify DRACS.

The second drawback is that DRACS does not perform wavelength calibration, which is included with the ESO pipeline. This means an external wavelength calibration was the only option (see Section 5.3.1). The last drawback is the discovery of artefacts present in the nod spectra, which are discussed in detail in Section 5.2.3.1.

In opposition to the official CRIRES pipeline, DRACS allows for a simple way to do homogeneous reduction of data. However, this pipeline resorts to the IRAF recipes, which in turn have to be fine tuned in detail thorough extensive parametrization to reduce the data correctly.

5.2.3 Pipeline comparison and selection

Both reduction methods were applied to the same CRIRES spectra to check the quality and consistency of both methods. Two examples of the extraction for HD 30501-1 (left) and HD 202206-1 (right) from both pipelines are provided in Figure 5.5. The blue lines are the extracted spectra from the ESO pipeline, the orange dashed lines are the optimal extraction from the DRACS pipeline, while the green dash-dotted line is the DRACS extraction after dealing with artefacts in the optimal extraction addressed in Section 5.2.3.1.

One of the important things checked was the line depths of each spectra to ensure that the pipelines were consistent. The ESO pipeline has noticeable issues, with many large spikes still present in the spectra, likely caused by bad pixels or cosmic rays that are not correctly removed. There also appears to be problems with the edges of the ESO reduced spectra, with very large spikes at either end.

At this stage the DRACS pipeline was chosen, as it was considered that the DRACS pipeline produced better extracted spectra than the ESO pipeline. This decision was based on the issues in the reduced spectra noted above, as well as the relative ease of use of the pipeline (being semi-automated once set up). Another deciding factor was the need to create software to remove the bad pixels observed in the ESO reduced spectra. However, this was unavoidable as it was eventually required for the DRACS reduced spectra (see Section 5.2.3.1). Though the ESO pipeline provided a wavelength solution for the spectra,

¹¹ The GASGANO GUI was helpful to identify the distinction of each fits file for a beginner.

¹² Such as at the http://stsdas.stsci.edu/gethelp/pkgindex_noao.html.

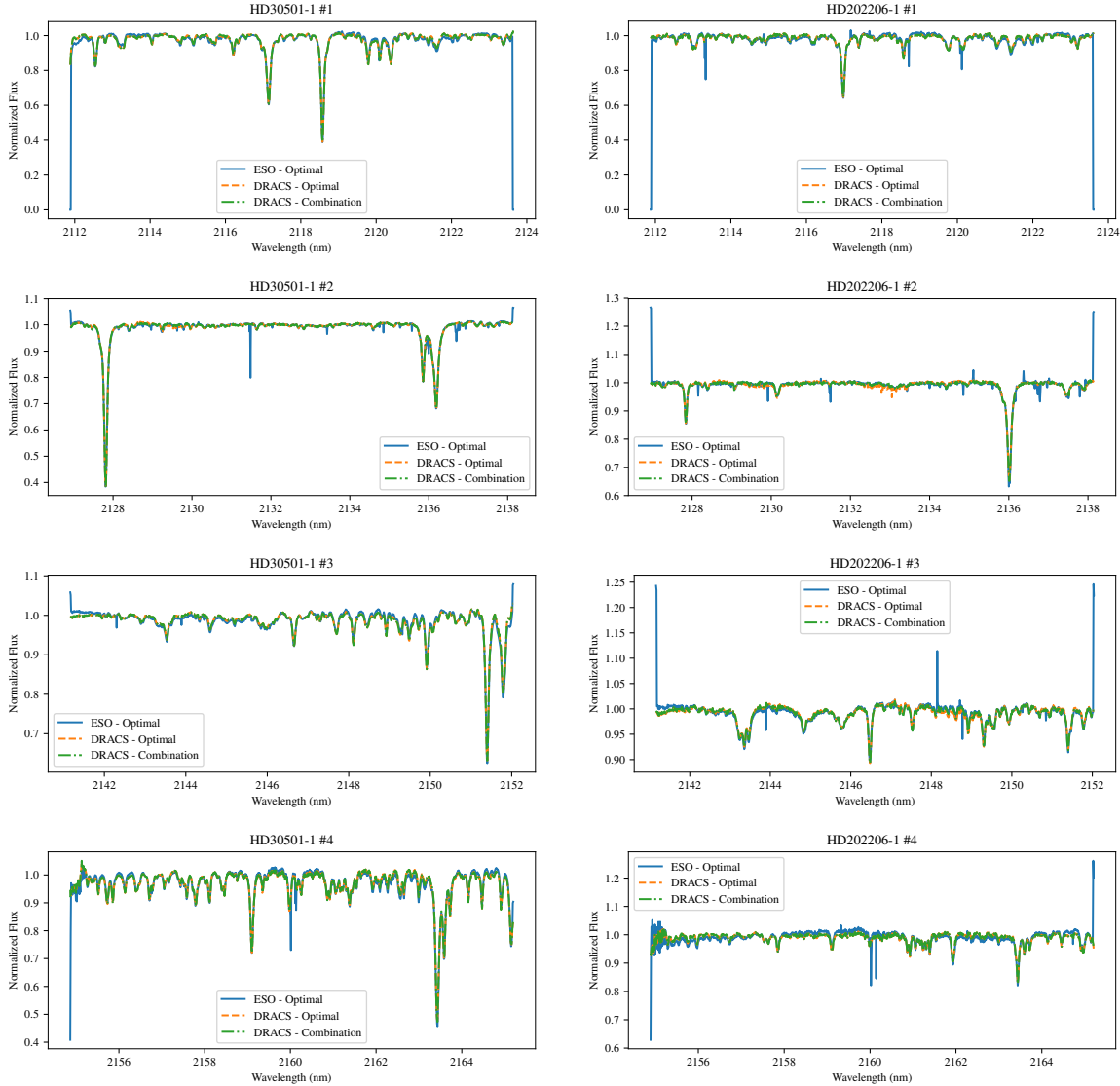


Figure 5.5: Comparison between the ESO pipeline and DRACS pipeline for two observations, HD30501-1 and HD202206-1. The blue lines are the extracted spectra from the ESO pipeline, the orange dashed lines are the combined optimal extraction from the DRACS pipeline, and the green dash-dotted line is the modified DRACS extraction (after removing artefacts addressed in Section 5.2.3.1). The wavelength information applied to both spectra is from the ESO pipeline.

this did not factor into the decision as it was considered too unreliable due to known issues with CRIRES wavelength calibration, necessitating a new wavelength calibration anyway.

The spectra for the pipeline comparison in Figure 5.5 are the combination of the 8 nod spectra. Later, it was discovered that individual nod spectra from the DRACS pipeline had issues (see Section 5.2.3.1). These are difficult to notice on this scale as they each constitute one eighth of the information in the combined spectrum. An example of this is seen in detector #2 of HD202206-1 in Figure 5.5. In Section 5.2.3.1 an artefact from a single nod spectra, is barely visible in the pipeline comparison of Figure 5.5, shown as a slight depression of the orange dashed line between 2132 and 2134 nm. The identification of these artefacts and how they are removed (green lines) are explained in the following section.

5.2.3.1 Reduction issues

After the decision to use the DRACS pipeline significant artefacts in the DRACS-extracted spectra were observed. An investigation into the cause of these artefacts was undertaken to identify their source and attempt to remove them from the spectra. The eight individual nod spectra were displayed side-by-side which revealed that occasionally the spectra from one of the nods deviated significantly from the others. Eventually it was identified that the artefacts were only in the *optimally* reduced spectra, and that they were not present in the *rectangular* extracted nods. An example is shown in Figure 5.6 in which sharp spikes in the middle panel (rectangular extraction) correspond to deviations observed in the top panel (optimal extraction). The bottom panel shows the difference in the combined average spectra from the optimal extraction and the corrected mixed spectrum resulting from the method given in this section to remove the artefacts. In this case the deviation in the combined spectra are at 2%. Further visual examples of artefacts, selected to show a variation in appearance, are given in Appendix B along with a table identifying the observations and nod spectra the artefacts were observed in.

It is clear that the artefacts in the optimal extraction occur when there is a corresponding “bad-pixel” spike¹³ in the rectangular extraction. However this is not always the case with many spikes observed (e.g. first nod around pixel 580 in Figure 5.6) that are automatically removed in the optimal extraction. The occurrence of artefacts in the observations did not appear to have a pattern with nod position or detector with 14% (79/544 spectra) of the nod spectra having an optimal extraction that seemed to misbehave. The artefacts in the optimal extraction are also largely extended, significantly affecting more of the spectrum than the individual spikes (up to 100s of pixels). Artefacts were observed arising from both large and small spikes alike while other large and small spikes are removed correctly. This possibly suggests that their size is of less important than some other unknown factor (possibly location).

As mentioned in Section 5.1.5 the *optimal* extraction includes variance weighting across the spatial direction. It appears that the presence of the bad pixel spikes heavily affects the variance weighting procedure during the *optimal* extraction.

Numerous parameters in the DRACS pipeline were experimented with in the attempt to remove the observed artefacts with limited success. For instance, no complete removal of the artefacts was found by adjusting the σ rejection limits (between $1 - 5\sigma$) or increasing the tracing width parameter in IRAFs DOSLIT¹⁴ recipe, although they did slightly affect the shape of the artefacts. Section 5.2.3.1 shows

¹³ Their exact origin is unknown but are likely uncorrected bad-pixels or a cosmic ray. Here they will be referred to as bad-pixels.

¹⁴ Documentation for DOSLIT can be found here <http://stsdas.stsci.edu/cgi-bin/gethelp.cgi?doslit>

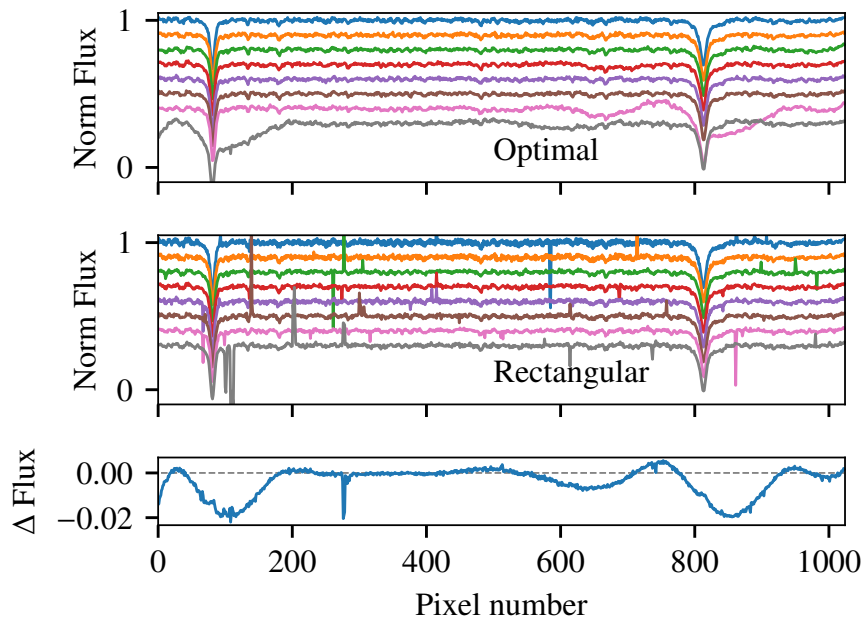


Figure 5.6: Example of DRACS artefacts in the optimally extracted spectra second detector of the first observation of HD 162020. top: The 8 normalized nod spectra obtained using *optimal* extraction, vertically offset from each other. middle: The 8 normalized nod spectra obtained using *rectangular* extraction, vertically offset from each other. bottom: Difference between the combined average spectra from the top and improved result from the mixed method developed here. The middle panel creates the small spikes, while the large deviations are due to the artefacts in the optimal reduction. There are three bad pixel spikes that cause artefacts in this optimal extraction. These are located in the seventh nod (pink) around pixel 850, and two in the eighth nod (grey) around pixel 100 and 620. Several other spikes do not cause any artefacts in the optimal reduction.

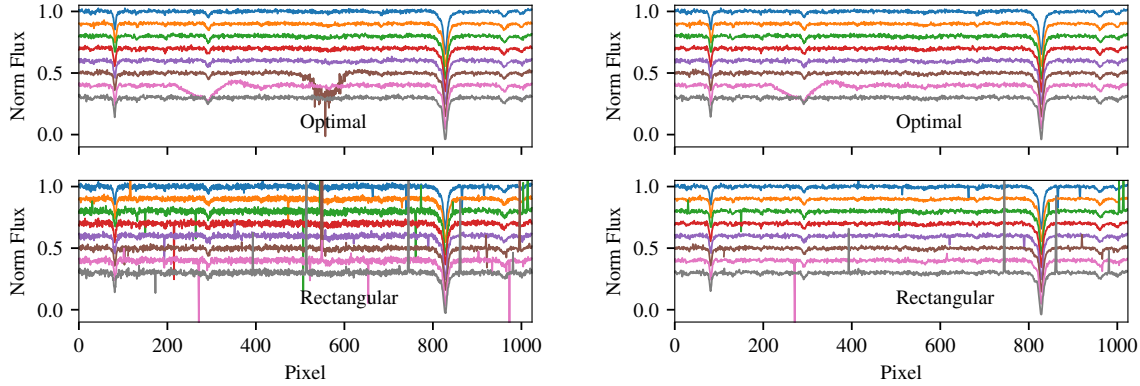


Figure 5.7: Two DRACS reductions for detector #2 of HD 202206-1 with one pipeline parameter changed. Left: The reduction with the DRACS pipeline with the “doslit.resize” set to “no”. Right: The reduction from the same pipeline but with “doslit.resize” set to “yes”, all else equal. During the order tracing the aperture size is automatically adjusted while the rest of the parameters remain identical. One large artefact is removed in the sixth nod (brown) while the artefact in the seventh nod (pink) is not removed.

the extraction of HD 202206 with one parameter changed in the reduction pipeline. The only difference between the left and right panels the automated aperture resizing¹⁵ was enabled by setting the “resize” parameter to *yes* in the right hand panel. This manages to remove an ugly artefact in the sixth nod (brown), but not the artefact in the seventh nod (pink). This was only discovered in the writing of this thesis so could not be utilized earlier. However, it does indicate that some improvements may be obtained with extensive time and patience tweaking the parameters of the DRACS pipeline.

The purpose of these observations was to detect faint companion spectra with expected flux ratios $F_2/F_1 < 1\%$. As the artefacts created large and extended deviations in the combined spectra (up to 2%) measures were needed to remove these artefacts from the combined spectra. To avoid contaminating the spectra of the faint companions.

After the unsuccessful tweaking of parameters the solution that was chosen was to replace the optimally extracted nods that contained artefacts with their rectangular counterparts. This would create a combined spectra that had a mix of optimally reduced and rectangularly reduced nod spectra, without any artefacts. To replace the spikes in the rectangular extraction that created the artefacts and others an iterative 4- σ ¹⁶ rejection algorithm¹⁷ was applied to the rectangular extractions. The σ for each pixel was calculated as the standard deviation of the nearest 2 pixels on either side of it, across all 8 nod spectra (a 5×8 grid). Any rejected pixels were replaced using linear interpolation along the spectra. The spectra that contained artefacts and that were replaced using this method are given in Table B.1.

Combined spectra were finally constructed by averaging the eight nod-cycle spectra together, where some of the optimally extracted spectra were replaced using the above method. The actual spectra from the two different methods can be seen in Figure 5.5 where orange is the combination of optimally reduced spectra only and green uses the replacement method outlined here. The easiest to notice a difference is HD 202206-1 #2 in which the artefacts from Section 5.2.3.1 are removed.

¹⁵ Using <http://stsdas.stsci.edu/cgi-bin/gethelp.cgi?apresize.hlp>

¹⁶ There is no scientific justification why 4- σ was chosen over the commonly used 3- σ .

¹⁷ Found at https://github.com/jason-neal/nod_combination

The continuum normalization of the spectra is performed in IRAF while the swapping of nods creating a mixed combination is carried out in Python along with the post reduction procedures detailed below.

The DRACS pipeline was originally chosen over the ESO CRIRES pipeline because it seemed relatively simpler to use, being semi-automated, and appeared to have less bad pixel/cosmic ray artefacts in the resulting spectra. In hindsight the DRACS pipeline had several unexpected challenges due to these artefacts which took time to investigate and find a solution for.

One hypothesis for these artefacts is detector glow, the heating of the detector by the nearby amplifiers in the chip (see Section 5.1.1). The artefacts in the *K*-band spectra were not observed in previous works in the *H*-band using this pipeline (e.g. Figueira et al., 2010), and as such may have a wavelength dependent effect, like detector glow. However, it seems plausible that a glow related effect would be spatially distributed like the glow shown in Figure 5.1, but the location of the artefacts do not seem to have a discernible pattern. It could also be that there were artefacts in intermediate steps of the previous works that were missed due to the semi-automated pipeline, with the resultant combined spectrum being only slightly affected at the level of $>1\%$ it could easily be missed (e.g. Figure 5.5). Another possibility is that the artefacts are bad pixels not removed correctly. Regardless, in the end they do not have a significant impact on the results found in this work, though it is expected that mixing the optimal and rectangular extracted spectra will have a slight negative impact on the noise or SNR of the combined spectrum. Much time and effort was invested attempting to extract the spectra, without artefacts, to have the best chance at obtaining high quality scientific results of the faint features sought after in this work.

5.2.4 Reduction experience

The experience gained in reducing CRIRES spectra enabled participation in collaboration with other science cases. The DRACS pipeline was used to extract the spectra of two other targets. The stellar target and a very brief objective of each science case is given below.

- Barnard’s Star¹⁸: The carefully reduced nIR spectra of Barnard’s Star was meant to extend the work of Andreasen et al. (2016) in deriving the spectroscopic parameters of cool M-stars in the nIR. Unfortunately the work did not advance enough to analyse M-star’s and a spectrum of Arcturus (K0) and a fully reduced spectrum of 10Leo (K1) from the CRIRES-POP library (Nicholls et al., 2017) were analysed instead in Andreasen et al. (in prep.).
- η Tel¹⁹: The spectra of a telluric standard star (HIP100090) and HR 7329-B (η Tel-B) a rapidly rotating Brown Dwarf, were reduced to accurately determine the BD rotation rate by measuring the line broadening. The results from this data will be published in an upcoming paper Hagelberg et al. (in prep.).
- The same spectra of HR 7329-B were also used in Ulmer-Moll et al. (2018) to compare different telluric correction methods in the nIR. An example from Ulmer-Moll et al. (2018, (B.3)) of the reduced target spectrum (black), the telluric model (red) and the telluric corrected spectrum (green) is provided in Figure 5.8.

For these works only the spectral extraction outlined above was performed. The post extraction and reduction steps detailed in the following sections were not.

¹⁸ Programme ID: 085.D-0161(A)

¹⁹ Programme ID: 083.C-0759(A)

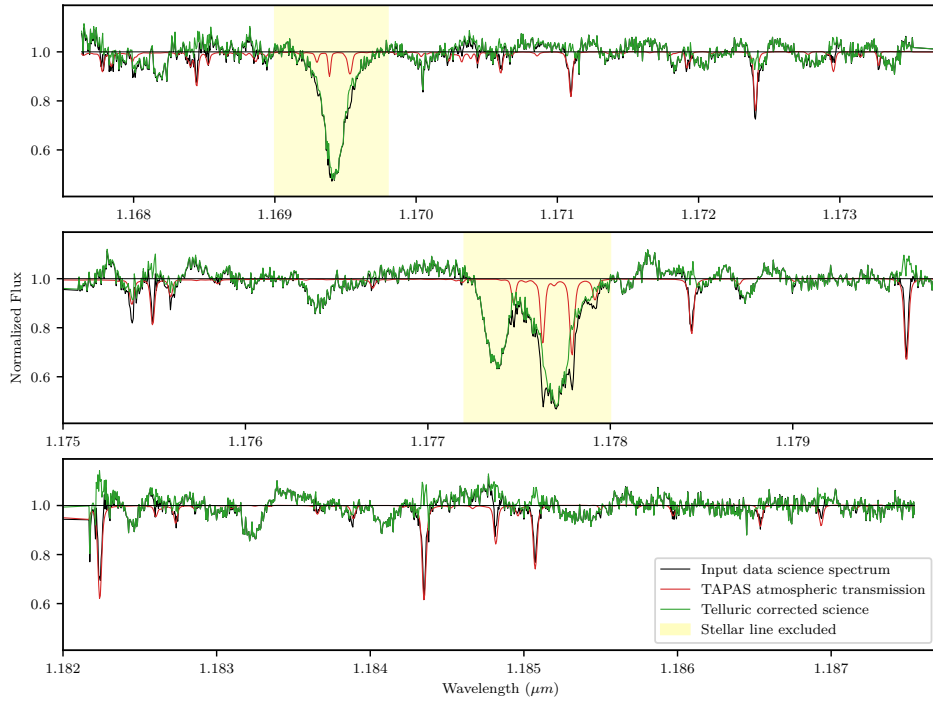


Figure 5.8: Example of telluric corrected spectrum of HR 7329-B using TAPAS. Credit Ulmer-Moll et al. (2018). The yellow shaded region is the region of stellar lines that was avoided while applying the correction methods.

5.3 Post reduction stages

From the DRACS pipeline the 1-D spectra of each target has been extracted. However, the spectra still need to undergo some post-extraction steps. In particular, wavelength calibration and telluric correction. A detailed look of how these steps were developed and performed are addressed in the following section.

5.3.1 Wavelength calibration

Wavelength calibration is the process of assigning accurate wavelength values to each pixel in the spectra. For CRIRES in the nIR this is challenging. CRIRES uses a Thorium-Argon (Th-Ar) lamp to place 6 emission spectra on the detector using fibres. The spectra of the Th-Ar emission lines are used to determine the spatial distribution of the wavelength solution across each detector using correlation with a spectral template. Th-Ar lamps are excellent at optical wavelengths where the numerous (several thousand) spectral lines enable radial velocity precisions of $\text{sub-}\text{m s}^{-1}$ when combined together, e.g. in the HARPS spectrograph. The precision of an individual Th-Ar line is of the order of m s^{-1} .

However, in the nIR there is a relatively low density of Th-Ar lines (Kerber et al., 2009), which, in combination with the alignment of the narrow wavelength range of the detector, causes a poor wavelength calibration to be obtained (e.g. CRIRES-POP (Nicholls et al., 2017)). Above $2.2\text{ }\mu\text{m}$ there are O-H sky lines that can be used for wavelength calibration but according to the CRIRES manual for observations below $2.2\text{ }\mu\text{m}$ they are too dim. These wavelength calibration issues were experienced when using the ESO CRIRES pipeline, with non-Th-Ar features sometimes affecting the correlation.

Between the wavelength range 2.1–2.17 μm there are roughly 80 Th-Ar lines across all four detectors, as seen in Figure 5.4. The DRACS pipeline does not use the Th-Ar lamp files for wavelength calibration and leaves this as a post reduction step.

A common method for wavelength calibration that does not rely on Th-Ar lamps of CRIRES involves using the telluric lines present to provide the wavelength solution (e.g. Brogi et al., 2012; Brogi et al., 2014; de Kok et al., 2013; Piskorz et al., 2016). This is made possible by the use of high resolution spectra, in which the telluric lines are well resolved, as well as accurate spectral information of the atmosphere.

Likewise, in this work the wavelength calibration is performed using the telluric absorption lines present in each observation as the wavelength reference. Instead of directly using the HITRAN database (Rothman et al., 2013) for the telluric line positions, such as Brogi et al. (2012), Brogi et al. (2014), and de Kok et al. (2013), use the TAPAS atmospheric transmission models (see Section 4.1.1). The TAPAS models use the HITRAN database but also includes atmospheric profiles and physical meteorological measurements to model the telluric absorption strength.

To calibrate the wavelength the telluric lines in the model need to be associated to the corresponding telluric lines in the observed spectrum. The centroid²⁰ of each telluric line in the model is obtained by fitting the telluric transmission spectrum, $T(\lambda)$, as a simple sum of Gaussian functions (subtracted from the continuum):

$$T(\lambda) = 1 - \sum_i G(\lambda, A_i, \mu_i, \sigma_i), \quad (5.1)$$

where G is a Gaussian function of the form

$$G(\lambda, A, \mu, \sigma) = A e^{-(\lambda-\mu)^2/2\sigma^2}, \quad (5.2)$$

and A , μ , σ are the amplitude, central wavelength, and standard deviation for each line respectively. Telluric lines actually have a Voigt profile²¹ although they are not fully resolved in the nIR and their shape is dominated by the instrumental profile. Seifahrt et al. (2010) measured the instrumental profile of CRIRES using singular-value decomposition and showed that it is extremely well represented by a single Gaussian below a SNR~300. Therefore, wavelength calibration using single Gaussian fits to each line is sufficient.

The observed spectra contain two different spectral components: stellar and telluric lines, which are multiplied together: The observed spectra are therefore fitted with a multiplication of two Gaussian-sum models.

$$\begin{aligned} I_{obs}(x) &= I_{tell}(x) \times I_{star}(x) \\ I_{obs}(x) &= \left(1 - \sum_j G(x, A_j, \mu_j, \sigma_j)\right)_{tell} \times \left(1 - \sum_k G(x, A_k, \mu_k, \sigma_k)\right)_{star}, \end{aligned} \quad (5.3)$$

where x is the pixel coordinates of the extracted spectra.

The identification between telluric and stellar lines is performed by hand for each spectra, using the telluric model as the reference. Care was taken to fit the correct components to blended spectra where possible to improve the number telluric lines use for calibration. The fits were inspected to ensure that

²⁰ Centre of the line

²¹ A Voigt profile is a convolution of two broadening profiles, a Gaussian and a Lorentzian. Gaussian broadening results from thermal Doppler broadening, and instrumental broadening while the Lorentzian broadening comes from molecular vibrational bands(Meier, 2005).

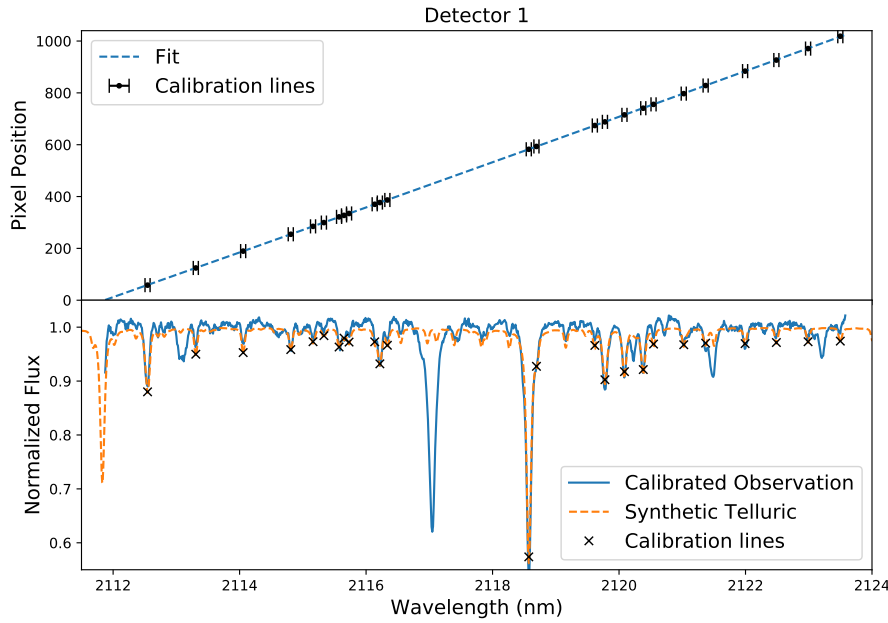


Figure 5.9: Example of the wavelength calibration using the synthetic telluric spectra. Top: The pixel/wavelength mapping and associated wavelength fit. The horizontal error bars shown are the Gaussian line width, around 0.04 nm. Bottom: The wavelength calibrated observation and the telluric model used for calibration. The black crosses indicate the peaks of the telluric lines used in the fitting process.

they reasonably matched the line positions. There was difficulty in identifying the shallow lines with depths below 1–2%, but these were needed in some spectra to obtain a suitable fit. If there were blended lines that did not appear to fit correctly they were not considered in the calibration step.

After fitting $I_{obs}(x)$ to the observed spectrum and $T(\lambda)$ to the telluric model, the wavelength solution was obtained by fitting a second order polynomial to the centroid values $\{\mu_j(x), \mu_i(\lambda)\}$ from the telluric components of the observed spectra and telluric model respectively. A second order polynomial has been shown to be sufficient for higher precision RV studies (e.g. Bean et al., 2010; Figueira et al., 2010). This polynomial is then used to map the whole spectrum from pixels into wavelength. Higher 3rd and 4th order polynomials that are also used in the literature (e.g. Seifahrt et al., 2010; Ulmer-Moll et al., 2018) were attempted but had limited success here due to the limited number and uneven spacing of telluric lines in the narrow wavelength range analysed, especially on the second detector. There were often large deviations due to the uneven spread of telluric lines, especially at the extremities. Higher order terms for wavelength calibration are usually used in regions with a higher density of telluric lines and/or a longer wavelength span (Piskorz et al., 2016; Seifahrt et al., 2010; Ulmer-Moll et al., 2018).

An example of the wavelength fitting is given in Figure 5.9. The top panel shows the (slightly) quadratic fit (blue dashed) to the centroid values $\{\mu_j(x), \mu_i(\lambda)\}$ (black) while the bottom panel shows the newly calibrated observation alongside the telluric spectrum. The black crosses indicate the lines used for calibration. To two decimal places the equation of the fit $\lambda = -1.85e^{-7}x^2 + 1.16e^{-2}x + 2111.86$.

Much like with the Th-Ar calibrations, this technique performs better when there is sufficient coverage

of telluric lines on the detectors. For the wavelength setting of these observations, the spectra from the second detector (top right panel of Figure 5.10) only has two large telluric lines present with several small lines, with relative depths smaller than 1%, which are often difficult to accurately identify. This deteriorated the calibration stability for the second detector. The second detector may have been ideal for the detection of a faint secondary spectra, with the lack of telluric contamination and stellar lines. Unfortunately the wavelength calibration quality varies in an inverse way, being more difficult with few lines.

It is noted that there are many variations on this wavelength calibration technique including those integrated within programs such as *TelFit* Gullikson et al. (2014), and ESO’s *Molecfit* Smette et al. (2015), that perform telluric correction and re-calibrate the wavelength axis themselves at the same time. It is recommended to attempt using those first before independently creating wavelength calibration software.

One improvement could have been to include a concurrent fitting of a stellar spectral model, adjusted for RV, along with the telluric model, which could help to improve the wavelength calibration performed here. Piskorz et al. (2016) performed wavelength calibration using only a telluric line model at other nIR wavelengths (*L*-band between 3.0–3.4 μm) successfully. However, around 2 μm they needed to include a fitted stellar model to obtain good wavelength calibration due to the weaker telluric lines in this region. This is the same wavelength region of the data analysed here. Having experience of performing wavelength calibration at other wavelengths may have revealed the difficulties of calibration from the telluric lines at 2 μm sooner.

A brief attempt of wavelength calibration using the iterative calibration method outlined in Brogi et al. (2016) was made. This involved generating a set of quadratic wavelength solutions for the observed spectrum and cross-correlating each one against the telluric model. The solutions for the next iteration are obtained by refining the parameters from the wavelength solution with the highest correlation. The method worked well for Brogi et al. (2016) as they included templates for both the star and telluric lines and they were observing in a wavelength domain in which there is a large number of strong and uniform stellar CO lines across the detector. The brief experiments with this method were not successful as they did not include a stellar model or mask, which lead to incorrect fitting solutions. Without adding any stellar masking the telluric lines would strongly correlate to the stellar lines present, especially where there were blended lines. This lead to visibly incorrect wavelength solutions and this method was abandoned. If a stellar mask was used it may have been possible to achieve more sensible results, although still challenging to the low density of telluric lines at this wavelength range.

At one point it was considered to attempt a global fit of the wavelength calibration, using all four CRIRES detectors together. This would create a consistent fit to the dispersion across all 4 detectors at once. This would require extra fitting parameters to define the size of the 3 gaps between the detectors and any vertical offsets. This fit may even need to be performed on the two-dimensional images, before the 1-D extraction. This may have allowed for the telluric lines from neighbouring detectors to help fit the calibration on detectors where there are very few telluric lines (e.g. detector #2). The fitted instrument parameters such as the detector gaps may even be constrained so that they are physically consistent across all observations. However, this idea was not explored further or implemented due to time constraints. An example of the wavelength calibration using all four detectors is provided in Appendix C. In the future it may be possible or necessary to combine all of the methods above, including the Th-Ar calibration lines, telluric models, stellar templates, and multiple detectors fitted at once to

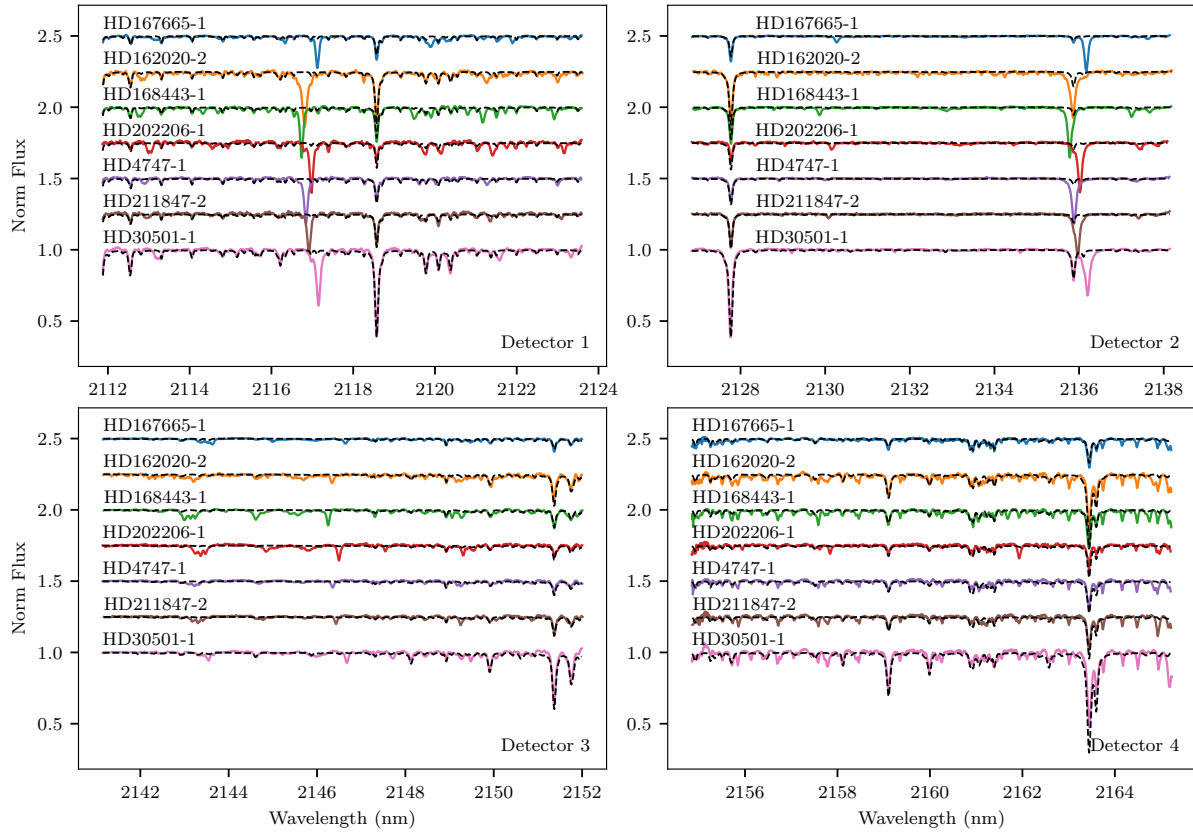


Figure 5.10: An example spectra for each target and each detector #1–4 in order of increasing wavelength. The solid lines are the spectra while the black dashed lines are the telluric models used for wavelength correction, showing good alignment with the spectra.

achieve precise wavelength calibration.

In hindsight using the wavelength solution from the ESO pipeline, or the linear solution from the CRIRES manual, may have been good starting points, rather than the pixel positions, for calibration of the DRACS reduced spectra. This may have made the line identification simpler.

In simulations of a differential technique similar to what is presented in Chapter 6, Kostogryz et al. (2013) simulate the affect of wavelength calibration errors on differential result. They found that calibration error >0.1 pixels will produce signals greater than the photon noise level in spectra with a SNR of around 500. They show that this upper limit only just the level achieved by (Brogi et al., 2012) calibrated using the telluric lines from the observation. This shows how important the wavelength calibration is to detect the spectra of the companion.

5.3.2 Telluric correction

Correction of the telluric lines is performed after wavelength correction, using the same TAPAS models. When inspecting the models and observations there was slight difference in the airmass, m , between the synthetic spectra and the airmass in the fits header. The depth of the telluric lines were re-scaled to match the airmass of the observations using the relation $T = T^\beta$, where T is the transmission of the telluric spectrum and β is the airmass ratio between the observation and model $\beta = m_{\text{observed}}/m_{\text{model}}$.

This scaling adjusted the depth of most absorption lines to better match the observations, but does not correctly scale the deeper H₂O lines, for which there were still differences.

The scaled telluric model is interpolated to the wavelengths of the observed spectrum and then used to correct the observed spectra through division, leaving behind a telluric corrected spectra. Telluric spectra used for correction can be observed alongside the non-corrected spectra in Figure 5.10 as the black dashed lines.

5.3.2.1 Separate H₂O scaling.

A technique suggested by Berta et al. (2014) was attempted to address the poor H₂O airmass scaling. This involved fitting a scaling factor to the H₂O absorption lines before convolution to the instrument resolution. This was achieved by first dividing the spectrum by a telluric model containing the non-H₂O constituents, convolved to the observed resolution, and scaled by the airmass to remove the non-H₂O lines. Then the telluric model with only H₂O lines at full resolution was scaled by a factor T^x and convolved to the instrumental resolution²² and compared to the remaining telluric lines in the observed spectra. This scaled and convolved model was fitted to the observations to find the best was fitted to find the best scaling factor x , for the H₂O lines.

It was found that for a few spectra in the sample this method corrected the deeper telluric lines well, but in many cases the fitted scaling factor was affected by the presence of blended stellar lines (attempting to fit those also). It was also strongly influenced by the deepest H₂O telluric lines present. The telluric correction of the deep H₂O lines could be improved with this technique, but at the cost of worsening the correction of the many smaller H₂O lines. Since the smaller H₂O lines covered more of the spectrum in this region than the larger lines, the separate H₂O scaling was not continued. One possible solution for this would be to perform a piece-wise telluric correction, performing this step only for the deeper H₂O lines. This technique could also benefit from a larger wavelength span that would enable blended lines to be ignored while having sufficient deep H₂O lines to fit the scaling factor correctly. This small experiment shows that a simple scaling is not enough to correct for the absorption of H₂O in an effective way, for this case. Another better solution would be using proper atmospheric fitting tools that fits the telluric model to the observations, such as Molecfit, in which the atmospheric composition can be changed to match the observed telluric line strengths.

5.3.3 Wavelength masking

Throughout the course of this work several wavelength regions were found where the extraction could not be performed reliably due to the wavelength calibration and telluric line corrections. Different wavelength masks are applied to these areas to remove them from the spectra. The main reasons that wavelength masking is used are collated below.

Firstly, regions near the edges of each detector where the wavelength solution is extrapolated outside of the calibrating telluric lines are removed, reducing the effective size of each detector by about 10% or ~ 100 pixels.

Secondly, any remaining artefacts present in the spectra and the centres of deep telluric lines where telluric correction was not corrected properly are masked out. The telluric correction sometimes results

²² R = 50 000 for this work

in “emission-like” peaks in the corrected spectrum, which are removed. These factors combined result in masking out around a further 10% of the observed spectra.

In Section 7.2 a further wavelength restriction is applied to mask out regions where there is a large mismatch between the observed spectrum and the closest synthetic spectra to the host. This significantly restricts the wavelength span utilized for that purpose to around only 43%. The masked regions created by this last mask are shown in Figure 7.4.

5.3.4 Barycentric RV correction

After the telluric correction is performed, the spectra are corrected for Earth’s barycentric motion. The orbital and rotational motion of the Earth imparts a daily and seasonal radial velocity measurement offset onto observations. To accurately compare the radial velocity (or spectral shift) between two measurements, they need to be translated into a common rest frame. The rest frame of choice is the barycentre of the Solar System. Equations to relate the observed spectral shift to the RV shift at the *Barycentric Celestial Reference Reference System* (Rickman, 2001) rest frame are provided in Lindegren et al. (2003).

In this work the barycentric velocity correction is calculated using PyAstronomy’s²³ *helcor* function ported from the REDUCE IDL package (see Piskunov et al. (2002)). This calculates radial velocity of the observer towards the astronomical target, accounting for Earth’s barycentric motion as well as Earth’s rotation, to the accuracy of $\sim 1 \text{ m s}^{-1}$ ²⁴. This computation requires the date and time of the observation, the location of the observatory and the celestial coordinates of the target. The observed spectra are Doppler shifted by the negative value of the barycentric velocity calculated, placing all spectra as if they were observed from the barycentre of the Solar System.

The maximum barycentric velocity of the Earth is around 30 km s^{-1} . Spectral regions within $\pm 30 \text{ km s}^{-1}$ of telluric lines with an absorption depth $> 2\%$ are commonly masked out to avoid them in analyses (such as RV determination), as these regions will overlap and be affected by the telluric lines at some point during the year.

²³ <https://pyastronomy.readthedocs.io>

²⁴ For corrections at an accuracy of 1 cm s^{-1} see Wright et al. (2014) and Shubham et al. (2018).

Chapter 6

Separating the spectra of faint companions

This chapter focuses on applying a direct subtraction method to near-infrared (nIR) spectra of FGK stars which have Brown Dwarf (BD) companions, with the goal to isolate the spectrum of the companions and determine their mass from the radial velocity difference. The CRIRES data used was obtained in 2012¹ with the purpose to apply the differential technique specifically. A level of trust was placed in the quality of the observations, which was unfortunately misplaced. This chapter begins by presenting a range of spectral separation techniques, followed by the motivation for the specific targets observed and details about the observations obtained. The direct subtraction technique is presented and its application to the observations is explored. The limits of the differential technique at low RV separations is given by simulation with synthetic spectra.

6.1 Spectral separation techniques

Spectral observations of binary systems contain the spectra of both bodies, in proportion to their flux ratio, and are Doppler shifted relative to each other due to their orbital motion. There are many disentangling techniques to separate mixed spectra of binary systems, (e.g. Hadrava, 2009, and references therein). These techniques were initially developed to identify and separate the spectra of binary stars, however the techniques and instrumentation have improved so that lower flux ratios from smaller BD and giant planet companions have begun to be detected. A small variety of these techniques will be briefly presented below before exploring the techniques used in this work in more depth.

Several disentangling techniques work on deriving the spectral components from several spectra at different orbital phases. At the minimum $n + 1$ observations can be used to set up a system of linear equations to solve for n spectral components. Each observation adds independent information to the system, with no redundant information, that is it cannot be reduced to a system of few equations with the same information. Works such as Simon et al. (1994) and Sablowski et al. (2016) use singular value decomposition SVD to solve the system for the spectral components. These work best with many well spaced observations, for example Sablowski et al. (2016) state their ideal situation is homogeneous samples over at least half the period, to identify the moving spectral components. Each extra spectrum in the system adds unique information, with no redundant

¹ Before this thesis began.

Tomographic techniques (e.g. Bagnuolo et al., 1991) and Fourier techniques (Hadrava, 1995) have also been developed for disentangling a series of binary spectra. Recently this has even been performed using Gaussian processes which simultaneously fits stellar (or exoplanet) orbits as well as their spectral components (Czekala et al., 2017).

A fairly common technique for deriving precise radial velocities of spectral components in binaries is to apply cross-correlation against a library of known spectra. TODCOR (Two-Dimensional CORrelation) (Zucker et al., 1994) is a commonly used algorithm for cross-correlation of two spectral components to revealing the RV of both components. It has been simulated to be able to detect secondaries with flux ratios down to $\sim 1/1000$ provided a sufficient SNR (e.g. Mazeh et al., 1994; Mazeh et al., 1997). TODCOR requires knowledge of the two spectral components; a series of spectral templates are used to correlate against the observation. These can either be other observed or synthetic stellar spectra, with the highest correlating spectral pair indicating the two components.

Recently this has been used to detect the emission spectra of non-transiting giant planets. Lockwood et al. (2014) and Piskorz et al. (2016) apply TODCOR, with specialized exoplanet spectrum templates used for the companion, to several epochs of high resolution and high SNR nIR spectra. They combine together the individual results in a maximum likelihood framework to obtain the orbital solution of the components.

χ^2 fitting of observations to a library of spectra can also be performed. Kolbl et al. (2015) perform spectral fitting against the SpecMatch library of observed optical spectra, achieving an 80% injection-recovery rate for a 3500 K M-dwarf companion to an 5000–6000 K host star at a 1% flux ratio. Unfortunately a thorough high-resolution spectral library in the nIR is not currently available, requiring synthetic spectral libraries to be used in this work instead.

Other methods for spectral separation focus on removing the spectral component of the host star. Rodler et al. (2012) do this by constructing a stellar mask for the host by constructively combining the host spectra from a number of different phases. The contribution of the faint companion to the mask, added at different phases, is significantly averaged out. The stellar mask is then subtracted from each individual observation to remove the host’s spectrum from all measurements, leaving the companion. González et al. (2006) present an iterative subtraction method in which the knowledge about two spectral components and their respective RVs are improved by alternately iterating them against two or more observations until convergence. The next companion spectrum is derived from an observation using the current host spectrum, then in the next iteration the new host spectrum is determined using the newest companion spectrum until convergence.

Ferluga et al. (1997) provide an analytical approach via secondary reconstruction through a differential spectrum. Spectra from different phases are shifted to the rest frame of the host star and subtracted to mutually cancel out the spectrum of the host star allowing the two copies of the faint companion spectra to become visible. Kostogryz et al. (2013) perform simulations of a similar direct subtraction approach, by simulating CRIRES observations of an M-dwarf with a low mass (likely BD) companion to recover the mass of the companion from the RV separation between the recovered companion spectra. A similar differential subtraction approach to this is used in this work, as the limited observations analysed are not suitable to apply the more advanced techniques that require several spectra from multiple phases.

6.2 Motivation and target selection

The work of Sahlmann et al. (2011) used the astrometry technique to identify several candidate brown dwarf companions of FGK stars with $M_2 \sin i$ values $> 10 M_{\text{Jup}}$. Seven candidates from Sahlmann et al. (2011), which were visible in Period 89 (2012), were selected for further observation in order to identify their stellar nature. That is, to refine the mass of the companions to distinguish if their companion is: a large giant planet ($M \lesssim 13 M_{\text{Jup}}$), a Brown dwarf ($13 \lesssim M \lesssim 80 M_{\text{Jup}}$), or a low-mass star ($M \gtrsim 80 M_{\text{Jup}}$).

The list of target host stars that were observed are presented in Table 6.1 along with their stellar parameters, while Table 6.2 details the orbital parameters of each system from the literature.

It is noted that the orbital parameters of some targets have been refined in the literature since the observations took place. For example three candidates have had their masses refined in recent works. The companion to HD 211847 was determined to be a low mass star with $M_2 = 155 M_{\text{Jup}}$ (Moutou et al., 2017), while the companion to HD 4747 was found to have a mass of $M_2 = 60 M_{\text{Jup}}$ (Crepp et al., 2016). The two companions of HD 202206 (B and c) were found to have masses of $M_B = 93.6 M_{\text{Jup}}$ and $M_c = 17.9 M_{\text{Jup}}$, respectively, classifying HD 202206c as a “circumbinary brown dwarf” (Benedict et al., 2017). These three companions with recently refined masses, along with HD 30501, create a good set of benchmarks to compare any results from the techniques used here, and show that the masses of these targets do span the BD to low-mass star range. All target companions except HD 162020 ($P=8.4$ days) are in (very) long period orbits ($P=0.7\text{--}38$ years) with masses (or $M_2 \sin i$) greater than $10 M_{\text{Jup}}$.

The spectral differential approach was chosen with the goal to constrain the companion masses while minimizing the observational time required to observe: in theory only requiring two observations. The observing proposal determined that it should be possible to obtain a detection of a companion with a 1% contrast ratio with an exposure time of around 20 minutes. Two observations at “clearly separate RVs” were requested to constrain each target. Observations were performed without telluric standard star observations to avoid the extra observing time overhead, choosing to instead rely on synthetic model correction (see Section 4.1.1). The K -band was chosen to achieve a high contrast relative to the host star, detected in the extreme V-K colour indexes (> 7.8), while the specific atmospheric window (2110–2070 nm) was chosen in order to reduce the absorption introduced by the atmosphere (J. R. Barnes et al., 2008).

Table 6.1: Stellar parameters of the host stars. V is the apparent visual magnitude taken from SIMBAD (Wenger et al., 2000). Distances were calculated using the GAIA DR2 parallax measurements.

Star	SpT	V	T_{eff} (K)	$\log g$ (cm s^{-2})	[Fe/H]	M_1 (M_{\odot})	Age (Gyr)	d (pc)	Reference
HD 4747	K0V	7.15	5316 ± 50	4.48 ± 0.10	-0.21 ± 0.05	0.81 ± 0.02	3.3 ± 2.3	18.80 ± 0.04	1, 2, 3, 8
HD 162020	K3V	9.12	4723 ± 71	4.31 ± 0.18	-0.10 ± 0.03	0.74 ± 0.07	3.1 ± 2.7	30.85 ± 0.06	4, 5, 6, 8
HD 167665	F9V	6.40	6224 ± 50	4.44 ± 0.10	0.05 ± 0.06	1.14 ± 0.03	$0.7 - 3.6$	31.24 ± 0.06	1, 8
HD 168443	G6V	6.92	5617 ± 35	4.22 ± 0.05	0.06 ± 0.05	1.01 ± 0.07	10.0 ± 0.3	39.67 ± 0.12	5, 6, 8
HD 202206	G6V	8.07	5757 ± 25	4.47 ± 0.03	0.29 ± 0.02	1.04 ± 0.07	2.9 ± 1.0	46.03 ± 0.14	5, 7, 8
HD 211847	G5V	8.62	5715 ± 24	4.49 ± 0.05	-0.08 ± 0.02	0.92 ± 0.07	$0.1 - 6.0$	48.81 ± 0.13	1, 2, 4, 8
HD 30501	K2V	7.59	5223 ± 50	4.56 ± 0.10	0.06 ± 0.06	0.81 ± 0.02	$0.8 - 7.0$	20.37 ± 0.01	1, 4, 8

References: (1) Sahlmann et al. (2011); (2) Santos et al. (2005); (3) Crepp et al. (2016); (4) Tsantaki et al. (2013); (5) Bonfanti et al. (2016); (6) Santos et al. (2004); (7) Sousa et al. (2008); (8) GAIA Collaboration et al. (2018).

Table 6.2: Orbital parameters for the BD companions obtained from the literature.

Object	γ (km s^{-1})	Period (day)	e	K_1 (m s^{-1})	T_0 (JD-2,450,000)	ω (deg)	$M_2 \sin i$ (M_{Jup})	M_2 (M_{Jup})	Ref.
HD 4747	0.215 ± 11	$13\,826.2 \pm 314.1$	0.740 ± 0.002	755.3 ± 12	463.1 ± 7.3	269.1 ± 0.6	39.6	60.2	1
HD 162020	-27.328 ± 0.002	$8.42819 \pm 6e^{-5}$	0.277 ± 0.002	$1\,813 \pm 4$	$1\,990.68 \pm 0.01$	28.4 ± 0.2	14.4	-	2
HD 167665	8.003 ± 0.008	$4\,451.8 \pm 27.6$	0.340 ± 0.005	609.5 ± 3.3	$6\,987.6 \pm 29$	-134.3 ± 0.9	50.3	-	3
HD 168443b	-0.047 ± 0.552	$58.1124 \pm 4e^{-4}$	0.529 ± 0.001	475.13 ± 0.9	$5\,626.20 \pm 0.02$	172.9 ± 0.1	7.7	-	4
HD 168443c	-0.047 ± 0.552	$1\,749.83 \pm 0.57$	0.211 ± 0.002	297.7 ± 0.6	$5\,521.3 \pm 2.2$	64.9 ± 0.5	17.1	-	4
HD 202206B	14.721	256.33 ± 0.02	0.432 ± 0.001	567 ± 1	$2\,176.14 \pm 0.12$	161.9 ± 0.2	17.4	93.2 ± 7.3	5, 6
HD 202206c	14.721	$1\,260 \pm 11$	0.22 ± 0.03	41 ± 1	$3\,103 \pm 452$	280 ± 4	2.3	17.9 ± 2.9	5, 6
HD 211847	6.689^a	$7\,929.4 \pm 2\,500$	0.685 ± 0.068	291.4 ± 12.2	$12\,030.1 \pm 2\,500$	159.2 ± 2.0	19.2	155	3, 7
HD 30501	23.710 ± 0.028	$2\,073.6 \pm 3.0$	0.741 ± 0.004	$1\,703.1 \pm 26.0$	$3\,851.5 \pm 3.0$	70.4 ± 0.7	62.3	89.6	3

References. (1) Crepp et al. (2016); (2) Udry et al. (2002); (3) Sahlmann et al. (2011); (4) Pilyavsky et al. (2011); (5) Correia et al. (2005); (6) Benedict et al. (2017); (7) Moutou et al. (2017).

Notes. ^(a) fixed

Table 6.3: Details regarding each of the CRIRES observations. The number of artefacts removed in Section 5.2.3.1 as well as the SNR of the combined spectra is provided. The last three columns are the RV calculated from the orbital solution for both the host and largest companion, and the RV difference between them.

Object	Obs. #	Start date (yyyy-mm-dd hh:mm:ss)	Filter	Airmass (at start)	Artefacts / 32	SNR	RV_1 km s^{-1}	RV_2 km s^{-1}	rv_2 km s^{-1}
HD 4747	1	2012-07-06 07:36:06	Ks	1.25	7	340	-0.219	-0.154	0.065
HD 162020	1	2012-07-04 06:23:22	Ks	1.30	2	127	-28.760	50.785 ^a	79.545 ^a
HD 162020	2	2012-07-04 06:57:48	Ks	1.44	2	128	-28.717	48.440 ^a	77.157 ^a
HD 167665	1	2012-07-28 05:00:53	Hx5e-2	1.24	7	371	7.581	18.024 ^a	10.443 ^a
HD 167665	2	2012-07-28 05:37:27	Hx5e-2	1.39	4	374	7.581	18.025 ^a	10.444 ^a
HD 167665	3	2012-08-05 02:54:03	Hx5e-2	1.04	4	358	7.575	18.163 ^a	10.588 ^a
HD 168443	1	2012-08-05 04:29:32	Ks	1.31	2	192	-0.121	50.932 ^{a,b}	51.053 ^{a,b}
HD 168443	2	2012-08-05 04:58:50	Ks	1.47	4	190	-0.121	51.189 ^{a,b}	51.310 ^{a,b}
HD 202206	1	2012-07-12 06:54:44	Ks	1.01	3	189	14.843	12.992 ^b	-1.851
HD 202206	2	2012-07-13 05:41:40	J	1.01	3	209	14.837	13.065 ^b	-1.772
HD 202206	3	2012-07-11 08:29:55	Ks	1.15	4	180	14.849	12.920 ^b	-1.929
HD 211847	1	2012-07-06 07:02:57	Ks	1.07	4	272	6.613	7.171	0.558
HD 211847	2	2012-07-13 06:54:37	Ks	1.05	5	283	6.614	7.167	0.553
HD 30501	1	2012-04-07 00:08:29	Hx5e-2	1.60	3	217	22.372	36.377	14.005
HD 30501	2	2012-08-01 09:17:30	Hx5e-2	1.42	10	212	22.505	35.120	12.615
HD 30501	3	2012-08-02 08:47:30	Hx5e-2	1.53	8	237	22.507	35.102	12.595
HD 30501	4	2012-08-06 09:42:07	Ks	1.28	7	235	22.514	35.031	12.517

^a Maximum RV given $M_2 \sin i$ only.

^b Largest mass companion only.

6.2.1 The CRIRES data

Observations were performed with the CRIRES instrument (Kaeufl et al., 2004) configured to observe a narrow wavelength domain of the *K*-band between 2120–2165 nm. The slit width of $0.4''$ resulted in an instrumental resolving power of $R = 50\,000^2$. No adaptive optics were used to ensure that the entrance slit was entirely covered by each target. This is to prevent strong slit illumination variations that could change the shape of spectral lines, and introduce and radial velocity variation on the data.

The observations were performed in service mode during Period 89 with run ID. 089.C-0977(A) between April and August 2012. The observing proposal is provided in Appendix E.7. A single observation is composed of eight individual spectra with an integration time of 180s each, observed in the ABBAABBA nod cycle pattern to obtain a high signal-to-noise ratio (>100) when combined. The list of observations obtained with CRIRES are provided in Table 6.3.

There is a slight inconsistency with some of the observations, taken in service mode. For instance HD 202206 has two observations taken with the *Ks* filter, while one is taken with the *J* filter. There is also the last observation of HD 30501 taken with a different filter compared to the others. The documents for the phase two observing proposal were unable to be obtained to determine if these ‘odd’ filters were requested or if this was an observational mistake.

There is also an inconsistency with the naming or ordering of the observations again with the target HD 202206. The observation that was performed first in time is labelled with the observation name of HD 202206-3 in the fits header file, while the second and third observations are labelled -1 and -2 respectively.

There could be two possible reasons for the single observation of HD 4747. The first reason could be that only one observation was requested due to the very long orbital period of the target, although this would not have fulfilled the scientific goal. The second and more likely reason is that these observations were performed in service mode, as a filler program, and there was no time to observe a second observation of HD 4747.

All observations were reduced using the DRACS pipeline with the artefact corrections method applied (see Section 5.2.3). Each observation was then: wavelength calibrated using a synthetic telluric spectrum, corrected for telluric absorption, and then corrected for the barycentric RV following Sections 5.3.1, 5.3.2 and 5.3.4.

6.3 Direct Subtraction Method

The basic premise of the direct subtraction method is to take two high resolution spectra of a binary system at separate phases, transform them to the rest frame of the star, calculate the difference so as to remove the spectrum of the host star, leaving behind a residual comprised of the difference between the two companion spectra with different Doppler shifts. Similar techniques were originally developed to separate the spectra of binary stars (e.g. Ferluga et al., 1997) while Kostogryz et al. (2013) performed promising simulations of an M-dwarf with a low-mass companion, if observed with CRIRES.

Assuming that the instrumental profile does not vary between observations and atmospheric absorption are dealt with appropriately, the spectra of the observed targets are assumed to be composed of two spectral components: a bright host star blended with the spectrum of a faint companion. The spectrum

² The rule of thumb resolution for CRIRES is $100\,000 \times \frac{0.2''}{\text{slit width}}$ with the slit width in arcseconds

received from the host-companion pair is given by the superposition of two spectral components (J_1, J_2):

$$I(\lambda) = J_1(\lambda - v_1) + J_2(\lambda - v_2), \quad (6.1)$$

where the subscripts 1 and 2 indicate the spectrum of the host and companion respectively, λ represents the wavelength of the spectra and $\lambda - v$ represents the Doppler shift $\lambda(1 - v/c)$ by a velocity v .

This can be shifted into the rest frame of the host star by applying the shift v_1 :

$$I(\lambda + v_1) = J_1(\lambda) + J_2(\lambda - v_2 + v_1). \quad (6.2)$$

To analyse J_2 , the spectral component of interest, the component from the host needs to be carefully removed. If two observations of the same target are observed, denoted with subscripts a and b , there will be relative motion between the components due to the orbit. Assuming that the stellar spectra do not change over time³ ($J_{1a} = J_{2a}$) and each spectrum can be individually Doppler shifted to the rest frame of the host star $J_1(\lambda)$, then the spectrum of the host star can be removed through subtraction of the two observations. Mutually cancelling the host component leaves two components of the companion subtracted from each other, with a relative Doppler shift between them.

$$\begin{aligned} S(\lambda) &= I_a(\lambda + v_{1a}) - I_b(\lambda + v_{1b}) \\ &= (J_{1a} + J_{2a}(\lambda - v_{2a} + v_{1a})) - (J_{2b} + J_{2b}(\lambda - v_{2b} + v_{1b})) \\ &= J_{2a}(\lambda - v_{2a} + v_{1a}) - J_{2b}(\lambda - v_{2b} + v_{1b}) \end{aligned} \quad (6.3)$$

$$S(\lambda + v_{2a} - v_{1a}) = J_{2a}(\lambda) - J_{2b}(\lambda - v_{2b} - v_{1a} + v_{1b} + v_{2a}) \quad (6.3)$$

$$S(\lambda') = J_{2a}(\lambda) - J_{2b}(\lambda - \Delta RV_2) \quad (6.4)$$

where,

$$\Delta RV_2 = v_{1a} - v_{1b} - v_{2a} + v_{2b} \quad (6.5)$$

is the RV difference between the two companion spectral components when the host components are mutually subtracted, and $\lambda' = \lambda + v_{2a} - v_{1a}$.

The resulting differential spectra $S(\lambda')$, dubbed *s-profile* by Ferluga et al. (1997), is composed of just the companion spectra, shifted and subtracted from itself.

Ferluga et al. (1997) provide an analytical form for the *s-profile* given a single Gaussian line of the form $J(\lambda) = 1 - D \cdot \exp^{-\pi(\lambda - \lambda_0)^2/W^2}$:

$$S(\lambda) = 2D \cdot \exp^{-\pi D^2[(\lambda - \lambda_0)^2 + (k/2)^2]/W^2} \cdot \sinh \frac{\pi D^2(\lambda - \lambda_0)k}{W^2}, \quad (6.6)$$

where λ_0 , D , and W are the central wavelength, depth and equivalent width of the Gaussian line, and $k = \Delta RV_2$ is the shift between the two companion spectra.

From binary dynamics (e.g. Murray et al., 2010) the RV amplitudes of the host and companion (ignoring the system velocity *gamma*) are related through the mass ratio, q , while having an opposite

³ (Kostogryz et al., 2013) find the stellar activity residual is smaller than the companion differential flux.

sign⁴ (see Section 2.1.2):

$$v_2 = -q * v_1 \quad (6.7)$$

Equation 6.5 can be simplified by expressing it in terms of the mass ratio and host RV only:

$$\begin{aligned} \Delta RV_2 &= qv_{1a} - qv_{1b} + v_{1a} - v_{1b} \\ &= (1 + q)(v_{1a} - v_{1b}). \end{aligned} \quad (6.8)$$

If the ΔRV_2 between the companion spectra is able to be constrained or derived from the s-profile (see Ferluga et al., 1997) then the mass ratio of the system, q , can be determined, thereby constraining the mass of the companion.

The values v_{1a} and v_{1b} are radial velocity of the host components. The host's RV are calculated using the Equation 2.6 with the orbital parameters from the literature and provided in Table 6.2. These are used to shift each spectrum into the rest frame of the host star to mutually cancel the host's spectrum. These components can also be determined directly from the spectrum by cross-correlating the observed spectrum with a stellar template of the host and gave results in reasonable agreement.

It is necessary to have a consistent instrumental setup (Ferluga et al., 1997; Hadraiva, 2009), to avoid introducing extra instrumental effects (e.g. slit-width and/or filters) into the spectral differentials and to always observe the same wavelength range and maximize the information to be extracted. For these observations, the second observation of HD 202206 and fourth of HD 30501 were taken with different filters compared to the other observations. This is according to the filter settings given in the fits file headers. Therefore, these two observations could not be used for this differential analysis. As noted in Hadraiva (2009), any spectral differences in the filters would add extra unknown signal/noise making it harder to disentangle the faint spectral differences.

6.3.1 Calculation of expected RV

In this section calculations are performed to estimate the RV of both spectral components in each observation and the likely RV separation between the two companions is estimated. To apply the differential method the observations need to be Doppler shifted so that the host spectra can be subtracted in the same reference frame. To do this the RV of the host in each observation is calculated from the orbital parameters in the literature. The time of each observation is used as input into Equation 2.6 combined with the orbital parameters from Table 6.2 to calculate the expected RV of the host star. These values calculated are given in Table 6.3 as RV_1 . The companion mass (M_2 or $M_2 \sin i$) is used alongside the stellar mass from Table 6.1 to also calculate the RV of the companion (see Section 2.1.2). This is given as RV_2 in Table 6.3. The RV difference between the host and companion for each observation is also computed and provided as $rv_2 = RV_2 - RV_1$ ⁵.

For these observations the maximum estimated RV separation between the two companion spectra in ΔRV is calculated following Equation 6.5 below and provided in Table 6.4. This table also contains the estimated semi-major RV amplitude for the companion K_2 (from Equation 2.14) and the phase coverage of the observations. The phase coverage is the maximum fraction of the orbit covered between

⁴ The opposite sign arises from a 180° difference in the angle of periaxis, ω , for the companion.

⁵ This will be used in Chapter 7

Table 6.4: Estimated orbital semi-amplitude and RV separation of the companions, given the companion mass (M_2 or $M_2 \sin i$) from Table 6.2 and observation times from Table 6.3.

Companion	Estimated K_2 (km s^{-1})	Estimated $ \Delta RV $ (m s^{-1})	Phase coverage (%)
HD 4747	-10.65	—	—
HD 162020	-98.92 ^a	2388	0.28
HD 167665	-14.47 ^a	145	0.18
HD 168443b	-64.65 ^a	258	0.035
HD 168443c	-18.05 ^a	<1	0.001
HD 202206B	-6.79	78	0.74
HD 202206c	-2.50	<1	0.15
HD 211847B	-1.85	5	0.09
HD 30501	-16.12	1410	5.8

^a Maximum K_2 only given $M_2 \sin i$.

the observations for each target. For HD 4747 the ΔRV and phase coverage values are missing due to the single observation.

The full orbital solution for the components along with the times of observations are displayed below in Section 6.5.

6.4 Results of spectral differential analysis

The spectral differential procedure outlined above was applied to the wavelength-calibrated, telluric- and barycentre-corrected CRIRES observations. The spectra were first Doppler shifted to the rest frame velocity of the system by applying a shift of $-\gamma$. Each spectra is then shifted by its $-RV_1$ so that the host lines are at rest. Finally one spectrum is subtracted from the other as described above.

Although this is attempted on all targets, only the most favourable case, HD 30501, is shown in Figure 6.1. It is favourable because it is the second largest companion in the sample at $90 \text{ M}_{\text{Jup}}$ but also has the second largest RV separation between observations. The top panel shows the reduced CRIRES spectrum of HD 30501 from detector 1 without telluric correction. The telluric model is also shown in the top panel. The middle panel shows the CRIRES spectra corrected with the telluric model. The differential spectra recovered for HD 30501 is shown at the bottom panel of Figure 6.1. The shaded regions indicate where the telluric green and host star blue spectra are $> 4\%$ deep. This indicates that the features of the differential spectrum near these shaded regions are likely due to imperfect telluric correction and host cancellation.

The mutual cancellation of the stellar host seems to work well for the $\sim 40\%$ deep line near 2117 nm, with the line being completely removed, but it does not do so well for the smaller $\sim 10\%$ deep line around 2121.5 nm. The residual for the large $\sim 40\%$ deep telluric line near 2118.5 nm is still quite prominent. Around 2120 nm there is wide negative residual around three neighbouring telluric lines, $\sim 10\%$ deep. One possible explanation for this is that the continuum normalization near 2120 nm was influenced by this grouping of lines.

To understand the observed differential signal, a series of simulations were performed of a differential

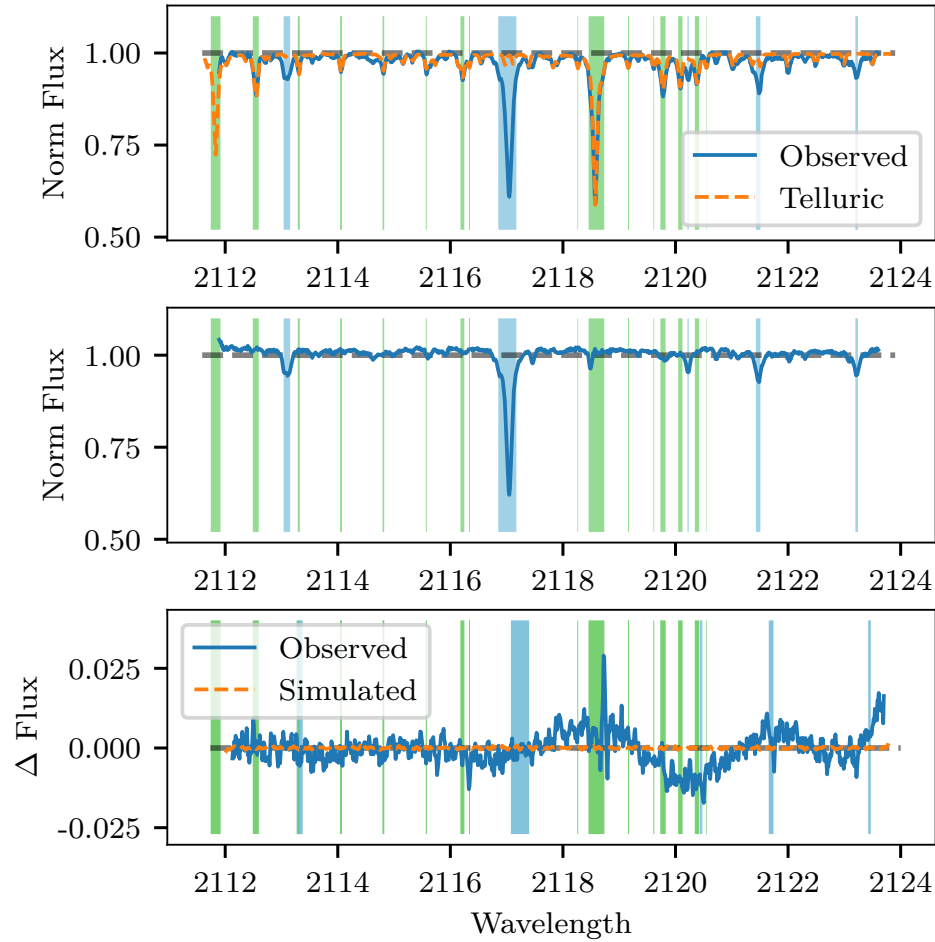


Figure 6.1: Top: A reduced CRIRES observation of HD 30501 (blue) for detector 1 between 2112–2124 nm along with the TAPAS telluric absorption model (orange dashed) used for the wavelength calibration and telluric correction. Middle: The telluric corrected spectra. Bottom: (blue) Differential spectra for HD 30501 between observations 1 and 3. (orange dashed) Simulated “perfect” differential using PHOENIX-ACES spectra with parameters $T_{\text{eff}}=2500$ K, $\log g=5.0$, and $[\text{Fe}/\text{H}]=0.0$, with the same ΔRV as the observations. The shaded regions indicate where the telluric green and host star blue spectra are > 4% deep.

spectrum of HD 30501 using a synthetic PHOENIX-ACES spectra with parameters $T_{\text{eff}}=2500 \text{ K}$, $\log g=5.0$, and $[\text{Fe}/\text{H}]=0.0$, with the RV offset estimated from the observation times. These parameters represent an estimated companion T_{eff} with the metallicity and $\log g$ similar to the host (closest grid model). The model spectra were convolved to $R = 50\,000$, continuum normalized and scaled by the estimated flux ratio of the companion. In this simulation a synthetic host or telluric spectra is not included and as such simulates the differential result of a “perfect” host cancellation with no telluric contamination present. This is the ideal-case scenario, and it is stressed that it is impossible to simulate the effect of improper telluric correction in a meaningful way. When comparing the simulated and observed differential in the bottom panel of Figure 6.1, there is a striking amplitude difference. The orange-dashed line of the simulated differential spectrum amplitude is of a much smaller scale than the observed differential. This simulation demonstrates that the expected amplitude of the differential signal of HD 30501 is much smaller than the residuals created by the differential technique applied to these observations.

The amplitude of the differential signal is lower than expected due to the very low ΔRV between the observation pairs. The maximum ΔRV between observational pairs, for the targets investigated in this work, are provided in Table 6.4. In the best target in this sample, HD 30501, the ΔRV_2 of the companion between observations is 1.41 km s^{-1} . For comparison, a single Gaussian absorption line, to be shifted by $\Delta\lambda = \text{FWHM}$ would need a ΔRV of $v_{\text{FWHM}} = c/R \approx \sim 6 \text{ km s}^{-1}$. Since the ΔRV_2 are shifted by a significant smaller value than the line FWHM, the spectral lines of the companion also mutually cancel themselves, diminishing the amplitude of the differential signal significantly. As the companion spectra are already faint (with a flux ratio at the percent level) the differential signal is not detectable in these observations at the achieved noise level.

When the ΔRV of the companion is smaller than the FWHM of a line, if the mutual subtraction of the host is performed, there is also a mutual subtraction of the companion spectra, diminishing the detected amplitude of the differential signal and reducing the ability to detect the companions using this method. The observations need to be spaced further apart in time/phase to achieve a larger ΔRV_2 separation and increase the amplitude of the differential. Once there is a separation there will be complex interactions between neighbouring lines that need to be accounted for.

6.4.1 Relative differential amplitude

Further investigation was performed into the differential subtraction when mutually subtracting the companion under small ΔRV . This is done by exploring the amplitude of the differential against a variation in RV. Simulations were performed creating a differential spectra for a range of ΔRV s between $\pm 10 \text{ km s}^{-1}$ using the same PHOENIX-ACES spectra for the companion of HD 30501 ($T_{\text{eff}}=2500 \text{ K}$, $\log g=5.0$, $[\text{Fe}/\text{H}]=0.0$) convolved to $R = 50\,000$. These simulations were focused on the wavelength range 2110–2123 nm, corresponding to detector #1 of the CRIRES observations. The differential spectra was created for each by taking the synthetic spectrum for the companion, Doppler shifting a copy of the spectrum and subtracting it from the original. At each RV step the maximum absolute differential amplitude (peak to peak) of the simulated differential spectrum observed was recorded. Again these simulations are performed assuming perfect telluric correction and removal of the host star by only considering the spectrum of the companion alone.

The result of this simulation is shown in Figure 6.2. As this absolute amplitude is specific to the lines present in the analysed wavelength range, the values were normalized by the median amplitude value outside of the line FWHM (dashed vertical lines), between $\pm(7 - 10) \text{ km s}^{-1}$, to give a relative

differential amplitude, independent from the depth of a specific line. Differential subtraction simulations were also performed using a spectrum made up of a single Gaussian or Lorentzian line; these are shown in Figure 6.2 as the orange dashed and green dash-dotted lines respectively. The spectral profile shape of the differential for the Gaussian line was also checked for consistency with the analytical form of the differential spectra from Ferluga et al. (1997, Equation A.1) (included above as Equation 6.6).

Figure 6.2 shows that with a ΔRV of zero between companion spectra the spectral lines of the companion completely cancel each other out, resulting in zero amplitude. As the RV separation increases in either direction, the individual lines stop completely cancelling each other as they begin to separate. A maximum differential amplitude is achieved when the individual lines are fully separated. The shape/width of the differential spectral lobes Ferluga et al. (e.g. 1997, eqn. A.1) was not considered, but this could also have been measured.

At simulated separations beyond 10 km s^{-1} the neighbouring spectral lines begin to strongly interfere, leading to a variable (quasi-sinusoidal) relative amplitude, although this is not shown here. The shape of the relative amplitude becomes complicated due to the line interaction and because the ΔRV for all observations fall well short of this region it was not investigated further. It is suspected that the interaction of neighbouring lines is one possible cause for the difference in the relative differential amplitude between the single theoretical line profiles and synthetic spectrum between 2 and 6 km s^{-1} .

The vertical dotted lines indicate the line FWHM = $\lambda/R = v/c$ with a velocity of 6 km s^{-1} at $2 \mu\text{m}$ with $R=50\,000$, showing that the amplitude is almost maximum when the lines are separated beyond their line width. The two solid vertical lines in Figure 6.2 indicate the $\Delta RV=1.41 \text{ km s}^{-1}$ separation calculated for our best target, HD 30501 from Table 6.4, given known orbital parameters and the observation times. This shows that our differentials have severely reduced amplitude, < 20% relative to well separated individual lines. As the companion spectra are already faint and in combination with a host star at >1% flux ratio the >80% extra reduction in signal amplitude makes this detection impossible with these observations.

6.5 Orbital Solutions

The insufficient observational spacing becomes clear when the orbits are visualized by plotting the RV variation. Figures 6.3 to 6.11 show the RV curves for each target observed for this project. For the targets that have two companions, the individual contributions are shown on separate figures. For each figure the left hand plot shows the RV variation across a full orbit of the companion, while the plot on the right shows the RV variation for the 6 month observation window of Period 89 only. The solid black line indicates the RV of the host star (with scale on the left hand axis), while the blue dashed line shows the RV of the companion (with the scale on the right hand axis). The orange crosses and red stars indicate on the RV curves the times at which observations were obtained for each target, for the host and companion respectively.

The first thing that is apparent is the variation of shape of the RV curves. This is normal with the variations in shape arising from the different orbital parameters of each target (provided in Table 6.2). In the left hand plots, in which a full orbit is shown, the different shapes are created from the eccentricity, e , and argument of periapsis, ω . In the right hand panels, for which a fixed time period is shown, the orbital period of the companion also plays a role. Specifically the ratio of orbital period to the 6 month observing period determines what fraction (or multiples) of the orbit is displayed.

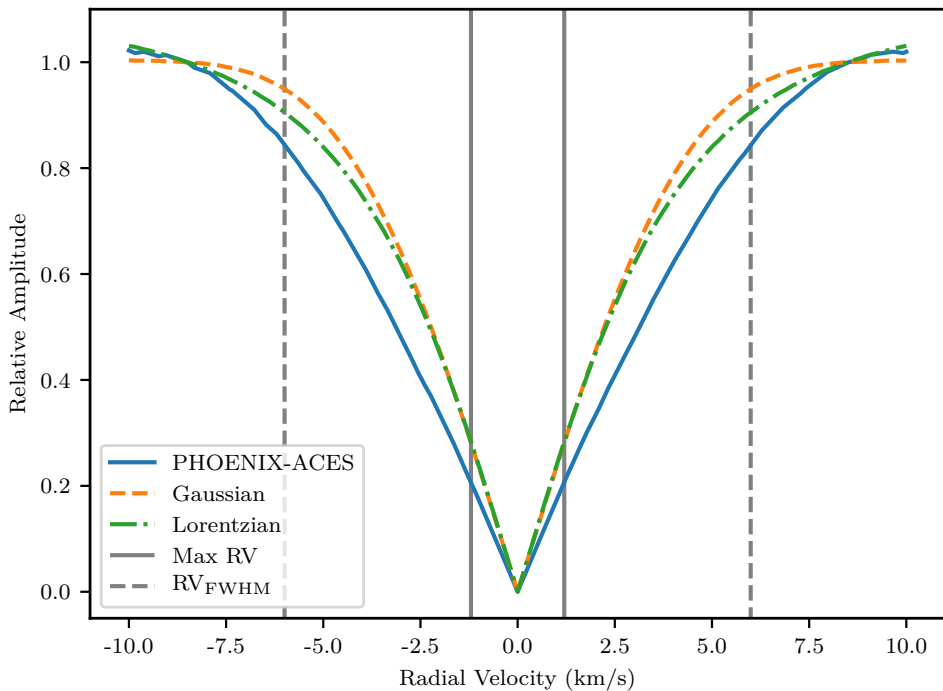


Figure 6.2: Simulated relative amplitude of differential spectra at different companion ΔRV separations revealing the diminished amplitude at very small orbital separations. The solid blue line shows the maximum relative amplitude of the differential signal (from a shifted copy of itself) of a PHOENIX-ACES spectrum with $T_{\text{eff}}=2500 \text{ K}$, $\log g=5.0$, $[\text{Fe}/\text{H}]=0.0$ in the wavelength region $2110\text{--}2123 \text{ nm}$. The maximum difference is normalized by the median amplitude between $\pm 7\text{--}10 \text{ km s}^{-1}$, representing a complete line separation. The orange (dashed) and green (dot-dashed) lines represent the relative amplitude of a spectrum differential for a spectrum containing a single Gaussian or Lorentzian absorption line respectively, each with a unitary amplitude and a FWHM = λ/R . The solid vertical lines indicate the estimated companion ΔRV in these observations while the dashed vertical lines indicate the RV corresponding to the FWHM at this wavelength and resolution.

The RV curves of the star and the planet mirror each other about the systems mean velocity, γ , with the amplitude scaled by their mass ratio, q (see Equation 2.14), and ω offset by 180° .

All the plots, apart from HD 4747, have more than one observations shown, although it can be difficult to see as the observational spacing is small.

For the companions HD 162020b (Figure 6.4) and HD 168443b (Figure 6.6) their orbital periods are shorter than 6 months, allowing for multiple orbits to occur during Period 89. As such the full amplitude range was available to measure in the observing period if observations were taken at correct times, at the locations of the extrema. It should have been possible to obtain observations in which the companion spectra were sufficiently separated for the differential separation technique. However in reality, the two observations for these two targets were taken immediately after each other, making any differential extremely small. This is ignoring the fact that the flux ratios (from Table 4.4) for these short period companions are estimated to be very low, meaning they would have been very difficult to detect even if observed at the extrema.

The larger companion HD 168443c in Figure 6.7 has a longer orbital period, so it appears as a straight line in the right hand panel, although the amplitude variation of the companion during Period 89 is about $8\text{--}9 \text{ km s}^{-1}$. Therefore observations taken at the extreme ends of Period 89 may have provided just enough separation to be suitable for the differential.

For HD 202206 about 3/4 of the orbit is covered in Period 89 with a RV amplitude of the companion possible of over 40 km s^{-1} . Therefore, in this case well separated RVs could have been obtained.

For the remaining targets with long periods, it is clear that sufficiently separated RVs were not obtained, but also that they were not possible within a single observing period with a RV variation less than 6 km s^{-1} during Period 89. For HD 30501 the largest time separation between observations obtained is clearly visible in Figure 6.11. Unfortunately, this did not result in a large enough companion separation. Looking at the full period, if the observations had been obtained in the previous period then sufficient separation could have possibly been obtained.

The code used to create orbital plots similar to those shown here is available under the iastropt/Observationtools *Github* repository with documentation available on Read the Docs.

The sampling of points in the orbit reveal that the choice of points was not favourable for the application of the direct subtraction technique. This was unfortunately discovered after attempting to apply the technique.

6.5.0.1 Differential scheduling challenges

This work has revealed that care needs to be taken in planning the observations for the application of the spectral differential technique of faint companions in the future. Future attempts need to pay attention in particular to: the FWHM of the lines in the region (governed by resolution and wavelength), the estimated companion separation ΔRV_2 ; and the previous observations from different observing periods, all while keeping the detector settings consistent.

The original goal for the observations was to obtain two different and “clearly separated radial-velocities” for the secondary companion. However, the program was assigned a low-priority (C, in ESO grading) and, possibly due to operational reasons, the original time requirements necessary to secure well separated RVs for the companion spectra could not be met. This meant that all observations were insufficiently separated to extract a differential spectra for the companion.

The long orbital periods of these targets is also a strong contributing factor to the insufficient

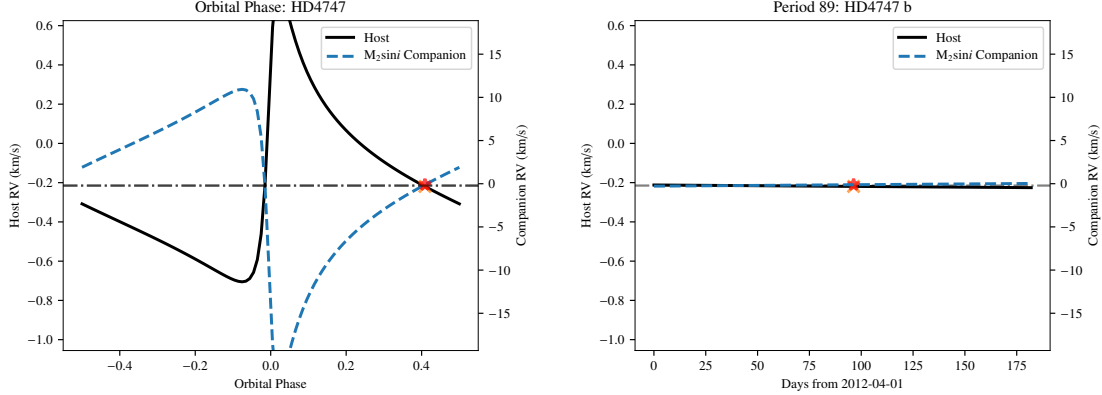


Figure 6.3: RV single companion Keplerian orbit for HD 4747. The left hand plot shows the RV curve for one full orbit while the right hand panel shows the RV curve over 6 months (Period 89). The solid black line indicates the RV of the host star (with scale on the left), while the blue dashed line indicates the RV of the companion (with scale on the right axis). The orange crosses and red stars indicate the times at which observations were obtained for the target, for the host and companion respectively.

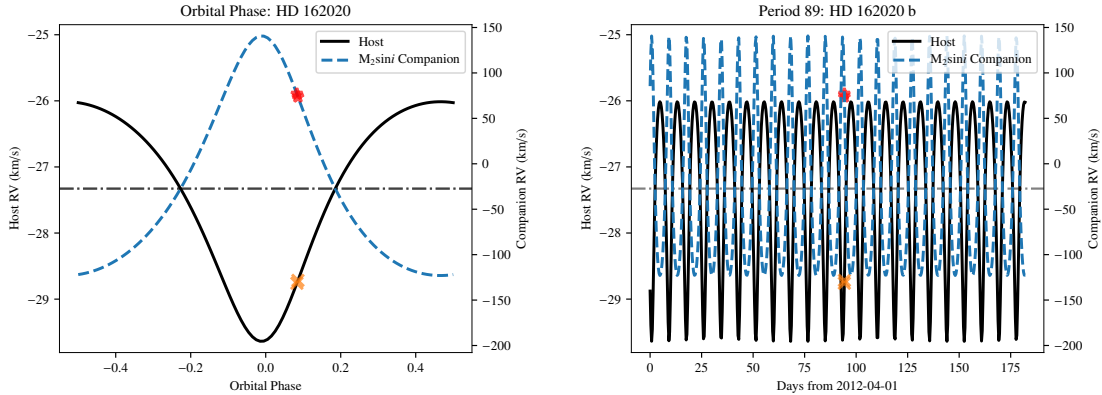


Figure 6.4: Same as Figure 6.3 but for HD 162020.

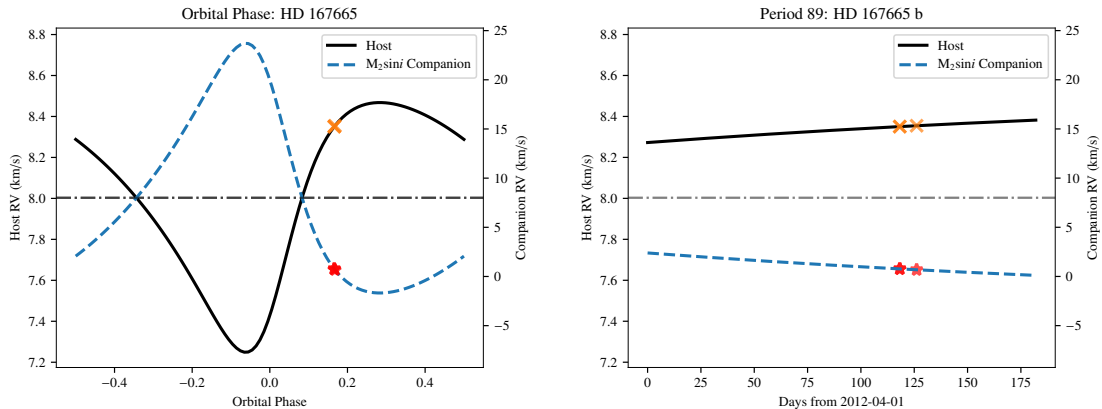


Figure 6.5: Same as Figure 6.3 but for HD 167665.

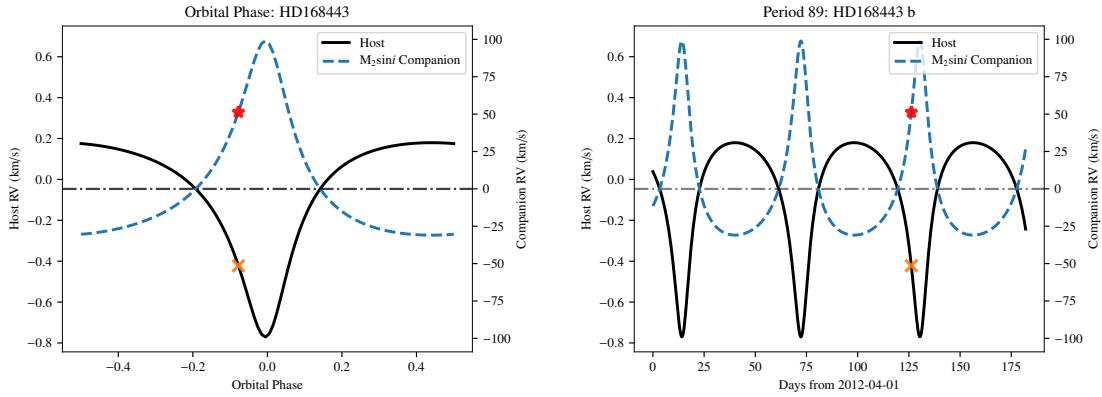


Figure 6.6: Same as Figure 6.3 but for HD 168443b. Analysed as if this was a single companion.

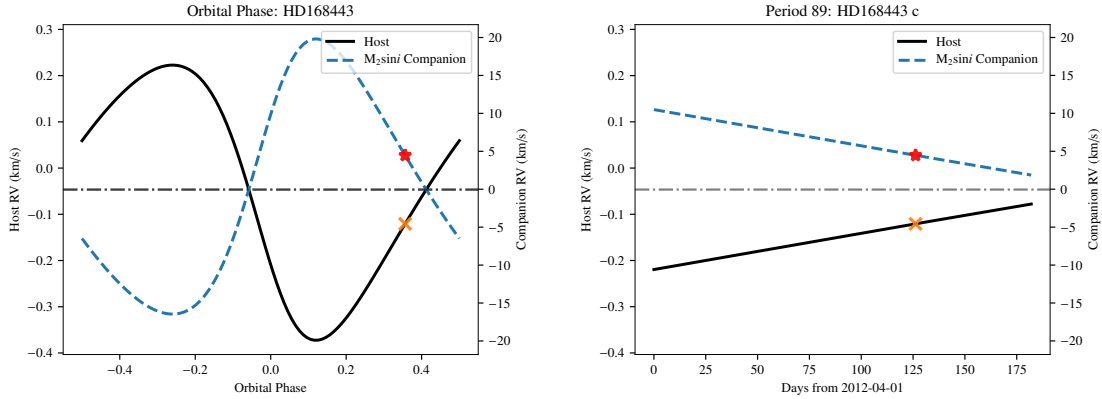


Figure 6.7: Same as Figure 6.3 but for HD 168443c. Analysed as if this was a single companion.

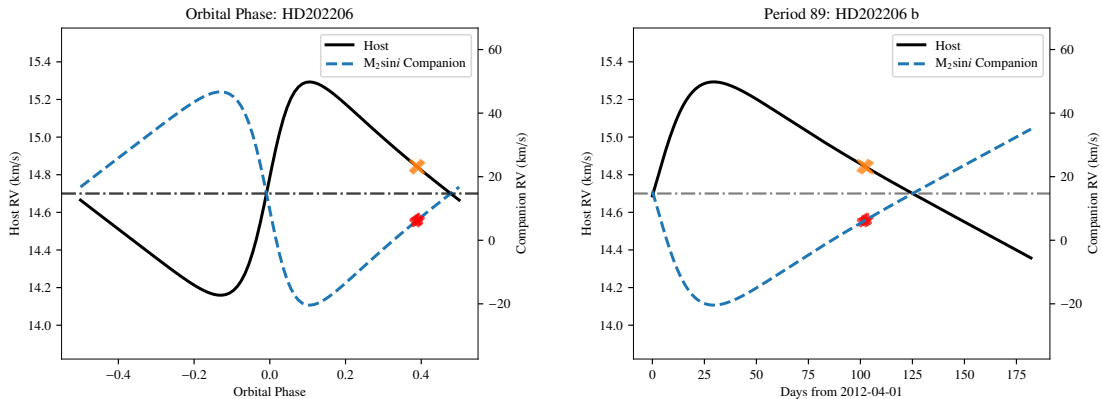


Figure 6.8: Same as Figure 6.3 but for HD 202206B. Analysed as if this was a single companion.

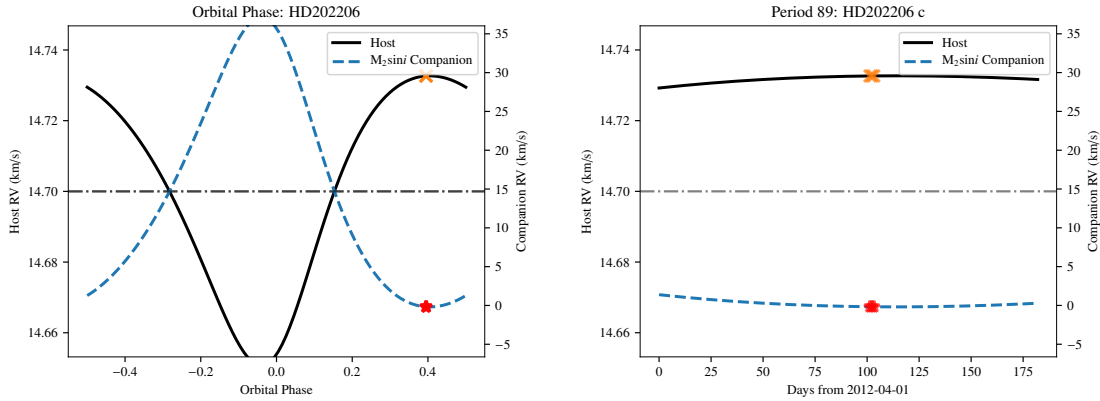


Figure 6.9: Same as Figure 6.3 but for HD 202206c. Analysed as if this was a single companion.

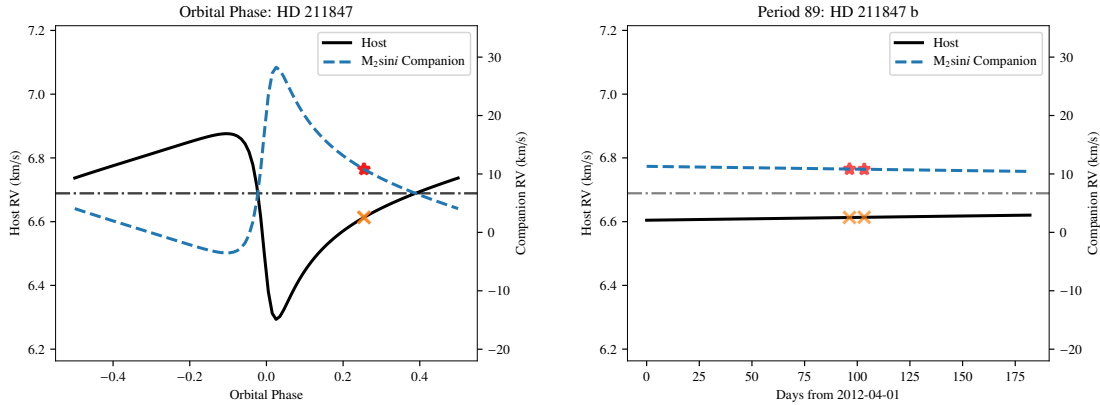


Figure 6.10: Same as Figure 6.3 but for HD 211847.

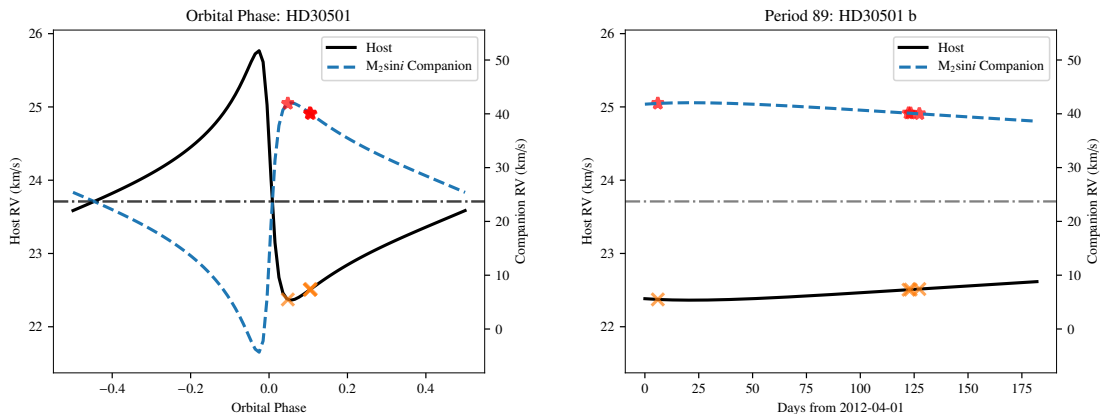


Figure 6.11: Same as Figure 6.3 but for HD 30501.

separations. Most of the targets observed here have orbital periods much longer than an observing semester (183 days). An optimal pair of observations (achieved at the extrema) would need to have been obtained from separate observing periods (between 2 months and 19 years apart). In some cases, even observations taken at the beginning and end of a single observing semester would not be sufficient to achieve a companion separation (depending on the phase and orbital parameters), requiring separate observing periods to even achieve the minimum ΔRV larger than the line FWHM. At the time (2012) it was impossible to ask for observation time over several semesters in a regular proposal.

This study demonstrates the importance of proposals for projects that need to be extended over several semesters or years. Community pressure from projects like this lead to the creation of the “Monitoring proposals” (e.g. ESO, 2017, pg. 18), in the ESO context, allowing for observations over multiple periods. Observations of the targets explored here, with long orbital periods in particular, would benefit from the new abilities for multi-period proposals and scheduling systems which allow for tighter scheduling constraints, such as a companion RV separation. However, the lack of BD companions on short periods has a very negative impact on projects like these as there are simply few targets to choose from to observe.

For future observations in the context of the differential subtraction technique it is suggested that the best possible orbital solution of the host and companion be used to estimate the companion’s RV curve during the observing period, with the companion $M_2 \sin i$ providing an RV upper-limit. Radial velocity constraints are also valid for other studies such as the detection of reflected light from exoplanets (Martins et al., 2015, e.g.). Knowing the instrumental wavelength and resolution, an observing constraint can be set to avoid taking observations when the companion spectra are insufficiently separated, or the $\Delta RV_2 < \text{FWHM}$. This constraint can be set using the absolute and relative *time-link* constraints available in ESO’s Phase 2 Proposal Preparation (P2PP) tool. Additionally, analysing the known orbital solution beforehand to determine RV constraints will also help identify the best time to observe, if observations from separate periods will be required or, if an optimally separated companion differential is even feasible. Again the P2PP documentation for this observational proposal could not be obtained to check if these observations had used any of these features, which were available at the time, and set any constraints.

6.6 Contrast to other works

As stated previously the differential technique is not new, being analytically formulated for binary star separation in Ferluga et al. (1997). This work tried to extend this to lower contrast ratios, to hosts with smaller companions.

For lack of high-resolution CRIRES data Kostogryz et al. (2013) explored simulations of the differential approach to a BD companion of a M-dwarf star, in which the contrast ratio is around 1/50 between 1/200 and were observed at the RV extrema. Their favourable wavelength choice to achieve a good contrast ratio is *K*-band, as done in this work, however they chose the CO line region ($\sim 2310 \text{ nm}$) where there is several narrow spectral lines. One thing explored in Kostogryz et al. (2013) that is not considered here is the effect of rotational broadening on the mass determination, finding that it should be possible to determine the mass of a slowly rotating companion, but a fast rotating companion is more difficult.

The limitations with regards to the RV separation between spectral components has also been observed in other works. Similarly to the companion-companion RV separation focused on here, Kolbl et al. (2015) find a limitation of $\sim 10 \text{ km s}^{-1}$ RV separation required between the host and the companion. This is because if lines of the host and companion are blended, it is likely the companion spectra will be fitted,

or incorporated into the hosts spectra, making it difficult to accurately detect the companion lines at a similar RV. The RV difference between the host and companion is given in the last column of Table 6.3 as rv_2 . It can be seen HD 4747, HD 202206, and HD 218447 do not exceed this 10 km s^{-1} separation with the obtained observations.

6.7 Direct recovery in the mIR

It was investigated if this differential technique could be extended into the mid-infrared mIR domain. There were two reasons for this: to develop experience with the mIR domain where the contrast ratios are higher, and the lack of high-resolution nIR spectrographs available at the time (see Section 3.4).

VISIR is a mIR spectrograph on the VLT, offering diffraction-limited imaging at high sensitivity in three mid-infrared (mIR) atmospheric windows: the *M*-band at $5 \mu\text{m}$, the *N*-band between $8\text{--}13 \mu\text{m}$ and the *Q*-band between $17\text{--}20 \mu\text{m}$, respectively. The use of VISIR to detect the spectra of Brown Dwarf companions in the mIR was briefly explored. The candidate selected as the best target to investigate was HD 219828 which has a hot-Neptune ($M_2 \sin i = 21 M_{\oplus}$) (Melo et al., 2007) and a recently discovered super Jupiter ($M_2 \sin i = 15.1 M_{\text{Jup}}$) on a long period (13 yr) eccentric orbit ($e=0.81$) (Santos et al., 2016).

Based on the spectra of cool brown dwarfs in the mIR, and the detector configuration available at the time, the best option for the observations was the low resolution mode covering the wavelength region $8\text{--}13 \mu\text{m}$. This wavelength region would have encompassed the NH_4 signature at $10.5 \mu\text{m}$ and the edge of a CH_4 band at $7.7 \mu\text{m}$, both large features in the BD mIR spectrum.

After performing flux ratio calculations between the host and companion using the Baraffe et al. (2003) models (see Section 4.3.1) and considering the performance of the VISIR instrument and the exposure time calculator, it was determined that observations with VISIR to achieve a SNR of 100 were infeasible, requiring 1000's of hours of observing time to achieve the necessary signal-to-noise level to separate the companion from a blended spectra. For a different target, HD 189733 it was calculated that with an exposure time of 2 hours the SNR of the host and companion would be 85 and 4 respectively, using the low resolution spectroscopy mode. As such the direct separation approach was not explored further in the mIR.

6.8 Summary

This chapter presented the observations that were gathered having in mind the application of a differential subtraction method to recover the spectra of the faint BD companions. Due to the poorly separated observation times relative to the long orbital periods, the differential subtraction method presented in Section 6.3 was revealed to be inappropriate for these observations as the RV separation of the companion spectra between observations is significantly smaller than the width of individual spectral lines. The small separation of the companion causes the lines of the companion to also mutually cancel, severely reducing the residual signal to well below the available noise level. The requirement of well separated RVs for the companion spectra was clearly stated in the original proposal but was not satisfied by the observations, however the very large orbital periods of some of the targets would not produce a sufficient RV signal during one semester was possibly an oversight during the proposal stage. In the following chapter a different technique will be explored in the attempt to extract details of the companion from these observations.

Chapter 7

Synthetic companion recovery

Following on from Chapter 6, in which the differential subtraction technique was unsuccessful due to the insufficient separation of the observations, a second method is attempted to detect the presence of the faint BD companions in the blended spectrum. In this chapter a χ^2 fitting approach is used to fit the observed spectra with a binary model comprised of two synthetic spectral components. An overview of the method is presented followed by the preparation of the models. A simulation with a larger M-dwarf companion to a G2V star is presented first, followed by a simulation and observations of HD 211847. Injection-recovery simulations are performed to understand the limitations of this method and the results obtained. A discussion of the results and a comparison to other similar techniques is given at the end.

7.1 Binary χ^2 spectral recovery

The approach developed here is to fit the observed CRIRES spectra, consisting of a FGK star with a BD companion, with a model comprised of a combination of two synthetic spectra, one for each component. This will be done using the χ^2 approach which has been extensively used in the literature (e.g. Astudillo-Defru et al., 2015; Passegger et al., 2016; Passegger et al., 2018; Zechmeister et al., 2018; Nemravová et al., 2016; Kolbl et al., 2015; Rajpurohit et al., 2018, to list a few). The recoverable information from the fitting will be the parameters of a synthetic spectra fitted to the host and companion. This will provide some indication of the companions temperature and spectral type, but it will not produce the directly constrained mass that was the original aim of the observations.

7.1.1 The χ^2 method

The well known χ^2 technique measures the weighted sum (for all data points i) of the squared deviation between the observation (O) and the computed models (C), with the minimum χ^2 value representing the best-fit parameters:

$$\chi^2 = \sum_i \frac{(O_i - C_i)^2}{\sigma_i^2}, \quad (7.1)$$

where σ_i is the error on each measurement.

The inverse survival function of the χ^2 distribution is used to determine the confidence levels of the resulting parameters from the minimum χ^2 . The inverse survival function returns a $\Delta\chi^2$ value from the minimum χ^2 value for a given σ level and degree of freedom. This can be achieved in Python with the SciPy package as the single line of code `dof)1-p)scipy.stats.chi2(.isf(`, where dof is the degree of freedom and p the probability; for example $p = 0.68$ for $1-\sigma$. For example, the $\Delta\chi^2$ for a single degree of freedom required for the 1-, 2-, and 3- σ confidence levels is 1, 4, and 9 respectively (Bevington et al., 2003). This method assumes that the measured flux is observed with a SNR sufficiently high so that the noise on the spectrum is approximately Gaussian, and the χ^2 method appropriate. If however there is a correlated signal or noise in the spectra then the χ^2 is inappropriate. The more advanced Gaussian processes techniques would be required to properly fit the data (Rasmussen et al., 2006, e.g.). This is beyond the scope performed here.

For a given observation, the χ^2_{red} is computed as $\chi^2_{red} = \chi^2/\nu$ where $\nu = n - m$, the number of observed pixels, n , minus the number of parameters of interest, m ¹. In the cases explored below the χ^2_{red} is only calculated after the summation across the detectors is performed.

For each observation O , the σ is estimated using the $\beta\sigma$ method (Czesla et al., 2018), using the MAD (median absolute deviation about the median) robust estimator. The $\beta\sigma$ method estimates the spectral noise of the spectra using a series of numerical derivatives². We followed the procedure outlined in Czesla et al. (2018) to analyse the results from successive parameter combinations to settle on an order of approximation (derivative level) of $N = 5$, and a jump parameter (pixels skipped to avoid correlations) of $j = 2$. The same σ value determined is applied to all points in the spectrum so that $\sigma_i = \sigma$. The $\beta\sigma$ method provides σ estimates for the target spectra which correspond inversely to SNR values between 100–400. These SNR values are similar to the values given in Table 6.3 which were calculated only using the standard deviation of the continuum of detector #2.

The computed models C are described in Section 7.1.2 and result in a multidimensional grid of χ^2 values for each combination of model parameters, namely the spectral parameters (e.g. T_{eff}), and the RV of the host and companion RV for each: detector, observation, and target.

The global minimum of the multidimensional χ^2 -space is used to represent the best fitting model combination to the observed spectra. The multidimensional χ^2 grid is summed across multiple detectors to also determine a global minimum χ^2 for the whole observation $\chi^2_{obs} = \sum_{n=1}^N \chi_n^2$, where N is the number of detectors used. However, the separate observations are not combined as the RV parameters of the host and companion will vary between each observation³. To incorporate the separate observations a model that incorporates the phase information will be required and is beyond the scope of this work due to the limited number of observations (1–4). A promising method to incorporate the phase information for the detection of exoplanetary spectra is given by Lockwood et al. (2014) and Piskorz et al. (2016). They detect evidence of an exoplanet spectrum with a contrast of order 10^{-4} using nIR (L - and K -band) spectra with a $\text{SNR} \approx 2000$ observed at six epochs over the whole orbit.

7.1.2 Computed model spectra

In this section the transformation of the synthetic PHOENIX-ACES spectra into the computed models (C) is explained. These computed models will then be fit to the observed spectra.

¹ $m = 2$ or $m = 4$ in the examples explored below.

² Applying a Taylor expansion to the spectra.

³ Since the current observations are insufficiently separated, it may be possible to combine the separate observations; but in general this would not be the case.

Firstly, this assumes that the synthetic spectra are loaded and converted to consistent units. The loading is easily performed using Starfish's GridTools (Czekala et al., 2015), which can load the library spectra with a list of stellar parameters [T_{eff} , $\log g$, [Fe/H], [α/Fe]]. The PHOENIX-ACES spectra are converted from the units of the spectral energy distribution ($\text{erg s}^{-1} \text{cm}^2 \text{cm}^{-1}$) (at the stellar surface) into photon flux ($\text{photons s}^{-1} \text{cm}^2$) by dividing by the photon energy⁴. This can be simply achieved by multiplying the spectrum by the wavelength (multiplicative constants ignored), as done in Figueira et al. (2016). The spectra are also convolved with a Gaussian kernel to the instrumental resolution of the observations, in this case $R=50\,000$. Due to the distributive property⁵ of convolution the instrumental broadening is performed on each individual library spectrum first. This is to avoid performing convolution for each combination of model parameters in the binary model after the spectra have been combined. It would be more computationally expensive to perform the convolution on every model combination, C .

These synthetic spectra are used individually for the single component model (Section 7.1.2.1) and also combined together into a binary model (Section 7.1.2.2). The results of these models are then interpolated to the wavelength grid of the observed spectra and the χ^2 calculated by comparing the model and observation at each wavelength point, i .

7.1.2.1 Single component model

The single component model C_i^1 comprises of a single synthetic spectrum, J , (with model parameters T_{eff} , $\log g$, [Fe/H], [α/Fe]) [α/Fe] that can be Doppler shifted by a RV value rv_1 .

$$C_i^1(\lambda) = J(\lambda_0(1 - \frac{rv_1}{c})) \quad (7.2)$$

where λ is the shifted wavelength, λ_0 , the model rest wavelength and, c , the speed of light in a vacuum. The model's flux in the wavelength region of the observations is continuum normalized to unity to match the observed spectra, and then interpolated to the wavelength grid of the observation.

This single component model analysis is similar to the Passegger et al. (2016) χ^2 fitting, using PHOENIX-ACES spectra to fit and determine the parameters of M-dwarf spectra. A similar re-normalization (see Section 7.1.3) as Passegger et al. (2016) is used to account for slight differences in the continuum level and possible linear trends between the normalized observation and models. However, unlike Passegger et al. (2016), no dynamical masking was applied to sensitive lines to make the χ^2 minima more distinct nor a linear interpolation of the stellar parameters between the grid models to obtain higher precision stellar parameters. This was because, at this stage, the techniques ability to detect the presence of the secondary was being tested, not a determination off the precise stellar parameters. These processes and others could however be included in the future to improve the detectability and precision of the best-fit model. Instead, a radial velocity component is included in the χ^2 fitting, which is not included in Passegger et al. (2016).

Rotational broadening of the host was not included in these models as an extra variable fitting parameter. In Passegger et al. (2018) rotational broadening is only included at the fine grid search stage, using only a fixed value for each target to determine, determined in a separate work, to reduce the number of parameters. A fine search is not attempted in this work.

In the presence of faint companions this single component model will give a fit of the host spectrum,

⁴ Photon energy $E = \frac{hc}{\lambda}$, where h , c and, λ are Plank's constant, the speed of light, and wavelength, respectively.
⁵ $I(\lambda) * (f(\lambda) + g(\lambda)) = I(\lambda) * f(\lambda) + I(\lambda) * g(\lambda)$

identifying the hosts parameters and be a good start for the parameters of the binary model or even fix them to reduce the parameters.

7.1.2.2 Binary model

In the binary model case the model is considered to be the superposition of two synthetic spectral components, one each for the host and companion respectively. Both components are Doppler shifted by rv_1 which represents the RV motion of the host star relative to Earth's barycentre, while the companion spectra is Doppler shifted a second time by rv_2 which represents the RV difference between of spectrum the host and companion. This coordinate choice is arbitrary⁶, but in this way the mean motion of the system relative to Earth is captured only in rv_1 , along with the orbital motion of the host. The two spectra are scaled by their radius squared as the spectra are provided in units relative to the per unit area on the surface (see Section 7.1.2.3). They are then added together, thus setting the relative amplitude of the two spectral components. Given two spectral components J_2 and J_2 with radii R_1 , R_2 this equates to

$$\begin{aligned} C_i^2(\lambda) = & J_2\left(\lambda_0\left(1 - \frac{rv_1}{c}\right)\right) \times R_1^2 + \\ & J_2\left(\lambda_0\left(1 - \frac{rv_1}{c}\right)\left(1 - \frac{rv_2}{c}\right)\right) \times R_2^2 \end{aligned} \quad (7.3)$$

The spectrum of the combined binary model is normalized by division with an exponential fitted to the continuum. Here at 2100 nm it assumed that the Rayleigh-Jeans regime is appropriate. This assumption is wavelength dependent and other continuum normalization techniques may also be valid. In the case of a BD companion around an FGK star investigated here, the continuum is dominated by the contribution from the host star, contributing the majority of the spectrum with flux ratios below $\sim 1\%$, in the wavelength range 2110–2165 nm.

Models are combined in this way to represent the correct absolute flux ratio of the spectral components. A further method could allow a variable flux ratio to be included as an extra parameter and be fitted as well. However, it would add an extra dimension to the χ^2 grid and potentially add more degeneracy between models of the companion. The median flux ratio between the two components is calculated for the wavelength range used here as an indication of the flux ratio level. This is given as F_2/F_1 in Table 7.1.

This binary model should provide meaningful information about the likely companion parameters (e.g. T_{eff}) and a possible estimate of the flux ratio of the system. These can be combined with the Baraffe et al. (2003) models to constrain the mass of the companion. However, care is needed with the binary model as the inclusion of extra spectral components and associated parameters could also provide a “better” fit to observations which have faint or even no companions, by fitting components of the noise.

The full list of grid parameters for the binary model are T_{eff}_1 , $\log g_1$, $[\text{Fe}/\text{H}]_1$, $[\alpha/\text{Fe}]_1$, rv_1 , T_{eff}_2 , $\log g_2$, $[\text{Fe}/\text{H}]_2$, $[\alpha/\text{Fe}]_2$, rv_2 where the subscripts 1 and 2 indicate the host and companion models respectively.

7.1.2.3 Effective radius

The PHOENIX-ACES spectra are provided per surface unit of the emitting star. To combine the two synthetic spectra with the correct absolute flux ratio the relative size of the two emitting bodies needs to

⁶ Having rv_2 as the companion's RV offset relative to the barycentre is also a valid choice.

be accounted for. The emitted flux needs to be integrated over the effective surface area of each emitting body respectively. Ignoring the common multiplicative constants that will not affect the ratio between spectra and disappear with normalization the two synthetic spectra of the binary model are individually scaled by the square of their respective radii, R_1 and R_2 . R_1 .

In this work the radius used to scale the spectra is the effective radius of each component from the PHOENIX model header; the PHXREFF keyword. This radius is utilized in the modelling of the PHOENIX-ACES stellar atmospheres. This is used as it is directly tied to each model spectrum, and already calculated and available. In this way it does not incorporate an extra assumption or model relating the library model parameters to a stellar radius. The ratio of the radii from the two synthetic spectra in the binary model examples presented are provided in Table 7.1 as R_1/R_2 .

Using the radii in this way for the companions has limitations because there are degeneracies in BD mass, age, and luminosity of the companion, in particular a combination of radius-mass and radius-age relationships (Sorahana et al., 2013). Using the effective radii from PHOENIX-ACES model does not allow for any independent age constraints to be incorporated into the stellar radius, or allow for any variability in the radii to account for uncertainties. Any age related effects on the spectra are not accounted for in this way.

The targets analysed here do not transit, but in cases that did transit the radius ratio can be independently determined from the photometric transit method (Deeg, 1998). This independent radius ratio could be used as a constraint when combining the binary model spectra.

7.1.3 Re-normalization

Slight trends in the continuum level between the observed spectra and computed models were removed using the re-normalization following Passegger et al. (2016):

$$F_{re-norm}^{obs} = F^{obs} \cdot \frac{\text{continuum fit}_{model}}{\text{continuum fit}_{observations}}. \quad (7.4)$$

Polynomials were fitted to both the continuum of the observations and the models. These continuum fits of the normalized observations and models are used to re-normalize the observed spectrum to the continuum of the models. For detectors #1–3 a polynomial of first degree was used, while for detector #4 a polynomial of second degree was needed to fit the edge of a strong Hydrogen line (Brackett- γ) at 2166 nm, which lies just off of the edge of detector #4. This broad line is only observed in the synthetic spectra but not in the reduced observations. It is assumed that the edge of this line was normalized out during the reduction process.

For each model the continuum level is further allowed to be slightly varied by ± 0.05 as a free parameter taking the model that fits with the smallest χ^2 value as the choice for this combination of binary parameters.

7.1.4 Reducing dimensionality

The high dimensionality of the binary model makes it computationally challenging and difficult to analyse the χ^2 space. This section discusses the choices made to reduce the dimensionality and the parameter space, to reduce the computation time. For reference, the parameter space of the models is multiplicative. That is, each new dimension or parameter added multiplies the number of possible model combinations.

When increasing from the single model to the binary model, the number of parameters doubles, but the number of possible models is actually squared, assuming that each spectral component can explore the full parameter space. The binary model is therefore more computationally expensive by a very large factor, making it potentially prohibitively expensive. In general the number of possible parameter combinations for k spectral components each with a grid of l models increases to k^l . If the full set of PHOENIX-ACES library spectra (66456) is explored with a binary fit then this naively balloons to over 4.4 billion possible combinations. This is only valid in the general case as half of the binary combinations are not unique as only host and companion components would be swapped. A number of assumptions are implemented to vastly reduce the parameter-space enabling faster computation.

The first assumption is to restrict the Alpha element abundance ($[\alpha/\text{Fe}]$) of the models to zero. This is likely a very good approximation as all the targets have solar metallicity and are thus very likely to belong to the thin disk of the Galaxy, where $[\alpha/\text{Fe}]$ values are close to zero, i.e. solar Adibekyan et al. (e.g. 2012). The second assumption is that the search space can be significantly reduced by using literature values of the host star given in Table 6.1. The metallicity of both model components are fixed to the closest grid to the literature value of the host star, usually $[\text{Fe}/\text{H}]=0.00$. The $\log g$ of the host star is also fixed to the closest grid literature value. The uncertainties on the literature measurements for $\log g$ (~ 0.1) and metallicity (~ 0.05) are both smaller than the grid steps of 0.5 for these parameters. The $\log g$ of the companion is obtained from the Baraffe et al. (2003) and Baraffe et al. (2015) evolutionary models for the given companion's mass (M_2 or $M_2 \sin i$) and host's age.

A starting point for $T_{\text{eff}2}$, the estimated companion temperature from the Baraffe evolutionary models is used, given the companion mass and stellar age. The temperature grid is extended about this value in each direction, within the temperature limits of the synthetic model limits. For example the companion temperature grid spans -600 to $+400$ K in Figure 7.1 and ± 400 K in Figures 7.2 and 7.3 about the estimated companion temperature.

The large number of possible combinations stated above also do not include the RV grid for each component, which can be chosen to meet a desired precision level by changing the step size and range of the Rv grid. For example, the number of models to compute increases with a decrease in the grid step size (a finer RV resolution) for a fixed RV range. The RV grid space can be reduced significantly by tailoring it to the target being examined. For each target and observation, the estimated RV values from Table 6.3 are used as a centre starting point for the rv_1 and rv_2 values and then incremented within a few FWHM around those values, or out to the targets K_1 or K_2 values.

An iterative process could potentially be implemented to refine the RV grids, starting with a larger grid with lower RV resolution and then performing a higher resolution grid about the minimum χ^2 RV values. This was attempted manually during testing but it could be easily automated in the future, at the cost of recalculating the χ^2 at different RV resolutions. One danger would be falling into a local minima, although one could expect that a good starting RV grid step be governed by the spectral resolution, e.g. comparable to the FWHM velocity.

If targets have a fully resolved orbit of the known RV of the host star, then rv_1 could also be held fixed. This was not held fixed in this work.

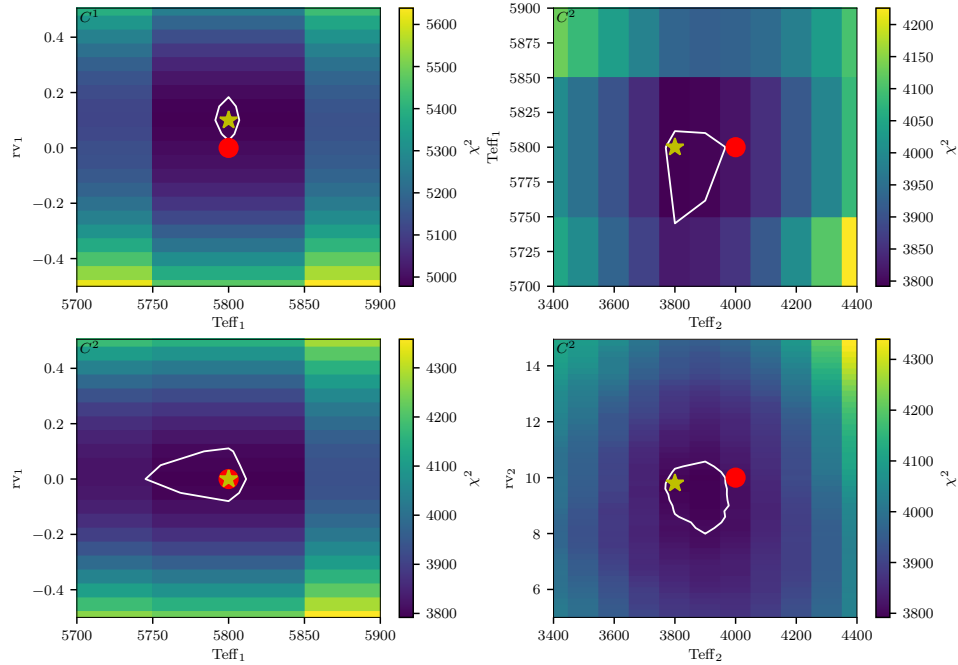


Figure 7.1: χ^2 results for companion recovery of a simulated binary observation of a Sun-like star ($T_{\text{eff}1} = 5800$ K) with an M-dwarf companion ($T_{\text{eff}2} = 4000$ K). The top right plot shows the application of a single component model (C^1) while the other three are using a binary model (C^2). Both left hand panels show the distribution of host temperature and host RV. The top right panel shows the distribution for host and companion temperature, and the bottom right the companion temperature and radial velocity. The red circle and yellow star indicate the location of the simulation input and recovered parameters respectively. The white line shows a 3- σ confidence level about the minimum χ^2 solution grid point. Each box is centred on the parameter values and shows the grid resolution.

Table 7.1: Input and recovered parameters on simulations and an observation when applying the single (C^1) and binary (C^2) models. The $\log g$ and metallicity were fixed at values of $\log g_1 = 4.50$, $\log g_2 = 5.0$ and $[\text{Fe}/\text{H}]_1 = [\text{Fe}/\text{H}]_2 = 0.0$. Gaussian noise with a SNR of 150 was added to both simulations. The number of data points and parameters used in each model are m and n respectively.

	Simulation 1			Simulation 2			Observed HD 211847		
	Input	Recovered		Input	Recovered		Expected	Recovered	
		C^1	C^2		C^1	C^2		C^1	C^2
$T_{\text{eff}1}$	5800	5800	5800	5700	5800	5700	5715 ± 24	5900	5800
$T_{\text{eff}2}$	4000	—	3800	3200	—	3100	~ 3200	—	$> 3800^{\text{a}}$
rv_1	0	0.1	0	6.6	6.6	6.6	6.6 ± 0.3	7	7.6
rv_2	10	—	9.8	0.5	—	-1	0.5 ± 2	—	-12.6
R_1/R_2	2.57	—	2.71	3.16	—	3.27	3.16	—	$< 2.71^{\text{a}}$
F_2/F_1	0.084	—	0.066	0.030	—	0.026	0.030	—	$> 0.066^{\text{a}}$
m	—	3072	3072	—	3072	3072	—	2612	2612
n	—	2	4	—	2	4	—	2	4
χ^2	—	4978	3792	—	3746	3630	—	37 688	33 860
χ^2_{red}	—	1.62	1.24	—	1.22	1.18	—	21.3	19.2
BIC	—	-20 145	-22 315	—	-21 477	-21 377	—	18 281	14 468

^a At the arbitrary upper limit for companion temperature grid (3800 K).

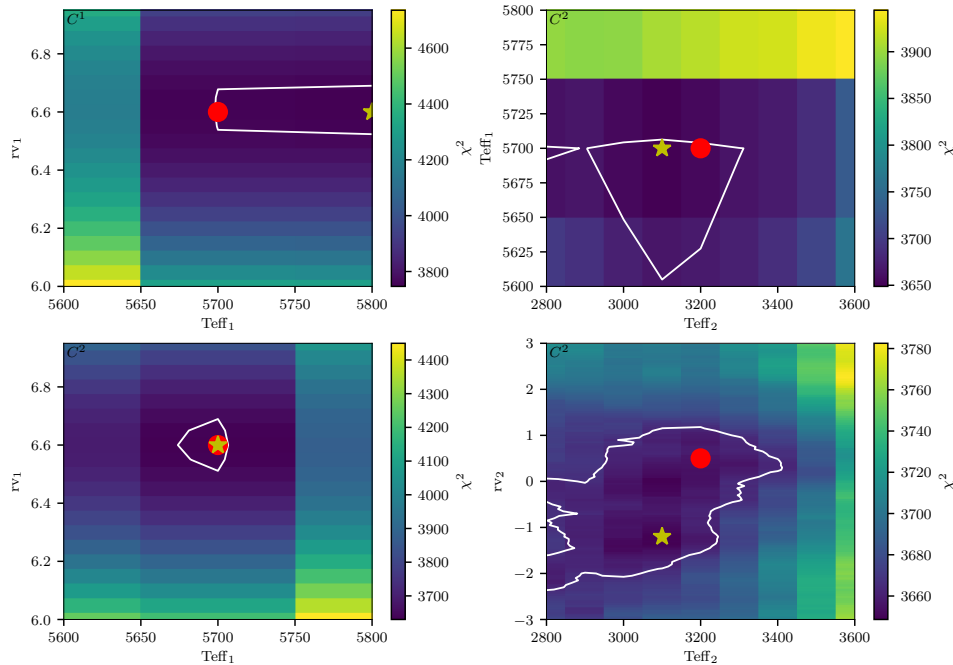


Figure 7.2: χ^2 results for companion recovery of a simulated binary observation similar to HD 211847, $T_{\text{eff}1} = 5800$ K, $T_{\text{eff}2} = 3200$ K, similar to Figure 7.1.

7.2 Simulation and results

In this section some results from applying the models for companion recovery model to simulated observations and to the observed target with the best estimated contrast are presented.

7.2.1 Simulated binaries

To test the companion recovery method, simulations of binary observations using PHOENIX-ACES spectra were performed. These are performed in the wavelength range between 2112–2152 nm, covering the first three detectors of CRIRES only, due to spectral mismatch observed later in the observed spectra. White noise was added to the simulated spectra at a standard deviation of $\sigma = 1/\text{SNR}$, for a given signal-to-noise (SNR) level. The χ^2 grid-search recovery technique detailed above is applied and the resulting parameters compared to the inputs.

The results of two example binary simulations are displayed in Figures 7.1 and 7.2, both simulated with a SNR of 150. In each figure the input and recovered parameters for the binary components are indicated by the red circles and yellow stars respectively, and are given in Table 7.1. The 3σ contour is shown with a white line on the plots to indicate the shape of the confidence level only. The 1σ contours are not shown here as they are much smaller than the temperature grid step and are difficult to visualize at this scale, often being smaller than the marker shown at the location of the minimum χ^2 . Each coloured rectangle is centred on a grid point, with its colour indicating the χ^2 value, and its shape indicating the resolution of the parameter grid space searched.

M-dwarf companion

The first simulation is for a Sun-like star with an M-dwarf companion with temperatures $T_{\text{eff}1} = 5800\text{ K}$, $T_{\text{eff}2} = 4000\text{ K}$. The results are shown in Figure 7.1. The top-left panel shows the recovered host parameters when only the single model is fitted to the spectra of the simulated binary. The top-right and both bottom panels show different parameter slices recovered when fitting with the binary model. Both left-hand panels display the parameters for the host, $T_{\text{eff}1}$ and rv_1 , to easily compare between the two models. With both models the host temperature $T_{\text{eff}1}$ is exactly recovered. The recovered host RV, rv_1 , is 0.1 km s^{-1} (two grid spaces) different from the input value in the single component model and is correctly recovered with the binary model.

For the companion the minimum χ^2 location for the companion temperature is 200 K below the simulated value, and the RV of the companion recovered is 0.2 km s^{-1} below the input value. The input values for the companion are just outside of the 3σ contours shown. The flux ratio for the input is 0.08 while the flux ratio recovered is 0.066. This begins to show the difficulty of recovering the correct companion parameters, specially at the level of $F_2/F_1 < 8\%$.

HD 211847 simulation

A second simulation is performed with parameters to mimic the observation of the target with highest flux ratio, HD 211847, and is shown in Figure 7.2. In this simulation the single component model recovers a host with the correct RV but a temperature 100 K higher than the input value (one grid step). Again, adding the companion with the binary model recovers the correct host temperature. The companion

temperature recovered is 100 K lower than the input temperature and the RV is different by 2 km s^{-1} which is around one third the FWHM.

In this case with a companion RV offset, rv_2 , near 0 km s^{-1} the host and companion lines are blended. The same spectral lines from both components are trying to match the same features of the spectra, making it more difficult to recover the companion parameters. In the bottom right panel there appears to be multiple minima for different rv_2 and $T_{\text{eff}2}$ combinations, with a complex $3-\sigma$ confidence contour. This is assumed to be partially due to the small rv_2 .

From the results summarized in Table 7.1, both simulations have a χ^2_{red} for the binary model closer to 1 than the single model. This is not surprising as the binary model contains extra parameters. As mentioned above, care is needed, as the extra components from the binary may just happen to fit components of the noise when a binary is not present, or at an extreme low contrast ratio as in this case. To further analyse the significance between the two models the “Bayesian Information Criterion” (BIC) (G. Schwarz, 1978) is used:

$$BIC = n \ln(m) - 2 \ln(\hat{L}). \quad (7.5)$$

Here n and m are the number of parameters and number of data points respectively and \hat{L} is the maximum of the Gaussian likelihood function,

$$\hat{L} = \left(\frac{1}{\sigma \sqrt{2\pi}} \right)^m \exp \left(-\frac{\chi^2}{2} \right), \quad (7.6)$$

written in terms of χ^2 and a fixed σ for all data points. The maximum likelihood of a Gaussian distribution is equivalent to minimizing the χ^2 . In both simulations the change in BIC between models is $\Delta BIC > 10$, so the preference of the binary model, with the lower BIC value, over the single component model is considered *significant* (Kass et al., 1995).

7.2.2 HD211847 observation

HD 211847 is the best candidate of the current targets for companion detection with the χ^2 binary model as it has a $155 M_{\text{Jup}}$ low-mass star companion Moutou et al. (2017). Even though it has been determined not a BD in the literature it has the highest estimated flux ratio out of the current sample, of 0.03 based on the Baraffe et al. (2015) evolution models and the known companion mass (see Table 4.4). Moutou et al. (2017) used Angular Differential Imaging (ADI) with SPHERE@VLT to observe an angular separation of the two bodies of 219.6 mas corresponding to a projected separation of 11.3 au. For comparison the CRIRES slit width on the sky is 400 mas ($0.4''$), so for any orientation of the star and companion the spectra will be blended. However, it was not determined if the orientation of the orbit was considered during the observation, to specifically align the slit along the orbit. The result of applying χ^2 fitting to the second observation of HD 211847 is given in Table 7.1 and visualized in Figure 7.3.

For the fitting of this target the metallicity of both components was fixed to 0.0 and the $\log g$ for the host was fixed at 4.5. The $\log g$ for the companion is also fixed to 5.0, based on the Baraffe et al. (2015) evolutionary models for the given companion mass and system age. The orbital solution of the target was used to define the initial RV search space of both components, however the first range for the companion RV was too narrow and was extended until the companion was recovered with a value inside the RV bounds.

Again the top left panel of Figure 7.3 shows the recovery with a single component model with the other three displaying parameter slices of the binary model. Here the red circle marks the location of the expected values from the literature while the yellow star indicates the location of the minimum χ^2 recovered parameters. The error bar on the host temperature also comes from the literature, while the error on estimated RV values, shown in Figure 7.3, is calculated by applying the general error propagation formula (Ku, 1966) to the RV equation (Equation 2.12) and using the errors on the published orbital parameters.

The fitted single component model finds a temperature of 5900 K for the host with a rv_1 of 7 km s^{-1} . The recovered $T_{\text{eff},1}$ is ~ 200 K higher than the expected value with rv_1 0.4 km s^{-1} above the expected parameters. The binary model finds a host temperature of 5800 K, which is the second closest model to the literature value, < 100 K different. The host RV value recovered with the binary model is 7.6 km s^{-1} , which is 1 km s^{-1} higher than expected, but again these RV differences are smaller than the FWHM of the lines. For the single component model there is a barely noticeable evidence of a secondary minima near this 7.6 km s^{-1} RV value which is recovered by the binary model. The 3σ contour in these plots is small due to the large gradient of the χ^2 ; it is just visible on the right hand side of the star in the bottom left panel, and hidden behind the markers in the other panels.

For the companion in the binary model, the right side of Figure 7.3 shows a problem. The minimum χ^2 for the companion temperature is at the upper limit of the grid shown. If the parameter grid is allowed to extend the recovered companion temperature continues increasing towards higher temperatures continually hitting the upper limit until it becomes comparable to the host temperature, more than 2000 K above the expected temperature for the companion. When the companion temperature becomes comparable to the host's it also affects the recovered parameters for the host star, rv_1 and $T_{\text{eff},1}$, due to the features of the brighter companion. Also the companion RV is $> 12 \text{ km s}^{-1}$ different than the expected value, around two FWHMs away. Obviously this is incorrect and the actual companion is not being detected.

The χ^2_{red} values for the single and binary models are 21 and 19 respectively, far from the value of 1, indicating that both models are a poor fit to the observations. The $\Delta BIC = 3812 > 10$ indicating that the binary model is preferred, i.e. the difference is *significant*. However, neither model is really an accurate representation of the data.

The spectrum of the best fit solution binary model is shown against the observed spectra in Figure 7.4. It is observed that there is a large spectral mismatch between the synthetic models and the observed spectra. Extra wavelength masking was applied to many of the largest mismatched synthetic lines to remove their influence on the χ^2 . The grey areas mark regions which have been masked out, either from the centres of deep telluric lines (the thin masks matching spectral gaps), or the more prominent mismatched lines in the synthetic spectrum excluded from the χ^2 analysis. One clear example of a mismatched line is a synthetic line at 2132.5 nm that is clearly not observed in detector #2 (top right). Even with the majority of the mismatched lines removed the detection of the companion was still unsuccessful. The shown results for the observed spectra include the wavelength masking.

For detectors #1 and #2 it appears that the synthetic spectra contain many more deeper lines than observed. For detector #3 the red half of the detector was masked out as there appears to be an RV offset between the observed lines and synthetic spectra. With 3–4 lines that appear to be consistently offset from the observation it could be a wavelength calibration issue, although the telluric lines appear to be sufficiently corrected in this region, attesting for the quality of the wavelength calibration, and

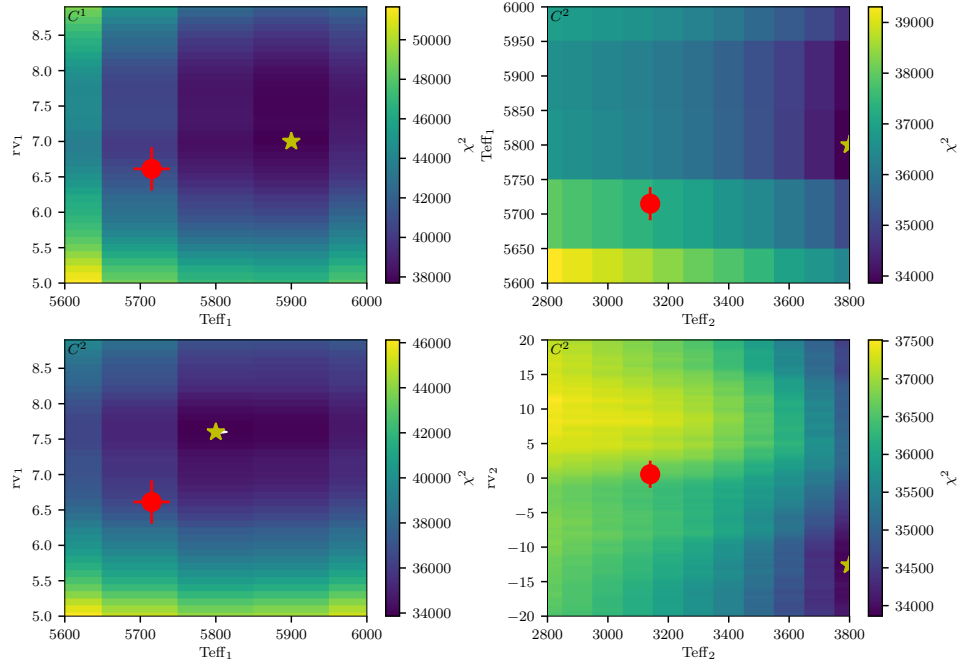


Figure 7.3: χ^2 result grid for the second observation of HD 211847, similar to Figures 7.1 and 7.2. The white line shows a $3-\sigma$ confidence level about the minimum χ^2 solution grid point, not always visible here due to the large χ^2 values. The error bar on T_{eff}_1 is from the literature while the error bars on rv_1 and rv_2 are calculated by propagating the orbital parameter uncertainties through the radial velocity equation (Equation 1.1).

making it incompatible with the offset.

For detector #4 the observed lines do not agree at all with the models. With many observed lines not in the model and only one line with some agreement in wavelength, detector #4 is masked out completely and not used in the χ^2 fit of the simulation or observed spectral fitting. Individual inspection of the χ^2 results for each detector also revealed that there was a large discrepancy between the detector #4 and the other three, with a different RV value for the host star and χ^2 values an order of magnitude higher. The edge of a deep Hydrogen line (Brackett- γ) off the edge of detector #4 is also clearly seen in the continuum of the model >2162 nm, and possibly part of the reason for the poor fitting.

The same method was applied to the remaining targets, all with similar results for the companion, having companion spectra well above the expected values. In brief, it is concluded that the companion spectra cannot be correctly detected in the observations presented here using this method.

7.2.3 Companion injection-recovery

To determine the detection limits for this method an injection-recovery approach was used to simulate spectra with a range of companions. This is done by using the observed spectra and injecting onto them a synthetic companion, at the absolute flux ratio to which it would have been added to a synthetic host with the same parameters. The RV of injected companion is set to 100 km s^{-1} so that the companion lines are well separated from the lines of the host. This separation chosen is slightly larger than the largest host-companion separation (HD 162020) in the observed targets, given in Table 6.3 rv_2 .

The search space for the injection-recovery is restricted by fixing the host parameters T_{eff}_1 and

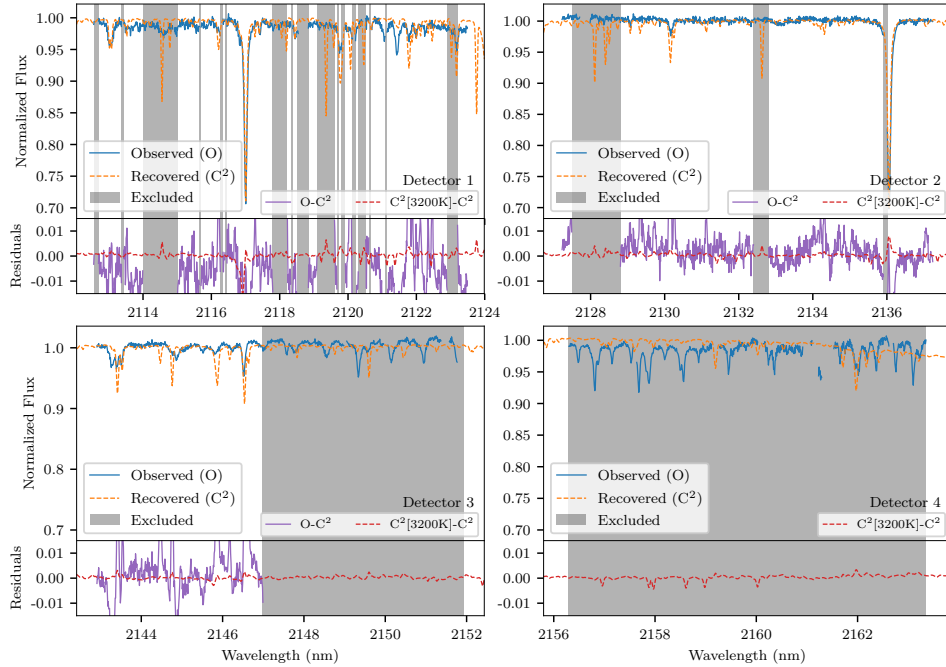


Figure 7.4: Comparison between the observed HD 211847 spectrum (blue) and the best fit synthetic binary model (orange dashed) for each detector. The bottom section of each panel shows the residuals between the parts of the observation used in the χ^2 fit and recovered binary model ($O - C^2$) in purple. The red dashed line shows the difference between the recovered binary model and the binary model with the exact same parameters except for the estimated companion temperature of 3200 K ($C^2[3200\text{K}] - C^2$). The grey shading indicated the wavelength regions where masking has been applied. The thinner masked regions that match with cuts in the observed spectra are where the centres of deep (>5%) telluric lines that have been masked out are.

$\log g_1$ to those recovered fitting the non-injected spectra by a single component model. This leaves only the companion $T_{\text{eff}2}$ and rv_2 parameters free, to recover the injected companion. Wavelength masking (Section 5.3.3) was employed to mask out regions of the spectrum that had the greatest discrepancy between the synthetic and observed spectra. This was in the attempt to reduce the effect of the discrepancies on the recovered companion. The spectra were injected with companions between 2500–5000 K and the companion recovery attempted on each.

The injection recovery was also performed on a synthetic host spectra representing each target as a comparison. For the synthetic host injection-recovery the wavelength range of the synthetic spectra used is three sections interpolated to 1024 values in the wavelength span of detectors #1, #2, and #3. For each section, Gaussian noise is added at the level measured in the corresponding detector in the observation of the target being represented.

In Figure 7.5 the results of the injection-recovery on HD 30501 show the injected companion temperature versus the companion temperature recovered. The blue dots represent the injection into the real observations, while the orange triangles represent injection into the synthetic host. Error bars of ± 100 K are included to indicate the temperature grid size only, and do not come from the recovery itself. The black dashed diagonal is the temperature 1:1 relation, where a correctly recovered companion should reside.

The grey shaded region indicates the ± 1000 K temperature range explored for the injection-recovery of the companion. This shows how the bounds of the grid can be recovered at low companion temperatures and that the recovered temperature deviates from the injected companion temperature around 3800 K.

For HD 30501 the injection onto synthetic and observed spectra produce similar results. At temperatures above 3800 K, in both the real and synthetic spectra, the injected companion is recovered within 100 K. For injected companion temperatures below 3800 K the temperature recovered is systematically higher than the injected value. This indicates that the companion is not correctly recovered and is affected by the added noise. The temperature of deviation is deemed to be the upper temperature limit for the recovery by this method. For the other stars, an upper limit from the injected observations could not be reliably determined, mainly due to spectral mismatch issues. In these cases the results from the synthetic injection are used to derive a temperature recovery cut-off for each target, each simulated with the closest synthetic spectrum to the host star.

Using the temperature cut-off values, an upper mass limit is derived for the companions around our stars using the Baraffe et al. (2015) evolutionary models, finding the closest point matching the spectral temperature cut-off and $\log g = 5.0$. These values are given in Table 7.2 and are between $560\text{--}618$ M_{Jup} . The flux ratio between the cut-off companion spectra and the host star are also calculated, being between 5–15% in this wavelength span.

7.3 Discussion

The spectral differential and the synthetic recovery methods attempted both in this chapter and in Chapter 6 were both unsuccessful in an actual detection of the BD companions focused in this work. The injection-recovery simulations at a SNR of 300 give a companion upper mass limit around 600^{+20}_{-40} , above which this method detects a simulated secondary spectra. This is very high, roughly six times higher than the BD mass limit $\sim 80\text{--}90 M_{\text{Jup}}$. Some potential reasons and solutions for these poor results are given below, that hopefully can provide some guidance for any future attempts with these methods.

Table 7.2: Upper mass limits of target companions assuming a companion $\log g=5.0$. Masses are derived from Baraffe et al. (2015) evolutionary models using T_{eff} and $\log g$. The flux ratio F_2/F_1 is the absolute flux ratio between the cut-off temperature and the target host star.

Target	T_{eff} cut-off (K)	F_2/F_1	Mass limit (M_{Jup})
HD 4747	3900	0.084	598
HD 162020	3900	0.147	598
HD 167665	3800	0.054	560
HD 168443	4000	0.094	618
HD 202206	3900	0.075	598
HD 211847	3900	0.079	598
HD 30501	3800 ^a	0.106	560

^a From observed spectra

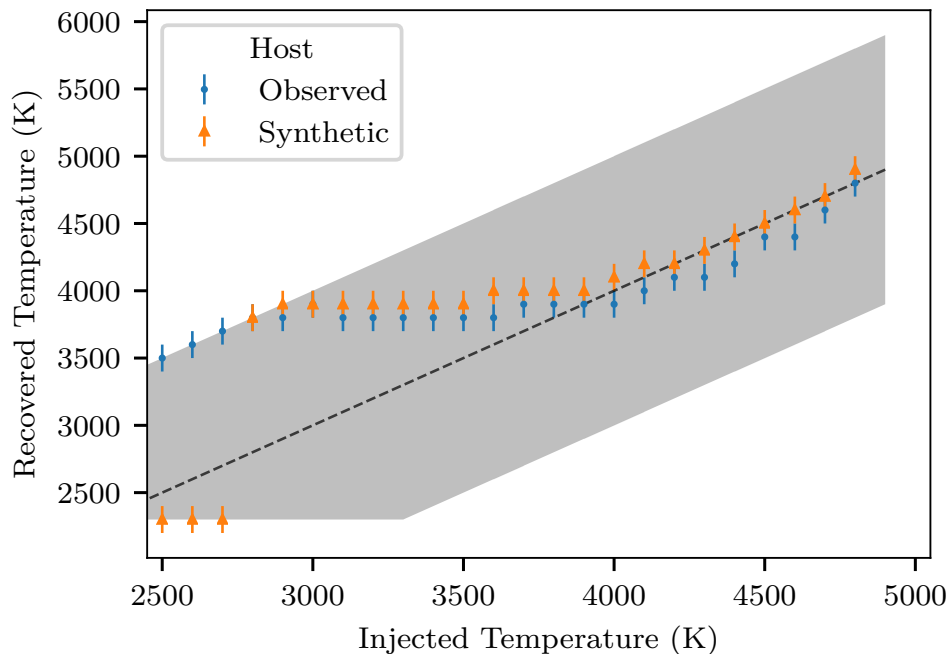


Figure 7.5: Result of simulated injection-recovery of synthetic companions on HD 30501. The blue dots and orange triangles indicate the recovered companion temperature for the observed and synthetic spectra respectively. The ± 100 K error bars are the grid step of the synthetic models. The black dashed diagonal shows the 1:1 temperature relation. The grey shaded region indicates the ± 1000 K temperature range explored. Gaussian noise added to the synthetic spectra was derived from the observed spectra.

7.3.1 Mismatch in synthetic models

It is believed that spectral mismatch between the observation and synthetic spectra is the main cause of the unsuccessful companion detection, impacting the recovery in two ways. The mismatch causes the χ^2 values to be large in general, but also causes the companion temperature to be pushed to higher temperatures in the fitting to the real observations.

In the examples shown the $\log g$ and metallicity of the synthetic models are held fixed, leaving only temperature to vary. The temperature impacts the synthetic spectral models in two main ways: the flux level of the continuum, and the number and strength of the absorption lines. In the binary model the contributions of the individual components is scaled by the flux ratio. If the temperature of the companion increases then the flux and radius of the companion increases and the flux ratio F_1/F_2 decreases. This effectively makes the lines in the host component relatively smaller in the normalized binary model spectrum. Due to the large initial mismatch of synthetic spectral lines of the host, a decrease in the relative strength of the host lines reduces the χ^2 value. This causes the recovered temperature of the companion to be higher than expected, >2000 K higher if allowed by the size of the exploration grid. The χ^2 approach is dominated by reducing the mismatch in the spectrum of the host rather than detecting the spectra of the companion. This spectral mismatch is not observed in the simulations in Section 7.2.1 because they are created using the synthetic spectra themselves, and hence they do not have this same problem with the companion temperature.

Although the newer generations synthetic spectral models are improving and match the overall spectral energy distribution reasonably well there are still regions in the H - and K -band where there is room for improvement (Rajpurohit et al., 2016). These can come in several forms, such as molecular line lists, abundance measurements, or further modelling. As one example in particular, Rajpurohit et al. (2016) previously inferred that the TiO line list poorly matches the real positions of TiO lines at spectral resolutions of $\sim 100\,000$. Passegger et al. (2018) has also noted inconsistencies in the line depth of synthetic spectra. The spectral mismatch in the region studied here is still too large for spectral recovery of companion brown dwarfs. In the nIR there is a compounding problem: the model input physics of sub-stellar temperatures and chemistry combined with the general difficulty of the nIR.

7.3.2 Line contribution of faint companions

One thing easy to overlook when attempting to detect the binary companion at low flux ratios is the actual contribution of the spectral lines of the companion. Here the line depths in the synthetic companion spectra are calculated to determine the SNR levels required to detect the lines of the binary companions.

The flux ratio of the continuum for the most promising target analysed here is $F_2/F_1 \sim 3\%$ with the other targets having an expected flux ratio below 1%. The spectral lines of the individual components, which are the features that allow the identification and recovery of the components, have depths on average around 10–20% of their respective continua; at least between 2110–2160 nm. In effect, the companion line features have a depth $\ll 1\%$ relative to the continuum of the combined spectrum.

In Table 7.3 some properties of the spectral lines in the PHOENIX-ACES library between 2110–2160 nm are calculated. The number of spectral lines (*no. lines*) deeper than 5% are counted and the the average depth (*avg. depth*) of these lines is calculated. The contribution depth *cont. depth* of the companion lines to a combined spectrum is calculated to account for the flux ratio between the two spectral components. Here a Sun-like host with $T_{\text{eff}1} = 5800$ K is used for the comparison. This simplified

combination neglects the continuum shapes of both spectral components and uses the average flux ratios for this wavelength range. The PHOENIX-ACES spectra in the temperature range of 2500–5000 K shown in Figure 7.7 can be used to get a visual indication of the line density and depth measured here.

For the lower temperature spectra there are more lines >5% deep, with 360–460 lines in this wavelength range, compared with only 31 deep absorption lines found in a Sun-like spectrum in this range. The average line depth of these lines is also larger than the Sun-like spectrum, around twice as deep. However, when accounting for the flux ratio, the contribution of the companion lines is 1–2 orders of magnitude smaller than the lines of the host.

For example, with the synthetic model for the companion of HD 211847, the average contributions of lines >5% become only 0.3% deep in a binary with the Sun-like spectrum. For a companion with a temperature of 2300 K (the lower PHOENIX-ACES temperature limit) the deepest lines contribute lines only around 0.1%.

The SNR of the observed spectra is between 100–300, which is below the SNR of 323 needed for the detection of the low-mass star companion of HD 211847 with temperature of 3200 K and $\log g$ 5.0. For the other targets with BD companions at and below the PHOENIX-ACES temperature range, a SNR >800 would be required to detect the individual spectral lines of the companion. With the SNR increasing with \sqrt{N} this would require the observational time for each target to be increased by a factor of $\sim 10\text{--}64$.

Our non-detection of binary companions with low flux ratios is consistent with other works. For example Nemravová et al. (2016) performed extensive spectral analysis of a quadruple-star system ξ Tauri using 227 spectra in 3 different wavelength bands with $R = 10\,000\text{--}48\,000$. Of the four stars in the system they were unable to detect the spectral component of the star which had a luminosity ratio below 1%.

7.3.3 χ^2 asymmetry

To try and understand the recovered companions further investigation into the χ^2 space was performed of the HD30501 synthetic simulation. The minimum χ^2 contours achieved for each companion temperature in the grid, regardless of rv_2 are shown in Figure 7.6. This is done for seven different injected companion temperatures, $T_{\text{eff},2}$, between 2500 and 4500 K. For the higher temperature companions, the χ^2 is parabolic in shape, recovering the correct temperature, as expected. At lower temperatures there is a strong asymmetry in the χ^2 with it flattening out on the lower temperature side. The 1-, 2-, 3- σ values (with two degrees of freedom) of 2, 6 and 11 above the minimum χ^2 are not shown in the bottom panel of Figure 7.6 which is a close-up around the minimum χ^2 as they are indistinguishable in the top panel due to the extreme χ^2 y-scale. The black vertical line indicates the 2300 K temperature limit of the PHOENIX-ACES models.

Figure 7.6 shows that the shape of the recovered χ^2 becomes asymmetric when dealing with companion temperatures below around 3800 K. A visual inspection of the spectra reveals the likely cause. In Figure 7.7 the spectra corresponding to the injected companions are shown between 2111–2165 nm. In the spectra, as the temperature decreases the strongest lines become less prominent, disappearing progressively among the other many small lines that appear at lower temperatures. At lower temperatures there are no strong companion lines to easily distinguish one temperature from another. In the flatter part of the χ^2 curves several low temperature companions are almost equally well fitted to the simulation/observation.

Figures 7.5 and 7.6 show slightly different recovered temperatures but both agree above 3800 K. A higher companion temperature is recovered between 2800–3800 K, where as in Figure 7.6 a lower

Table 7.3: Contribution of synthetic lines within 2110–2160 nm of synthetic PHOENIX-ACES spectra to a binary model. F_2/F_1 is the continuum flux ratio between a spectrum with the given T_{eff} and $\log g$ and a Sun-like spectrum with $T_{\text{eff}}=5800$, $\log g=4.5$ (right most column). *No. lines* is the number of spectral lines deeper than 5% from the continuum of the individual spectra while *avg. depth* is the mean depth of those lines. *Cont. depth* is the average contribution, or depth, of these lines in the combined spectrum of a binary with a Sun-like spectrum. The SNR is signal-to-noise level required to have Gaussian noise $\sigma = 1/\text{SNR}$ equal to the *cont. depth* level in the binary model. All synthetic spectra used here have $[\text{Fe}/\text{H}]=0.0$.

T_{eff} (K)	2300		3200		5800 (F_1)
	$\log g$	5.0	4.5	5.0	4.5
F_2/F_1	0.006	0.019	0.029	0.091	1.000
no. lines	464	463	365	413	31
avg. depth	0.2	0.23	0.11	0.12	0.10
cont. depth ^a	0.0012	0.0043	0.0031	0.0100	0.0833 ^b
SNR	833	232	323	100	12

^a avg. depth $\times F_2/(F_1 + F_2)$, where F_1 is the component in the far right column.

^b avg. depth $\times F_1/(F_1 + F_2)$, where F_2 is for the companion with $T_{\text{eff}}=3200$, $\log g=4.5$.

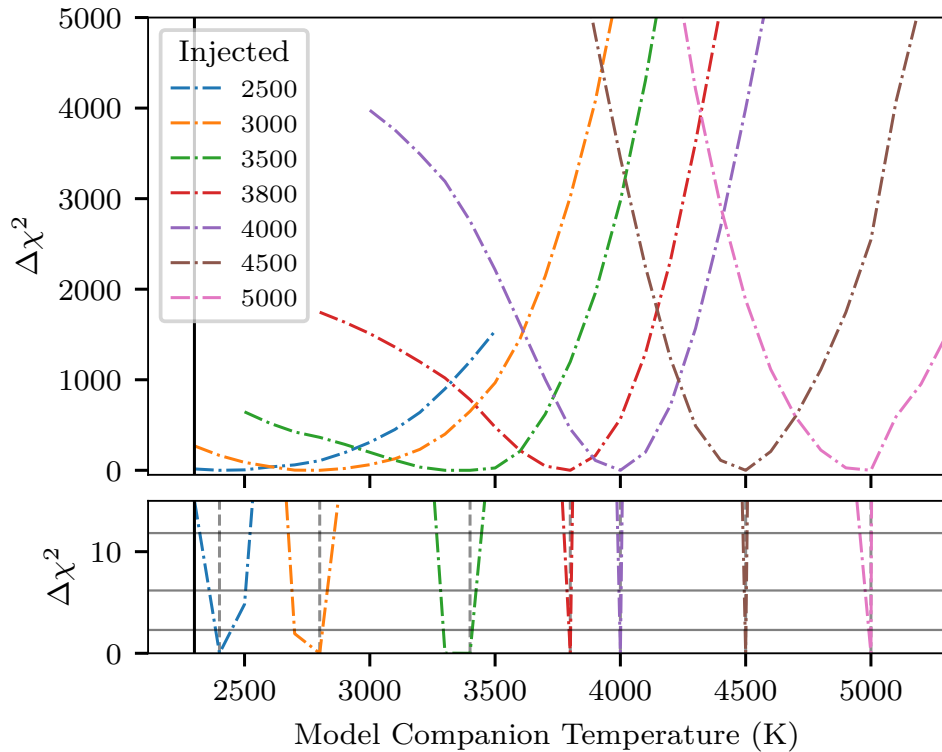


Figure 7.6: Top: Companion temperature versus χ^2 for simulations with different injected companion temperatures. The other fixed parameters for these fully synthetic simulations was $T_{\text{eff}1} = 5200$ K, $\log g_1 = 4.5$, $\log g_2 = 5.0$, and both $[\text{Fe}/\text{H}] = 0.0$. A fixed Gaussian noise corresponding to a SNR of 300 was used. Bottom: A close up view of χ^2 below 15. The three horizontal grey lines indicate the 1-, 2-, 3- σ with two degrees of freedom. The vertical dotted lines indicate the location of the minimum χ^2 recovered for each companion. The black solid vertical line in both panels shows the 2300 K cut-off of the PHOENIX-ACES models.

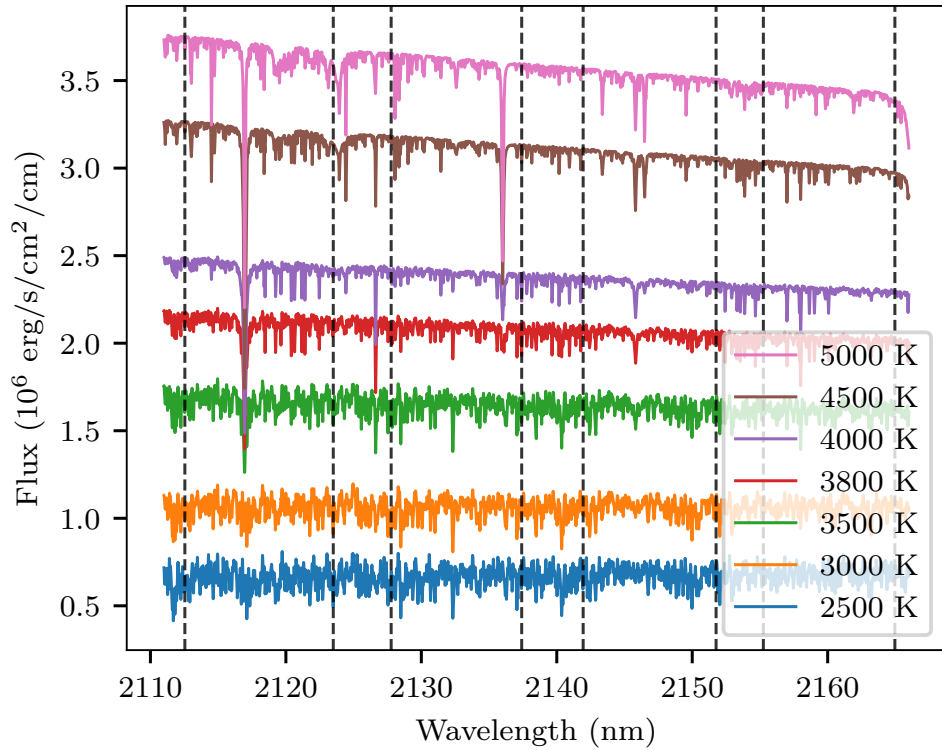


Figure 7.7: PHOENIX-ACES spectra for temperatures between 2500 and 5000 K, corresponding to the same lines in Figure 7.6. The flux units are the native units of the PHOENIX-ACES spectrum, ($\text{erg s}^{-1} \text{cm}^2 \text{cm}^{-1}$), and have not been scaled by the stellar radii. All spectra have a $\log g=5.0$ and $[\text{Fe}/\text{H}]=0.0$. The vertical dotted lines indicate the edges of the CRIRES detectors.

temperature is recovered. This is probably due to a combination of the level of noise added, and the asymmetries of the χ^2 lines. Figure 7.5 uses the noise level measured from the observed spectrum while Figure 7.6 has a SNR of 300. This large asymmetry observed can also explain the jump observed in the synthetic recovery temperature around 2700 K in Figure 7.5.

The asymmetry also causes an asymmetry in the confidence level bounds which can be seen in the bottom panel of Figure 7.6. For instance the recovered value and $1-\sigma$ error bars on the 3000 K injected companion is 2800^{+20}_{-100} , with an asymmetric error bar skewed towards lower temperatures.

There is a slight bump observed at 5100 K in the χ^2 curves for the injected companions of 4500 and 5000 K. This is believed to be due to a discontinuity in the PHOENIX-ACES modelling. The ‘‘reference wavelength defining the mean optical depth grid’’ is changed at 5000 K (Husser et al., 2013, Section 2.3). More care needs to be taken if trying to detect a companion near this temperature.

7.3.4 Component RV separation

Another factor which could contribute to an unsuccessful detection is the RV separation between the host and companion, is rv_2 . Estimates for the observations are given in the last column of Table 6.3. If rv_2 is small compared to the line width, then all the same lines of both components will be blended. For example, Kolbl et al. (2015) have difficulty separating blended spectra which have a component

RV separation below 10 km s^{-1} . This is indeed the case for HD 4747, HD 211847, and HD 202206 with expected $|rv_2| < 2 \text{ km s}^{-1}$. This may have contributed to the lack of recovery with both components of the binary model trying to fit to the same features. This may even cause some correlation between the parameters of the two components. The RV separation of the two components changes with orbital phase. Having multiple spectra of the same target distributed in phase may allow the RV of the spectral components to be better recovered (e.g. Czekala et al., 2017; Sablowski et al., 2016; Piskorz et al., 2016).

7.3.5 Wavelength range

The wavelength choice for the spectra analysed here, observed with the intention to apply the spectral differential technique, was selected due to the location of the K -band telluric absorption window. While there was minimum telluric contamination in this window there is also a limited number telluric lines to perform wavelength calibration. With small number of spectra lines, and the model discrepancies this wavelength range is not the best choice for the techniques applied here. This is not helped by the narrow wavelength range $\sim 50 \text{ nm}$ set by the CRIRES instrument.

For comparison Passegger et al. (2016) used four different spectral regions for the precise parameter determination of M-dwarfs using χ^2 methods. Specific lines in the different wavelength regions are affected differently by the model parameters: T_{eff} , $\log g$, and $[\text{Fe}/\text{H}]$; and are used to break degeneracies in the PHOENIX-ACES parameter space.

Changing the wavelength coverage to regions with lines sensitive to stellar parameters for both stars and BDs, as well as using a larger wavelength range that will be achieved by CRIRES+, may help to improve the recovery results of the companion recovery technique presented here.

Several works (e.g. Brogi et al., 2014; Brogi et al., 2016; Piskorz et al., 2016) have had successful molecule and companion detections in the wavelength range around 2300 nm due to strong CO lines. This wavelength region has already been shown to be promising for simulations of the differential technique in Kostogryz et al. (2013). This is clearly one wavelength region in particular to focus attention on in the future.

7.3.6 The BT-Settl models

The PHOENIX-ACES models were not the only spectral libraries available with the other notable library considered for this work being the BT-Settl models (Allard et al., 2010; Allard, 2013; Baraffe et al., 2015) (see Section 4.2.2).

As the BT-Settl models are suitable to model the atmospheres of the brown dwarfs they would have been useful for the companion recovery technique developed here. However, due to the derived a temperature upper limit of around 3800 K, this method was unable to achieve a successful recovery of the $155 \text{ M}_{\text{Jup}}$ ($T_{\text{eff}} \sim 3200 \text{ K}$) low mass star companion of HD 211847 as shown in Sections 7.2.2 and 7.2.3. These temperatures are both well above the 2300 K cut-off of the PHOENIX-ACES models and for the onset of dust- and cloud-formation phenomena, at 2600 K.

As shown in Section 4.2.4 the PHOENIX-ACES and BT-Settl spectra are fairly similar. Figure 7.8 shows again the minimum χ^2 solution for detector #1 of the second HD 211847 observation, this time including the BT-Settl solution with the same parameters. Although the PHOENIX-ACES and BT-Settl models differ slightly they both have large spectral discrepancies to the observations. As such the BT-Settl models were not used in the χ^2 simulations and results as there did not seem to be any special advantage

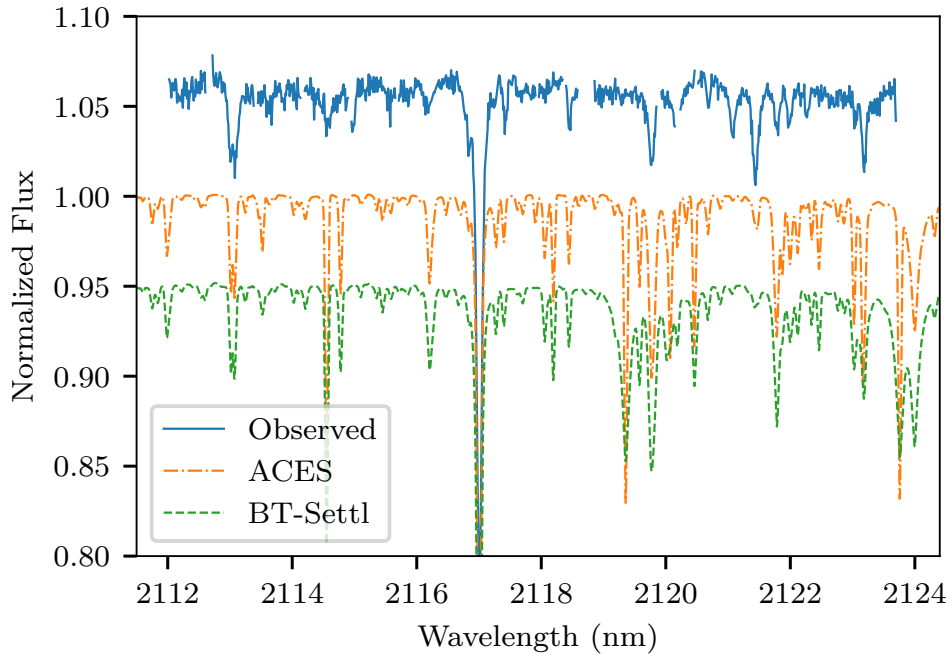


Figure 7.8: Detector #1 spectrum for HD 211847 (blue) alongside the PHOENIX-ACES (orange dash-dot) and BT-Settl (green dashed) synthetic spectra for the host star only, with parameters $T_{\text{eff}}=5700$ K, $\log g=4.5$ and $[\text{Fe}/\text{H}]=0.0$. Both synthetic models have been normalized and convolved to $R = 50\,000$. There is a 0.05 off-set between each spectrum.

in using them. If promising results had been obtained with the PHOENIX-ACES models, or had there been a substantial difference between the synthetic spectral models, more focus on the BT-Settl models would have occurred.

7.3.7 Impact of $\log g$

The surface gravity of a star, measured as $\log g$, is related to evolutionary state and the size of the star. Smaller $\log g$ values usually indicate bigger stars with larger radii. This parameter has a large impact on the radius and thus flux ratio of the binary models. In experimenting with the $\log g$ value of the PHOENIX-ACES models a decrease in $\log g$ from 5.0 to 4.5 increases the models effective radius by ~ 1.75 in the temperature range investigated here. This change in radius alone roughly triples the absolute flux of the synthetic spectrum (1.75^2), neglecting any changes to the shape of the actual spectrum. Therefore, there are large jumps in the model flux ratios, and the χ^2 solutions if the $\log g$ is allowed to vary. Like with higher companion temperatures, a lower $\log g$ value for the companion is favoured as the increased flux ratio reduces the spectral mismatch of the host component to the observations. This large impact of $\log g$ on the spectral library absolute flux is one reason for keeping the $\log g$ of each component fixed in the χ^2 results presented in Section 7.2. While the $\log g$ values do have a large impact on the flux of the models, there is no reason to believe that the $\log g$ of the targets were so badly determined that they were the reason for non-detection. The other issues seem far more likely.

7.3.8 Interpolation

One procedure not incorporated into this χ^2 procedure is spectral interpolation between spectral grid points. It is common to interpolate between the synthetic spectral grids to fit and derive parameters in between the grid points such as performed in Nemravová et al. (2016) and Passegger et al. (2016). At a more advanced stage, instead of interpolation, Czekala et al. (2015) use a spectral emulator and Principal Component Analysis (PCA) to create eigenspectra for the synthetic library and Gaussian processes to derive a probability distribution function of possible interpolation spectra to account for uncertainties in the interpolation required for high signal-to-noise spectra.

Interpolation could be added to this work in the future to refine the recovered parameters, and to help the transition between the grid $\log g$ values. Codes are readily available to perform spectral interpolation which could be utilized for this, two of them are *pyterpol*⁷ (Nemravová et al., 2016) and *Starfish*⁸ (Czekala et al., 2015).

7.3.9 Comparisons to other works

In this work the techniques attempted were unsuccessful in detecting the companions. Here some relevant comparisons are made to recent positive detections in the literature.

Passegger et al. (2016) apply χ^2 fitting of M-dwarf spectra in the nIR to PHOENIX-ACES models, incorporating inter-grid interpolation to determine M-dwarf parameters. Reaching a level inherent uncertainties on the parameters of $\sigma_{T_{\text{eff}}} = 35 \text{ K}$, $\sigma_{\log g} = 0.14$, and $\sigma_{[\text{Fe}/\text{H}]} = 0.11$, on four stars. Passegger et al. (2018) further extend this method to the 300 stars of the CARMENES library with optical and nIR spectra, achieving uncertainties of $\sigma_{T_{\text{eff}}} = 51 \text{ K}$, $\sigma_{\log g} = 0.07$ and $\sigma_{[\text{Fe}/\text{H}]} = 0.16$. The temperatures recovered are in line with the literature values while their metallicity determination has a larger spread when compared to the literature. These uncertainties are much smaller than the library grid spacing due to the fine-grid search achieved by interpolation.

Rajpurohit et al. (2018) perform similar parameter determinations, using the recent BT-Settl models instead, exploring more lower temperature M-dwarfs than Passegger et al. (2018), at which point dust clouds begin to form. The results of Rajpurohit et al. (2018) are in agreement with (Gaidos et al., 2014) but they find a disagreement to the Passegger et al. (2018) parameters, particularly T_{eff} , with up to a 200–300 K difference between the PHOENIX-ACES and BT-Settl results. Differences are also observed between the $\log g$ and $[\text{Fe}/\text{H}]$ recovered by the two works. Both these works use a much larger wavelength range (~ 500 – 1700 nm) than utilized here.

In trying to detect secondary stellar spectra in optical spectra at $R = 60\,000$, (Kolbl et al., 2015) are able to detect secondary spectra down to a 1% flux ratio, by matching to a library of real spectra. The work performed in this thesis aimed at flux ratios starting at and below this 1% flux ratio limit, even after taking advantage of the increased flux ratio in the nIR. Attempting to fit smaller than at flux ratios below 1% resulted in the issues mentioned above.

One promising technique with a success in detecting faint companion emission spectra is presented by Lockwood et al. (2014). Applying the TODCOR correlation to several spectra at different epochs and combining the observations while accounting for the orbits using a maximum likelihood framework, they confirm the water emission signature in τ Boötis and find a 1σ upper limit high resolution ($R = 24\,000$) spectroscopic flux ratio of 10^{-4} at $3.3 \mu\text{m}$.

⁷ <https://github.com/chrysante87/pyterpol>

⁸ <https://github.com/iancze/Starfish>

Piskorz et al. (2016) used this same technique to achieve a detection of a non-transiting hot gas giant HD 88133b, with a flux ratio near 10^{-5} . This is achieved with spectra from nine epochs; six in the *L*-band and three epochs in the *K*-band with the Keck NIRPSEC instrument ($R=25\,000$ – $30\,000$). Each epoch has a combined exposure time of 60–180 minutes reaching a SNR between 1600–3000 allowing for the planetary emission spectra to be recovered around a flux ratio of 10^{-5} .

These successful works clearly reveal the difficulty faced with the spectra analysed in this current work. Particularly, the SNR in Piskorz et al. (2016) is an order of magnitude higher and the wavelength coverage is significantly larger, due to the cross-dispersion of NIRPSEC. Also the multi-epoch approach allows for the RV of the two components to be monitored and some orbital parameters determined. The narrow wavelength coverage CRIRES spectra analysed here, at SNR=100–300 are insufficient. The poorly separated epochs, were also a problem as addressed in Section 6.4.

Chapter 8

Information content in the nIR

The work presented in this chapter focuses on calculating and analysing the information content of stellar spectra, specifically the radial velocity RV precision of M-dwarf spectra in the nIR. M-dwarfs are a source of focus in the community with several new instruments dedicated specifically to detecting planet around M-dwarfs (e.g. Quirrenbach et al., 2014; Bouchy et al., 2017; Artigau et al., 2014, among others). The fundamental radial velocity precision of M-dwarf spectra attainable at different wavelength regions calculated in Figueira et al. (2016) was used to inform some design choices of two nIR spectrographs, SPIRou and NIRPS. Understanding the underlying precision of different spectral types can also allow RV surveys to adjust the focus of the target selection, or optimize the exposure time of different spectral types. This can help in detecting the presence of “habitable Earth-like” planets around M-dwarfs which have become a prime target with the recent nIR spectrographs.

The purpose of the work presented in this chapter is to extend the work of Figueira et al. (2016), computing the theoretical RV precision of synthetic stellar spectra over a wider range of situations. A investigation into the effect of $\log g$ and [Fe/H] on precision is performed and a preliminary comparison of RV precision of the recently observed nIR M-dwarf spectra from CARMENES library and their synthetic counterparts is given. This is to test how the RV precision of synthetic models compares to reality. New computations of the RV precision of synthetic spectral libraries are also given, which were provided for exposure time calculators of NIRPS and SPIRou.

8.1 Overview

The pursuit of detecting exoplanets, especially “habitable” and “Earth-like” planets, requires state-of-the-art instrumentation with high precision. Several new high-resolution nIR spectrographs are becoming available now and in the near future, not limited to CARMENES, NIRPS, SPIRou and CRIRES+ (see Section 3.4). One science objective common to all four instruments is the detection of small mass planets around M-dwarf stars utilizing the radial velocity technique, an objective strived for in the literature (e.g. Reiners et al., 2010; Rodler et al., 2011; Plavchan et al., 2015). As the RV amplitude is $K_1 \propto P^{-1/2} M_1^{-2/3}$ (Equation 2.11), the induced RV wobble from a similarly massive exoplanet is larger around an M-dwarf star, making the RV signal from lower mass exoplanets easier to detect. Also the cooler M-dwarfs have habitable zones closer to the star, at shorter orbital periods, that again have a

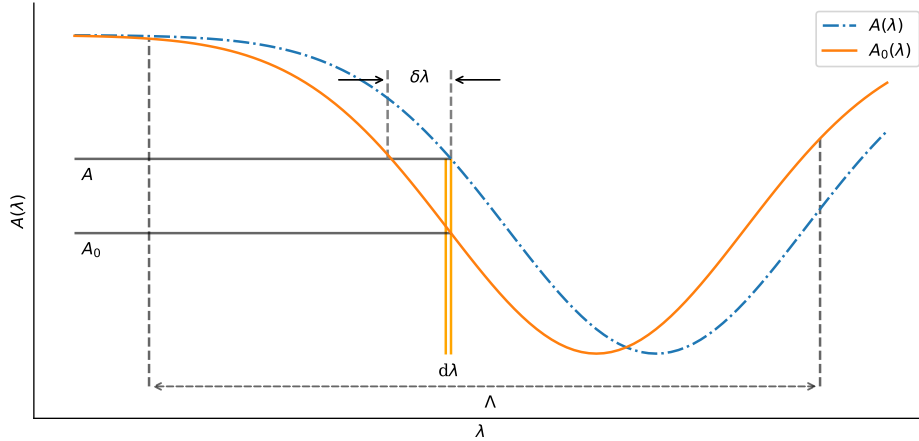


Figure 8.1: Arbitrary spectral line with a shift $\delta\lambda$, inspired by Connes (1985). Λ is the wavelength range considered.

stronger RV amplitude making it easier to detect small mass planets in the habitable zone of M-Dwarfs.

To calculate and predict the information content attainable from M-dwarfs in the nIR, Figueira et al. (2016) utilized the PHOENIX-ACES library of synthetic spectra. This helped at the early stages of instrument design by identifying the wavelength regions with the best RV precision, but can also help in the planning of observations, by understanding how the precision changes with spectral type and observed SNR. However, the synthetic spectra do not quite match reality and a comparison between theoretical and observed is needed. Artigau et al. (2018) recently compared optical (HARPS, ESpaDOnS) and nIR (CRIRES) archival spectra of the M-dwarf, Barnard’s Star, to synthetic spectra. They found that state-of-the-art atmosphere models over-predict the RV content Y - and J -band RV by more than a factor of ~ 2 , while under-predicting the H - and K -band content by half. A similar comparison will be made in this work to CARMENES spectra.

Recent results regarding the measured performance of the CARMENES survey (Reiners et al., 2018; Quirrenbach et al., 2018) find that the RV in the nIR is worse than the pre-survey predictions. Precisions of $1\text{--}2\,\text{m s}^{-1}$ have been achieved in the optical but only $5\text{--}10\,\text{m s}^{-1}$ in the nIR. However, comparing RV precision in different wavelength bands Quirrenbach et al. (2018) found a “sweet spot” around $0.7\text{--}0.8\,\mu\text{m}$ with deep TiO bands providing rich RV information in mid-M dwarfs.

The number of papers on this thematic, the number of open questions, and the impact on the design of instrumentation, particularly in the nIR, show that this is an important topic as of today.

8.1.1 Fundamental photon noise limitation

A technique to calculate the theoretical radial velocity precision of a spectrum using the full spectral information in an optimal way was first presented by Connes (1985). Here the radial velocity precision derivation following Connes (1985), Bouchy et al. (2001), and Figueira et al. (2016) is provided.

For demonstration purposes Figure 8.1 shows a portion of an arbitrary spectrum $A(\lambda)$, over a wavelength range Λ . Here $A_0(\lambda)$ is the reference spectrum while $A(\lambda)$ is observed some later time with an apparent wavelength shift observed. A Gaussian line is shown, but the presence of spectral lines is not a requirement for the derivation.

The Doppler shift of a spectrum is given by:

$$\frac{\delta V}{c} = \frac{\delta \lambda}{\lambda}, \quad (8.1)$$

where c is the speed of light in a vacuum, and $\delta \lambda$ is the shift in wavelength λ due to the velocity δV .

Using $\delta y = \frac{\partial y}{\partial x} \delta x$, and for a Doppler shift that is small compared to the line-width¹, the observable intensity change in a wavelength slice $d\lambda$ (or at a given pixel) can be expressed by:

$$\delta A(i) = A(i) - A_0(i) \simeq \frac{\partial A_0(i)}{\partial \lambda(i)} \delta \lambda = \frac{\partial A_0(i)}{\partial \lambda(i)} \frac{\delta V(i)}{c} \lambda(i). \quad (8.2)$$

Rearranging Equation 8.2 for $\delta \lambda$ and combining it with Equation 8.1, the Doppler shift then becomes:

$$\frac{\delta V(i)}{c} = \frac{A(i) - A_0(i)}{\lambda(i)(\partial A_0(i)/\partial \lambda(i))} \quad (8.3)$$

This equation shows that the radial velocity at pixel i is measured through a change in the intensity in the recorded spectrum, $A(i) - A_0(i)$, and is inversely proportional to the slope of the spectrum, $\partial A_0(i)/\partial \lambda(i)$. Equation 8.3 provides a separate measurement of the radial velocity shift for every pixel, i , in the spectrum. The sensitivity of the velocity measurement can be improved, and the noise decreased by using the information from the whole spectral range, Λ . This is achieved by taking the weighted average² over all pixels in the spectral range using an optimal pixel weight $W(i)$.

$$\frac{\overline{\delta V}}{c} = \frac{\sum \frac{\delta V(i)}{c} W(i)}{\sum W(i)}. \quad (8.4)$$

Statistically, the optimal weights are proportional to the inverse square of the individual dispersion (variance),

$$W(i) = \frac{1}{\left(\frac{\delta V_{\text{RMS}}(i)}{c}\right)^2}, \quad (8.5)$$

where X_{RMS} is the dispersion on the quantity X .

The individual dispersion of the velocity measurement $\delta V_{\text{RMS}}(i)$ is the dispersion that would result from several measurements of the reference spectrum all with the same Doppler shift (e.g. zero). Equation 8.3 thus becomes:

$$\frac{\delta V_{\text{RMS}}(i)}{c} = \frac{[A(i) - A_0(i)]_{\text{RMS}}}{\lambda(i)(\partial A_0(i)/\partial \lambda(i))}. \quad (8.6)$$

The noise of the spectrum A is the quadratic sum of the photon noise \sqrt{A} and the detector noise σ_D .

¹ However, Connes (1985) also shows that the approximation in Equation 8.2 is adequate under all circumstances.

² Weighted average on x is $\bar{x} = \frac{\sum x(i)W(i)}{\sum W(i)}$

The spectrum A_0 is considered noise free.

$$[A(i) - A_0(i)]_{\text{RMS}} = [A(i) - 0]_{\text{RMS}} = \sqrt{\sqrt{A(i)}^2 + \sigma_D^2} \quad (8.7)$$

Considering that the Doppler shift is small and that A and A_0 have the same intensity level, then $A = A_0$ can be set. Using Equations 8.3, 8.5 and 8.7 the optimum weights then become solely dependent on the reference spectrum.

$$W(i) = \frac{\lambda^2(i)(\partial A_0(i)/\partial \lambda(i))^2}{A_0(i) + \sigma_D^2} \quad (8.8)$$

This weighting function can be modified to mask out and eliminate unwanted lines in the spectrum (see Section 8.4.1), for instance setting the particular pixel weights to zero to remove any telluric absorption lines in the observed spectra.

With the optimal weights set, the weighed average velocity change measured from the full spectral range Λ , is given by:

$$\frac{\overline{\delta V}}{c} = \frac{\sum \frac{A(i) - A_0(i)}{\lambda(i)(\partial A_0(i)/\partial \lambda(i))} W(i)}{\sum W(i)} \quad (8.9)$$

$$= \frac{\sum \frac{A(i) - A_0(i)}{\lambda(i)(\partial A_0(i)/\partial \lambda(i))} \frac{\lambda^2(i)(\partial A_0(i)/\partial \lambda(i))^2}{A_0(i) + \sigma_D^2}}{\sum W(i)} \quad (8.10)$$

$$= \frac{\sum (A(i) - A_0(i)) \frac{\lambda(i)\partial A_0(i)/\partial \lambda(i)}{A_0(i) + \sigma_D^2}}{\sum W(i)} \quad (8.11)$$

$$= \frac{\sum (A(i) - A_0(i)) \left(\frac{W(i)}{A_0(i) + \sigma_D^2} \right)^{1/2}}{\sum W(i)} \quad (8.12)$$

The important quantity for RV measurements is not just the velocity values themselves but also the dispersion (or uncertainty) on the measured velocity, the RV precision δV_{RMS} , from the spectrum. This allows one to assess the planetary detectability limitations attainable in the spectra. From rearranging Equation 8.5 the dispersion is given by:

$$\frac{\overline{\delta V_{\text{RMS}}}}{c} = \frac{1}{\sqrt{\sum W(i)}} = \frac{1}{Q \sqrt{\sum A_0(i)}}. \quad (8.13)$$

With Equation 8.13 the velocity precision is inversely proportional to the sum of the optimal pixel weights. Here Q is a spectral quality factor, defined for the pure photon noise case in Connes (1985) and Connes et al. (1996), as:

$$Q \equiv \frac{\sqrt{\sum W(i)}}{\sqrt{\sum A_0(i)}} = \frac{\sqrt{\sum \frac{\lambda^2(i)(\partial A_0(i)/\partial \lambda(i))^2}{A_0(i) + \sigma_D^2}}}{\sqrt{\sum A_0(i)}}. \quad (8.14)$$

The pure photon noise case is exclusively considered here in a high signal-to-noise regime in which

$A(i) + \sigma_D^2 \sim A(i)$ can be approximated. The quality factor, Q , becomes flux independent and is purely a function of the spectral profile within the spectral range considered³. It is a measure of the line richness i.e. the quantity and depth of the lines. For example a spectrum with many sharp lines will have a high Q . The instrumental resolution of the spectrograph also affects the spectral quality as it induces line broadening.

The radial velocity precision or uncertainty can be rearranged in terms of the spectral quality:

$$\delta V_{\text{RMS}} = \frac{c}{Q \sqrt{\sum A_0(i)}} = \frac{c}{Q \sqrt{N_{e^-}}} \approx \frac{c}{Q \cdot \text{SNR}}, \quad (8.15)$$

where $\sum A_0(i) = N_{e^-}$ is considered to be the total number of photo-electrons N_{e^-} counted in the spectral range considered, and $\text{SNR} = \sqrt{N_{e^-}}$ for large N_{e^-} .

The number of photo-electrons counted N_{e^-} in an observed spectrum depends on many factors, such as: the stellar magnitude, detector efficiency and integration time. It can be estimated using

$$N_{e^-} = P_{\text{avg}} * S_{\text{tel}} * T_{\text{exp}} * \alpha * \Lambda, \quad (8.16)$$

where P_{avg} is the average monochromatic stellar brightness, in $\text{photons s}^{-1} \text{cm}^{-2} \text{cm}^{-1}$, across the wavelength range Λ , S_{tel} is the telescope collecting area in cm^2 , T_{exp} is the integration time in s, and α the is overall system efficiency (including atmosphere, telescope, spectrograph and detector).

This technique has been tested and demonstrated on observations by Connes et al. (1996) and been used to predict the accuracy or performance limits of new spectrograph instrumentation (e.g. Connes, 1985; Butler et al., 1996a; Bouchy et al., 2001) and has informed the design (and use) of spectrographs, e.g. SPIRou (Artigau et al., 2014; Figueira et al., 2016). However, Figueira et al. (2016) bypass the calculation of N_{e^-} in Equation 8.16 by scaling the synthetic spectral models to a specific SNR level instead.

In the case of several δV measurements computed for k spectral slices (or spectral orders) then the error on the average $\overline{\delta V}$ is given by the error on a weighted average:

$$\overline{\delta V_{\text{RMS}}} = \frac{1}{\sqrt{\sum_k \left(\frac{1}{\delta V_{\text{RMS}(k)}} \right)^2}}. \quad (8.17)$$

A separate general formula for RV precision, discussed in Section 2.3, is given by Hatzes et al. (1992) in terms of general spectral parameters:

$$\delta V_{\text{RMS}} = \frac{1}{\sqrt{F} \sqrt{\Lambda} R^{1.5}} \quad (8.18)$$

where \sqrt{F} represents the SNR of the spectrum in the Poisson-noise dominated regime, and R is the spectral resolution. The Λ comes from assuming a homogeneous distribution of lines, with the same line properties, per unit length.

³ In the case of pure detector noise case the fluctuations in A are independent of the spectrum A and the quality factor is $Q_D = \frac{\sqrt{\sum \lambda^2 (\partial A_0(i) / \partial \lambda(i))^2}}{\sum A_0(i)}$ as derived by Connes (1985).

8.2 Deriving RV precision of synthetic spectra

The work of this chapter extends the work of Figueira et al. (2016). To contrast the software improvements made here the details of Figueira et al. (2016) are first presented, then the important factors that were considered in preparing and using the synthetic spectra to apply the RV precision formulation of Equations 8.13 and 8.17 are discussed.

8.2.1 Prepare PHOENIX-ACES models

Four PHOENIX-ACES spectra were selected, spanning the M-dwarfs regime (M0, M3, M6, M9) with model temperatures 3900, 3500, 2800 and 2600 K respectively. The other model parameters were $\log g=4.5$, $[\text{Fe}/\text{H}]=0$ and $[\alpha/\text{Fe}]=0$ representing values typical for M-dwarfs. The flux (spectral energy distribution) given by the library spectra ($\text{ergs/s/cm}^2/\text{cm}$) are converted into photon counts by dividing the flux by the energy of a photon, $E_p = hc/\lambda$. Neglecting the multiplicative constants, this corresponds to multiplying the flux values by the respective wavelength. In this case the absolute values do not matter, just the spectral shape, as the spectra will be scaled to a given SNR level.

8.2.2 Convolution

To match realistic observations the spectra are convolved by a rotation kernel followed by a Gaussian instrumental kernel to broaden the spectra lines. The details of these kernels and implementation of numerical convolution are given below.

Rotational convolution

Stellar rotation has the effect of broadening spectral lines as the different portions of the stellar surface have a different radial velocity between $\pm v \sin i$. Rotation is applied to a non-rotating spectrum by convolution with a rotation kernel. The stellar rotational kernel used follows Gray (2005);

$$G(\Delta\lambda) = \frac{2(1-\varepsilon)[1 - (\Delta\lambda/\Delta\lambda_L)^2]^{1/2} + \frac{1}{2}\pi\varepsilon[1 - (\Delta\lambda/\Delta\lambda_L)^2]}{\pi(1-\varepsilon/3)v \sin i} \quad (8.19)$$

$$= c_1[1 - (\Delta\lambda/\Delta\lambda_L)^2]^{1/2} + c_2[1 - (\Delta\lambda/\Delta\lambda_L)^2] \quad (8.20)$$

where

$$c_1 = \frac{2(1-\varepsilon)}{\pi(1-\varepsilon/3)v \sin i}, \quad c_2 = \frac{\frac{1}{2}\pi\varepsilon}{\pi(1-\varepsilon/3)v \sin i}, \quad (8.21)$$

are constants which depend on the equatorial rotational velocity $v \sin i$.

Here $\Delta\lambda$ is the wavelength position from the non-rotating line centre, while $\Delta\lambda_L$ is the maximum line shift of the line centre at the edge of the stellar disk where the Doppler shift is $v \sin i$; $\Delta\lambda_L = \lambda \frac{v \sin i}{c}$.

This kernel arises from integrating the rotational velocity profile across the surface of the stellar disk as a series of strips with different Doppler shifts. As such the rotation kernel is bounded in the range $[-\Delta\lambda_L, \Delta\lambda_L]$ from the line centre. This can be seen in Figure 8.2 with a diagram of the stellar disk on the left, and the profile of the rotational kernel on the right, split into the two components from

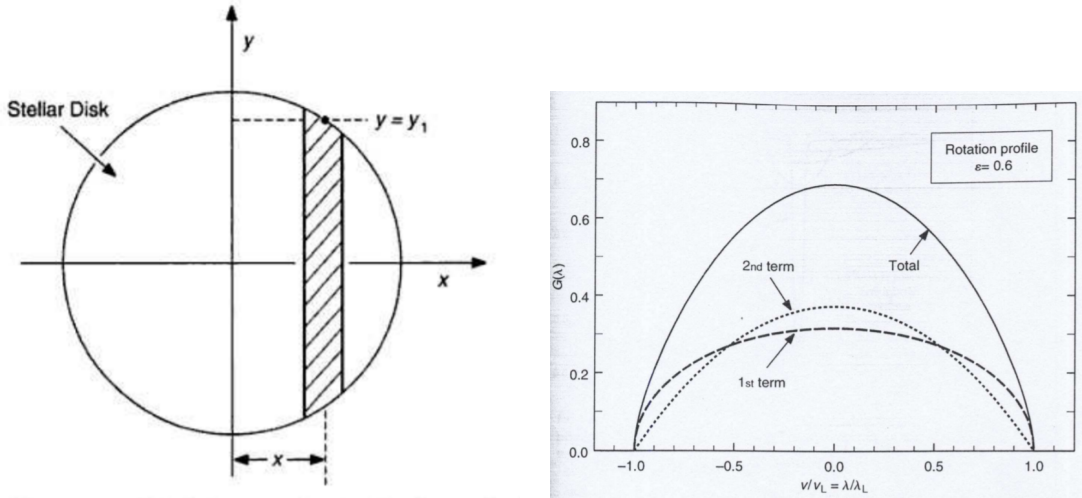


Figure 8.2: Left: Apparent disk of the star, thought of as a series of strips parallel to the projected rotation axis, each with the Doppler shift proportional to x . The amount of light at each Doppler shift varies with the length of the strip, from $-y_1$ to $+y_1$, where $y_1 = \sqrt{R^2 - x^2}$ for a circular disk. Right: The rotation profile, Equation 8.20, is shown by the solid black line for a limb darkening coefficient $\varepsilon = 0.6$ and labelled “total”. It is the sum of the “1st term” and “2nd term” curves. These are reproductions of Figures 18.3 and 18.5 from Gray (2005).

Equation 8.20. This kernel also accounts for limb-darkening on the stellar disk with the linear limb darkening coefficient used in this work fixed at $\varepsilon = 0.6$ as done in Figueira et al. (2016).

As the Doppler shift $v \sin i$ is transformed into wavelength by multiplication of λ/c there is a wavelength dependence on the rotation kernel shape. That is, the rotation kernel at each pixel is unique, requiring individual calculations.

Instrumental convolution

Following the rotational convolution the spectra are convolved with Gaussian instrumental profile (IP) with the FWHM constrained by the given spectral resolution R , $\text{FWHM} = \lambda/R$.

The Gaussian convolution kernel is of the form

$$IP(\Delta\lambda) = \frac{1}{\sigma\sqrt{2\pi}} \exp^{-\frac{\Delta\lambda^2}{2\sigma^2}} \quad (8.22)$$

with $\sigma = \frac{\text{FWHM}}{2\sqrt{2\ln(2)}}$, and $\Delta\lambda$ is again the difference from the line centre⁴.

This assumes that the instrument profile of a particular instrument is in-fact Gaussian. This assumption of a Gaussian instrumental profile is a good starting point for high-resolution spectrographs, and shown to be valid for CRIRES (Seifahrt et al., 2010). If a non-Gaussian instrument profile is particularly well characterized, then it could be used to replace the Gaussian profile used here.

For instance Artigau et al. (2018) state that the instrumental profile of a (circular) fibre-fed spectrograph such as HARPS is mathematically equivalent to a cosine between $-\frac{\pi}{2}$ and $\frac{\pi}{2}$ with a width

⁴ Normally this is written as $(x - \mu)$ with μ as the Gaussian centre.

equivalent to the Gaussian FWHM. From this description the integration of a circular fibre is given by

$$\text{IP}_{\text{fibre}(\Delta\lambda)} = \cos(B \cdot \Delta\lambda), \quad [-\frac{\pi}{2B}, \frac{\pi}{2B}], \quad (8.23)$$

where $B = \frac{\text{FWHM}_0}{\text{FWHM}}$ is scaled to give the same area. Artigau et al. (2018) also mention that the RV precision results using this IP_{fibre} are all consistent with the results from a Gaussian kernel. It only provides a small correction to the Gaussian profile of a standard spectrograph, and is only necessary if one is resolution-limited by the slit.

Numerical Convolution

Both convolutions are performed numerically, by iterating over all pixels in the spectrum. Convolution is a continuous mathematical operation in which one signal modifies the shape of another. In the cases here the rotation and instrument modify the shape of spectral lines. The continuous broadening functions/kernels are applied to the sampled (non-continuous) spectrum numerically by computing the kernels at the location of pixels in the spectrum and summing the result.

At each pixel, a window of neighbouring pixels is selected that fall within the convolution window⁵, e.g. $5 \times \text{FWHM}$ for that pixel. The convolution kernel is calculated for the window, multiplied by the spectral flux and then summed to produce the new value for the pixel of the iteration. The shape of the convolution kernels and the size of convolution window are wavelength dependant ($\Delta\lambda_L = \lambda \frac{v \sin i}{c}$ and $\text{FWHM} = \frac{\lambda}{R}$) and must be calculated separately for each pixel, making the convolution computationally expensive.

This convolution method allows for the spectrum to be non-uniformly spaced, unlike other methods that usually require a uniform spacing e.g. the implementation in PyAstronomy. One factor that needs consideration when convolving with a non-uniformly spaced spectrum is the discretization of the kernel onto the wavelength grid. For instance the number of points inside the convolution window, due to the sampling, as well as their specific location inside the kernel will have a slight affect on the kernel area. The convolution result is normalized by dividing it by the result of the convolution kernel applied to a unitary spectrum of ‘1’s on the same wavelength grid. Figueira et al. (2016) performed this unitary convolution separately and applied the normalization correction afterwards. In the improved implementation of Section 8.3 the convolution normalization is performed inside the loop over the pixels, for each pixel directly, following the convolution calculation result for that pixel.

Edge effects occur in convolution, where pixels near the ends are not symmetrically convolved, as there are not pixels outside the bounds. For the synthetic spectra here, the convolution is performed on a slightly wider spectrum, so that the desired output wavelength range does not contain edge effects. In this case, since two convolutions are performed, the first input spectrum is chosen by default to be sufficiently wide, such that any pixel possibly altered by the edge effects not will be present in the final output spectrum after both convolutions.

8.2.3 Interpolation

To simulate the sampling effect of high-resolution spectrographs, interpolation is used to re-sample the spectrum to three pixels per resolution element. This corresponds to a spacing between pixels at λ

⁵ Region in which the convolution kernel will affect this particular pixel.

of $(\lambda/3R)$. For echelle spectrographs, for which $\Delta\lambda/\lambda$ is constant, the number of pixels per resolution element is also constant. A sampling of three is chosen to be above the Nyquist limit of two pixels per resolution element, to not lose any spectral information, and commonly achieved by current spectrographs, e.g. a sampling of 3.3 for HARPS (Mayor et al., 2003). This interpolation of the synthetic spectra is performed after the convolution and before the SNR scaling below.

8.2.4 SNR scaling

The purpose of Figueira et al. (2016) was to compute only the relative precisions between the synthetic models. This was done by normalizing each spectrum, after convolution, to a SNR of 100 at the centre of the J -band. Specifically this is achieved by summing the number of pixels within one resolution element (three in this case), governed by the sampling, centred at $1.25 \mu\text{m}$ and scaling the result so that the sum becomes 100^2 . In this way the $\text{SNR} = \sqrt{F}$ is 100, where F is the sum of the three pixels. The specific scaling values for the analysed spectra, $v \sin i$, and resolution combinations were hard coded into the software, making it impossible to analyse a new spectrum without modification of the source code.

8.2.5 Bands

To analyse the precision in different wavelength bands the spectra are split into several chunks. The bands studied are the Z , Y , J , H , and K -bands with the specific wavelength bounds given in Table 4.1. These are the nIR wavelength bands created by regions of strong water absorption in the Earth’s atmosphere. These strong H_2O regions that defined these bands can be seen in the telluric spectrum given in Figure 4.1 or in the CARMENES spectrum in Figure 8.10.

8.2.6 Precision calculations

Finally the computation of the RV precision application of Equation 8.13 is applied to the individual convolved spectra, normalized, and split into separate bands. The RV precision calculations were performed under three separate conditions to assess different telluric line treatments. The same three conditions are explored in this work, and to avoid repetition these conditions are detailed below in Section 8.4.1.

8.3 *eniric*: Extended nIR information content

Here the software developed to compute the RV precisions is presented. It is an extension of the code used for the calculations of Figueira et al. (2016). This section documents the vast improvements (optimizations and extensions) made to the software. Changes made that affect the derived RV precision attained are specifically documented in detail, with the relative precision changes provided. This work resulted in a submission of a publication⁶ to *The Journal of Open Source Software*⁷ (JOSS) (Neal and Figueira 2019) with the source code openly available on Github⁸. This should be accepted shortly as only minor changes to the paper have been requested by the reviewer.

⁶ Available at <http://joss.theoj.org/papers/384bfc031df47ecf2d88328f63e5479>

⁷ joss.theoj.org/.

⁸ <https://github.com/jason-neal/eniric>

8.3.1 Automated testing

Before the changes to the software are detailed, a note about software testing. Automated software testing is an important practise to ensure that the code written is correct, and that new changes do not break the previously written code. This practice is crucial in computer science and professional software engineering but seldom encouraged or practised in scientific programming (Storer, 2017). It is however starting to becoming increasingly encouraged as part of the movement towards open and reproducible science.

After inheriting the code-base from Figueira et al. (2016), software tests were added for a number of purposes: to learn and explore the code-base, to check and test the original codes functionality, and to identify if any changes implemented break the original functionality. Version control practises were used to incrementally add small separate changes to the code base one at a time, regularly testing in a continuous integration manner. This is done by sending the code-base to a repository⁹ on Github¹⁰. Automated tools and services then forward the project for testing, code style checking, or other continuous-integration services (e.g. Travis-CI) which either run the automated tests, or other checks on each new change. The public Travis-CI record of the test for *eniric* can be found at <https://travis-ci.org/jason-neal/eniric>.

This process was valuable in preventing the introduction of errors, but also in identifying errors in the Figueira et al. (2016) results which are outlined in Section 8.4.3. Based on this experience it is a practise that is highly recommended for scientific programming.

8.3.2 Performance

The software performance is one aspect that was addressed in the upgrades. The original code used in Figueira et al. (2016) was very slow, taking around two hours per parameter combination. This led to multiple weeks worth of processing time required to compute the RV precision for the original paper (180 combinations). The latest implementation of *eniric* can compute all 180 combinations in less than two hours.

The major performance bottleneck was identified in the convolution stage. Starting with a NumPy array containing the spectrum, the algorithm looped though each pixel in the spectrum, selecting a suitable window around the given pixel with a *comprehension list*¹¹. The output is a list¹² which was turned back into a NumPy array, eventually summed and then appended to a new list. This list was once again converted into NumPy array. The main performance issue is a Python implementation detail to do with a type checking overhead when converting between NumPy and native data types. These conversions were performed 2–3 times for every pixel in the large spectral arrays of order 10^4 pixels.

Remaining entirely in the fast compiled NumPy code and not changing data types a performance gain of around $250 \times X$ was achieved. This is done by using boolean masks instead of comprehension lists and pre-allocating a NumPy array to store the results.

The convolution computation of individual pixels is an “embarrassingly parallel”¹³ problem. What this means is that convolution result for pixel $i + 1$ does not depend on the convolution result obtained of pixel i , as each can be computed independently. Therefore, parallel processing was also added into the

⁹ Public or private.

¹⁰ Bitbucket and GitLab are other popular options.

¹¹ Example usage can be found [here](#).

¹² A list is a native Python data structure.

¹³ https://en.wikipedia.org/wiki/Embarrassingly_parallel.

convolution to further improve the performance, roughly dividing the convolution time by the number of processors used.

As the convolution step is the main bottleneck, caching of the convolution results was included using the Joblib package. Caching the convolution function stores the input parameters and the convolution result together. If the same input parameters are passed to the convolution function again, it fetches the computed results from memory, rather than recomputing the time intensive convolutions. This avoids unnecessary wasted computation time computing the same convolution results, improving the performance of repeated runs of the software.

The PyAstronomy package has a “slow” version of the rotational convolution, which has a wavelength dependent kernel as done here. They also provide “fast” convolution kernels that used a fixed kernel, taking the central wavelength value. These are significantly faster but are only valid for very short wavelength regions, in which the kernels do not significantly change. They are not deemed suitable for use in this work due to the large wavelength span of spectroscopic bands and the wavelength dependant spacing of the spectra considered here. A comparison of the performance between the PyAstronomy convolutions and the convolutions implemented in *eniric* and used here are provided in a *Jupyter* notebook in the Github repository of “eniric”¹⁴; basically they fall in between the “fast” and “slow” implementation of PyAstronomy.

8.3.3 Model extension

The original software hard-coded the range of 180 model combinations computed, specifically by identifying the spectra by their spectral type and setting the SNR scaling values. These combinations were the four model spectra (M0, M3, M6, M9), three resolutions (60 000, 80 000, 100 000), three $v \sin i$ values (1.0, 5.0, 10.0 km s⁻¹) and the five spectral bands (*Z*, *Y*, *J*, *H*, *K*).

The software was extended to be able to load and prepare any spectrum from the PHOENIX-ACES spectral library provided the four identifying parameters [T_{eff}, log *g*, [Fe/H], [α/Fe]]. This allows for any spectra of current or future interest to be quickly analysed, matching any of the parameters in Table 4.2. The instrumental resolution, *R*, and rotation velocity $v \sin i$ were also extended to any suitable value, not restricted to only three values each. The nIR wavelength bands are still configured to the same wavelength regions but are able to be extended by the user, either over-writing the current band limits, or defining new bands with custom wavelength limits. For example, in Table 8.1 bands (and corresponding wavelengths) with labels VIS, CARM_{VIS}, NIR and CARM_{NIR} are shown which represent the visible and nIR wavelengths and the corresponding coverage of the CARMENES spectrograph in each. This allows for increased flexibility in using *eniric*; for instance tailoring the calculation to a specific instrument with a known or theoretical resolution (see Section 8.7), but opens up essentially an infinite possible combination of spectral parameters (with an infinite compute time).

A further extension was made to also allow for the use of the BT-Settl (CIFIST2011_2015) synthetic spectra, allowing for a comparison of RV precisions between different models. Like the PHOENIX-ACES models the BT-Settl spectra undergo a conversion from an energy flux to photon counts. The incorporation of any model from the PHOENIX-ACES and BT-Settl libraries with only the four model parameters is performed simply using the “grid tools” module from the Starfish package (Czekala et al., 2015).

A command line application is now available with *eniric*, which will load spectra and calculate RV precision for all combinations of valid input parameters. Examples of use are given in Appendix A,

¹⁴ https://github.com/jason-neal/eniric/blob/master/docs/Notebooks/Convolution_speeds.ipynb.

specifically all parameter combinations from Figueira et al. (2016) can be performed using Listing A.1.

8.4 Numerical Gradient

One of the key insights from Equations 8.8 and 8.13 is that the radial velocity precision is inversely proportional to the gradient (first order derivative) of the spectra. In numerically computing the RV precision, the result is dependent on the numerical method used to compute the gradient. In the original code used in Figueira et al. (2016) the gradient is approximated using the forward finite difference (FFD) method. In *eniric* the method for computing the gradient is changed to the `numpy.gradient()` function from the NumPy package. This uses more advanced numerical methods to compute a more precise gradient. A comparison between both gradient methods and the effect on the precisions result are presented here.

The simplest way to calculate the derivative is using finite difference methods (Quarteroni et al., 2000). These arise from Newton's definition of the derivative for a continuous function $f(x)$ which should be familiar from introductory calculus:

$$f'(x) = \lim_{h \rightarrow 0} \frac{f(x + h) - f(x)}{h} .$$

The three common varieties of the finite difference are,

$$FFD = \frac{f(x + h) - f(x)}{h}, CFD = \frac{f(x + \frac{1}{2}h) - f(x - \frac{1}{2}h)}{h}, BFD = \frac{f(x) - f(x - h)}{h}, \quad (8.24)$$

and are called the forwards (FFD), central (CFD), and backwards (BFD) finite differences respectively. The order of uncertainty on the FFD/BFD methods is $\mathcal{O}(h)$ while for the CFD it is $\mathcal{O}(h^2)$ (Quarteroni et al., 2000). As the wavelength spacing between samples/pixels (h) is small the CFD will be a more precise value for the gradient at each pixel.

In this case h is the difference in wavelength between the two pixels considered. In the FFD case the gradient at pixel i becomes:

$$\frac{\partial A_0(i)}{\partial \lambda(i)} = \frac{A_0(i+1) - A_0(i)}{\lambda(i+1) - \lambda(i)}, \quad 1 \leq i \leq n-1. \quad (8.25)$$

At each pixel the numerical derivative is evaluated to be the average slope between itself and the following pixel and is an approximation to the derivative. This only extends to $i = n-1$, where n is the number of points in the spectrum, and the last pixel is dropped from the RV calculation. This is important in the case of Condition #2 (Equation 8.28) from Figueira et al. (2016).

The `numpy.gradient()`¹⁵ function contains a more advanced numerical method to calculate the derivative. It uses a *compact difference* method (Quarteroni et al., 2000) which expands the finite differences using a Taylor expansion and then selects coefficients to minimize the *consistency error*. From the NumPy documentation the consistency error here is

$$\eta_i = \partial f(x_i)/\partial x - [\alpha f(x_i) + \beta f(x_i + h_d) + \gamma f(x_i - h_s)],$$

where h_s and h_d are the spacing to the left and right of i respectively. With Taylor expansion this turns

¹⁵ Documentation available at <https://docs.scipy.org/doc/numpy/reference/generated/numpy.gradient.html#id1>.

Table 8.1: The affect of the numerical gradient function on RV precision. The bands labelled VIS and NIR indicate the full visible and nIR bands while CARM_{VIS} and CARM_{NIR} indicate the two wavelength bands of the CARMENES spectrograph. Column A is the RV precisions calculated using the FFD gradient. Column B contains the FFD gradient method but applied with a wavelength shift of $\Delta\lambda/2$ in between pixels for this comparison only. Column C contains the RV precision calculation using the `numpy.gradient()` function. The final two columns give the relative precision change between gradient method A and the other two, as a percentage. The M0 spectra used here had no rotation, or instrument broadening performed and was normalized to a maximum of 1 in each band. The values given here are for accessing the relative precision change due to the different gradient methods only.

Gradient method		A	B	C	(B-A)/A	(C-A)/A
Band	λ range (μm)	FFD	δV_{rms} (m s^{-1})	Numpy	$\Delta\delta V$ ratio (%)	$\Delta\delta V$ ratio (%)
VIS	0.38 – 0.78	16.1	16.2	16.9	0.6	4.9
CARM _{VIS}	0.52 – 0.96	20.9	21.0	22.0	0.3	5.2
Z	0.83 – 0.93	76.9	77.0	78.8	0.1	2.5
Y	1.00 – 1.10	78.3	78.5	83.8	0.2	7.0
J	1.17 – 1.33	149.3	149.4	156.4	0.1	4.7
H	1.50 – 1.75	119.4	119.5	122.3	0.1	2.5
K	2.07 – 2.35	153.4	153.7	157.7	0.2	2.8
CARM _{NIR}	0.96 – 1.71	46.1	46.2	48.0	0.1	4.2
NIR	0.83 – 2.35	36.9	36.9	38.2	0.1	3.6

into solving a linear system of equations:

$$\begin{cases} \alpha + \beta + \gamma = 0 \\ -\beta h_d + \gamma h_s = 1 \\ \beta h_d^2 + \gamma h_s^2 = 0 \end{cases}$$

which result in the approximation of the gradient of the central values to be

$$\frac{\partial f(x_i)}{\partial x} = \frac{h_s^2 f(x_i + h_d) + (h_d^2 - h_s^2) f(x_i) - h_d^2 f(x_i - h_s)}{h_s h_d (h_d + h_s)} + \mathcal{O}\left(\frac{h_d h_s^2 + h_s h_d^2}{h_d + h_s}\right).$$

If the spectrum is evenly spaced, $h_s = h_d$ reduces to the standard second order CFD approximation:

$$\frac{\partial f(x_i)}{\partial x} = \frac{f(x_{i+1}) - f(x_{i-1})}{2h} + \mathcal{O}(h^2).$$

Applying this to the situation presented here, similar to Equation 8.25, results in:

$$\frac{\partial A_0(i)}{\partial \lambda(i)} = \frac{\lambda(i-1)^2 A_0(i+1) + (\lambda(i+1)^2 - \lambda(i-1)^2) A_0(i) - \lambda(i+1)^2 A_0(i-1)}{\lambda(i-1)\lambda(i+1)(\lambda(i+1) + \lambda(i-1))}, \quad 2 \leq i \leq n-1$$

with an uncertainty of $\mathcal{O}\left(\frac{\lambda(i+1)\lambda(i-1)^2 + \lambda(i-1)\lambda(i+1)^2}{\lambda(i+1) + \lambda(i-1)}\right)$.

The `numpy.gradient()` function implements central differences for the interior points, accurate to second order, and first order accurate one-sided (forward or backward) differences at the boundaries, computed using the same compact difference procedure.

Figure 8.3 visualizes two small spectral regions with the gradients computed with the original FFD

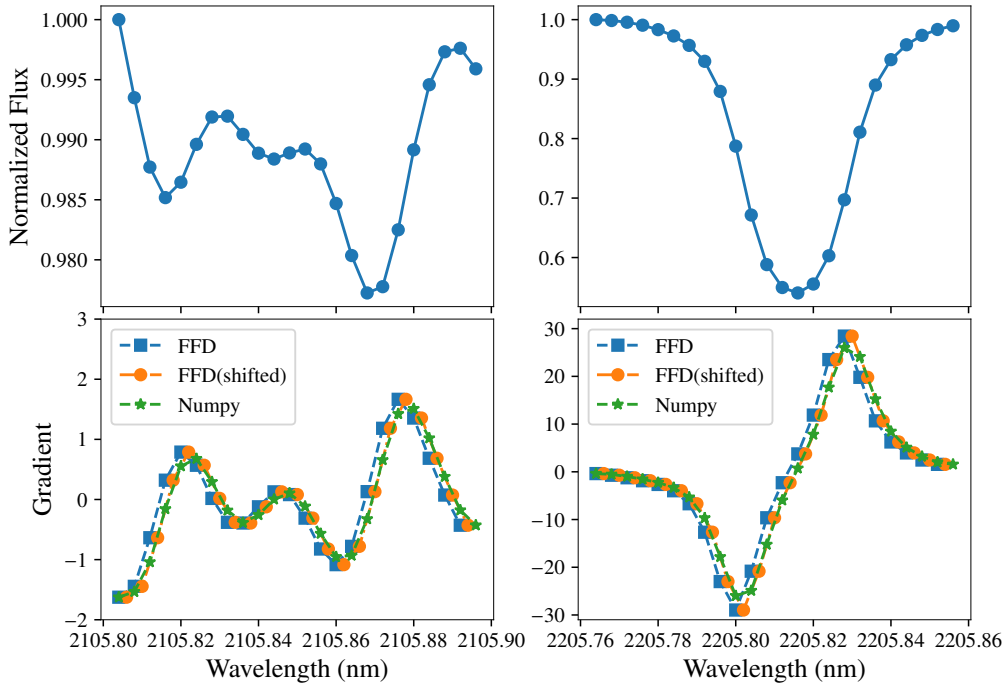


Figure 8.3: Visualization of the numerical gradient of some spectral lines. Top: The two spectral regions of a stellar spectrum: the left hand side contains short lines near the normalized continuum while on the right a single deep absorption line is shown. Bottom: The numerical gradients for the spectra shown in the top panels: the original FFD method is displayed with *blue squares* while NumPy gradient is shown with *green stars*. The *orange circles* are the FFD version shifted to the mid-points between pixels for illustrative purposes.

and the `numpy.gradient()` methods. The top panels contain a small section of a simulated spectrum, comprised of three small blended lines, and a large single line respectively. The derivative of the spectrum for the FFD method (blue squares) and `numpy.gradient()` method (green stars) are shown in the bottom panels. The *orange circles* are the same as the FFD method but shifted horizontally to the midpoints between the pixels for which the gradient is calculated at. This is for illustrative purposes and to assess the effect of this offset when calculating the pixel weights.

There are three notable features observed between gradient methods. The first, which is expected from the FFD formulation is that the FFD gradient is offset to the left by half of a pixel. The second is that when the horizontal offset is adjusted (orange circles) the two gradients lie along the same curve. Both methods are trying to approximate the real gradient function of the spectrum so it is expected that they should agree. The most important feature observed in this though is that there is a slight over-estimate of the gradient by the FFD method at the peak of each extrema. The points of highest gradient are always from the FFD method (blue/orange). This is the case for all spectral lines and as the optimal pixel weights are proportional to the gradient squared the FFD method will apply slightly higher pixel weights to these values, two points per line in the spectrum. Therefore, the FFD gradient produces a slightly smaller δV_{RMS} error compared to the more precise gradient function.

The numerical differences between the gradient methods on the relative RV precisions is given in Table 8.1. The δV_{RMS} is calculated using both gradient methods on a PHOENIX-ACES spectrum with $T_{\text{eff}}=3900\text{ K}$, corresponding to M0 spectral type. The full theoretical precision is calculated (no telluric masking applied) with no rotational or instrumental broadening and with the maximum of the continuum of each band scaled to 1. In this case the RV precisions are not comparable between bands and are used only to assess the direct effect of the numerical gradient. The band names and the spanned wavelengths are given along with the RV precision calculated with different gradients in columns A, B, and C. A is the original FFD method, B is the FFD method offset by $\Delta\lambda$, and C is the `numpy.gradient()`. The δV ratios are the relative difference in RV when changing from method A (the original FFD) to methods B and C.

As the pixel weights from Equation 8.8 are proportional to λ^2 , column B was computed to assess the affect of the slight wavelength offset on the RV precision, visible in Figure 8.3. Table 8.1 shows that wavelength offset of $\Delta\lambda/2$ contributes 0.1–0.6% to the RV precision values, an order of magnitude smaller than the change from A to C. Changing from the FFD method to `numpy.gradient()` to use the gradient from NumPy, increases the δV_{RMS} by 2.5–7%, decreasing the RV precision. After ruling out the wavelength offset with B, it is assumed that this difference is due mainly to the over-estimated gradient from the FFD method, shown in Figure 8.3

Changing the method of numerical derivatives will change all the precision values given in Figueira et al. (2016). This has a small impact on the precision compared to other components of the RV precision. For instance from Equation 8.15 an increase in δV_{RMS} of between 2.5–7% could equally be caused by a small decrease in the SNR from 100 (the value used in Figueira et al. (2016)) to between 95–98.

The current version of the software is now implemented with the gradient method provided by the NumPy package, and as such there is a small difference in RV precision values calculated, compared to Figueira et al. (2016).

8.4.1 Masking Function

Another change made to the software is in the application of the masking function, and the treatment of telluric lines. As suggested in Connes (1985) and Bouchy et al. (2001) a custom masking function can be applied to the individual pixel weights in Equation 8.8, such as:

$$W'(i) = W(i)\mathcal{M}(i), \quad (8.26)$$

where $\mathcal{M}(i)$ is the masking function and $W'(i)$ are the modified pixel weights. This masking function can be used in particular for the removal of telluric lines, setting those weights to zero and is in essence what is done when wavelength selection is performed: zero weight is assigned to all pixels outside the desired wavelength range.

This masking function can be used to easily apply the three conditions presented in Figueira et al. (2016). The three masking functions incorporated into *eniric* are defined here, followed by the quantification of how they differ from the previous implementation. The subscripts on the masking functions \mathcal{M} correspond to the three conditions.

$$\mathcal{M}_1(i) = 1 \quad (8.27)$$

$$\mathcal{M}_2(i) = \begin{cases} 0, & T(i) < \tau \\ 1, & T(i) \geq \tau \end{cases} \quad (8.28)$$

$$\mathcal{M}_3(i) = T(i)^2 \quad (8.29)$$

Here, $T(i)$ is the telluric transmission spectrum, while τ is the transmission depth cut-off. For instance to mask out telluric lines deeper than 2% the value of τ would be set at 0.98.

- Condition #1: The first mask, \mathcal{M}_1 , is the simplest case in which all pixel weights are treated equally. No telluric line masking is considered, and the full theoretical precision of the spectrum is obtained.
- Condition #2: In the second mask, \mathcal{M}_2 , the telluric line transmission, $T(i)$ is used to create a boolean mask of 0's and 1's. When applying this mask to the pixel weights, the pixels that are affected by telluric lines are given a weight of 0, removing their contribution to δV_{RMS} . Accounting for seasonal variation in Earth's barycentric motion can be easily incorporated into this mask by increasing the width of the regions masked out.
- Condition #3: This condition assumes the application of perfect telluric correction in which variance (photon noise contribution) in the denominator of Equation 8.8 is amplified by the telluric correction. In Figueira et al. (2016) the pixel weighting for this condition becomes:

$$W(i) = \frac{\lambda^2(i)(\partial A_0(i)/\partial \lambda(i))^2}{A_0(i) + \sigma_D^2/T(i)^2} \quad (8.30)$$

As the telluric transmission spectrum is a division in the denominator it is equivalent to multiplying the pixel weights by a mask of the form \mathcal{M}_3 .

Having the three masks defined in this way makes the implementation of the pixel weight calculations simpler. In the original version there were three separate implementations, one for each condition. With

three separate functions there is more room for mistakes, which there was with Condition #2 as will be discussed in Section 8.4.3. In the new implementation there is a single function that calculates the pixel weights from the spectrum, which can incorporate a masking function. The three masks mentioned here are implemented and used, and there is even the option for a user defined pixel mask to be used.

8.4.1.1 Masking order

The order in which the masking is performed was found to affect the recovered RV precisions. That is, the application of weight masking must be applied to the spectrum only after the calculation of the pixel weights.

In the original implementation of Condition #2, the full spectral band was split into small wavelength regions (sub-spectra) in between the telluric lines, following the masking by \mathcal{M}_2 . The δV_{RMS} was calculated using the FFD gradient for each small region with the results combined as the error on the weighted average in Equation 8.17. Analytically this result is identical to masking out the pixel weights with \mathcal{M}_2 but, in practice, it is not when numerically implemented.

When the spectrum is split into many small sections the number of edges increases and so does the number of pixels affected by edge effects. As shown in Section 8.4 the FFD method only computes $n - 1$ gradients from n pixels: the last pixel is removed/lost. A spectrum split into m sub-spectra will therefore lose m pixels due to this edge effect. This is in contrast to computing the weights first and then masking or splitting the spectrum in which only 1 pixel from the full spectrum is lost with the FFD gradient. Even the `numpy.gradient()` is not immune to the edge effects in the sub-spectra when the spectral splitting is performed first. Although there are no pixels lost, the first and last pixels of each sub-spectra are computed using forward or backward differences, rather than central differences (as they would be in the full spectrum). Hence, the gradients obtained and subsequent pixels weights of the sub-spectra edge pixels are slightly altered due to the spectral splitting occurring first.

The effect of masking and splitting the spectrum before and after calculating the pixel weights is quantified in Table 8.2. The columns labelled *Split* represents splitting the spectrum before calculating the pixel weights, while the columns labelled *Mask* calculate all the pixel weights first and then apply the \mathcal{M}_2 mask. The difference in RV precision between both situations and for both gradient methods are provided. For the FFD gradient, changing the ordering of splitting/masking from before the weight calculation to after decreases (improves) the δV_{RMS} by 0.2–0.7%, while for `numpy.gradient()` the δV_{RMS} is increased but at an order of magnitude smaller than the FFD method, only between 0.01–0.13%. In this case the FFD method has a larger change observed due to the addition of the $n - 2$ pixels that were originally lost. With the `numpy.gradient()` all pixels are always included, and the end values only slightly change. The last column of Table 8.2 is the difference ratio between the *Mask* column of both gradient methods. These are consistent with the values obtained in Table 8.1 with the differences between the two gradient methods of 2–7%. This table also shows that the difference induced on the RV precisions from changing the order of weight calculation and masking is 1–2 orders of magnitude smaller than the change from the new gradient method.

Eniric has been adjusted to consistently apply the masking after the pixel weights are calculated, simplifying the implementation. This retains the most pixels, with the most accurate pixel weights (less edge effects). It has also been changed to only apply the \mathcal{M}_2 and not split the spectrum into small sub-spectra then perform the weighted error calculation of Equation 8.17. The functionality to perform the weighted error is still present and can be used to combine the RV precision of larger spectral chunks,

Table 8.2: Relative RV precision difference for Condition #2 due to spectral splitting and order of applying the pixel mask. The input parameters were for an M0 spectral type spectrum, with $v \sin i = 1.0$ and $R=100\,000$. The Δ ratios are the percentage difference between *Split* and *Masked* implementations while using the same gradient method. The last column is the ratio between the *Masked* implementations using the FFD and `numpy.gradient()` methods and are consistent with Table 8.1.

Gradient Band	Split m s^{-1}	Masked FFD m s^{-1}	Δ Ratio %	Split m s^{-1}	Masked NumPy m s^{-1}	Δ Ratio %	Masked Δ Ratio %
Z	7.42	7.38	-0.66	7.76	7.77	0.13	5.3
Y	4.75	4.74	-0.22	5.06	5.06	0.06	6.8
J	18.58	18.53	-0.29	19.57	19.57	0.01	5.6
H	6.08	6.05	-0.53	6.25	6.26	0.08	3.5
K	32.21	32.14	-0.22	33.48	33.49	0.05	4.2

such as the separate nIR bands or the different spectral orders in a cross-dispersed spectrograph.

The ordering of the masking does not affect the results of Condition #1 or #3 that were not split into sub-spectra to calculate the RV precisions. Although there are differences from the old and new implementation of Condition #2 (splitting to only masking) the differences observed between Figueira et al. (2016) and this work are dominated by a found bug, see Section 8.4.3.

8.4.2 SNR scaling

For the analysis of relative synthetic spectral precision between different spectra, a common reference point is needed. Similarly to Figueira et al. (2016) in Section 8.2.4 this is achieved by normalizing the synthetic spectra to a specific SNR per resolution element level at a particular wavelength. However, unlike Figueira et al. (2016), this is not held fixed at $\text{SNR}=100$ in the middle of the *J*-band at $1.25\,\mu\text{m}$.

Eniric now contains an automated SNR scaling procedure (Equation 8.31), to remove the need for the hard-coded scaling values, and extends the precision calculations to any SNR, sampling, and wavelength specifications.

The procedure first identifies the wavelength value λ' to perform the scaling at; this can be either a user defined wavelength value, or more commonly the centre of a user selected band is automatically computed from the configured band limits. The number of pixels within one resolution element λ/R , is defined by the sampling, s , used to interpolate the spectrum Section 8.2.3. The photons within one resolution element are calculated by summing s pixels, ($N = \sum^s A_0$), centred on λ' . The current SNR of the resolution element is calculated as $\text{SNR} = \sqrt{N}$ assuming a large N . A scaling factor, SF , is defined so that when it is multiplied by the spectrum, the SNR of the resolution element at λ' becomes the desired value, $\text{SNR}_{\text{desired}}$:

$$SF = \frac{\sqrt{\sum^s A}}{\text{SNR}_{\text{desired}}}. \quad (8.31)$$

Automating the calculation of the scaling factor enabled several new scenarios to analyse the relative precisions, not previously possible. Four are given here:

- The ability to easily analyse new spectral models, not just the four spectra corresponding to M0,

M3, M6, M9 spectral types, which scaling factors had been manually calculated for.

- The ability to scale to a SNR per pixel value other than 100.
- Allow for the correct scaling when a different sampling, s , is used. Not just restricted to $s=3$.
- Allow for relative precisions to be referenced to a different band or wavelength. Results are not limited to being referenced relative to the J -band.

This last point is of note as it allows the relative precisions not to be tied to a single band, allowing the testing of different SNR values achievable at different wavelengths. For instance, all RV precisions can now be calculated relative to a given SNR at the centre of the K -band. This was important for computing Figueira et al. (2016)-like precisions requested for the NIRPS and SPIRou Exposure Time Calculators (ETC). NIRPS specifically requested precision values at a SNR relative to the individual bands (the precision of the K -band spectrum relative to SNR=100 at the centre of the K -band), while SPIRou requested precisions relative to the J - and H -bands only. These calculations were not easily possible in the original code version, and this extension has made computations for different SNR level and reference points easy to calculate, with minimal configuration.

The default values set in *eniric* match the Figueira et al. (2016) value, a $s=3$ and SNR=100 in the J -band. The centre of each band was visually checked to ensure that default, central band reference locations did not coincide with a spectral line. If the reference point was automatically chosen at the centre of an absorption line, then the counts N would be lower and the spectrum would be scaled to a higher continuum. This would artificially decrease (improve) the δV_{RMS} recovered. At rest, the centres of the Z -, Y -, J -, H -, and K -bands as defined in Table 4.1 do not coincide with a spectral line. However, if any Doppler shifting is performed to move the spectral lines, then care must be taken to ensure the correct scaling is applied to the continuum.

As shown in Equation 8.15 the RV precision is inversely proportional to the SNR level. To access the relative RV precision of any of the values calculated at a different SNR level you can apply the following:

$$\delta V_{\text{SNR}_2} = \delta V_{\text{SNR}_1} * \frac{\text{SNR}_1}{\text{SNR}_2}, \quad (8.32)$$

where δV_{SNR_1} is the relative precision calculated at SNR_1 and δV_{SNR_2} is the new precision if observed instead with a SNR of SNR_2 .

8.4.3 Atmospheric masking bug

Applying testing practises of Section 8.3.1 during the extension of *eniric* revealed an error in the application of Condition #2 in Figueira et al. (2016). When the telluric line mask was broadened to account for the barycentric motion of the Earth, and a requirement requiring three consecutive pixels (the sampling rate) to exceed the cut-off limit to be considered masked out, there was a software bug. This meant that the masking applied for Condition #2 was incorrect and not physically meaningful. It essentially randomly masked portions of the spectra, not physically meaning full to the treatment of the telluric lines. The synthetic spectra did not have telluric line contamination themselves, but the proportion and location spectrum supposed to be mask to represent telluric contamination masking applied was incorrect.

A check for this issue was discovered using this unit test (Listing 8.1), written under the pytest framework. Essentially, this takes a given transmission (telluric line) spectrum and creates a telluric mask

at a line depth of 2%. It then transforms the mask by the function `barycentre_broaden()`, the function under test here, which performs the $\pm 30 \text{ km s}^{-1}$ barycentre broadening to account for the yearly motion of the Earth, and consecutive pixel check. The assert statement performs the actual test, checking that if the new broadened mask is applied to the original transmission spectrum, then all values are greater or equal to the masking limit. That is, the telluric lines are still completely masked out.

This is not the only test required to sufficiently test the “correctness” of `barycentre_broaden()`, but it is a simple unit test¹⁶ that would have caught the bug that was present.

Listing 8.1: Example unit test to catch the masking bug. The assert statement checks that the mask continues to remove all telluric lines deeper than 2%.

```
def test_telluric_masking(wavelength, transmission):
    """Check the mask still masks out all telluric lines > 0.98 after
    broadening the mask to account for the barycentre motion."""
    mask = telluric_mask(transmission, depth=0.98)      # Create mask
    mask = barycentre_broaden(wavelength, mask)          # Extend mask
    assert numpy.all(transmission[mask] >= 0.98)       # Assert condition
```

Due to this bug the published RV precision values for Condition #2 in Figueira et al. (2016) are all incorrect. As the masking was unevenly applied the new “correct” RV precision values do not all change in the same direction or in the same proportion. For example, the largest difference is seen in the *J*- and *K*-bands, with changes over 20 m s^{-1} , while other wavelength bands are essentially unchanged. The differences can be seen in the shaded areas of Figure 8.4 comparing the Figueira et al. (2016) results to the updated values, with the upper edge defined by Condition #2. Even though there is an error with the values of Condition #2 they do not change the overall conclusions of the paper.

8.5 RV precision update

As detailed in the Section 8.3 updating the software introduced several changes that affect the RV precisions values slightly, the numerical gradient, and the masking order for Condition #2 and more importantly the bug also found with Condition #2.

The 180 spectral combinations from Figueira et al. (2016), are repeated here using *eniric* to have an updated and corrected table of relative RV precisions. This table is given in Table A.1, calculated using the PHOENIX-ACES spectra and also the BT-Settl models.

The precision changes are visually represented in Figure 8.4 by comparing Figure 1 of Figueira et al. (2016) (top) to the updated precisions using *eniric* with the PHOENIX-ACES (bottom-left) and BT-Settl (bottom-right) models. Each panel shows the precision achieved as a function of spectral band for stars with a rotational velocity of $v \sin i = 1.0 \text{ km s}^{-1}$ and spectral types M0 (3900 K), M3 (3500 K), M6 (2800 K), and M9 (2600 K). The dashed line represents the theoretical limits imposed by Condition #1, and the filled area represents the values within the limits set by Conditions #2 (circles) and #3 (triangles); blue, green, and red represent the results obtained for resolutions of 60 000, 80 000, and 100 000, respectively. The spectra were normalized to have a SNR of 100 per resolution element as measured at the centre of the *J*-band.

¹⁶ A unit test only tests single specific piece of code or functionality at a time.

Figueira et al. (2016)

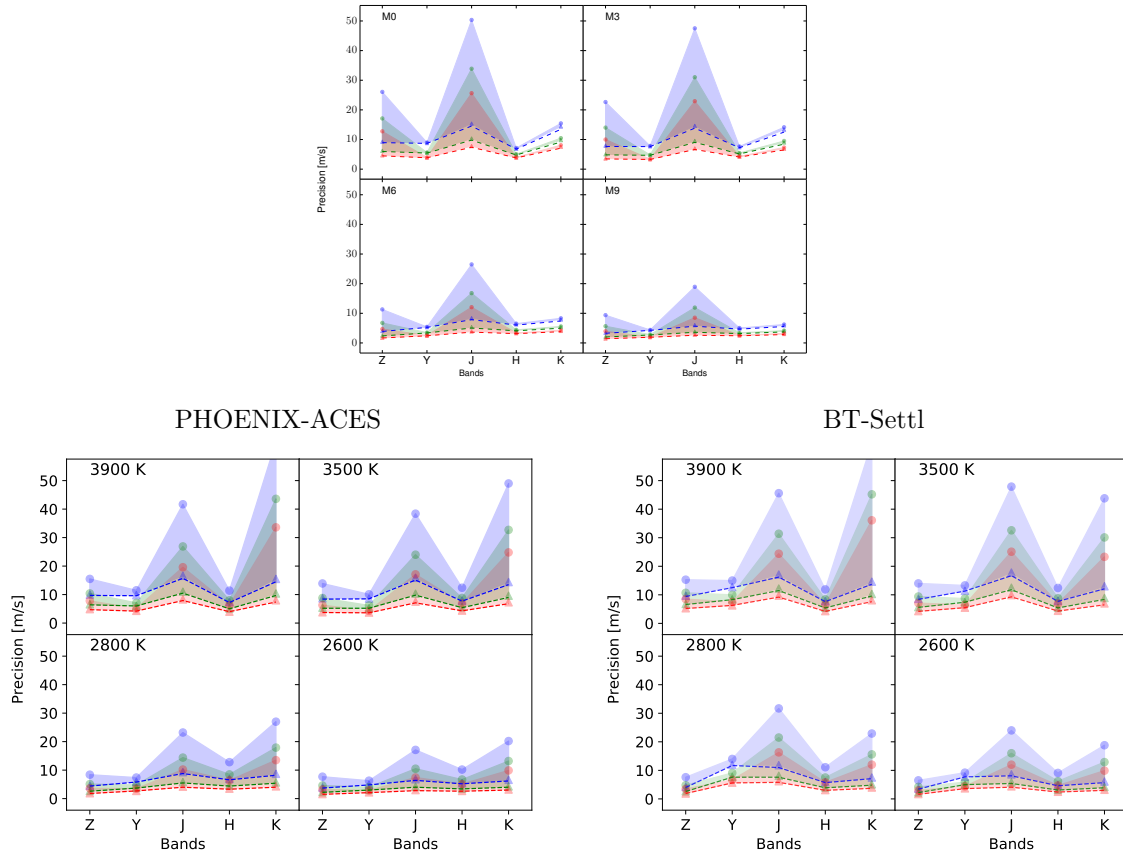


Figure 8.4: Comparison of the updated precision values to the original values. Top: Figure 1 from Figueira et al. (2016). Bottom: Updated precision values computed using *eniric* using the PHOENIX-ACES (left) and the BT-Settl (right) models. Each panel shows the precision achieved as a function of spectral band for stars with a rotational velocity of $v \sin i = 1.0 \text{ km s}^{-1}$ and spectral types M0 (3900 K), M3 (3500 K), M6 (2800 K), and M9 (2600 K). The dashed line represents the theoretical limits imposed by Condition #1, and the filled area represents the values within the limits set by Conditions #2 (circles) and #3 (triangles); blue, green, and red represent the results obtained for resolutions of 60 000, 80 000, and 100 000, respectively. The spectra were normalized to have a SNR of 100 per resolution element as measured at the centre of the *J*-band.

The values for Condition #1 and #3 only have small differences which is barely noticeable, while Condition #2 has large band dependant changes, shown by the change in the shaded areas. For example note that Z and J -band RV precisions decrease with the new results, while the K -band gets substantially worse. This occurs because the software did not mask many of the regions affected by telluric lines, where as in the new results, a significant portion is masked out due to the overlap of telluric lines, leading to a higher δV_{RMS} value. The H -band also sees a small increase in δV_{RMS} .

As stated previously the discovery of the bug affecting telluric masking does not change the conclusions of Figueira et al. (2016). These updated PHOENIX-ACES values will be published in an upcoming work as an amendment to the Figueira et al. (2016) values.

In comparing the bottom two panels between the PHOENIX-ACES and BT-Settl models, there are only small differences, most identifiable in the Condition #2 values of the J -band. This shows again that the PHOENIX-ACES and BT-Settl models are fairly consistent. This was also visually observed in Section 4.2.4.

8.6 Metallicity and $\log g$

With the ability to explore a wider range of parameters the range of PHOENIX-ACES models were extended to explore the affect of $\log g$ and [Fe/H] on the relative RV precision. Remember that $\log g$ is a measure of the stellar surface gravity, the gravitational acceleration at the equator expressed in cgs units of cm s^{-2} then taking the logarithm of base-10. The surface gravity is $g \propto \frac{M}{R^2}$ so larger $\log g$ values correspond to stars with smaller radii. While the metallicity, [Fe/H], is a measure of the abundance of elements heavier than Hydrogen and Helium, it is often measured as the ratio of Iron to Hydrogen relative to the Sun. That is a [Fe/H]=0 has the same metal ratio as the Sun, a positive [Fe/H] has more metals, and a negative [Fe/H] has less metals than the Sun. The higher abundance of metals creates stronger absorption lines.

Eniric was used to compute the spectral quality factor, Q (Equation 8.14), and RV precision for all PHOENIX-ACES models with $\log g$ between 4.0–5.5 and [Fe/H] between -1–1, inclusive. The spectral factor is used for the comparison following Artigau et al. (2018) in which it was used to compare between models, and observed spectra, independent of the flux levels. Since Q is inversely proportional to δV_{RMS} a higher Q is better.

The spectral quality factor variations for the M-dwarfs M0, M3, M6, M9, with a broadening of $R=100\,000$ and $v \sin i = 1.0 \text{ km s}^{-1}$ across the NIR bands is shown in Figure 8.5. The top row shows the quality for model spectra with a fixed $\log g=4.5$ but having a variable [Fe/H] between -1.0 to 1.0. The bottom row shows the opposite: a fixed [Fe/H]=0.0 while the $\log g$ is varied between 4 and 5.5. The five separate plots in each row represent the NIR wavelength bands $Z-K$ and the four different coloured lines are the different M-dwarfs (blue M9, orange M6, green M3, red M0).

Multiple effects are observed in this figure which are identified below, organized into the separate bands. Note that the cooler M-dwarfs (M6, M9) almost consistently have higher spectral quality factors, corresponding to lower δV_{RMS} (improved relative precision), if observed at the same relative SNR level, as can be seen in Figure 8.4.

- Z -band

The Z -band has a large separation in spectral quality due to spectral type, this is because the continuum of the Z -band is severely eroded in the spectra of late M's as they cool. Each spectral

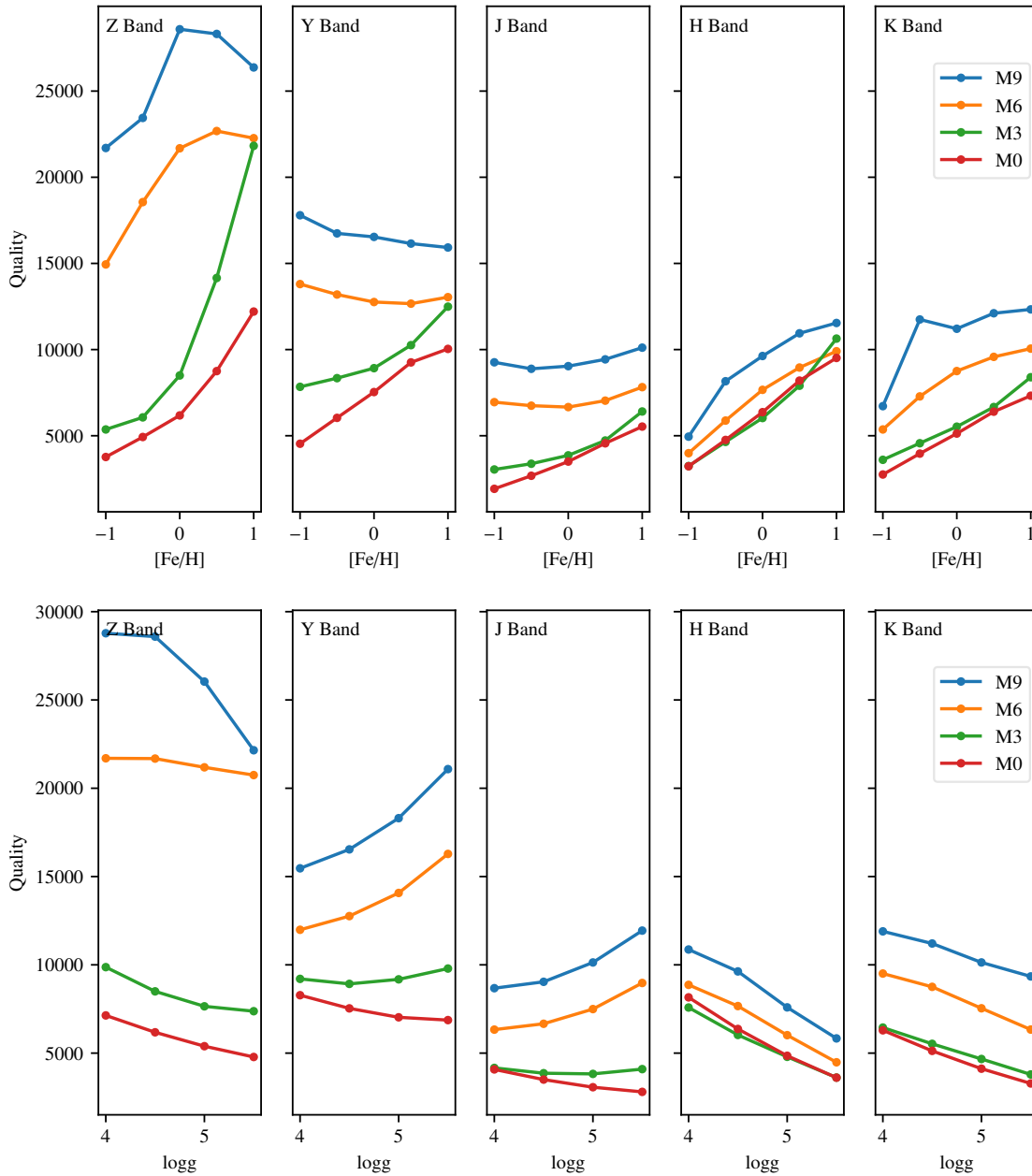


Figure 8.5: Quality factor changes across spectral type and bands for variations in $[Fe/H]$ and $\log g$. Broadening values are $R=100\,000$ and $v \sin i=1.0\,km\,s^{-1}$. Top: Quality factor variation of $[Fe/H]$ between -1.0 to 1.0 at a fixed $\log g=4.5$. Bottom: Quality factor variation of $\log g$ between 4 and 5.5 with fixed $[Fe/H]=0.0$. Note a higher quality factor corresponds to an increased RV precision.

type also behaves very differently to a change in [Fe/H] and $\log g$. For M0 and M3 there is a small increase with increasing [Fe/H] below solar metallicity; above solar metallicity the slopes of the lines dramatically increase, especially for M3 where the quality more than doubles between a [Fe/H] value of 0.0 to 1.0. For M6 and M9 there is a sharp decrease in quality as [Fe/H] falls below solar metallicity (0.0). The quality seems to peak between [Fe/H]=0.0–0.5 and begins to decrease at higher metallicity.

As $\log g$ increases in the Z -band there is a decrease in spectral quality. There is a consistent and large separation between early and late M's that. The quality for M6 is very shallow, while for M9 the quality is nearly flat for $\log g=4.0$ and 4.5 but then decreases sharply at higher $\log g$.

- Y -band and J -band

The spectral quality in the Y -band is interesting, as the quality appears to converge and diverge with increasing [Fe/H] and $\log g$ respectively. For M0 and M3 there is an increase in quality as the metallicity increases in both bands, while for M6 and M9 there is a decrease in quality in the Y -band, converging together beyond [Fe/H]=1.0. In the J -band the M6 and M9 are almost flat with a gentle decrease then increase in quality.

For the $\log g$ variation the opposite occurs. As the $\log g$ increases from 4.0 to 5.5 M0 has a small gradual decrease in the spectral quality with M3 remaining relatively flat. M6 and M9 both increase with increasing $\log g$ so overall there is a divergence in the spectral quality at a larger $\log g$ in both bands.

- H -band and K -band

The H -band and K -band also have similar patterns between [Fe/H], $\log g$ and quality for all spectral types, with only a small change between the different spectral types. The spectral quality increases fairly consistently as [Fe/H] increases and decreases with an increase in $\log g$. There does however, appear to be one point that looks out of place in the M9 spectrum with [Fe/H]=-0.5.

Looking at the bigger picture, there is a striking difference in the quality between the bands. For the M0 and M3 spectra the quality mostly stays under 10 000, apart from a four points in the Z and Y -bands at high [Fe/H]. For the cooler M6 and M9 quality values however there is a large contrast between the Z and Y -bands, which have a much higher quality, and the other three bands which have a similar quality level.

This difference in spectral quality in the Z -band becomes apparent when visualizing the spectra. The Z -band and J -band spectra for all four spectral types from Figueira et al. (2016) are reproduced here in Figure 8.6. They show flux as a function of wavelength in the Z -band (top) and J -band (bottom) for a $v \sin i=1.0 \text{ km s}^{-1}$ and spectral types M0, M3, M6, and M9 (*top to bottom* panels), when seen at a resolution of 100 000. The Z -band has substantial erosion of the continuum in the M6 and M9 spectra, compared to the other spectra, even of the same spectral type. The higher number of lines in the M8 and M9 spectra show why the spectral quality is higher.

This work begins to reveal how the spectral parameters $\log g$ and [Fe/H] begin to affect the RV precision obtained. It shows that there are some fairly consistent trends at the longer wavelength bands, but in the Z -, H -, and J -bands the effect clearly also depends on the spectral type. This is just the first look into the relationships between [Fe/H] and $\log g$ in relation to the spectral quality.

With the possibility to simply compute the quality and precision of a large range of synthetic spectral parameters, a comparison of spectral quality over all synthetic spectra or just all in the M-dwarf

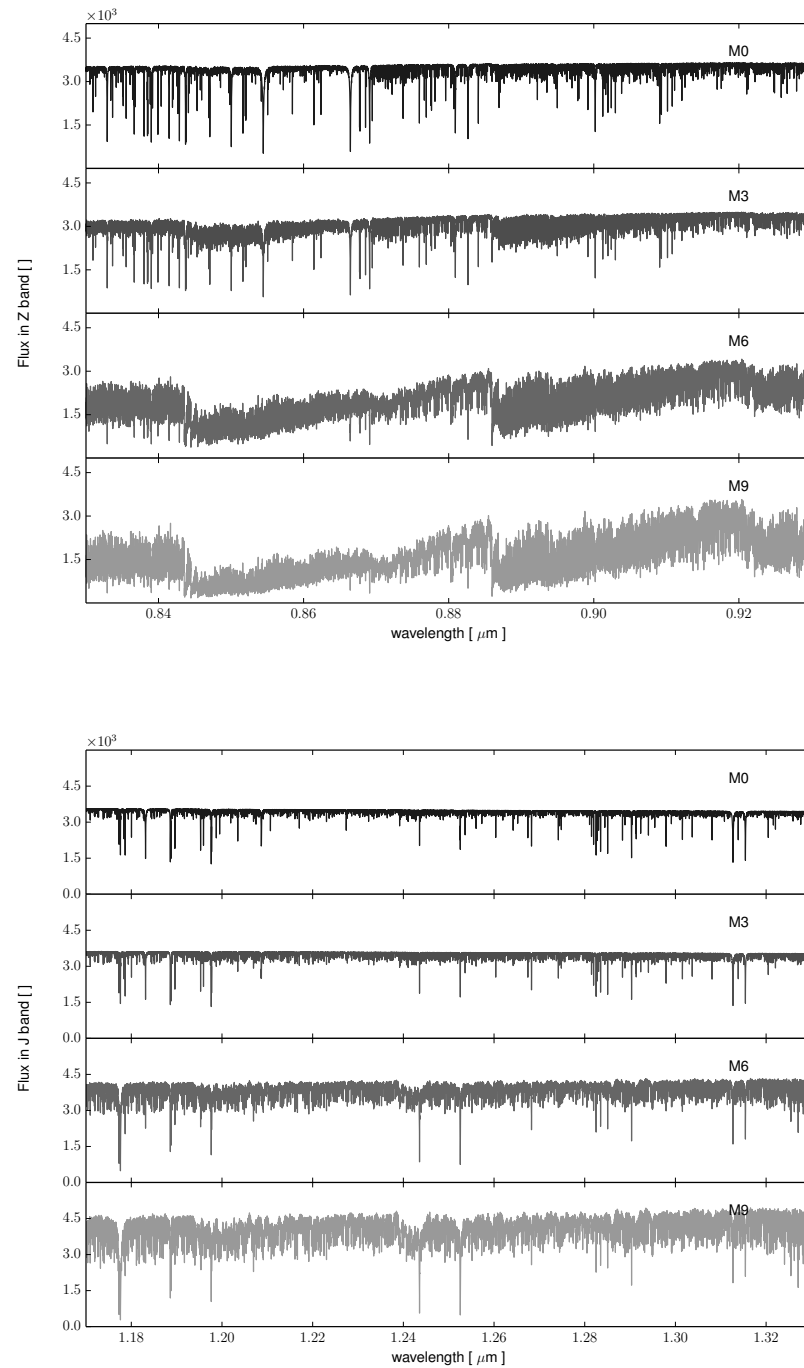


Figure 8.6: Flux as a function of wavelength in the *Z*-band (top) and *J*-band (bottom) for the $v \sin i = 1.0 \text{ km s}^{-1}$ and spectral types M0, M3, M6, and M9 (*top to bottom* panels), when seen at a resolution at 100 000. Flux units are arbitrary. Reproduced from Figueira et al. (2016).

temperature range, may help solidify or extend the trends observed here. For example, this work has yet assessed the spectral quality when both [Fe/H] and $\log g$ are changed together.

In the context of selecting M-dwarf targets for RV measurements, if the goal is to achieve a high spectral quality, then it follows from Figure 8.5 that generally for M0-M3 spectral types, and in the H - and K -band, an observation of a metal-rich ($[\text{Fe}/\text{H}] > 0$) M-dwarf with a lower $\log g$ value would have a higher spectral quality. In practise, the spectral quality is only one component to the precision, and probably the more important, and observer adjustable, contribution to spectral precision is the number of photons counted (or the SNR achieved). For cool M6 and M9 spectral types this is important as longer exposure times are needed to achieve a similar SNR level due to their lower luminosity.

8.7 SPIRou and NIRPS ETC

Having *eniric* as a tool to calculate RV precisions efficiently lead to contributions to the Exposure Time Calculators (ETC) for both the SPIRou and NIRPS spectrographs. In this way the expected radial velocity precision of the targets can be estimated and provided to those preparing to observe with these spectrographs. The calculations were performed at the individual request of both instruments.

In September 2017 *eniric* was used to provide precision calculations for the SPIRou ETC¹⁷. These were the same spectral parameters as Figueira et al. (2016) except with the precisions for each band referenced to SNR=100 in its own band. The modification of Section 8.4.2 was made to fulfil this request. These values are given in Table A.2.

In May 2018 *eniric* was used to provide precision calculations for the NIRPS ETC. This extended the spectral range from M0, M3, M6, M9 at 3900, 3500, 2800, 2600 K respectively, to all temperatures between 2500 K and 4000 K inclusively. This provides a finer resolution coverage over the M spectral type, allowed by the PHOENIX-ACES library. Instrumental resolutions of 75 000 and 100 000 were requested to match the NIRPS instrument. The $\log g$, metallicity, and sampling rate remained at the Figueira et al. (2016) levels of 4.5, 0.0 and 3.0 respectively. Precisions were provided for SNR of 100 relative to the J - and H -bands as well as to each band individually. Artigau (*priv. comm.* 2018) suggested the truly relevant values would be the SNR in H -band for NIRPS instrument. The values calculated for NIRPS are given in Table A.3.

The resulting tables, along with the command line incantations to produce them are detailed in Appendix A.

¹⁷ http://www.cfht.hawaii.edu/Instruments/SPIRou/SPIRou_etc.php

8.8 Application to CARMENES spectra

One of the main reasons for focusing on extending the work of Figueira et al. (2016) was to analyse the differences in RV precision of synthetic spectra and observed nIR. This is important for the community to understand the accuracy of synthetic spectra. Artigau et al. (2018) recently found band-specific discrepancies in the theoretical precision between real and synthetic nIR spectra of Barnard’s Star. In 2018 CARMENES openly released a spectral library containing one spectrum for each target in their 324 M-dwarf RV survey in Reiners et al. (2018). With this they provide details on the empirical δV_{rms} measured during their RV processing with their RV analysis code, SERVAL (Zechmeister et al., 2018), using all available spectra of each target. Spectra from this library has been used to compare the theoretical precision of observed CARMENES spectra to synthetic models, and is still in the preliminary stages, with the progress so far demonstrated here.

8.8.1 Target selection

To analyse the precision in different spectral types, a few specific M-dwarfs were selected. These were selected from the 324 spectra of the CARMENES M-dwarf library from Reiners et al. (2018) available at <http://carmenes.cab.inta-csic.es/gto/>, along with the achieved SNR in the visible and nIR spectra.

The spectral library data was downloaded, divided into spectral type and ordered by the stated nIR SNR, to select targets at the high SNR end. To cover the M-dwarf range, targets were selected near each of the spectral types M0, M3, M6 and M9. For each spectral type (within ± 0.5) two stars are selected that have high SNR values. This will give eight spectra over the M-dwarf range to analysis. One of the two selected targets for the M3 type is Barnard’s star which has been analysed extensively in Artigau et al. (2018), in particular with CRIRES spectra for the nIR domain, allowing for direct comparisons between the two works. The other criteria used for selection was to select targets with a varied range of $\log g$ and [Fe/H] values if possible.

The selected targets from the CARMENES library are provided in Table 8.3. The spectral parameters (T_{eff} , $\log g$, [Fe/H]) for these targets are from Passegger et al. (2018) and Rajpurohit et al. (2018) who performed spectral fits of the CARMENES spectra with the PHOENIX-ACES and BT-Settl models respectively. The uncertainties in the Rajpurohit et al. (2018) parameters are $\sigma_{T_{\text{eff}}}=100 \text{ K}$, $\sigma_{\log g}=0.3$, and $\sigma_{[\text{Fe}/\text{H}]}=0.3$ while the uncertainties on the Passegger et al. (2018) values are $\sigma_{T_{\text{eff}}}=51 \text{ K}$, $\sigma_{\log g}=0.07$, and $\sigma_{[\text{Fe}/\text{H}]}=0.16$. There are gaps in the Passegger et al. (2018) values for stars that have the lower SNR levels as they are more difficult to analyse/fit. Neither one has parameters for Luyten’s Star, for which the parameters given are from SIMBAD.

Table 8.3: Selected CARMENES targets with stellar parameters from both Rajpurohit et al. (2018) and Passegger et al. (2018).

Karmn	Name	SpT	V mag	SNR _{nIR}	Rajpurohit et al. (2018)			Passegger et al. (2018)		
					T _{eff} K	log g cm s ⁻²	[Fe/H]	T _{eff} K	log g cm s ⁻²	[Fe/H]
J20533+621	BD+61 2068	M0.5	8.6	257	3900	5.5	-0.5	3828	4.71	0.03
J04290+219	BD+21 652	M0.5	8.3	212	4000	5.5	0.5	4194	4.59	0.20
J07274+052	Luyten's Star	M3.5	9.9	254	3467 ^a	-	-0.1 ^a	-	-	-
J17578+046	Barnard's Star	M3.5	9.5	236	3400	5.5	0.1	3278	5.10	-0.12
J11055+435	WX UMa	M5.5	14.5	140	3000	5.5	0.3	-	-	-
J10564+070	CN Leo	M6.0	13.5	133	2900	5.4	0.1	-	-	-
J18356+329	LSR J1835+3259	M8.5	18.3	50	2400	5.0	-0.1	-	-	-
J04198+425	LSR J0419+4233	M8.5	11.1	42	2400	4.9	0.1	-	-	-

^a From SIMBAD.

8.8.1.1 Spectral preparation and Telluric correction

The spectra in the CARMENES library have not been corrected for telluric lines. To properly assess the theoretical RV precision attainable in the CARMENES spectra they need to be corrected for telluric lines. Telluric correction is performed with the Molecfit software (Smette et al., 2015) in collaboration with Soléne Ulmer-moll, who has Molecfit experience (Ulmer-Moll et al., 2018).

The separate spectral orders first need to be combined into a single spectrum. At this stage, where spectral orders overlap only the flux from one order is kept for simplicity. The overlapping regions could be combined by taking the mean because the overlapping orders are well aligned in wavelength, but this was not performed at this exploratory stage.

The telluric correction is performed by dividing the CARMENES spectrum by a telluric transmission spectrum fitted with Molecfit. The fitting with Molecfit has been attempted two different ways. The first correction performs the fitting on the full nIR spectrum, while the second splits the spectrum into three parts and fits them separately. This was done because it was noticed that the spectral line shape changes significantly from $0.9\text{ }\mu\text{m}$ to $1.7\text{ }\mu\text{m}$.

Different molecules are fitted in the three separate parts. In the first part (0.9 – $1.1\text{ }\mu\text{m}$) H_2O is fitted, in the second (1.1 – $1.5\text{ }\mu\text{m}$) O_2 is fitted while CO_2 and CH_4 are fitted in the third section (1.5 – $1.71\text{ }\mu\text{m}$). After this all molecule abundances are fixed and the final fit is performed on each of the three parts.

In the end, splitting the spectrum into three does not seem to improve the telluric correction considerably. The telluric spectrum fitted from both attempts is shown in the top panel of Figure 8.7. The difference between the two telluric spectra changes is shown in the bottom panel.

It is unknown whether the full telluric correction of the CARMENES nIR spectrum has been performed before. There has been one publication known which uses Molecfit to correct a CARMENES spectrum, but only in a very narrow spectral range (1.082 – $1.084\text{ }\mu\text{m}$) (Allart et al., 2018). As such there is not yet a definitive guide to achieve the best telluric correction of CARMENES spectra with Molecfit.

In this work only one spectrum has been telluric corrected to compare the difference between the two Molecfit corrections and their improvement over complete telluric masking on spectral quality and RV precision. This was to see if it is worth investing time to improve the telluric correction step.

After telluric correction the spectrum was corrected for bad pixels by linear interpolation across them. Some examples of bad pixels can be seen in a narrow wavelength range in Figure 8.8. The lines with orange circles and green crosses are the original and telluric corrected spectra, respectively. They both show individual bad pixel spikes throughout the spectrum. The black line is the spectrum corrected from the bad pixels (labelled ‘fixed’) for the bad pixels. The blue line is a “quality flag” output (0 or 1) from Molecfit, indicating where the spectrum has a flux below or equal to zero. It correctly identifies one of the bad pixels but not the others that have a flux above zero. Within the Y -, J -, and H -bands there are around $213/66069 \sim 0.3\%$ bad pixels identified with an automated algorithm, based on a maximum derivative threshold (the bad pixels have very high derivatives).

The removal of bad pixels, which introduce pixels with very high derivatives (and pixel weight, $W(i)$), is essential for an accurate computation of the spectral quality and RV precision. The sharp lines with high derivatives would artificially increase the calculated spectral quality, Q , masquerading as very deep and narrow spectral lines.

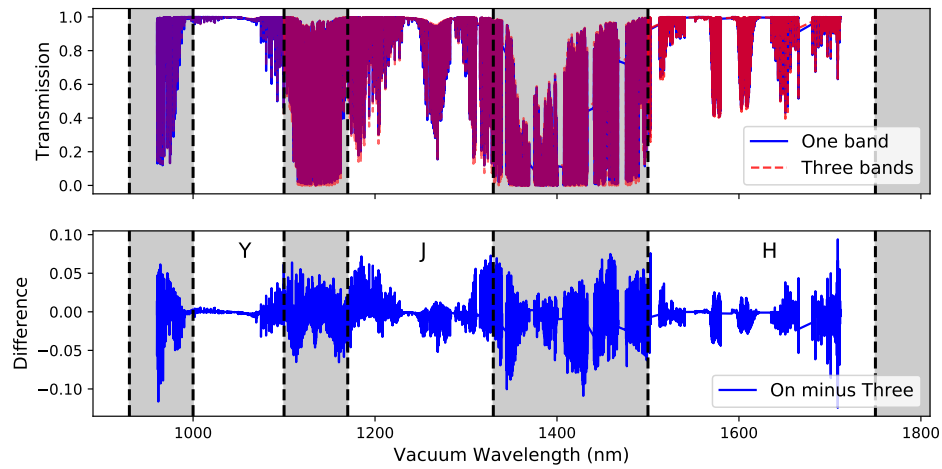


Figure 8.7: Comparison of telluric models in pursuit of a better correction. Top: The two synthetic telluric spectra. The blue shows the result from Molecfit after treating the full spectrum as one, while the shaded red telluric spectrum has been derived with three separate bands, fitted individually. Bottom: The difference in the telluric spectrum between the fit to the full spectrum, and the fit with the spectrum split into three. The regions of deep H_2O absorption lines which defined the nIR bands are shaded grey. The bounds of each band from Table 4.1 are indicated with vertical black dashed lines.

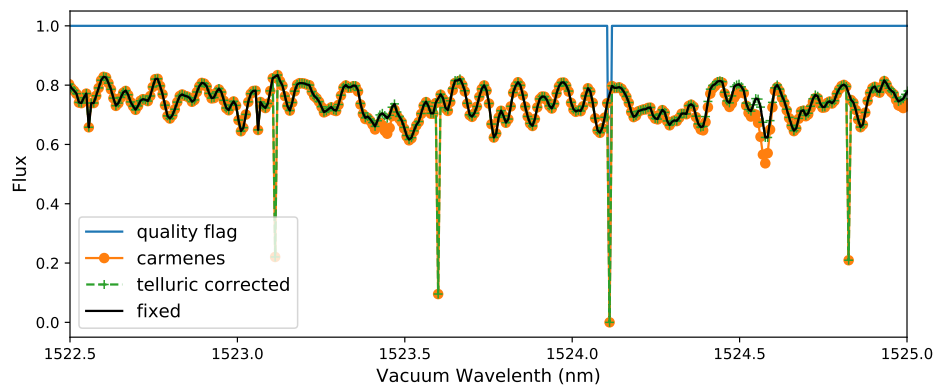


Figure 8.8: Removal of bad pixels from the CARMENES spectrum. The orange line with circles and green line with pluses are the original and telluric corrected spectra from CARMENES. The black solid line shows the spectrum after correction from bad pixels. The blue line shows the “quality flag” (0 or 1) output from the Molecfit software.

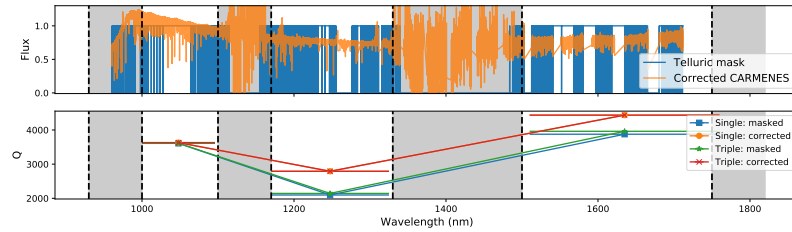


Figure 8.9: Measured spectral quality, Q , in the three nIR bands of Barnard’s star to assess the gain from telluric correction. Top: The telluric corrected CARMENES spectrum (orange) along with the binary mask for telluric lines $>2\%$ depth (blue). Bottom: The spectral quality in the three spectral bands, for different telluric treatment. ‘single’ indicates the Molecfit results from the single fit to the spectrum, while ‘triple’ indicates the fit to the three wavelength bands. ‘masked’ indicates that telluric masking of the lines deeper than 2% was performed and while ‘corrected’ is just the telluric corrected spectrum.

8.8.2 Impact of telluric correction

Here the impact of the telluric correction on the spectral quality of the CARMENES spectrum is assessed. This was done by calculating, Q , with the original telluric lines deeper than 2% masked out, and with the telluric correction performed. This was done for both fitting methods attempted with Molecfit and displayed in Figure 8.9. The top panel shows the telluric corrected spectrum (orange) along with the telluric mask that was applied (blue). The bottom panel shows the spectral quality for the three spectral bands Y , J , and H .

Figure 8.9 shows that there is a benefit (gain in quality) from telluric correction in the J and H -bands, where there are numerous telluric lines. However, in the Y -band where there is little telluric masking performed there is only a slight gain. Performing telluric correction of the CARMENES spectra over telluric masking causes a gain the the spectral quality by 1%, 30%, 12% in the Y -band, J , and H -bands respectively. As the spectral quality is related to the RV precision, this will lead to a 10-30% improvement in the RV precision in the J - and H -bands. This indicated that it is worth performing telluric correction on the other seven CARMENES targets selected. This also shows that the extra effort from three separate telluric fittings does not lead to a significant gain in quality.

8.8.3 Barnard’s star

Currently only Barnard’s star has had the telluric correction performed, and as such the analysis for this target is shown. The spectral content of Barnard’s star was extensively explored in Artigau et al. (2018) comparing the synthetic model to observations from HARPS, ESPaDOns and CRIRES in the range 380–2300 nm. Agreement was found in the optical but the nIR bands had significant differences between the observations and models. The goal of this analysis is to check if the same results are obtainable in the CARMENES spectrum of Barnard’s star.

(Artigau et al., 2018) tabulated several literature values for the stellar properties of Barnard’s star and identified the closest matching PHOENIX-ACES model. The synthetic model adopted for Barnard’s star is $T_{\text{eff}}=3200$ K, $\log g=5.0$, and $[\text{Fe}/\text{H}]=-0.5$. This same model was adopted here. This is tabulated in with other parameters from Artigau et al. (2018) in Table 8.4.

A series of spectra are shown in Figure 8.10. The uncorrected CARMENES spectrum of Barnard’s

Table 8.4: Properties of Barnard’s star from (Artigau et al., 2018). T_{eff} , [Fe/H] and $\log g$ values are only the adopted (closest) model parameters.

Parameter	Value
SpType	M4 Ve
Rotation Period	~ 130 days
$v \sin i$	$\leq 80 \text{ m s}^{-1}$
T_{eff}	3200 K
$\log g$	5.0
[Fe/H]	-0.5

Star is shown in the first panel. The second panel shows telluric model from Molecfit, while the third panel shows the telluric corrected spectrum. In the telluric corrected spectrum there are several deep spikes which are bad pixels. Most of these are corrected for in the fourth panel, although it appears there may be a few still present in the spectrum. The fifth panel contains the synthetic PHOENIX-ACES spectrum of Barnard’s star, used to compare the spectral quality. The model has been convolved by an instrumental profile with $R=80\,400$, but not rotationally broadened since the $v \sin i$ is low. The flux units of the spectra are arbitrary, and the synthetic model has been converted into photon counts.

To compare the model to the observation it is interpolated to the pixel positions of the CARMENES spectrum. The spectral quality is calculated for both on small wavelength bins with a width 0.2% the central wavelength similar to (Artigau et al., 2018). The top panel of Figure 8.11 shows the results of the comparison, with the spectral quality in 0.2% λ width bins for the observation (orange squares) and the model (blue stars) in the top panel. The ratio between the spectral quality of the observation and the model is given in the bottom panel. It shows that in this instance the Y - and J -bands have a similar spectral quality, while there is a large difference in the H -band with the CARMENES observation having a spectral quality 3–4× greater than the model.

Figure 8.12 from (Artigau et al., 2018) is shown for comparison. In the Y - and J -bands ?? obtains a lower spectral quality (50%) compared to the model. However in this work the model and observation have a similar spectral quality in these bands, although the ratio does drop to 50% in the latter apart of the J . In the H -band of both works the observed quality is higher then the model, however the CARMENES spectral quality is 3× higher, instead of only 1.5× in (Artigau et al., 2018). This is a significant difference.

(Artigau et al., 2018) only apply telluric masking in their analysis, whereas here the telluric corrected spectra were used. This could be part of the reason for the largely improved results in the H . As shown in Section 8.8.2 the telluric correction can improve the quality by 12–30%. However, this does not fully explain the increase by a factor of 2. This requires further investigation.

8.8.3.1 Future tasks

These results are still preliminary analyses, and a few things can be improved. For instance the observed and model spectra have not yet been Doppler shifted to the same frame. A Doppler shift of a few nm is unlikely to affect the results shown in Figure 8.11 significantly. There are also a few bad pixels that are still present in the observation that should be properly removed.

Adding the analysis of several CARMENES spectra across the M-dwarf range would be an important

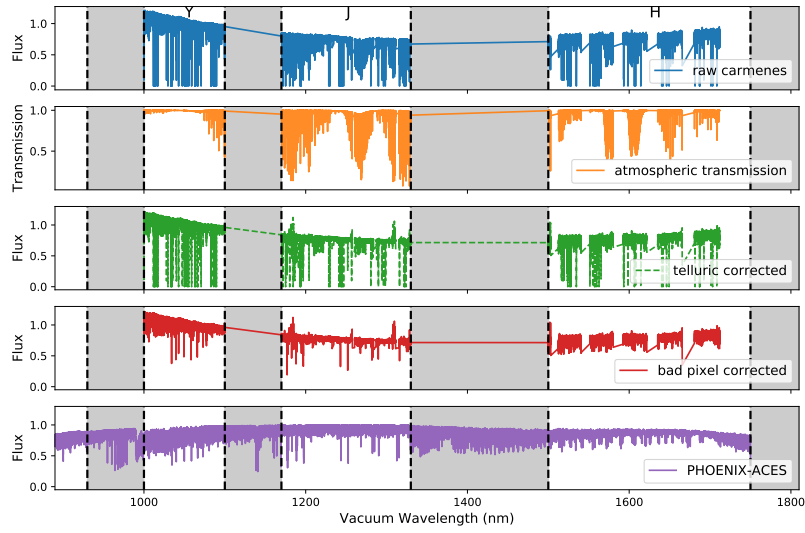


Figure 8.10: Telluric correction of the CARMENES nIR spectrum. First: Uncorrected spectrum of Barnard’s Star between 960–1710 nm from CARMENES. Second: The synthetic telluric transmission spectrum fitted with Molecfit. Third: Telluric corrected spectrum by division of the telluric spectrum. The regions of deep H_2O absorption lines which defined the nIR bands are shaded grey. Fourth: The telluric corrected spectra after the bad pixels are removed. Fifth: Synthetic PHOENIX-ACES model for Barnard’s star, convolved to $R=80\,400$. The bounds of each band from Table 4.1 are indicated with vertical black dashed lines. The flux units of the spectra are arbitrary

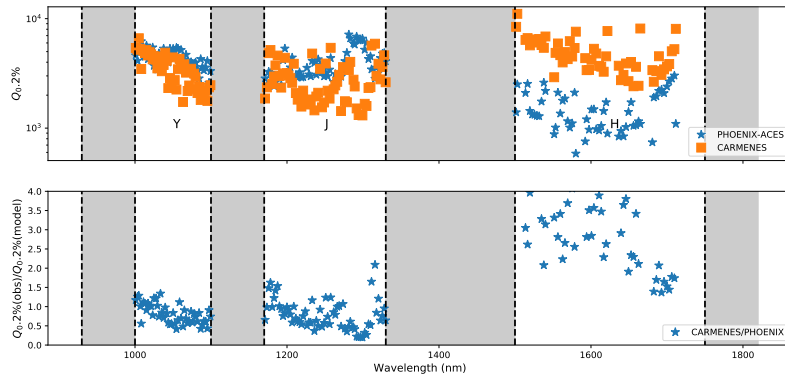


Figure 8.11: Measured RV content of Barnard’s star over the near-infrared domain, from CARMENES. Top: The spectral quality in $0.2\% \lambda$ width bins for CARMENES (orange squares) and the model (blue stars). Bottom: The ratio of spectral quality observed/model.

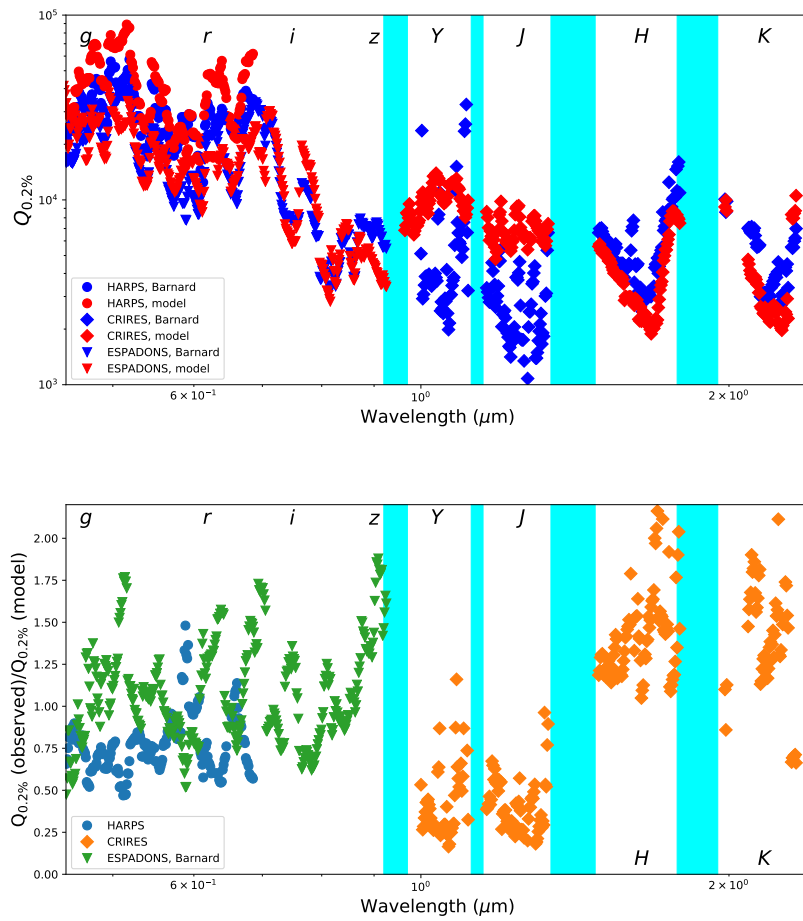


Figure 8.12: Measured RV content of Barnard’s star over the optical and near-infrared domain. Overall measured (blue) and model (red) RV density are well matched blueward of $\sim 1\mu\text{m}$. The agreement is poorer in the near-infrared domain with an over-prediction of RV content in Y and J bands and an under-prediction in H and K . Bottom: Ratio of observed to model $Q_{0.2\%}$ values. Areas unusable for RV measurements because of strong telluric absorption are filled in light blue. Reproduced from Artigau et al., 2018.

addition to this work to see if these results are consistent for all spectra, or if they are dependant on the stellar parameters.

8.9 Summary

Significant advancements in the *eniric* software have been made to expand and simplify the computation of synthetic RV precision. This software has been used to begin exploring the effect of $\log g$ and [Fe/H] on the spectral precision of M-dwarfs, as well as comparing the RV precision of synthetic spectra to observed M-dwarf spectra from CARMENES. Open to the community, it is available to aid in RV precision calculations.

Chapter 9

Conclusions

This work aimed at pushing down the detection limit of faint companions, using high resolution near-infrared spectra. Two methods, differential subtraction and χ^2 spectral recovery, were explored with many limitations uncovered in the observations and methods.

The objective of the observations acquired in this program was to apply the spectral differential technique. Unfortunately, due to operational reasons, the required conditions for this method were not met, in particular a sufficient RV separation. When two insufficiently separated observations were subtracted to mutually cancel the spectrum of the host, the spectra of the faint companions were also mutually cancelled, diminishing the amplitude and increasing the difficulty of detection.

An alternative χ^2 spectral recovery method was developed, which ended up revealing different difficulties. This fitted the observed spectra with a binary model comprised of two synthetic spectra.

During the preparation of the observed spectra two different reduction pipelines were compared. The DRACS pipeline was favoured over the ESO pipeline due to its ability to reduce spectra in a consistent manner. However, artefacts were found in the DRACS reduced spectra pipeline in individual nods due to the optimal extraction. The individual nod spectra with artefacts were replaced by their rectangularly extracted counterparts as they introduced errors into the combined spectra at the level of 2%, larger than the expected signal of companion spectra.

A discrepancy between the models and the observed spectra in the nIR negatively affected the recovery performance of the synthetic recovery technique on the observed spectra, while injection-recovery simulations at a SNR=300 were unable to correctly recover the companions below ~ 3800 K at a companion/host flux ratio of 5–15%. With both methods a successful detection of the BD companions in nIR was not achieved.

This work highlights many of the difficulties when dealing with the spectral recovery of nIR spectra. The obstacles to overcome include the data reduction of nIR CMOS detectors, that are not yet at the level of visible CCDs, along with a precise telluric correction and wavelength calibration (two interrelated aspects, as previously discussed). Another important aspect is the discrepancy between nIR high-resolution spectra and the observed spectra. In spite of the continuous effort of the modelling community, this work, along with several cited contemporary ones, shows that this mismatch is still one of the main factors preventing proper spectral recovery in the nIR. This work highlights that this is a compound problem for Brown Dwarfs, for which the spectral models are less informed due to lack of observations at high-resolution.

Other than the improvement of the spectral models, the observing community can increase their odds of success by paying attention to the scheduling of observations and the wavelength domains to explore. This work shows that observing in the areas of lower telluric absorption, as is frequently done, is not a guarantee of success due to the scarcity of deep lines in cold objects.

This work also made improvements to software used to compute the RV precision of synthetic spectra, publishing and releasing *enric* openly. This work identified and corrected problems with the previous results, and extended the ability of the software to analyse all available spectra in the PHOENIX-ACES and BT-Settl synthetic libraries. This was used to provide relative RV precision values for the NIRPS and SPIRou instruments, tailored to each instrument by request. This also allowed for the exploration of the affect of $\log g$ and [Fe/H] on the spectral quality of the synthetic models, with the identification of band-specific trends in the quality.

Preliminary analysis into the comparison between observed CARMENES spectra and synthetic models were performed for Barnard’s Star finding similar results to other works in which the observed spectral quality in the *J* band is lower than the model quality, but higher than the model in the *H*. In the CARMENES case the spectral quality in the *H*-band is $3\times$ that of the model. Performing telluric correction also gains about 10–30% improvement in the spectral quality over telluric masking in the *J* and *H*-bands. The other chosen targets are still to be analysed due to difficulties in the telluric correction of CARMENES.

9.1 Future prospects

Although not successful with the CRIRES data used here, with many high-resolution nIR spectrographs becoming available, the instrumental stage is set to attempt the techniques presented here using the next-generation of high resolution spectrographs. For instance, the upgrade of CRIRES to CRIRES+ will increase the wavelength coverage of a single shot capture by at least a factor of 3–5. This larger wavelength span would be extremely beneficial for the χ^2 performance of the spectral recovery method, increasing the number of useful lines and spectral features to be fitted with the models.

From this work it is clear that tighter constraints need to be placed on the observations, with a large RV separation ideally at both extrema. This potentially requires taking observations in separate observing periods. These methods would benefit not only from a longer wavelength range but also from observations at a wavelength that has more stellar lines and spectral information. For instance, the wavelength region around $2.3\,\mu\text{m}$ is popular, due to a large number of stellar CO lines. Longer exposure times would be needed to achieve higher SNR as it has been shown here that a SNR of 100–300 was not sufficient to recover the faint companions.

On the modelling side, there are continual improvements in atmospheric modelling and their associated synthetic spectral libraries as seen with the evolution of the PHOENIX-based models. With additional physics and improved line lists and solar abundances, the synthetic libraries are reaching a better agreement with nIR observations. An improved agreement between the nIR observations and synthetic spectra in the future will be crucial to improve the performance of the spectral recovery technique presented here.

Other recent data-driven methods (e.g. Piskorz et al., 2016; Czekala et al., 2017) have shown more promising results to disentangle binary spectra, even down to planetary companions. They are more advanced than the differential subtraction method but both require a series of observations at high SNR.

The differential method may still be useful when only two observations can be obtained, provided a sufficient separation and SNR.

The RV precision of the M-dwarfs, particularly in the nIR, is still highly important in the community with several new nIR spectrographs and RV surveys being started. With the vast growth in the number of nIR spectra that will be obtained, there will be plenty of opportunity to contrast the obtained precisions to the theoretical spectra. In depth comparison between the precision of synthetic and observed M-dwarf spectra still needs to be preformed across the M-dwarf range. *Eniric* can aid in this by providing a simple way to perform RV precision computations. One opportunity currently available is to continue with the analysis of the CARMENES spectra.

Another opportunity made possible with *eniric* is to attempt to use machine learning techniques to model the relations between the RV precision (or spectral quality) and the spectral and observational parameters. One could envision several tens of thousands of RV precisions being calculated from the synthetic spectral library, altering not only the spectral parameters, (T_{eff} , $\log g$, [Fe/H], [α /Fe]) but also λ , R , $v \sin i$ and SNR. This could be used to build a predictive model to estimate the RV precision for a star with parameters different from the library grid, observed with an arbitrary spectrograph. This would also enable any correlations between the parameters, such as seen with $\log g$ and [Fe/H] to be identified, and confirm the theoretical relationship with R . With the large growth in machine learning technologies and libraries available this could be implemented relatively easily.

The future of exoplanetary detection and characterization is promising. It is hoped that this work can act as a guide for the planning of future observations of faint BD and planetary companions with the upcoming generation of high resolution spectrographs in the near- and mid- infrared.

Appendix **A**

RV Precision Tables

The updated relative RV precision (σ_{RV} or dV_{RMS}) results attainable from nIR spectra are presented in the following tables. Table A.1 shows the precision results for the same M-dwarfs analysed in Figueira et al. (2016). That is stellar temperatures 3900, 3500, 2800, 2600 K corresponding to spectral types M0, M3, M6, M9 respectively, $\log g=4.5$ and $[Fe/H]=0.0$. The rotation applied are $v \sin i=1, 5, 10 \text{ km s}^{-1}$ and instrumental profiles with $R=60\,000, 80\,000, 100\,000$.

Columns 2–4 contain the RV precision calculated using PHOENIX-ACES spectra, as done in Figueira et al. (2016). These values differ from two effects. There is small difference in Conditions #1 and #3 from the change in numerical differentiation implemented (see Section 8.4). The values for Condition 2 however, are completely different due to the implementation error in the telluric masking discovered (see Section 8.4.3).

In columns 5–7 are the same RV precision calculation but using the BT-Settl spectral library instead (with same spectral parameters), a recent addition in *eniric*.

The PHOENIX-ACES RV precisions in Table A.1 can be created with *eniric* using the following shell incantation (after installation and configuration):

Listing A.1: Command line incantation to calculate the PHOENIX-ACES RV precisions; with comments.

```
phoenix_precision.py -t 3900 3500 2800 2600 \
                     -l 4.5 -m 0.5 \
                     -r 60000 80000 100000 \
                     -v 1.0 5.0 10.0 \
                     -b Z Y J H K \
                     --snr 100 \
                     --ref_band J \
                     --model aces
```

Temperature
Logg and Metalicity
Resolutions
Rotational velocities
Wavelength bands
Relative SNR
SNR reference band
Spectral model

Eniric was also used to calculate RV precision for the NIRPS and SPIRou. For SPIRou the requested precisions were provided with the SNR relative to the centre of each individual band. The values are provided in Table A.2 and can be generated with the following code; note the change in the ‘ref_band’ parameter.

Listing A.2: Shell incantation for the SPIRou ETC RV precisions.

```
phoenix_precision.py -t 3900 3500 2800 2600 -l 4.5, -m 0.5 \
-r 60000 80000 100000 -v 1.0 5.0 10.0 -b Z Y J H K      \
--snr 100 --ref_band self
```

Changing the reference band for the SNR scaling increases and decreases the precision in different bands due to the shape of the spectral profile. Comparing the precision values between Table A.1 and Table A.2, it has the effect of decreasing the σ_{RV} (increasing precision) in the H - and K -bands while increasing the σ_{RV} (decreasing precision) in the Z - and Y -bands. The RV precision for the J -band remains unchanged, so is not included in Table A.2.

For the NIRPS spectrograph, RV precisions with an instrumental resolution of 75 000 was requested to match the NIRPS instrument, and provided relative to the J - and H -bands. The results for the NIRPS precision relative to the J -band are given in Table A.3, and can be reproduced with the following code.

Listing A.3: Shell incantation for the NIRPS ETC RV precisions.

```
phoenix_precision.py -t 3900 3500 2800 2600 -l 4.5, -m 0.5 \
-r 60000 75000 80000 100000 -v 1.0 5.0 10.0           \
-b Z Y J H K --snr 100 --ref_band J                  \
```

Table A.1: RV precisions for the PHOENIX-ACES and BT-Settl synthetic spectral libraries. The PHOENIX-ACES values given here are the updated version of Table A.1 of Figueira et al. (2016). The RV precisions are calculated relative to a SNR=100 at the centre of the J -band for the simulation parameters given.

Simulation (SpTp - Band - $v \cdot \sin i$ - R)	PHOENIX-ACES			BT-SETTL		
	σ_{RV}	σ_{RV}	σ_{RV}	σ_{RV}	σ_{RV}	σ_{RV}
	Cond. 1	Cond. 2	Cond. 3	Cond. 1	Cond. 2	Cond. 3
[m/s]	[m/s]	[m/s]	[m/s]	[m/s]	[m/s]	[m/s]
3900-Z-1.0-60k	9.7	15.5	10.0	9.4	15.3	9.7
3900-Z-1.0-80k	6.4	10.4	6.6	6.6	10.7	6.8
3900-Z-1.0-100k	4.7	7.8	4.9	5.2	8.5	5.3
3900-Z-5.0-60k	14.2	22.6	14.6	13.0	21.0	13.4
3900-Z-5.0-80k	10.9	17.6	11.3	10.1	16.4	10.5
3900-Z-5.0-100k	9.2	14.8	9.5	8.6	13.9	8.9
3900-Z-10.0-60k	24.5	38.6	25.3	21.8	35.1	22.4
3900-Z-10.0-80k	20.3	32.2	21.0	18.1	29.2	18.7
3900-Z-10.0-100k	17.8	28.2	18.3	15.9	25.6	16.3
3900-Y-1.0-60k	9.6	11.5	9.8	12.5	15.0	12.7
3900-Y-1.0-80k	6.0	7.1	6.0	8.3	10.0	8.4
3900-Y-1.0-100k	4.2	5.1	4.3	6.3	7.5	6.3
3900-Y-5.0-60k	15.5	18.4	15.7	18.6	22.3	18.9
3900-Y-5.0-80k	11.6	13.8	11.8	14.3	17.0	14.4
3900-Y-5.0-100k	9.7	11.5	9.8	11.9	14.3	12.1
3900-Y-10.0-60k	30.8	36.8	31.2	34.8	41.6	35.2
3900-Y-10.0-80k	25.2	30.1	25.5	28.6	34.3	29.0

Table A.1: continued.

Simulation	PHOENIX-ACES			BT-SETTL		
	σ_{RV}	σ_{RV}	σ_{RV}	σ_{RV}	σ_{RV}	σ_{RV}
Cond. 1	Cond. 2	Cond. 3	Cond. 1	Cond. 2	Cond. 3	
3900-Y-10.0-100k	21.8	26.0	22.1	24.9	29.9	25.2
3900-J-1.0-60k	15.7	41.7	16.6	16.2	45.6	17.1
3900-J-1.0-80k	10.5	26.9	11.0	11.5	31.4	12.2
3900-J-1.0-100k	7.9	19.6	8.3	9.2	24.4	9.7
3900-J-5.0-60k	22.7	63.6	24.0	21.8	65.6	23.1
3900-J-5.0-80k	17.5	48.1	18.5	17.1	50.2	18.2
3900-J-5.0-100k	14.8	40.3	15.6	14.6	42.1	15.4
3900-J-10.0-60k	38.6	122.9	41.0	35.4	122.3	37.7
3900-J-10.0-80k	32.0	100.7	34.0	29.5	100.5	31.4
3900-J-10.0-100k	28.0	87.6	29.8	25.9	87.5	27.6
3900-H-1.0-60k	7.2	11.4	7.4	7.6	11.9	7.8
3900-H-1.0-80k	5.0	8.0	5.1	5.4	8.4	5.5
3900-H-1.0-100k	4.0	6.3	4.0	4.2	6.6	4.3
3900-H-5.0-60k	10.1	15.9	10.3	10.8	16.8	11.0
3900-H-5.0-80k	7.9	12.4	8.0	8.3	13.1	8.5
3900-H-5.0-100k	6.6	10.5	6.8	7.0	11.0	7.2
3900-H-10.0-60k	17.5	27.3	17.9	18.8	29.4	19.2
3900-H-10.0-80k	14.5	22.7	14.9	15.6	24.4	16.0
3900-H-10.0-100k	12.7	19.9	13.0	13.6	21.3	14.0
3900-K-1.0-60k	14.5	63.7	15.5	13.7	63.2	14.6
3900-K-1.0-80k	9.7	43.6	10.4	9.6	45.2	10.3
3900-K-1.0-100k	7.4	33.6	8.0	7.6	36.1	8.1
3900-K-5.0-60k	21.7	90.3	23.2	19.4	85.4	20.8
3900-K-5.0-80k	16.6	70.0	17.7	15.0	67.0	16.1
3900-K-5.0-100k	13.9	59.2	14.8	12.6	56.9	13.5
3900-K-10.0-60k	39.4	155.8	42.1	34.2	142.8	36.6
3900-K-10.0-80k	32.6	128.9	34.9	28.4	118.5	30.4
3900-K-10.0-100k	28.5	112.5	30.5	24.8	104.0	26.6
3500-Z-1.0-60k	8.4	13.9	8.7	8.4	14.0	8.6
3500-Z-1.0-80k	5.2	8.8	5.4	5.6	9.4	5.7
3500-Z-1.0-100k	3.7	6.3	3.8	4.2	7.1	4.3
3500-Z-5.0-60k	13.2	21.3	13.6	12.3	20.1	12.7
3500-Z-5.0-80k	10.0	16.4	10.3	9.4	15.5	9.7
3500-Z-5.0-100k	8.3	13.6	8.6	7.9	13.0	8.2
3500-Z-10.0-60k	24.6	39.1	25.4	21.9	35.1	22.5
3500-Z-10.0-80k	20.3	32.4	20.9	18.1	29.1	18.6
3500-Z-10.0-100k	17.6	28.2	18.2	15.8	25.4	16.3
3500-Y-1.0-60k	8.5	10.1	8.6	11.3	13.3	11.4

Table A.1: continued.

Simulation	PHOENIX-ACES			BT-SETTL		
	σ_{RV}	σ_{RV}	σ_{RV}	σ_{RV}	σ_{RV}	σ_{RV}
Cond. 1	Cond. 2	Cond. 3	Cond. 1	Cond. 2	Cond. 3	
3500-Y-1.0-80k	5.2	6.2	5.2	7.4	8.7	7.4
3500-Y-1.0-100k	3.6	4.3	3.7	5.5	6.5	5.5
3500-Y-5.0-60k	13.9	16.5	14.1	17.1	20.2	17.3
3500-Y-5.0-80k	10.4	12.3	10.5	13.0	15.3	13.1
3500-Y-5.0-100k	8.6	10.2	8.7	10.9	12.8	11.0
3500-Y-10.0-60k	28.2	33.5	28.5	32.4	38.4	32.8
3500-Y-10.0-80k	23.0	27.3	23.3	26.7	31.5	27.0
3500-Y-10.0-100k	19.9	23.6	20.1	23.2	27.4	23.5
3500-J-1.0-60k	15.1	38.4	15.9	16.7	47.9	17.8
3500-J-1.0-80k	9.8	24.0	10.3	11.8	32.6	12.5
3500-J-1.0-100k	7.1	17.1	7.5	9.3	25.1	9.9
3500-J-5.0-60k	22.5	60.2	23.8	22.9	69.2	24.4
3500-J-5.0-80k	17.3	45.4	18.3	17.9	52.9	19.0
3500-J-5.0-100k	14.5	37.8	15.3	15.2	44.4	16.2
3500-J-10.0-60k	39.9	117.8	42.4	37.9	129.4	40.5
3500-J-10.0-80k	33.0	96.4	35.1	31.5	106.4	33.7
3500-J-10.0-100k	28.8	83.7	30.6	27.6	92.6	29.5
3500-H-1.0-60k	7.7	12.4	7.9	7.7	12.4	7.9
3500-H-1.0-80k	5.4	8.8	5.6	5.4	8.8	5.5
3500-H-1.0-100k	4.3	6.9	4.4	4.3	6.9	4.4
3500-H-5.0-60k	10.7	17.1	10.9	10.9	17.5	11.2
3500-H-5.0-80k	8.3	13.3	8.5	8.4	13.5	8.6
3500-H-5.0-100k	7.1	11.3	7.2	7.1	11.4	7.3
3500-H-10.0-60k	18.1	28.7	18.5	19.5	31.4	20.0
3500-H-10.0-80k	15.0	23.9	15.4	16.1	26.0	16.6
3500-H-10.0-100k	13.1	20.9	13.5	14.1	22.7	14.5
3500-K-1.0-60k	13.5	49.0	14.4	12.1	43.8	13.0
3500-K-1.0-80k	9.0	32.7	9.6	8.4	30.1	8.9
3500-K-1.0-100k	6.8	24.8	7.3	6.5	23.3	7.0
3500-K-5.0-60k	20.4	71.7	21.7	17.6	62.6	18.8
3500-K-5.0-80k	15.5	55.2	16.5	13.5	48.4	14.4
3500-K-5.0-100k	13.0	46.4	13.9	11.4	40.8	12.1
3500-K-10.0-60k	37.5	126.6	39.9	31.8	109.6	34.0
3500-K-10.0-80k	30.9	104.6	33.0	26.3	90.7	28.1
3500-K-10.0-100k	27.0	91.3	28.8	23.0	79.3	24.6
2800-Z-1.0-60k	4.4	8.4	4.5	4.0	7.6	4.2
2800-Z-1.0-80k	2.6	5.1	2.7	2.6	4.8	2.7
2800-Z-1.0-100k	1.8	3.6	1.9	1.9	3.5	1.9

Table A.1: continued.

Simulation	PHOENIX-ACES			BT-SETTL		
	σ_{RV}	σ_{RV}	σ_{RV}	σ_{RV}	σ_{RV}	σ_{RV}
Cond. 1	Cond. 2	Cond. 3	Cond. 1	Cond. 2	Cond. 3	
2800-Z-5.0-60k	7.2	13.7	7.5	6.3	11.7	6.6
2800-Z-5.0-80k	5.4	10.3	5.6	4.8	8.8	4.9
2800-Z-5.0-100k	4.4	8.5	4.6	4.0	7.3	4.1
2800-Z-10.0-60k	14.6	27.3	15.2	12.6	22.8	13.0
2800-Z-10.0-80k	11.9	22.4	12.4	10.3	18.6	10.6
2800-Z-10.0-100k	10.3	19.3	10.7	8.9	16.2	9.2
2800-Y-1.0-60k	5.8	7.4	5.9	11.7	14.0	11.9
2800-Y-1.0-80k	3.7	4.8	3.8	7.6	9.1	7.7
2800-Y-1.0-100k	2.7	3.5	2.7	5.6	6.7	5.7
2800-Y-5.0-60k	8.7	10.7	8.8	17.7	21.3	17.9
2800-Y-5.0-80k	6.7	8.3	6.8	13.5	16.2	13.7
2800-Y-5.0-100k	5.6	7.0	5.7	11.3	13.6	11.4
2800-Y-10.0-60k	14.7	17.5	14.9	32.5	39.0	32.9
2800-Y-10.0-80k	12.2	14.6	12.4	26.8	32.1	27.1
2800-Y-10.0-100k	10.7	12.8	10.8	23.3	28.0	23.6
2800-J-1.0-60k	8.8	23.2	9.3	11.0	31.7	11.8
2800-J-1.0-80k	5.5	14.4	5.8	7.6	21.5	8.1
2800-J-1.0-100k	4.0	10.2	4.2	5.8	16.3	6.2
2800-J-5.0-60k	13.5	35.9	14.3	15.6	45.3	16.7
2800-J-5.0-80k	10.3	27.3	10.9	12.1	35.1	13.0
2800-J-5.0-100k	8.6	22.8	9.1	10.2	29.6	10.9
2800-J-10.0-60k	24.3	63.8	25.7	26.7	78.5	28.5
2800-J-10.0-80k	20.1	52.9	21.2	22.2	65.1	23.7
2800-J-10.0-100k	17.5	46.1	18.5	19.4	57.0	20.7
2800-H-1.0-60k	6.6	12.8	6.9	5.7	11.1	5.9
2800-H-1.0-80k	4.4	8.5	4.6	3.9	7.5	4.0
2800-H-1.0-100k	3.3	6.4	3.5	3.0	5.8	3.1
2800-H-5.0-60k	9.8	18.8	10.2	8.4	16.4	8.7
2800-H-5.0-80k	7.5	14.4	7.8	6.5	12.6	6.7
2800-H-5.0-100k	6.3	12.1	6.5	5.4	10.5	5.6
2800-H-10.0-60k	17.8	34.7	18.4	15.6	31.0	16.2
2800-H-10.0-80k	14.7	28.7	15.2	12.9	25.5	13.3
2800-H-10.0-100k	12.8	25.0	13.3	11.2	22.2	11.6
2800-K-1.0-60k	8.2	27.0	8.7	7.1	22.9	7.5
2800-K-1.0-80k	5.4	17.9	5.7	4.8	15.6	5.1
2800-K-1.0-100k	4.0	13.5	4.3	3.7	12.0	4.0
2800-K-5.0-60k	12.4	39.7	13.2	10.3	33.3	11.0
2800-K-5.0-80k	9.4	30.5	10.0	7.9	25.6	8.4

Table A.1: continued.

Simulation	PHOENIX-ACES			BT-SETTL		
	σ_{RV}	σ_{RV}	σ_{RV}	σ_{RV}	σ_{RV}	σ_{RV}
Cond. 1	Cond. 2	Cond. 3	Cond. 1	Cond. 2	Cond. 3	
2800-K-5.0-100k	7.9	25.6	8.4	6.6	21.5	7.1
2800-K-10.0-60k	23.0	70.7	24.6	19.1	59.6	20.4
2800-K-10.0-80k	19.0	58.5	20.3	15.8	49.3	16.8
2800-K-10.0-100k	16.6	51.1	17.7	13.8	43.0	14.7
2600-Z-1.0-60k	3.7	7.7	3.9	3.4	6.5	3.6
2600-Z-1.0-80k	2.2	4.6	2.3	2.2	4.2	2.3
2600-Z-1.0-100k	1.5	3.2	1.6	1.6	3.0	1.7
2600-Z-5.0-60k	6.1	12.5	6.4	5.4	10.0	5.6
2600-Z-5.0-80k	4.6	9.4	4.8	4.0	7.6	4.2
2600-Z-5.0-100k	3.8	7.8	3.9	3.4	6.3	3.5
2600-Z-10.0-60k	12.3	24.9	12.9	10.6	19.6	11.0
2600-Z-10.0-80k	10.1	20.4	10.5	8.7	16.0	9.0
2600-Z-10.0-100k	8.7	17.6	9.1	7.5	13.9	7.8
2600-Y-1.0-60k	4.8	6.3	4.9	7.7	9.2	7.8
2600-Y-1.0-80k	3.0	4.0	3.1	5.0	5.9	5.0
2600-Y-1.0-100k	2.1	2.9	2.2	3.6	4.4	3.7
2600-Y-5.0-60k	7.2	9.1	7.3	11.7	14.2	11.9
2600-Y-5.0-80k	5.6	7.0	5.6	8.9	10.8	9.0
2600-Y-5.0-100k	4.7	5.9	4.7	7.4	9.0	7.5
2600-Y-10.0-60k	12.1	14.6	12.2	22.0	26.3	22.2
2600-Y-10.0-80k	10.1	12.2	10.2	18.0	21.6	18.3
2600-Y-10.0-100k	8.8	10.7	8.9	15.7	18.8	15.9
2600-J-1.0-60k	6.4	17.1	6.8	8.1	24.0	8.6
2600-J-1.0-80k	4.0	10.5	4.2	5.4	16.0	5.8
2600-J-1.0-100k	2.8	7.4	3.0	4.1	12.0	4.4
2600-J-5.0-60k	10.0	26.9	10.6	11.7	35.0	12.5
2600-J-5.0-80k	7.6	20.4	8.0	9.0	26.9	9.6
2600-J-5.0-100k	6.3	17.0	6.7	7.6	22.6	8.1
2600-J-10.0-60k	18.1	47.2	19.1	20.8	60.7	22.2
2600-J-10.0-80k	15.0	39.2	15.8	17.2	50.4	18.3
2600-J-10.0-100k	13.0	34.2	13.8	15.0	44.1	16.0
2600-H-1.0-60k	5.2	10.2	5.4	4.6	9.1	4.8
2600-H-1.0-80k	3.4	6.7	3.5	3.1	6.2	3.2
2600-H-1.0-100k	2.6	5.1	2.7	2.4	4.7	2.5
2600-H-5.0-60k	7.8	15.4	8.0	6.8	13.5	7.0
2600-H-5.0-80k	5.9	11.7	6.2	5.2	10.3	5.4
2600-H-5.0-100k	5.0	9.8	5.2	4.4	8.6	4.5
2600-H-10.0-60k	14.2	28.9	14.7	12.6	25.5	13.0

Table A.1: continued.

Simulation	PHOENIX-ACES			BT-SETTL		
	σ_{RV}	σ_{RV}	σ_{RV}	σ_{RV}	σ_{RV}	σ_{RV}
	Cond. 1	Cond. 2	Cond. 3	Cond. 1	Cond. 2	Cond. 3
2600-H-10.0-80k	11.7	23.8	12.1	10.3	21.0	10.7
2600-H-10.0-100k	10.2	20.7	10.6	9.0	18.3	9.4
2600-K-1.0-60k	6.2	20.2	6.6	5.7	18.8	6.1
2600-K-1.0-80k	4.0	13.2	4.3	3.9	12.9	4.2
2600-K-1.0-100k	3.0	9.9	3.2	3.0	9.9	3.2
2600-K-5.0-60k	9.4	30.1	10.0	8.3	27.2	8.9
2600-K-5.0-80k	7.1	23.0	7.6	6.4	20.9	6.8
2600-K-5.0-100k	6.0	19.3	6.4	5.3	17.6	5.7
2600-K-10.0-60k	17.4	54.0	18.6	15.2	48.5	16.2
2600-K-10.0-80k	14.4	44.7	15.3	12.5	40.1	13.4
2600-K-10.0-100k	12.5	39.1	13.4	10.9	35.0	11.7

Table A.2: RV precisions calculated for the SPIRou ETC. These use the same PHOENIX-ACES parameter combinations as Table A.1 but with the precision calculated relative to a SNR=100 at the centre of each bands individually. The J -band precisions are not included here as they are identical to Table A.1.

Simulation (T_{eff} -Band- $v \cdot \sin i$ -R)	σ_{RV} (Cond. 1) [m/s]	σ_{RV} (Cond. 2) [m/s]	σ_{RV} (Cond. 3) [m/s]
3900-Z-1.0-60k	9.9	16.0	10.3
3900-Z-1.0-80k	6.6	10.7	6.8
3900-Z-1.0-100k	4.9	8.1	5.1
3900-Z-5.0-60k	14.5	23.2	15.0
3900-Z-5.0-80k	11.2	18.0	11.6
3900-Z-5.0-100k	9.4	15.2	9.7
3900-Z-10.0-60k	25.0	39.4	25.8
3900-Z-10.0-80k	20.7	32.9	21.4
3900-Z-10.0-100k	18.1	28.8	18.7
3900-Y-1.0-60k	10.0	11.9	10.1
3900-Y-1.0-80k	6.2	7.4	6.3
3900-Y-1.0-100k	4.4	5.3	4.5
3900-Y-5.0-60k	15.9	19.0	16.1
3900-Y-5.0-80k	12.0	14.3	12.1
3900-Y-5.0-100k	10.0	11.8	10.1
3900-Y-10.0-60k	31.6	37.8	32.0
3900-Y-10.0-80k	25.8	30.8	26.1
3900-Y-10.0-100k	22.4	26.7	22.6
3900-H-1.0-60k	7.3	11.5	7.4
3900-H-1.0-80k	5.1	8.1	5.2
3900-H-1.0-100k	4.0	6.4	4.1
3900-H-5.0-60k	10.2	16.0	10.4
3900-H-5.0-80k	7.9	12.5	8.1
3900-H-5.0-100k	6.7	10.5	6.8
3900-H-10.0-60k	17.5	27.3	17.9
3900-H-10.0-80k	14.5	22.7	14.8
3900-H-10.0-100k	12.7	19.8	13.0
3900-K-1.0-60k	10.5	46.3	11.3
3900-K-1.0-80k	7.1	31.8	7.6
3900-K-1.0-100k	5.4	24.5	5.8
3900-K-5.0-60k	15.7	65.4	16.8
3900-K-5.0-80k	12.0	50.8	12.8
3900-K-5.0-100k	10.1	42.9	10.8
3900-K-10.0-60k	28.5	112.6	30.4
3900-K-10.0-80k	23.6	93.1	25.2
3900-K-10.0-100k	20.6	81.2	22.0
3500-Z-1.0-60k	8.3	13.7	8.6

Table A.2: continued.

Simulation	σ_{RV} (Cond. 1)	σ_{RV} (Cond. 2)	σ_{RV} (Cond. 3)
3500-Z-1.0-80k	5.2	8.7	5.4
3500-Z-1.0-100k	3.7	6.3	3.8
3500-Z-5.0-60k	12.9	20.9	13.3
3500-Z-5.0-80k	9.8	16.0	10.1
3500-Z-5.0-100k	8.2	13.4	8.5
3500-Z-10.0-60k	24.0	38.1	24.8
3500-Z-10.0-80k	19.7	31.5	20.4
3500-Z-10.0-100k	17.2	27.5	17.7
3500-Y-1.0-60k	8.7	10.3	8.8
3500-Y-1.0-80k	5.3	6.3	5.4
3500-Y-1.0-100k	3.7	4.5	3.8
3500-Y-5.0-60k	14.1	16.7	14.3
3500-Y-5.0-80k	10.6	12.5	10.7
3500-Y-5.0-100k	8.8	10.4	8.9
3500-Y-10.0-60k	28.5	33.9	28.8
3500-Y-10.0-80k	23.2	27.6	23.5
3500-Y-10.0-100k	20.1	23.9	20.3
3500-H-1.0-60k	7.6	12.2	7.8
3500-H-1.0-80k	5.4	8.7	5.5
3500-H-1.0-100k	4.2	6.9	4.3
3500-H-5.0-60k	10.5	16.7	10.7
3500-H-5.0-80k	8.2	13.1	8.4
3500-H-5.0-100k	6.9	11.1	7.1
3500-H-10.0-60k	17.6	28.0	18.1
3500-H-10.0-80k	14.6	23.3	15.0
3500-H-10.0-100k	12.8	20.4	13.1
3500-K-1.0-60k	9.9	35.8	10.6
3500-K-1.0-80k	6.6	24.0	7.0
3500-K-1.0-100k	5.0	18.2	5.3
3500-K-5.0-60k	14.8	52.3	15.8
3500-K-5.0-80k	11.3	40.2	12.1
3500-K-5.0-100k	9.5	33.8	10.1
3500-K-10.0-60k	27.2	92.1	29.1
3500-K-10.0-80k	22.5	76.0	24.0
3500-K-10.0-100k	19.6	66.3	20.9
2800-Z-1.0-60k	3.8	7.3	3.9
2800-Z-1.0-80k	2.3	4.5	2.4
2800-Z-1.0-100k	1.6	3.2	1.7
2800-Z-5.0-60k	6.1	11.6	6.4
2800-Z-5.0-80k	4.6	8.8	4.8

Table A.2: continued.

Simulation	σ_{RV} (Cond. 1)	σ_{RV} (Cond. 2)	σ_{RV} (Cond. 3)
2800-Z-5.0-100k	3.8	7.3	4.0
2800-Z-10.0-60k	12.2	22.8	12.7
2800-Z-10.0-80k	9.9	18.7	10.4
2800-Z-10.0-100k	8.6	16.2	9.0
2800-Y-1.0-60k	5.6	7.1	5.7
2800-Y-1.0-80k	3.6	4.7	3.7
2800-Y-1.0-100k	2.6	3.4	2.7
2800-Y-5.0-60k	8.3	10.1	8.4
2800-Y-5.0-80k	6.4	7.9	6.5
2800-Y-5.0-100k	5.4	6.7	5.5
2800-Y-10.0-60k	13.8	16.4	13.9
2800-Y-10.0-80k	11.4	13.7	11.6
2800-Y-10.0-100k	10.0	12.0	10.1
2800-H-1.0-60k	6.5	12.6	6.8
2800-H-1.0-80k	4.4	8.5	4.6
2800-H-1.0-100k	3.3	6.4	3.5
2800-H-5.0-60k	9.6	18.3	9.9
2800-H-5.0-80k	7.3	14.1	7.6
2800-H-5.0-100k	6.2	11.8	6.4
2800-H-10.0-60k	17.2	33.5	17.8
2800-H-10.0-80k	14.2	27.6	14.7
2800-H-10.0-100k	12.4	24.1	12.8
2800-K-1.0-60k	6.3	20.8	6.7
2800-K-1.0-80k	4.2	13.9	4.5
2800-K-1.0-100k	3.1	10.5	3.4
2800-K-5.0-60k	9.5	30.4	10.1
2800-K-5.0-80k	7.2	23.3	7.7
2800-K-5.0-100k	6.0	19.6	6.4
2800-K-10.0-60k	17.5	53.7	18.7
2800-K-10.0-80k	14.4	44.4	15.4
2800-K-10.0-100k	12.6	38.8	13.4
2600-Z-1.0-60k	3.0	6.2	3.1
2600-Z-1.0-80k	1.8	3.8	1.9
2600-Z-1.0-100k	1.3	2.7	1.4
2600-Z-5.0-60k	4.8	9.8	5.0
2600-Z-5.0-80k	3.6	7.4	3.8
2600-Z-5.0-100k	3.0	6.2	3.2
2600-Z-10.0-60k	9.5	19.2	9.9
2600-Z-10.0-80k	7.7	15.7	8.1
2600-Z-10.0-100k	6.7	13.6	7.1

Table A.2: continued.

Simulation	σ_{RV} (Cond. 1)	σ_{RV} (Cond. 2)	σ_{RV} (Cond. 3)
2600-Y-1.0-60k	4.4	5.8	4.5
2600-Y-1.0-80k	2.8	3.8	2.9
2600-Y-1.0-100k	2.0	2.7	2.1
2600-Y-5.0-60k	6.5	8.2	6.6
2600-Y-5.0-80k	5.1	6.4	5.1
2600-Y-5.0-100k	4.3	5.4	4.3
2600-Y-10.0-60k	10.7	12.9	10.8
2600-Y-10.0-80k	8.9	10.8	9.0
2600-Y-10.0-100k	7.8	9.5	7.9
2600-H-1.0-60k	5.2	10.3	5.4
2600-H-1.0-80k	3.5	6.9	3.6
2600-H-1.0-100k	2.7	5.2	2.8
2600-H-5.0-60k	7.7	15.3	8.0
2600-H-5.0-80k	5.9	11.7	6.1
2600-H-5.0-100k	5.0	9.8	5.2
2600-H-10.0-60k	13.9	28.4	14.5
2600-H-10.0-80k	11.5	23.3	11.9
2600-H-10.0-100k	10.0	20.4	10.4
2600-K-1.0-60k	5.0	16.2	5.3
2600-K-1.0-80k	3.3	10.7	3.5
2600-K-1.0-100k	2.5	8.0	2.6
2600-K-5.0-60k	7.4	23.9	7.9
2600-K-5.0-80k	5.7	18.3	6.1
2600-K-5.0-100k	4.8	15.4	5.1
2600-K-10.0-60k	13.7	42.5	14.6
2600-K-10.0-80k	11.3	35.1	12.1
2600-K-10.0-100k	9.9	30.7	10.5

Table A.3: RV precisions calculated for the NIRPS ETC. The precisions are calculated for all PHOENIX-ACES temperatures spanning 2500–4000 K at a resolution of 75 000 and 100 000 only. They are calculated relative to a SNR=100 in the J -band.

Simulation (T_{eff} -Band- $v \cdot \sin i$ -R)	σ_{RV} (Cond. 1) [m/s]	σ_{RV} (Cond. 2) [m/s]	σ_{RV} (Cond. 3) [m/s]
4000-Z-1.0-75k	6.9	11.2	7.1
4000-Z-1.0-100k	4.7	7.7	4.9
4000-Z-5.0-75k	11.2	18.2	11.6
4000-Z-5.0-100k	9.0	14.5	9.3
4000-Z-10.0-75k	20.5	32.6	21.1
4000-Z-10.0-100k	17.2	27.4	17.8

Table A.3: continued.

Simulation	σ_{RV} (Cond. 1)	σ_{RV} (Cond. 2)	σ_{RV} (Cond. 3)
4000-Y-1.0-75k	6.8	8.1	6.8
4000-Y-1.0-100k	4.4	5.2	4.4
4000-Y-5.0-75k	12.5	14.9	12.6
4000-Y-5.0-100k	9.8	11.7	9.9
4000-Y-10.0-75k	26.4	31.6	26.8
4000-Y-10.0-100k	21.9	26.2	22.2
4000-J-1.0-75k	11.3	29.3	11.9
4000-J-1.0-100k	7.8	19.7	8.2
4000-J-5.0-75k	18.1	50.1	19.1
4000-J-5.0-100k	14.5	39.7	15.3
4000-J-10.0-75k	32.3	102.4	34.3
4000-J-10.0-100k	27.2	85.5	28.9
4000-H-1.0-75k	5.4	8.5	5.5
4000-H-1.0-100k	3.9	6.2	4.0
4000-H-5.0-75k	8.2	13.0	8.4
4000-H-5.0-100k	6.6	10.4	6.7
4000-H-10.0-75k	15.0	23.5	15.4
4000-H-10.0-100k	12.6	19.7	12.9
4000-K-1.0-75k	10.4	47.3	11.1
4000-K-1.0-100k	7.3	33.7	7.8
4000-K-5.0-75k	17.2	73.5	18.4
4000-K-5.0-100k	13.7	59.0	14.6
4000-K-10.0-75k	33.4	132.8	35.7
4000-K-10.0-100k	28.0	111.8	29.9
3900-Z-1.0-75k	7.0	11.4	7.2
3900-Z-1.0-100k	4.7	7.8	4.9
3900-Z-5.0-75k	11.5	18.6	11.9
3900-Z-5.0-100k	9.2	14.8	9.5
3900-Z-10.0-75k	21.2	33.6	21.8
3900-Z-10.0-100k	17.8	28.2	18.3
3900-Y-1.0-75k	6.6	7.9	6.7
3900-Y-1.0-100k	4.2	5.1	4.3
3900-Y-5.0-75k	12.3	14.7	12.5
3900-Y-5.0-100k	9.7	11.5	9.8
3900-Y-10.0-75k	26.3	31.4	26.6
3900-Y-10.0-100k	21.8	26.0	22.1
3900-J-1.0-75k	11.5	29.5	12.1
3900-J-1.0-100k	7.9	19.6	8.3
3900-J-5.0-75k	18.5	50.9	19.6
3900-J-5.0-100k	14.8	40.3	15.6

Table A.3: continued.

Simulation	σ_{RV} (Cond. 1)	σ_{RV} (Cond. 2)	σ_{RV} (Cond. 3)
3900-J-10.0-75k	33.4	104.9	35.4
3900-J-10.0-100k	28.0	87.6	29.8
3900-H-1.0-75k	5.4	8.6	5.5
3900-H-1.0-100k	4.0	6.3	4.0
3900-H-5.0-75k	8.3	13.0	8.5
3900-H-5.0-100k	6.6	10.5	6.8
3900-H-10.0-75k	15.1	23.6	15.5
3900-H-10.0-100k	12.7	19.9	13.0
3900-K-1.0-75k	10.6	47.3	11.3
3900-K-1.0-100k	7.4	33.6	8.0
3900-K-5.0-75k	17.5	73.8	18.7
3900-K-5.0-100k	13.9	59.2	14.8
3900-K-10.0-75k	34.0	133.7	36.3
3900-K-10.0-100k	28.5	112.5	30.5
3800-Z-1.0-75k	6.9	11.3	7.2
3800-Z-1.0-100k	4.7	7.7	4.8
3800-Z-5.0-75k	11.7	18.7	12.0
3800-Z-5.0-100k	9.3	14.9	9.6
3800-Z-10.0-75k	21.7	34.2	22.4
3800-Z-10.0-100k	18.2	28.7	18.8
3800-Y-1.0-75k	6.5	7.7	6.5
3800-Y-1.0-100k	4.1	4.9	4.2
3800-Y-5.0-75k	12.1	14.4	12.3
3800-Y-5.0-100k	9.5	11.3	9.6
3800-Y-10.0-75k	26.0	31.0	26.3
3800-Y-10.0-100k	21.5	25.7	21.8
3800-J-1.0-75k	11.5	29.3	12.1
3800-J-1.0-100k	7.8	19.4	8.2
3800-J-5.0-75k	18.7	51.2	19.8
3800-J-5.0-100k	14.9	40.5	15.8
3800-J-10.0-75k	34.1	106.2	36.2
3800-J-10.0-100k	28.7	88.6	30.4
3800-H-1.0-75k	5.5	8.8	5.7
3800-H-1.0-100k	4.1	6.4	4.1
3800-H-5.0-75k	8.4	13.2	8.6
3800-H-5.0-100k	6.7	10.6	6.9
3800-H-10.0-75k	15.2	23.7	15.6
3800-H-10.0-100k	12.8	20.0	13.1
3800-K-1.0-75k	10.7	46.0	11.4
3800-K-1.0-100k	7.5	32.5	8.0

Table A.3: continued.

Simulation	σ_{RV} (Cond. 1)	σ_{RV} (Cond. 2)	σ_{RV} (Cond. 3)
3800-K-5.0-75k	17.7	72.6	18.9
3800-K-5.0-100k	14.0	58.2	15.0
3800-K-10.0-75k	34.4	132.6	36.7
3800-K-10.0-100k	28.8	111.5	30.8
3700-Z-1.0-75k	6.8	11.1	7.0
3700-Z-1.0-100k	4.5	7.4	4.6
3700-Z-5.0-75k	11.6	18.7	12.0
3700-Z-5.0-100k	9.2	14.8	9.5
3700-Z-10.0-75k	22.0	34.6	22.7
3700-Z-10.0-100k	18.4	29.1	19.0
3700-Y-1.0-75k	6.3	7.5	6.3
3700-Y-1.0-100k	4.0	4.8	4.0
3700-Y-5.0-75k	11.9	14.1	12.0
3700-Y-5.0-100k	9.3	11.0	9.4
3700-Y-10.0-75k	25.6	30.4	25.9
3700-Y-10.0-100k	21.2	25.2	21.4
3700-J-1.0-75k	11.4	28.8	12.0
3700-J-1.0-100k	7.7	18.9	8.1
3700-J-5.0-75k	18.8	50.9	19.9
3700-J-5.0-100k	15.0	40.2	15.8
3700-J-10.0-75k	34.7	106.0	36.8
3700-J-10.0-100k	29.1	88.4	30.9
3700-H-1.0-75k	5.7	9.0	5.8
3700-H-1.0-100k	4.2	6.6	4.3
3700-H-5.0-75k	8.5	13.4	8.7
3700-H-5.0-100k	6.8	10.8	7.0
3700-H-10.0-75k	15.3	24.0	15.7
3700-H-10.0-100k	12.9	20.2	13.2
3700-K-1.0-75k	10.6	43.7	11.4
3700-K-1.0-100k	7.5	30.7	8.0
3700-K-5.0-75k	17.7	70.1	18.9
3700-K-5.0-100k	14.0	56.0	15.0
3700-K-10.0-75k	34.5	128.8	36.8
3700-K-10.0-100k	28.9	108.3	30.9
3600-Z-1.0-75k	6.3	10.5	6.6
3600-Z-1.0-100k	4.1	6.9	4.3
3600-Z-5.0-75k	11.2	18.2	11.6
3600-Z-5.0-100k	8.9	14.4	9.2
3600-Z-10.0-75k	21.8	34.5	22.5
3600-Z-10.0-100k	18.2	28.9	18.8

Table A.3: continued.

Simulation	σ_{RV} (Cond. 1)	σ_{RV} (Cond. 2)	σ_{RV} (Cond. 3)
3600-Y-1.0-75k	6.0	7.2	6.1
3600-Y-1.0-100k	3.8	4.6	3.9
3600-Y-5.0-75k	11.5	13.6	11.6
3600-Y-5.0-100k	9.0	10.6	9.1
3600-Y-10.0-75k	24.9	29.6	25.2
3600-Y-10.0-100k	20.6	24.5	20.9
3600-J-1.0-75k	11.1	27.9	11.7
3600-J-1.0-100k	7.5	18.1	7.8
3600-J-5.0-75k	18.7	49.8	19.7
3600-J-5.0-100k	14.8	39.3	15.7
3600-J-10.0-75k	34.7	104.0	36.9
3600-J-10.0-100k	29.1	86.7	30.9
3600-H-1.0-75k	5.8	9.2	5.9
3600-H-1.0-100k	4.3	6.8	4.3
3600-H-5.0-75k	8.6	13.7	8.8
3600-H-5.0-100k	6.9	11.0	7.1
3600-H-10.0-75k	15.4	24.3	15.8
3600-H-10.0-100k	13.0	20.5	13.3
3600-K-1.0-75k	10.3	39.8	11.0
3600-K-1.0-100k	7.2	27.8	7.7
3600-K-5.0-75k	17.2	64.7	18.4
3600-K-5.0-100k	13.7	51.6	14.6
3600-K-10.0-75k	33.7	120.0	36.0
3600-K-10.0-100k	28.2	100.8	30.2
3500-Z-1.0-75k	5.8	9.7	6.0
3500-Z-1.0-100k	3.7	6.3	3.8
3500-Z-5.0-75k	10.6	17.3	10.9
3500-Z-5.0-100k	8.3	13.6	8.6
3500-Z-10.0-75k	21.1	33.8	21.8
3500-Z-10.0-100k	17.6	28.2	18.2
3500-Y-1.0-75k	5.8	6.9	5.8
3500-Y-1.0-100k	3.6	4.3	3.7
3500-Y-5.0-75k	11.0	13.1	11.2
3500-Y-5.0-100k	8.6	10.2	8.7
3500-Y-10.0-75k	24.0	28.5	24.3
3500-Y-10.0-100k	19.9	23.6	20.1
3500-J-1.0-75k	10.7	26.6	11.3
3500-J-1.0-100k	7.1	17.1	7.5
3500-J-5.0-75k	18.3	48.1	19.3
3500-J-5.0-100k	14.5	37.8	15.3

Table A.3: continued.

Simulation	σ_{RV} (Cond. 1)	σ_{RV} (Cond. 2)	σ_{RV} (Cond. 3)
3500-J-10.0-75k	34.4	100.5	36.5
3500-J-10.0-100k	28.8	83.7	30.6
3500-H-1.0-75k	5.8	9.4	6.0
3500-H-1.0-100k	4.3	6.9	4.4
3500-H-5.0-75k	8.8	14.0	9.0
3500-H-5.0-100k	7.1	11.3	7.2
3500-H-10.0-75k	15.6	24.8	16.0
3500-H-10.0-100k	13.1	20.9	13.5
3500-K-1.0-75k	9.8	35.7	10.5
3500-K-1.0-100k	6.8	24.8	7.3
3500-K-5.0-75k	16.4	58.2	17.5
3500-K-5.0-100k	13.0	46.4	13.9
3500-K-10.0-75k	32.2	108.7	34.4
3500-K-10.0-100k	27.0	91.3	28.8
3400-Z-1.0-75k	5.3	8.9	5.5
3400-Z-1.0-100k	3.3	5.7	3.5
3400-Z-5.0-75k	9.8	16.3	10.2
3400-Z-5.0-100k	7.7	12.8	8.0
3400-Z-10.0-75k	20.2	32.7	20.8
3400-Z-10.0-100k	16.8	27.2	17.3
3400-Y-1.0-75k	5.5	6.6	5.6
3400-Y-1.0-100k	3.5	4.2	3.5
3400-Y-5.0-75k	10.5	12.4	10.6
3400-Y-5.0-100k	8.2	9.7	8.3
3400-Y-10.0-75k	22.3	26.4	22.5
3400-Y-10.0-100k	18.5	21.9	18.7
3400-J-1.0-75k	10.2	25.0	10.8
3400-J-1.0-100k	6.7	15.9	7.1
3400-J-5.0-75k	17.6	45.6	18.6
3400-J-5.0-100k	14.0	35.9	14.7
3400-J-10.0-75k	33.6	95.5	35.7
3400-J-10.0-100k	28.1	79.4	29.9
3400-H-1.0-75k	5.9	9.7	6.0
3400-H-1.0-100k	4.3	7.1	4.4
3400-H-5.0-75k	8.9	14.5	9.2
3400-H-5.0-100k	7.2	11.7	7.4
3400-H-10.0-75k	16.0	25.8	16.4
3400-H-10.0-100k	13.4	21.7	13.8
3400-K-1.0-75k	9.2	31.8	9.8
3400-K-1.0-100k	6.4	22.2	6.8

Table A.3: continued.

Simulation	σ_{RV} (Cond. 1)	σ_{RV} (Cond. 2)	σ_{RV} (Cond. 3)
3400-K-5.0-75k	15.4	52.0	16.4
3400-K-5.0-100k	12.2	41.4	13.0
3400-K-10.0-75k	30.5	97.5	32.4
3400-K-10.0-100k	25.5	81.8	27.2
3300-Z-1.0-75k	4.8	8.2	5.0
3300-Z-1.0-100k	3.0	5.2	3.1
3300-Z-5.0-75k	9.1	15.3	9.4
3300-Z-5.0-100k	7.1	11.9	7.3
3300-Z-10.0-75k	19.0	31.3	19.7
3300-Z-10.0-100k	15.8	26.0	16.4
3300-Y-1.0-75k	5.8	7.1	5.9
3300-Y-1.0-100k	3.8	4.6	3.8
3300-Y-5.0-75k	10.3	12.2	10.4
3300-Y-5.0-100k	8.1	9.7	8.2
3300-Y-10.0-75k	19.9	23.5	20.1
3300-Y-10.0-100k	16.6	19.6	16.8
3300-J-1.0-75k	9.5	23.0	10.1
3300-J-1.0-100k	6.2	14.6	6.6
3300-J-5.0-75k	16.7	42.5	17.7
3300-J-5.0-100k	13.2	33.3	13.9
3300-J-10.0-75k	32.3	89.0	34.3
3300-J-10.0-100k	27.0	74.0	28.6
3300-H-1.0-75k	5.9	10.0	6.1
3300-H-1.0-100k	4.3	7.2	4.4
3300-H-5.0-75k	9.1	15.2	9.4
3300-H-5.0-100k	7.3	12.2	7.5
3300-H-10.0-75k	16.5	27.3	16.9
3300-H-10.0-100k	13.9	22.9	14.2
3300-K-1.0-75k	8.7	28.9	9.2
3300-K-1.0-100k	6.0	20.2	6.4
3300-K-5.0-75k	14.6	47.2	15.5
3300-K-5.0-100k	11.5	37.6	12.3
3300-K-10.0-75k	28.8	88.8	30.7
3300-K-10.0-100k	24.1	74.6	25.7
3200-Z-1.0-75k	4.3	7.5	4.5
3200-Z-1.0-100k	2.7	4.7	2.8
3200-Z-5.0-75k	8.3	14.2	8.6
3200-Z-5.0-100k	6.5	11.1	6.7
3200-Z-10.0-75k	17.8	29.8	18.4
3200-Z-10.0-100k	14.7	24.7	15.3

Table A.3: continued.

Simulation	σ_{RV} (Cond. 1)	σ_{RV} (Cond. 2)	σ_{RV} (Cond. 3)
3200-Y-1.0-75k	5.5	6.7	5.6
3200-Y-1.0-100k	3.6	4.4	3.6
3200-Y-5.0-75k	9.7	11.6	9.8
3200-Y-5.0-100k	7.6	9.2	7.7
3200-Y-10.0-75k	18.4	21.7	18.6
3200-Y-10.0-100k	15.4	18.2	15.6
3200-J-1.0-75k	8.7	20.6	9.2
3200-J-1.0-100k	5.6	13.0	5.9
3200-J-5.0-75k	15.5	38.5	16.3
3200-J-5.0-100k	12.2	30.2	12.9
3200-J-10.0-75k	30.3	80.8	32.1
3200-J-10.0-100k	25.3	67.2	26.8
3200-H-1.0-75k	5.9	10.3	6.1
3200-H-1.0-100k	4.2	7.4	4.3
3200-H-5.0-75k	9.3	15.9	9.6
3200-H-5.0-100k	7.4	12.7	7.7
3200-H-10.0-75k	17.0	29.0	17.5
3200-H-10.0-100k	14.3	24.4	14.7
3200-K-1.0-75k	8.2	26.9	8.7
3200-K-1.0-100k	5.7	18.8	6.1
3200-K-5.0-75k	13.8	43.9	14.7
3200-K-5.0-100k	10.9	34.9	11.6
3200-K-10.0-75k	27.4	82.7	29.2
3200-K-10.0-100k	22.9	69.4	24.4
3100-Z-1.0-75k	4.0	7.3	4.2
3100-Z-1.0-100k	2.5	4.6	2.6
3100-Z-5.0-75k	7.8	13.8	8.1
3100-Z-5.0-100k	6.1	10.8	6.3
3100-Z-10.0-75k	16.7	29.0	17.3
3100-Z-10.0-100k	13.9	24.1	14.4
3100-Y-1.0-75k	5.5	6.8	5.6
3100-Y-1.0-100k	3.6	4.5	3.7
3100-Y-5.0-75k	9.4	11.3	9.5
3100-Y-5.0-100k	7.5	9.0	7.5
3100-Y-10.0-75k	17.3	20.5	17.5
3100-Y-10.0-100k	14.5	17.2	14.7
3100-J-1.0-75k	7.7	17.9	8.1
3100-J-1.0-100k	5.0	11.2	5.2
3100-J-5.0-75k	13.9	34.0	14.7
3100-J-5.0-100k	11.0	26.6	11.6

Table A.3: continued.

Simulation	σ_{RV} (Cond. 1)	σ_{RV} (Cond. 2)	σ_{RV} (Cond. 3)
3100-J-10.0-75k	27.7	71.5	29.3
3100-J-10.0-100k	23.1	59.4	24.4
3100-H-1.0-75k	5.8	10.4	6.0
3100-H-1.0-100k	4.1	7.4	4.3
3100-H-5.0-75k	9.3	16.4	9.6
3100-H-5.0-100k	7.4	13.1	7.7
3100-H-10.0-75k	17.3	30.6	17.9
3100-H-10.0-100k	14.5	25.6	15.0
3100-K-1.0-75k	7.7	25.2	8.2
3100-K-1.0-100k	5.4	17.6	5.7
3100-K-5.0-75k	13.1	41.3	13.9
3100-K-5.0-100k	10.3	32.8	11.0
3100-K-10.0-75k	26.0	77.9	27.7
3100-K-10.0-100k	21.7	65.4	23.1
3000-Z-1.0-75k	3.6	6.8	3.8
3000-Z-1.0-100k	2.3	4.2	2.4
3000-Z-5.0-75k	7.1	12.9	7.4
3000-Z-5.0-100k	5.5	10.0	5.7
3000-Z-10.0-75k	15.3	27.1	15.9
3000-Z-10.0-100k	12.7	22.5	13.2
3000-Y-1.0-75k	5.0	6.3	5.1
3000-Y-1.0-100k	3.3	4.2	3.4
3000-Y-5.0-75k	8.6	10.4	8.7
3000-Y-5.0-100k	6.8	8.3	6.9
3000-Y-10.0-75k	15.7	18.6	15.9
3000-Y-10.0-100k	13.2	15.7	13.3
3000-J-1.0-75k	7.9	20.4	8.3
3000-J-1.0-100k	5.1	13.1	5.4
3000-J-5.0-75k	13.9	37.0	14.7
3000-J-5.0-100k	11.0	29.1	11.6
3000-J-10.0-75k	26.7	72.6	28.3
3000-J-10.0-100k	22.3	60.8	23.7
3000-H-1.0-75k	5.6	10.3	5.8
3000-H-1.0-100k	3.9	7.3	4.1
3000-H-5.0-75k	9.1	16.5	9.4
3000-H-5.0-100k	7.2	13.2	7.5
3000-H-10.0-75k	17.2	31.4	17.8
3000-H-10.0-100k	14.4	26.3	14.9
3000-K-1.0-75k	7.2	23.5	7.7
3000-K-1.0-100k	5.0	16.4	5.3

Table A.3: continued.

Simulation	σ_{RV} (Cond. 1)	σ_{RV} (Cond. 2)	σ_{RV} (Cond. 3)
3000-K-5.0-75k	12.2	38.6	13.0
3000-K-5.0-100k	9.6	30.7	10.2
3000-K-10.0-75k	24.2	73.0	25.8
3000-K-10.0-100k	20.3	61.2	21.6
2900-Z-1.0-75k	3.3	6.2	3.4
2900-Z-1.0-100k	2.0	3.9	2.1
2900-Z-5.0-75k	6.4	11.8	6.6
2900-Z-5.0-100k	4.9	9.2	5.1
2900-Z-10.0-75k	13.8	25.1	14.4
2900-Z-10.0-100k	11.4	20.8	11.9
2900-Y-1.0-75k	4.6	5.8	4.6
2900-Y-1.0-100k	3.0	3.9	3.0
2900-Y-5.0-75k	7.8	9.6	7.9
2900-Y-5.0-100k	6.2	7.6	6.3
2900-Y-10.0-75k	14.2	16.8	14.3
2900-Y-10.0-100k	11.9	14.2	12.0
2900-J-1.0-75k	7.1	18.6	7.5
2900-J-1.0-100k	4.6	12.0	4.9
2900-J-5.0-75k	12.5	33.5	13.3
2900-J-5.0-100k	9.9	26.4	10.5
2900-J-10.0-75k	24.0	64.3	25.5
2900-J-10.0-100k	20.1	53.9	21.3
2900-H-1.0-75k	5.3	9.9	5.4
2900-H-1.0-100k	3.7	6.9	3.8
2900-H-5.0-75k	8.6	16.1	8.9
2900-H-5.0-100k	6.9	12.8	7.1
2900-H-10.0-75k	16.5	31.2	17.1
2900-H-10.0-100k	13.8	26.1	14.3
2900-K-1.0-75k	6.6	21.6	7.0
2900-K-1.0-100k	4.5	15.0	4.8
2900-K-5.0-75k	11.1	35.5	11.8
2900-K-5.0-100k	8.8	28.3	9.4
2900-K-10.0-75k	22.1	67.3	23.6
2900-K-10.0-100k	18.5	56.5	19.7
2800-Z-1.0-75k	2.9	5.7	3.0
2800-Z-1.0-100k	1.8	3.6	1.9
2800-Z-5.0-75k	5.7	10.9	5.9
2800-Z-5.0-100k	4.4	8.5	4.6
2800-Z-10.0-75k	12.4	23.3	13.0
2800-Z-10.0-100k	10.3	19.3	10.7

Table A.3: continued.

Simulation	σ_{RV} (Cond. 1)	σ_{RV} (Cond. 2)	σ_{RV} (Cond. 3)
2800-Y-1.0-75k	4.1	5.3	4.2
2800-Y-1.0-100k	2.7	3.5	2.7
2800-Y-5.0-75k	7.1	8.7	7.2
2800-Y-5.0-100k	5.6	7.0	5.7
2800-Y-10.0-75k	12.7	15.2	12.9
2800-Y-10.0-100k	10.7	12.8	10.8
2800-J-1.0-75k	6.1	16.0	6.5
2800-J-1.0-100k	4.0	10.2	4.2
2800-J-5.0-75k	10.9	28.9	11.5
2800-J-5.0-100k	8.6	22.8	9.1
2800-J-10.0-75k	20.9	55.0	22.1
2800-J-10.0-100k	17.5	46.1	18.5
2800-H-1.0-75k	4.8	9.3	5.0
2800-H-1.0-100k	3.3	6.4	3.5
2800-H-5.0-75k	8.0	15.3	8.2
2800-H-5.0-100k	6.3	12.1	6.5
2800-H-10.0-75k	15.3	29.9	15.9
2800-H-10.0-100k	12.8	25.0	13.3
2800-K-1.0-75k	5.9	19.5	6.3
2800-K-1.0-100k	4.0	13.5	4.3
2800-K-5.0-75k	10.0	32.2	10.6
2800-K-5.0-100k	7.9	25.6	8.4
2800-K-10.0-75k	19.8	60.9	21.1
2800-K-10.0-100k	16.6	51.1	17.7
2700-Z-1.0-75k	2.6	5.3	2.7
2700-Z-1.0-100k	1.6	3.3	1.7
2700-Z-5.0-75k	5.2	10.2	5.4
2700-Z-5.0-100k	4.0	7.9	4.2
2700-Z-10.0-75k	11.3	21.9	11.8
2700-Z-10.0-100k	9.3	18.1	9.7
2700-Y-1.0-75k	3.7	4.8	3.7
2700-Y-1.0-100k	2.4	3.2	2.4
2700-Y-5.0-75k	6.4	8.0	6.5
2700-Y-5.0-100k	5.1	6.4	5.2
2700-Y-10.0-75k	11.5	13.8	11.6
2700-Y-10.0-100k	9.7	11.6	9.8
2700-J-1.0-75k	5.2	13.6	5.5
2700-J-1.0-100k	3.4	8.7	3.5
2700-J-5.0-75k	9.3	24.9	9.9
2700-J-5.0-100k	7.4	19.6	7.8

Table A.3: continued.

Simulation	σ_{RV} (Cond. 1)	σ_{RV} (Cond. 2)	σ_{RV} (Cond. 3)
2700-J-10.0-75k	18.0	47.1	19.1
2700-J-10.0-100k	15.1	39.5	16.0
2700-H-1.0-75k	4.3	8.3	4.4
2700-H-1.0-100k	3.0	5.8	3.1
2700-H-5.0-75k	7.1	13.9	7.4
2700-H-5.0-100k	5.7	11.0	5.9
2700-H-10.0-75k	13.8	27.6	14.3
2700-H-10.0-100k	11.5	23.1	12.0
2700-K-1.0-75k	5.2	17.2	5.5
2700-K-1.0-100k	3.5	11.9	3.8
2700-K-5.0-75k	8.8	28.5	9.4
2700-K-5.0-100k	6.9	22.7	7.4
2700-K-10.0-75k	17.4	54.0	18.6
2700-K-10.0-100k	14.6	45.3	15.5
2600-Z-1.0-75k	2.5	5.2	2.6
2600-Z-1.0-100k	1.5	3.2	1.6
2600-Z-5.0-75k	4.8	9.9	5.1
2600-Z-5.0-100k	3.8	7.8	3.9
2600-Z-10.0-75k	10.5	21.3	11.0
2600-Z-10.0-100k	8.7	17.6	9.1
2600-Y-1.0-75k	3.3	4.4	3.4
2600-Y-1.0-100k	2.1	2.9	2.2
2600-Y-5.0-75k	5.9	7.4	6.0
2600-Y-5.0-100k	4.7	5.9	4.7
2600-Y-10.0-75k	10.5	12.7	10.6
2600-Y-10.0-100k	8.8	10.7	8.9
2600-J-1.0-75k	4.4	11.7	4.7
2600-J-1.0-100k	2.8	7.4	3.0
2600-J-5.0-75k	8.0	21.6	8.5
2600-J-5.0-100k	6.3	17.0	6.7
2600-J-10.0-75k	15.6	40.8	16.5
2600-J-10.0-100k	13.0	34.2	13.8
2600-H-1.0-75k	3.7	7.4	3.9
2600-H-1.0-100k	2.6	5.1	2.7
2600-H-5.0-75k	6.3	12.4	6.5
2600-H-5.0-100k	5.0	9.8	5.2
2600-H-10.0-75k	12.2	24.8	12.7
2600-H-10.0-100k	10.2	20.7	10.6
2600-K-1.0-75k	4.4	14.4	4.7
2600-K-1.0-100k	3.0	9.9	3.2

Table A.3: continued.

Simulation	σ_{RV} (Cond. 1)	σ_{RV} (Cond. 2)	σ_{RV} (Cond. 3)
2600-K-5.0-75k	7.6	24.3	8.1
2600-K-5.0-100k	6.0	19.3	6.4
2600-K-10.0-75k	15.0	46.5	16.0
2600-K-10.0-100k	12.5	39.1	13.4
2500-Z-1.0-75k	2.5	5.5	2.6
2500-Z-1.0-100k	1.6	3.5	1.6
2500-Z-5.0-75k	4.8	10.4	5.0
2500-Z-5.0-100k	3.7	8.2	3.9
2500-Z-10.0-75k	10.3	22.0	10.9
2500-Z-10.0-100k	8.6	18.3	9.0
2500-Y-1.0-75k	3.1	4.2	3.1
2500-Y-1.0-100k	2.0	2.7	2.0
2500-Y-5.0-75k	5.5	7.1	5.6
2500-Y-5.0-100k	4.4	5.7	4.4
2500-Y-10.0-75k	9.9	12.2	10.0
2500-Y-10.0-100k	8.4	10.3	8.5
2500-J-1.0-75k	3.7	10.0	3.9
2500-J-1.0-100k	2.4	6.3	2.5
2500-J-5.0-75k	6.8	18.7	7.3
2500-J-5.0-100k	5.4	14.7	5.7
2500-J-10.0-75k	13.5	35.7	14.3
2500-J-10.0-100k	11.3	29.9	11.9
2500-H-1.0-75k	3.3	6.5	3.4
2500-H-1.0-100k	2.3	4.4	2.4
2500-H-5.0-75k	5.5	11.0	5.7
2500-H-5.0-100k	4.4	8.7	4.5
2500-H-10.0-75k	10.7	21.9	11.1
2500-H-10.0-100k	9.0	18.3	9.3
2500-K-1.0-75k	3.8	11.8	4.0
2500-K-1.0-100k	2.6	8.0	2.7
2500-K-5.0-75k	6.5	20.5	6.9
2500-K-5.0-100k	5.1	16.2	5.5
2500-K-10.0-75k	12.8	39.8	13.7
2500-K-10.0-100k	10.8	33.4	11.5

Appendix B

Artefacts in Optimal Extraction

As mentioned in Section 5.2.3.1 there were several artefacts observed in the *optimal* reduction of the DRACS pipeline, coinciding with spikes in the *rectangular* reduction. A list of all specific nods of each observation and detector that were observed to contain artefacts and were replaced with the method developed are provided in Table B.1.

With 8 nods per observation, and 4 CRIRES detectors for the 17 observations there are 544 individual nod spectra. Table B.1 identifies the 79 individual nods (14.5%) that were found to contain artefacts while Table B.2 provides a tally of the frequency of artefacts occurring within each nod position of the nod cycle. Only 16/68 (23.5%) detector-observations have all nods without any artefacts while no observation is completely free of artefacts across all 4 detectors.

Tallying the number of artefacts that occur per detector and nod position reveals three main features. The first is that there are around $1.3\text{--}1.5\times$ more artefacts that occur on the second detector compared to the other three detectors individually. This may be due to a physical defect with this detector, such as the large scratch seen in Figure 5.2, or it is possibly due to the relatively featureless spectrum on the second detector. Either will make it easier to visually detect artefacts in the spectra, or easier for artefacts to be created by the pipeline. The second is that there are more artefacts in the seventh and eighth nods with $\sim 40\%$ of the artefacts in the last 2/8 of observations (see Table B.2). As the artefacts occur later in the nod cycle this suggests that they may be related to the operation of the instrumentation, for which the probability is built up over the repeated nod cycle observations, however this is just speculation.

There does not seem to be a connection between the nod position as both position A and B have half of the artefacts. There is a higher number of artefacts occurring in the last two nods, suggesting that there may be some correlation to the length of the observation. The growth in artefacts over time is not linear with a rapid increase starting around the sixth nod.

The third thing that is noticed is the difference in the number of artefacts seen in the first observation of HD 30501 compared to the other three. This was observed four months before the others, which were observed within the same week. The later three observations all have larger number of artefacts $2\text{--}3\times$ compared to the first observation.

The ideas presented here are only observations and speculation on the causes. Tests for statistical significance of the differences observed have not been performed and is beyond the scope of this work.

Figures B.1 to B.6 show more examples of observed spectra in which spikes and artefacts are observed. One example is given for each target, selected to show a variety of the artefacts observed.

Table B.1: Identification of all the optimally reduced nod spectra which had artefacts and were replaced by the rectangular extractions, after correction for bad pixel spikes. The numbers represent the position (1–8) in the nod cycle ABBAABBA. The number of the observation for each target is given in the second column (#).

Target	#	Detector					Total
		1	2	3	4		
HD 4747	1	8	5, 8	8	1, 5, 8		7
HD 162020	1	-	7, 8	-	-		2
HD 162020	2	-	2	-	8		2
HD 167665	1	2, 4	8	1, 6	4, 5		7
HD 167665	2	2	3	1	8		4
HD 167665	3	6	3, 7	-	8		4
HD 168443	1	-	-	-	7, 8		2
HD 168443	2	-	2, 4	6	8		4
HD 202206	1	-	6, 7	1	-		3
HD 202206	2	5	-	7, 8	-		3
HD 202206	3	8	3	6	6		4
HD 211847	1	-	5, 7	2	4		4
HD 211847	2	2	1, 7	7	8		5
HD 30501	1	7	7	-	8		3
HD 30501	2	7, 8	3, 5, 7, 8	2, 7	2, 3		10
HD 30501	3	4, 8	2, 6, 7	4, 8	7		8
HD 30501	4	1, 2, 4	3	5, 6	6		7
		16	27	17	19	79/544	

Table B.2: Tally of nod cycle positions in which their optimally reduced spectra were affected by these artefacts and replaced.

Nod Number	1	2	3	4	5	6	7	8	Total
Nod Position	A	B	B	A	A	B	B	A	
Tally	6	10	6	7	7	9	15	19	79

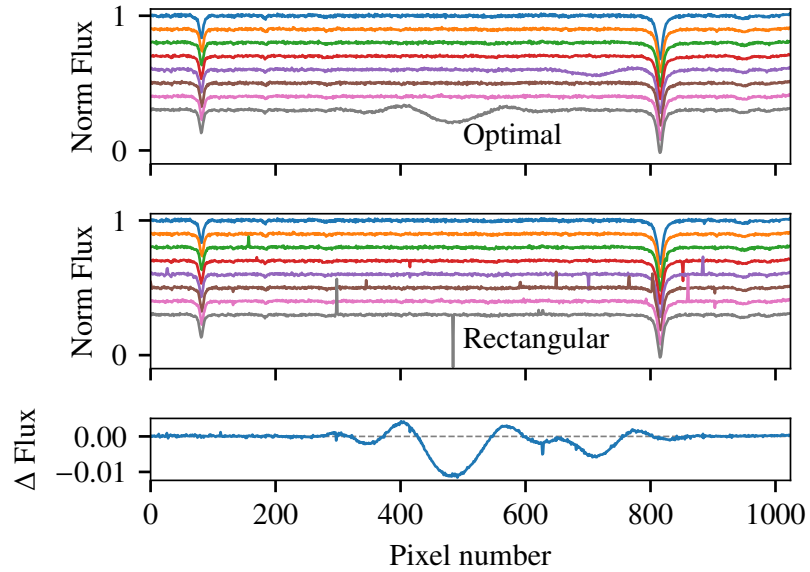


Figure B.1: Artefact example for the second detector of HD 4747. The top panel contains the eight normalized nod spectra obtained using optimal extraction. The middle panel shows nod spectra using only rectangular extraction. The bottom panel shows the difference between a combined spectrum using optimal nods only and a combined spectrum in which the identified nods are replaced with their rectangular counterparts as per Section 5.2.3.1. A vertical offset is included between each spectra for clarity. The nod spectra are in observation order from top to bottom. In this example there are artefacts in the 5th (purple) and eighth (grey) nod spectra around 700 and 500 pixels respectively.

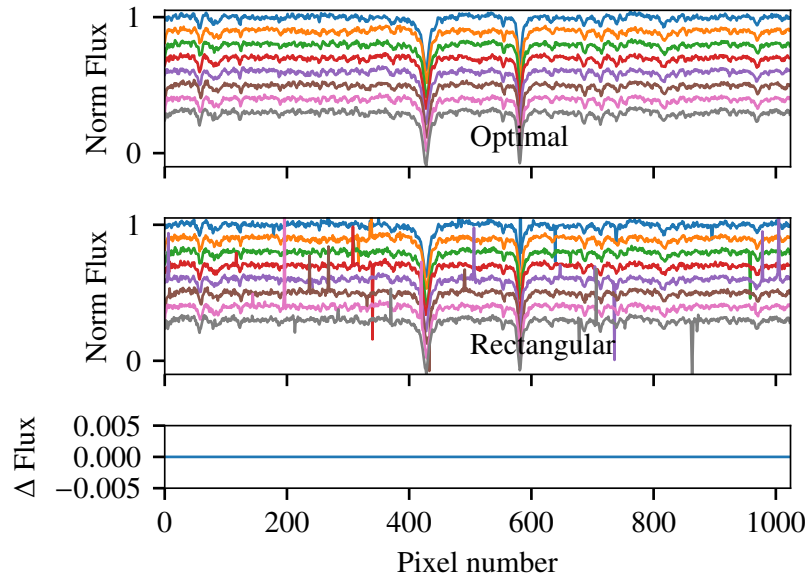


Figure B.2: Same as Figure B.1 but for the first detector of the second observation of HD 162020. In this example there are several large spikes observed in the rectangular extraction but they do not appear to effect the optimally extracted nods (there are no artefacts).

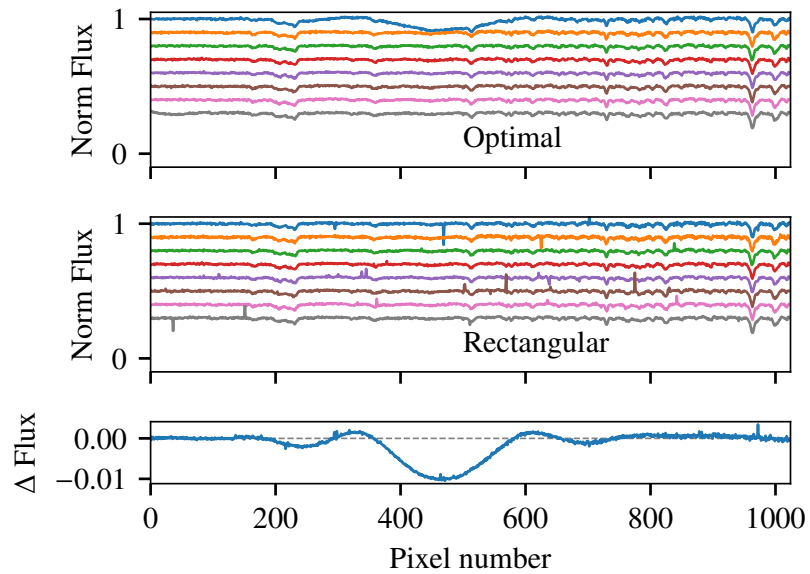


Figure B.3: Same as Figure B.1 but for the third detector of the second observation of HD 167665. In this example a small spike in the first spectrum (blue) around pixel 450 causes an extended dip in the optimally extracted nod.

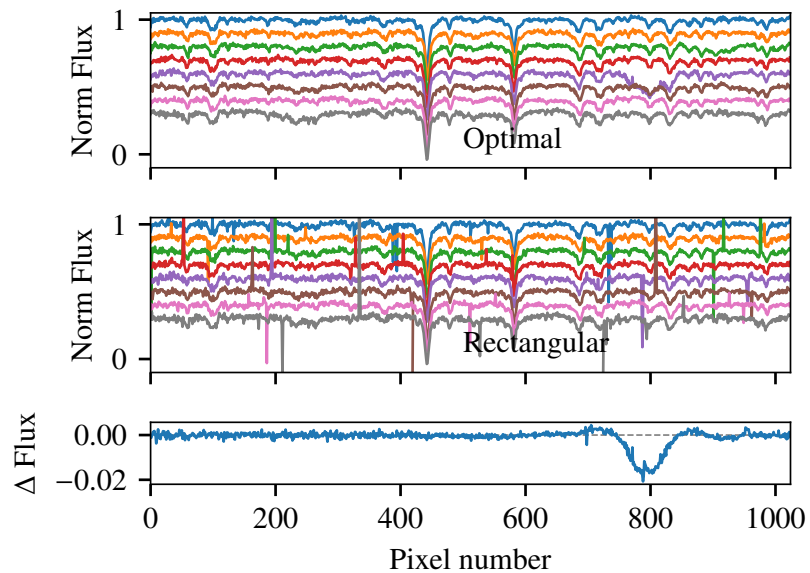


Figure B.4: Same as Figure B.1 but for the 1st detector of the second observation of HD 202206. In this example there are several large spikes but only one produces an artefact. This is on the 5th nod (purple) around pixel 800.

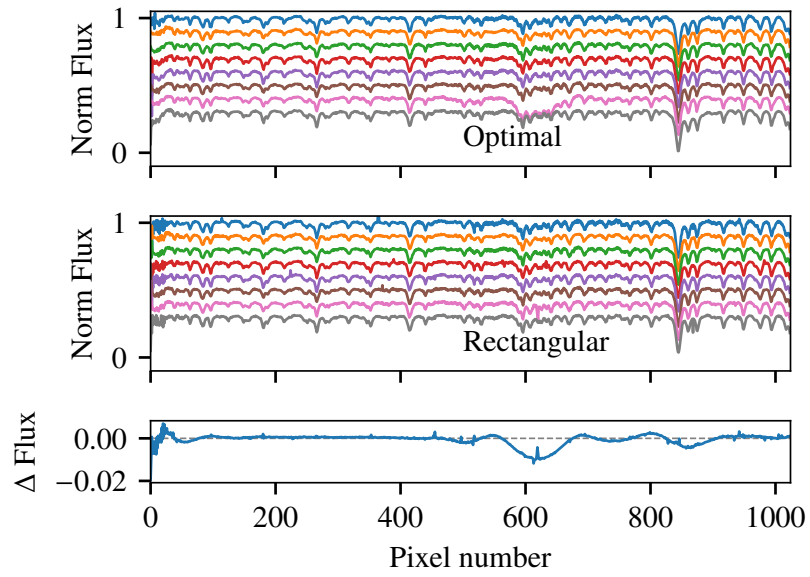


Figure B.5: Same as Figure B.1 but for the fourth detector of the first observation of HD 168443. In this example a barely visible spike on the 7th nod (pink) causes a deviation in the optimal nod around pixel 610. There is also a second small spike on the eighth nod (grey) around pixel 850, between two spectral lines.

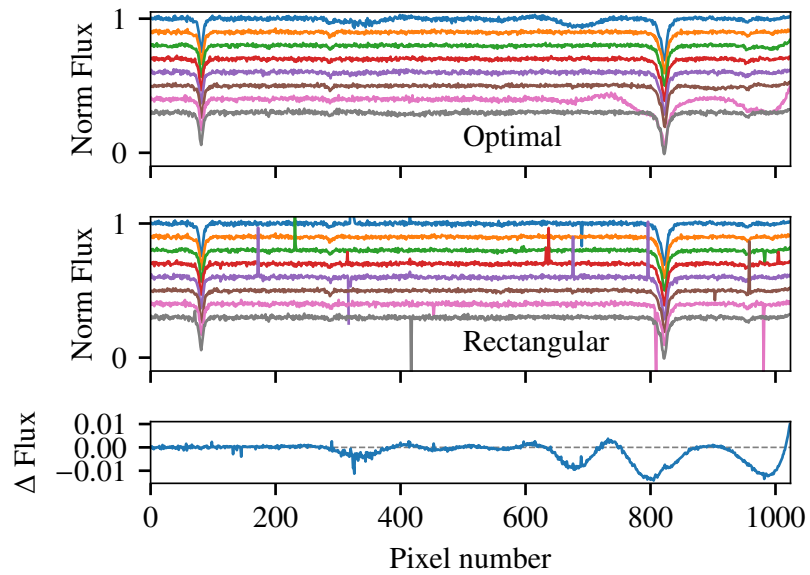


Figure B.6: Same as Figure B.1 but for the second detector of the second observation of HD 211847. In this example two large spikes around 800 and 1000 in the 7th nod (pink) create large deviations in the optimally reduced spectra. A spike in the first nod (blue) around pixel 700 also causes a bump. There is also some extra noise in the first nod around pixel 350.

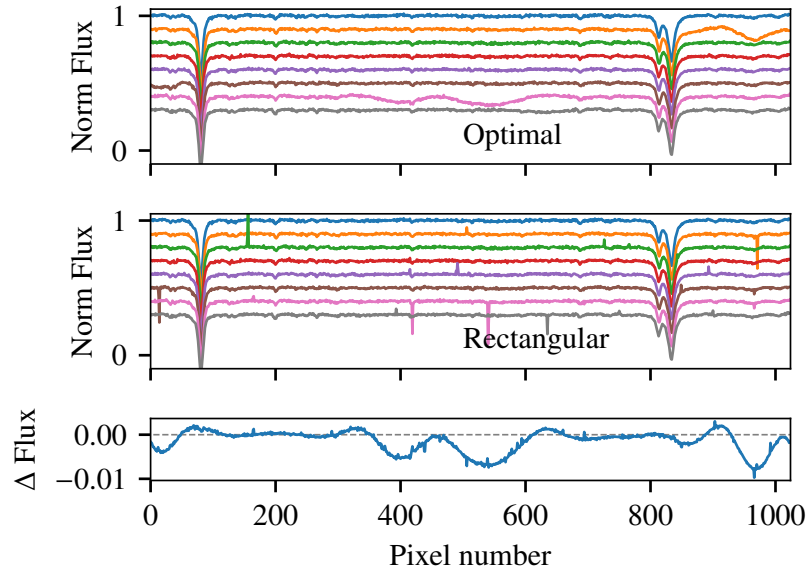


Figure B.7: Same as Figure B.1 but for the second detector of the second observation of HD 30501. In this example there are artefact causing spikes in four places. The second nod (orange) around pixel 950, the 6th nod (brown) around pixel 20 and two spikes in the 7th nod (pink) around pixels 400 and 550.

In each image the top panel contains the 8 nod spectra extracted using the optimal method, which includes variance weighting. The middle panel contains the rectangular extraction only (no variance weighting). The bottom panel shows the difference between the average combined spectra from the top and middle panels.

It is clear that the large extracted artefacts occur due to single spikes observed in the rectangular extraction. What is unclear is the other factors that affect their cause. For example in Figure B.2 several spikes are seen but no artefacts are created.

Multi-detector wavelength calibration

An example of multi-detector wavelength calibration is provided here. This is an idea to improve the wavelength calibration on the detectors in which a limited number of telluric lines fall.

The spectrum recorded across the four CRIRES detectors is created from a single dispersion and should, in theory, be able to be modelled by a single polynomial. Figure C.1 shows the pixel-wavelength calibration points for the four detectors, along with the individual detector fits extended over all detectors. At this scale all four lines are basically similar except for the fourth detector fit (pink) near the first detector where the wavelengths are higher. On top of the four individual fits is also a black line indicating a polynomial fit made using the points from all detectors incorporating fixed detector gaps.

Figure C.2 shows the difference between the individual detector fits and the combined fit. Within the individual detectors the absolute wavelength difference to the combined fit is small. It is worst at the edges of detector #1 with a maximum difference of 0.05 nm, however the differences exceed 0.3 nm outside of the original detector. The differences are quadratic in shape as the individual fits are quadratic hence their differences are also quadratic.

The combined fit is made by first assigning each horizontal pixel of each detector the position between 0 and 4095 in pixel coordinates of the CRIRES detectors. A transformation is made into a pseudo-physical pixel coordinates from the left edge of the first detector by including the gaps between the detectors (in pixels). The parameters gap_1 , gap_2 , gap_3 are the three gaps between neighbouring detectors gaps and are defined in pixel space as follows:

$$gap = \begin{cases} 0, & 0 = < psl < 1024 \\ gap_1, & 1024 = < psl < 2048 \\ gap_1 + gap_2, & 2048 = < psl < 3072 \\ gap_1 + gap_2 + gap_3, & 3072 = < psl < 4096 \end{cases}$$

This example does not include the height on the detectors that the spectrum falls or any skewness of the spectrum to pixel rows or any miss-alignment between the detectors. All which could have some affect on a global wavelength calibration.

The pixel widths of these gaps can be fixed to known values (e.g. 282, 278, and 275 pixels (Brogi et al., 2016)) as done in Figure C.1 or allowed to vary and included in the fitting process.

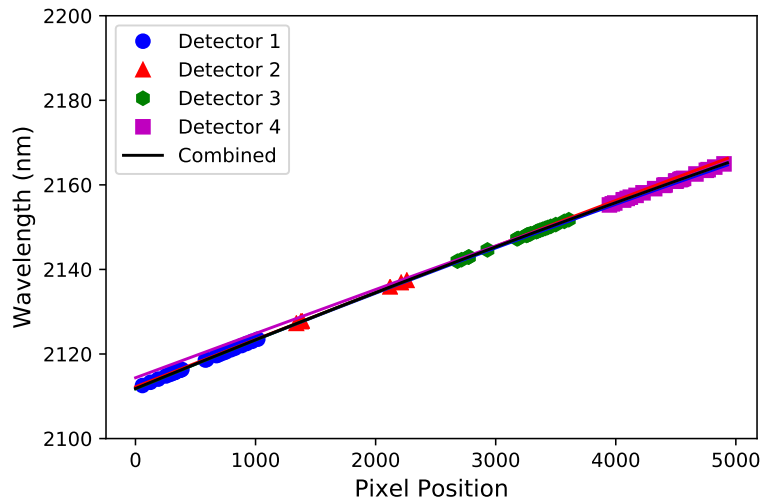


Figure C.1: Pixel-wavelength calibration points for each detector are given by the different markers. The quadratic fit of each individual detector is given with the same corresponding colour. A combined quadratic fit, using fixed detector gaps is shown in black.

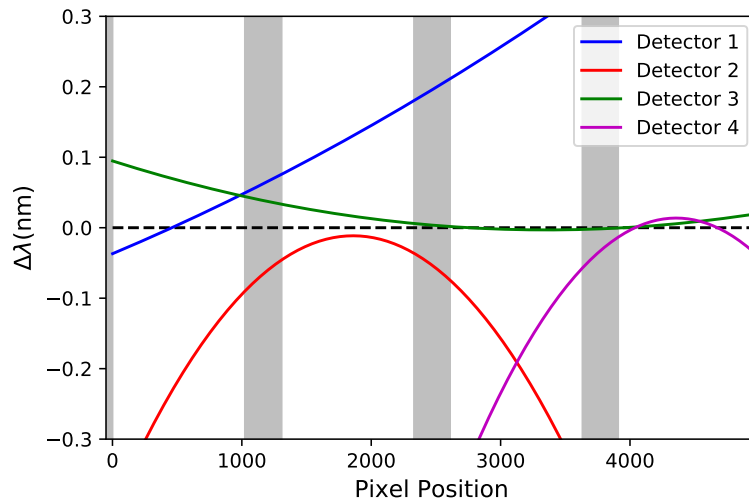


Figure C.2: Wavelength difference of individual quadratic fits to the quadratic fit combined all four detectors and fixed gaps.

Table C.1: Example of multi-detector fitting parameters obtained for the second observation of HD 30501 under different scenarios. Second and third order polynomials are indicated by 2° and 3° respectively.

	Fixed Gaps		Variable Gaps	
Order	2nd	3rd	2nd	3rd
a3 (u)	-	$(-2 \pm 3) \times 10^{-12}$	-	$(-2 \pm 1) \times 10^{-12}$
a2 (q)	$(-1.77 \pm 0.03) \times 10^{-7}$	$(-1.6 \pm 0.2) \times 10^{-7}$	$(-1.65 \pm 0.06) \times 10^{-7}$	$(-1.47 \pm 0.07) \times 10^{-7}$
a1 (m)	0.01170 ± 0.00002	0.01167 ± 0.00005	0.01162149 ± 0.00004	0.01160 ± 0.00001
a0 (b)	2111.83 ± 0.01	2111.84 ± 0.02	2111.86 ± 0.02	2111.87 ± 0.01
gap ₁	283	283	291.7 ± 3.5	291.2 ± 0.9
gap ₂	561	561	570.5 ± 5.4	567.9 ± 1.7
gap ₃	836	836	844.2 ± 7.1	841.3 ± 2.1
χ^2	11.2	10.7	4.6	4.2
χ^2_{red}	0.156	0.151	0.066	0.061
BIC	-129.3	-128.6	-184.1	-186.7

To explore this the same pixels-wavelength points from all detectors are fitted with a second and third order polynomial that includes variable or fixed gaps. Table C.1 shows the fit parameters obtained as well as some fit statistics.

Figure C.3 also show the distribution of the fit parameters for the quadratic fit with fixed (left) and variable gaps (right). These were distributions were obtained using the *emcee* Python package¹, which performs a Markov chain Monte Carlo simulation over the parameter space. The shapes of the cloud of points reveal correlations between different parameters. For instance the narrow diagonals indicate a strong correlation between the parameters given on the axis. There are strong correlations between the quadratic parameters, q, m, b with m being negatively correlated to all other parameters. It also shows strong positive correlations between the variable detector gaps.

The correlations between the polynomial parameters with either fix or variable gaps are almost identical. These are the plot on the left and the top three rows of the right hand plot.

This is just a simple representation of the idea. It has not been pursued further and was not used in this thesis for the wavelength calibration.

¹ <http://dfm.io/emcee/current/>

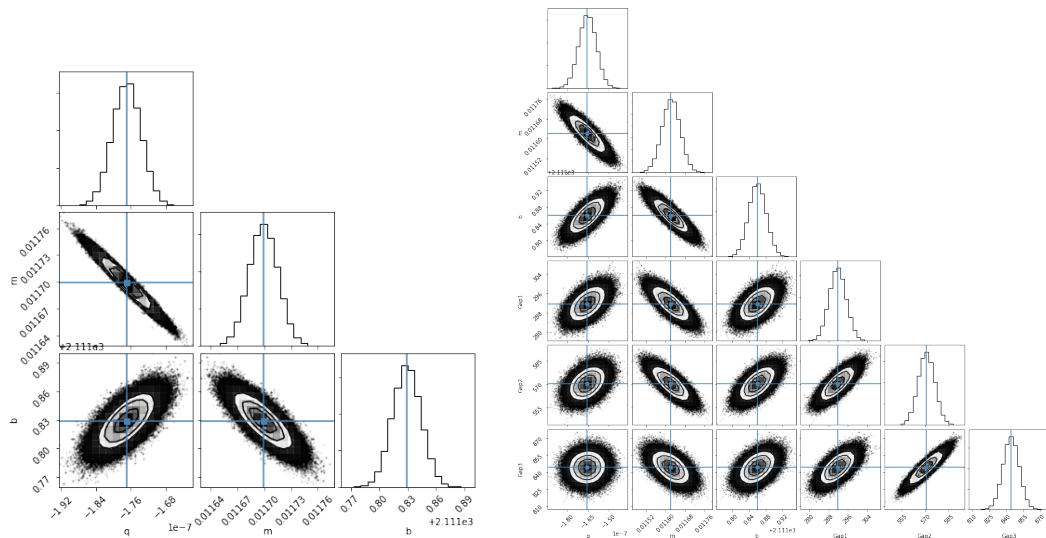


Figure C.3: Corner plots of combined fitting across four detectors. The elliptical point clouds indicate there are correlations between parameters. Left: The combined detector fit with fixed gaps. Right: The combined detector fit with variable gaps.

Appendix D

Vacuum wavelengths

Astronomical light is refracted as it enters Earth's atmosphere, as the medium changes from the vacuum of space and to air. The index of refraction, n , is the factor at which the velocity, v , and wavelength λ of electromagnetic radiation changes from their values in a vacuum.

$$n = \frac{\lambda_{vac}}{\lambda_{air}}, \frac{v_{vac}}{v_{air}} \quad (\text{D.1})$$

The index of refraction of air is very close to 1, but has a complex wavelength dependence which also depends on atmospheric composition (e.g. CO₂, H₂O), temperature and pressure. There are several empirical formula for the index of refraction of air (e.g. Edlén, 1953; Peck et al., 1972; Ciddor, 1996). As an example the refractive index given by Ciddor (1996), based on optical and infrared measurements and valid up to 1.7 μm, is:

$$n - 1 = \frac{0.05792105}{238.0185 - \lambda^{-2}} + \frac{0.00167917}{57.362 - \lambda^{-2}}. \quad (\text{D.2})$$

This is measured at standard, dry air at 15°C, 101.325 kPa and with 450 ppm CO₂. Beyond 1.7 μm there are only theoretical models of the refractive index of air, due to lack of experimental data. For example Mathar (2007) provides theoretical values between 1.3–24 μm for common air pressure and temperature of ground-based observatories.

In this work the spectral wavelengths are extensively specified in a vacuum. The first is because the empirical relations are not valid beyond 1.7 μm, while the CRIRES spectra investigated are observed around 2.1 μm and the CRIRES instrument manual provides all measurements in vacuum wavelengths.

The TAPAS synthetic transmission models Bertaux et al. (2014) used for telluric correction are available for download in vacuum wavelengths or air wavelengths¹. The PHOENIX-ACES library of synthetic spectra used also provide spectra in vacuum wavelengths. Remaining exclusively in vacuum wavelengths means that no errors are introduced from the conversion between air and vacuum wavelengths in the nIR. As such, the vacuum TAPAS models are obtained and the observations calibrated using vacuum wavelengths.

¹ The wavenumber, $1/\lambda$, is also available.

Appendix E

PhD output

This section lists the activities in which I have been involved over the duration of my doctoral training.

In summary, over the duration of my doctoral training:

- I have two first author publications under review, one with the Monthly Notices of the Royal Astronomical Society (MNRAS) and one with Journal of Open Source Software (JOSS) (only requiring minor corrections). A third paper is in preparation.
- I was also involved as a co-author in five more articles (Figueira et al., 2016; Barros et al., 2017; Santerne et al., 2018; Lillo-Box et al., 2018; Ulmer-Moll et al., 2018),
- I also had the opportunity to attend one international conferences, two international schools and one national conference, in which I presented an oral contribution and a poster.
- I tutored at the 11th, 12th, and 13th edition of the Physics Summer School for the Faculty of Science of the University of Porto.
- I was invited to be an English proofreader for an outreach book Figueira et al. (2015).
- I also gained experience as an astronomical observer, with two observing runs, using HARPS-N and ESPRESSO.

This list is detailed further below.

E.1 Publications

A&A 586, A101 (2016)
 DOI: 10.1051/0004-6361/201526900
 © ESO 2016

**Astronomy
 &
 Astrophysics**

Radial velocity information content of M dwarf spectra in the near-infrared

P. Figueira¹, V. Zh. Adibekyan¹, M. Oshagh¹, J. J. Neal^{1,2}, B. Rojas-Ayala¹, C. Lovis³, C. Melo⁴, F. Pepe³, N. C. Santos^{1,2}, and M. Tsantaki¹

¹ Instituto de Astrofísica e Ciências do Espaço, Universidade do Porto, CAUP, Rua das Estrelas, 4150-762 Porto, Portugal
 e-mail: pedro.figueira@astro.up.pt

² Departamento de Física e Astronomia, Faculdade de Ciências, Universidade do Porto, Portugal

³ Observatoire Astronomique de l'Université de Genève, 51 Ch. des Maillettes, – Sauverny – 1290 Versoix, Suisse

⁴ European Southern Observatory, Alonso de Córdova 3107, Vitacura, Casilla 19001, Santiago 19, Chile

Received 6 July 2015 / Accepted 16 October 2015

ABSTRACT

Aims. We evaluate the radial velocity (RV) information content and achievable precision on M0–M9 spectra covering the ZYJHK bands. We do so while considering both a perfect atmospheric transmission correction and discarding areas polluted by deep telluric features, as done in previous works.

Methods. To simulate the M-dwarf spectra, PHOENIX-ACES model spectra were employed; they were convolved with rotational kernels and instrumental profiles to reproduce stars with a $v \sin i$ of 1.0, 5.0, and 10.0 km s⁻¹ when observed at resolutions of 60 000, 80 000, and 100 000. We considered the RV precision as calculated on the whole spectra, after discarding strongly polluted areas, and after applying a perfect telluric correction. In the latter option, we took into account the reduction in the number of recorded photons due to a transmittance lower than unity and considered its effect on the noise of the recorded spectra. In our simulations we paid particular attention to the details of the convolution and sampling of the spectra, and we discuss their impact on the final spectra.

Results. Our simulations show that the most important parameter ruling the difference in attainable precision between the considered bands is the spectral type. For M0–M3 stars, the bands that deliver the most precise RV measurements are the Z, Y, and H band, with relative merits depending on the parameters of the simulation. For M6–M9 stars, the bands show a difference in precision that is within a factor of ~2 and does not clearly depend on the band; this difference is reduced to a factor smaller than ~1.5 if we consider a non-rotating star seen at high resolution. We also show that an M6–M9 spectrum will deliver a precision about two times better as an M0–M3 spectra with the same signal-to-noise ratio. Finally, we note that the details of modeling the Earth atmosphere and interpreting the results have a significant impact on which wavelength regions are discarded when setting a limit threshold at 2–3%. The resolution element sampling on the observed spectra plays an important role in the atmospheric transmission characterization. As a result of the multiparameter nature of the problem, it is very difficult to precisely quantify the impact of absorption by the telluric lines on the RV precision, but it is an important limiting factor to the achievable RV precision.

Key words. techniques: radial velocities – instrumentation: spectrographs – methods: data analysis – stars: low-mass

1. Introduction

The technique of spectroscopy is central to the study of stars and has allowed astronomy to gather a significant body of knowledge from the few photons a star provides us. During the past 20 years, spectroscopy was extensively applied in an emerging field in astronomy: the study of extrasolar planets. Following the discovery of 51 Peg b in 1995 (Mayor & Queloz 1995), more than 1900 planets were discovered, with masses and radii down to those of Earth (e.g., Dumusque et al. 2012; Barclay et al. 2013; Pepe et al. 2013). The radial velocity (RV) technique, with which the very first planet around a solar-type star was found, is still one of the most widely used detection methods; it is the main contributor to our knowledge of the mass of known exoplanets. The hunt for the exoplanet with the lowest mass pushed the RV precision down to the subm/s domain and motivated the construction of instruments such as ESPRESSO, which aims at a precision of 10 cm/s (Mégevand et al. 2012; Pepe et al. 2014b).

The RV signature of a planet scales with the mass of the star with $M_*^{-2/3}$ and with the planetary orbital period with $P_{\text{orb}}^{-1/3}$. For an Earth-mass planet orbiting inside the habitable zone around a solar-type star, the RV amplitude is 10 cm/s, while for a planet with the same characteristics but orbiting an M7 dwarf, the RV amplitude is larger than 1 m/s. This is due to both a lower host mass and a closer habitable zone (a consequence of the lower luminosity output of these hosts). This relatively high amplitude contributed to an increased interest in the search for exoplanets around the low-mass M-dwarf (0.5–0.08 M_\odot) and led to the first estimates of the fraction of M dwarfs hosting Earth-mass planets inside the habitable zone (Bonfils et al. 2013). The intrinsic faintness of the stars in the visible domain limited these surveys to the brightest one hundred stars of our neighborhood and, along with activity, photon noise contribution to the noise budget proved to be the limiting factor. Spurred by the abundance of exoplanets, the exoplanet hunters did not rest in their efforts, and in the last several years, a new research direction

Precise masses for the transiting planetary system HD 106315 with HARPS \star

S. C. C. Barros^{1,2*}, H. Gosselin^{2,23}, J. Lillo-Box³, D. Bayliss⁴, E. Delgado Mena¹, B. Brugger², A. Santerne², D. J. Armstrong⁵, V. Adibekyan¹, J. D. Armstrong⁶, D. Barrado⁷, J. Bento⁸, I. Boisse², A. S. Bonomo⁹, F. Bouchy⁴, D. J. A. Brown⁵, W. D. Cochran¹⁰, A. Collier Cameron¹¹, M. Deleuil², O. Demangeon¹, R. F. Diaz^{4,12,13}, A. Doyle⁵, X. Dumusque⁴, D. Ehrenreich⁴, N. Espinoza^{14,15}, F. Faedi⁵, J. P. Faria^{1,16}, P. Figueira¹, E. Foxell⁵, G. Hébrard^{17,18}, S. Hojjatpanah^{1,16}, J. Jackman⁵, M. Lendl¹⁹, R. Ligi², C. Lovis⁴, C. Melo³, O. Mousis², J. J. Neal^{1,16}, H. P. Osborn⁵, D. Pollacco⁵, N. C. Santos^{1,16}, R. Sefako²⁰, A. Shporer²¹, S. G. Sousa¹, A. H. M. J. Triaud²², S. Udry⁴, A. Vigan², and A. Wyttenbach⁴

¹ Instituto de Astrofísica e Ciências do Espaço, Universidade do Porto, CAUP, Rua das Estrelas, PT4150-762 Porto, Portugal e-mail: susana.barros@astro.up.pt

² Aix Marseille Univ, CNRS, LAM, Laboratoire d'Astrophysique de Marseille, Marseille, France

³ European Southern Observatory (ESO), Alonso de Cordova 3107, Vitacura, Casilla 19001, Santiago de Chile, Chile

⁴ Observatoire Astronomique de l'Université de Genève, 51 Chemin des Maillettes, 1290 Versoix, Switzerland

⁵ Department of Physics, University of Warwick, Gibbet Hill Road, Coventry, CV4 7AL, UK

⁶ Institute for Astronomy, University of Hawaii, 34 Ohia Ku Street, Pukalani, Maui, Hawaii 96790

⁷ Depto. de Astrofísica, Centro de Astrobiología (CSIC-INTA), ESAC campus 28692 Villanueva de la Cañada (Madrid), Spain

⁸ Research School of Astronomy and Astrophysics, Australian National University, Mount Stromlo Observatory, Cotter Road, Weston Creek, ACT 2611, Australia

⁹ INAF – Osservatorio Astrofisico di Torino, Strada Osservatorio 20, I-10025, Pino Torinese (TO), Italy

¹⁰ McDonald Observatory and Department of Astronomy, The University of Texas at Austin, Austin Texas USA

¹¹ Centre for Exoplanet Science, SUPA School of Physics & Astronomy, University of St Andrews, North Haugh ST ANDREWS, Fife, KY16 9SS

¹² Universidad de Buenos Aires, Facultad de Ciencias Exactas y Naturales, Buenos Aires, Argentina

¹³ CONICET - Universidad de Buenos Aires, Instituto de Astronomía y Física del Espacio (IAFE), Buenos Aires, Argentina.

¹⁴ Instituto de Astrofísica, Facultad de Física, Pontificia Universidad Católica de Chile, Av. Vicuña Mackenna 4860, 782-0436 Macul, Santiago, Chile

¹⁵ Millennium Institute of Astrophysics, Av. Vicuña Mackenna 4860, 782-0436 Macul, Santiago, Chile

¹⁶ Departamento de Física e Astronomia, Faculdade de Ciências, Universidade do Porto, Rua Campo Alegre, 4169-007 Porto, Portugal

¹⁷ Institut d'Astrophysique de Paris, UMR7095 CNRS, Université Pierre & Marie Curie, 98bis boulevard Arago, 75014 Paris, France

¹⁸ Aix Marseille Univ, CNRS, OHP, Observatoire de Haute Provence, Saint Michel l'Observatoire, France

¹⁹ Space Research Institute, Austrian Academy of Sciences, Schmiedlstr. 6, 8042, Graz, Austria

²⁰ South African Astronomical Observatory, PO Box 9, Observatory, 7935

²¹ Division of Geological and Planetary Sciences, California Institute of Technology, Pasadena, CA 91125, USA

²² Institute of Astronomy, University of Cambridge, Madingley Road, CB3 0HA, Cambridge, United Kingdom

²³ Université de Toulouse, UPS-OMP, IRAP, Toulouse, France

Received ??, ??; accepted ??

ABSTRACT

Context. The multi-planetary system HD 106315 was recently found in K2 data. The planets have periods of $P_b \sim 9.55$ and $P_c \sim 21.06$ days, and radii of $r_b = 2.44 \pm 0.17 R_\oplus$ and $r_c = 4.35 \pm 0.23 R_\oplus$. The brightness of the host star ($V=9.0$ mag) makes it an excellent target for transmission spectroscopy. However, to interpret transmission spectra it is crucial to measure the planetary masses.

Aims. We obtained high successional radial velocities for HD 106315 to determine the mass of the two transiting planets discovered with Kepler K2. Our successful observation strategy was carefully tailored to mitigate the effect of stellar variability.

Methods. We modelled the new radial velocity data together with the K2 transit photometry and a new ground-based partial transit of HD 106315c to derive system parameters.

Results. We estimate the mass of HD 106315b to be $12.6 \pm 3.2 M_\oplus$ and the density to be $4.7 \pm 1.7 g cm^{-3}$, while for HD 106315c we estimate a mass of $15.2 \pm 3.7 M_\oplus$ and a density of $1.01 \pm 0.29 g cm^{-3}$. Hence, despite planet c having a radius almost twice as large as planet b, their masses are consistent with one another.

Conclusions. We conclude that HD 106315c has a thick hydrogen-helium gaseous envelope. A detailed investigation of HD 106315b using a planetary interior model constrains the core mass fraction to be 5–29%, and the water mass fraction to be 10–50%. An alternative, not considered by our model, is that HD 106315b is composed of a large rocky core with a thick H-He envelope. Transmission spectroscopy of these planets will give insight into their atmospheric compositions and also help constrain their core compositions.

Key words. planetary systems: detection – planetary systems: fundamental parameters – planetary systems: composition— stars: individual HD 106315, EPIC 201437844 – techniques: photometric – techniques: radial velocities

An Earth-sized exoplanet with a Mercury-like composition

A. Santerne¹, B. Brugger¹, D. J. Armstrong², V. Adibekyan³, J. Lillo-Box⁴, H. Gosselin^{1,5}, A. Aguichine^{1,6}, J.-M. Almenara⁷, D. Barrado⁸, S. C. C. Barros³, D. Bayliss⁷, I. Boisse¹, A. S. Bonomo⁹, F. Bouchy⁷, D. J. A. Brown², M. Deleuil¹, E. Delgado Mena³, O. Demangeon³, R. F. Díaz^{10,11,7}, A. Doyle², X. Dumusque⁷, F. Faedi^{2,12}, J. P. Faria^{3,13}, P. Figueira^{4,3}, E. Foxell², H. Giles⁷, G. Hébrard^{14,15}, S. Hojjatpanah^{3,13}, M. Hobson¹, J. Jackman², G. King², J. Kirk², K. W. F. Lam², R. Ligi¹, C. Lovis⁷, T. Louden², J. McCormac², O. Mousis¹, J. J. Neal^{3,13}, H. P. Osborn^{2,1}, F. Pepe⁷, D. Pollacco², N. C. Santos^{3,13}, S. G. Sousa³, S. Udry⁷ & A. Vigan¹

¹Aix Marseille Univ, CNRS, CNES, LAM, Marseille, France

²Department of Physics, University of Warwick, Gibbet Hill Road, Coventry, CV4 7AL, UK

³Instituto de Astrofísica e Ciências do Espaço, Universidade do Porto, CAUP, Rua das Estrelas, 4150-762 Porto, Portugal

⁴European Southern Observatory (ESO), Alonso de Cordova 3107, Vitacura, Casilla 19001, Santiago de Chile, Chile

⁵Université de Toulouse, UPS-OMP, IRAP, Toulouse, France

⁶Paris-Saclay Université, ENS Cachan, 61 av. du Président Wilson, 94230 Cachan, France

⁷Observatoire Astronomique de l'Université de Genève, 51 Chemin des Maillettes, 1290 Versoix, Switzerland

⁸Dept. de Astrofísica, Centro de Astrobiología (CSIC-INTA), ESAC campus 28692 Villanueva de la Cañada (Madrid), Spain

⁹INAF – Osservatorio Astrofisico di Torino, Strada Osservatorio 20, I-10025, Pino Torinese (TO), Italy

¹⁰Universidad de Buenos Aires, Facultad de Ciencias Exactas y Naturales. Buenos Aires, Argentina

¹¹CONICET - Universidad de Buenos Aires. Instituto de Astronomía y Física del Espacio (IAFE). Buenos Aires, Argentina

¹²INAF – Osservatorio Atrofisico di Catania, via S. Sofia 78, 95123, Catania, Italy

¹³Departamento de Física e Astronomia, Faculdade de Ciencias, Universidade do Porto, Rua Campo Alegre, 4169-007 Porto, Portugal

¹⁴Institut d'Astrophysique de Paris, UMR7095 CNRS, Universite Pierre & Marie Curie, 98bis boulevard Arago, 75014 Paris, France

¹⁵Aix Marseille Univ, CNRS, OHP, Observatoire de Haute Provence, Saint Michel l'Observatoire, France

The Earth, Venus, Mars, and some extrasolar terrestrial planets¹ have a mass and radius that is consistent with a mass fraction of about 30% metallic core and 70% silicate mantle². At the inner frontier of the solar system, Mercury has a completely different composition, with a mass fraction of about 70% metallic core and 30% silicate mantle³. Several formation or evolution scenarios are proposed to explain this metal-rich composition, such as a

The *TROY* project: II. Multi-technique constraints on exotrojans in nine planetary systems ★,★★,★★★

J. Lillo-Box¹, A. Leleu², H. Parviainen^{3,4,5}, P. Figueira^{1,6}, M. Mallonn⁷, A.C.M. Correia^{8,9,10}, N.C. Santos^{6,11}, P. Robutel⁸, M. Lendl¹², H.M.J. Boffin¹³, J.P. Faria^{6,11}, D. Barrado¹⁴, J. Neal^{6,11}

¹ European Southern Observatory (ESO), Alonso de Cordova 3107, Vitacura Casilla 19001, Santiago 19, Chile
 e-mail: jllollobox@eso.org

² Physics Institute, Space Research and Planetary Sciences, Center for Space and Habitability - NCCR PlanetS, University of Bern, Bern, Switzerland

³ Instituto de Astrofísica de Canarias (IAC), E-38200 La Laguna, Tenerife, Spain

⁴ Dept. Astrofísica, Universidad de La Laguna (ULL), E-38206 La Laguna, Tenerife, Spain

⁵ Sub-department of Astrophysics, Department of Physics, University of Oxford, Oxford, OX1 3RH, UK

⁶ Instituto de Astrofísica e Ciências do Espaço, Universidade do Porto, CAUP, Rua das Estrelas, PT4150-762 Porto, Portugal

⁷ Leibniz-Institut für Astrophysik Potsdam, An der Sternwarte 16, D-14482 Potsdam, Germany

⁸ IMCCE, Observatoire de Paris - PSL Research University, UPMC Univ. Paris 06, Univ. Lille 1, CNRS, 77 Avenue Denfert-Rochereau, 75014 Paris, France

⁹ Department of Physics, University of Coimbra, 3004-516 Coimbra, Portugal

¹⁰ CIDMA, Departamento de Física, Universidade de Aveiro, Campus de Santiago, 3810-193 Aveiro, Portugal

¹¹ Departamento de Física e Astronomia, Faculdade de Ciências, Universidade do Porto, Portugal

¹² Space Research Institute, Austrian Academy of Sciences, Schmiedlstr. 6, 8042 Graz, Austria

¹³ ESO, Karl Schwarzschild Strasse 2, 85748 Garching, Germany

¹⁴ Depto. de Astrofísica, Centro de Astrobiología (CSIC-INTA), ESAC campus 28692 Villanueva de la Cañada (Madrid), Spain

In preparation

ABSTRACT

Context. Co-orbital bodies are the byproduct of planet formation and evolution, as we know from the Solar System. Although planet-size co-orbitals do not exist in our planetary system, dynamical studies show that they can remain stable for long periods of time in the gravitational well of massive planets. Should they exist, their detection is feasible with the current instrumentation.

Aims. In this paper, we present new ground-based observations searching for these bodies co-orbiting with nine close-in ($P < 5$ days) planets, using different observing techniques. The combination of all of them allows us to restrict the parameter space of any possible trojan in the system.

Methods. We use multi-technique observations (radial velocity, precision photometry and transit timing variations), both newly acquired in the context of the *TROY* project and publicly available, to constrain the presence of planet-size trojans in the Lagrangian points of nine known exoplanets.

Results. We find no clear evidence of trojans in these nine systems through any of the techniques used down to the precision of the observations. However, this allows us to constrain the presence of any potential trojan in the system, specially in the trojan mass/radius versus libration amplitude plane. In particular, we can set upper mass limits in the super-Earth mass regime for six of the studied systems.

Key words. Planets and satellites: gaseous planets, fundamental parameters; Techniques: radial velocity, transits; Minor planets, asteroids: general

1. Introduction

The development of state-of-the-art instrumentation and space-based facilities in the past decades boosted the discovery of extrasolar planets up to several thousands of detections¹. This

plethora has shown the wide diversity of intrinsic and orbital properties that planets can have. Exoplanet research is currently focused on the deep understanding of the planet composition, structure and atmosphere, in parallel to the search for Earth analogues. From our own system, we know that extrasolar systems should also host other components that also played an important role in moulding the architecture and properties of the planets. In the Solar System, moons and more recently trojans (e.g., Lucy mission, Levison et al. 2017) are targets for *in situ* exploration since they contain clues on the formation and early evolution of our planetary system (e.g., Morbidelli et al. 2005; Borisov et al. 2017).

Trojan bodies co-rotate with planets in a wide variety of orbital configurations, mainly in tadpole (orbiting the gravity

* Based on observations collected at the Centro Astronómico Hispano Alemán (CAHA) at Calar Alto, operated jointly by the Max-Planck Institut für Astronomie and the Instituto de Astrofísica de Andalucía (CSIC).

** Partly based on data obtained with the STELLA robotic telescopes in Tenerife, an AIP facility jointly operated by AIP and IAC.

*** Based on observations collected at the European Organisation for Astronomical Research in the Southern Hemisphere under ESO programmes 297.C-5051, 098.C-0440(A), and 298.C-5009

¹ <http://exoplanet.eu>

Telluric correction in the near-infrared: Standard star or synthetic transmission?

S. Ulmer-Moll^{1,2}, P. Figueira^{3,1}, J. J. Neal^{1,2}, N. C. Santos^{1,2}, and M. Bonnefoy⁴

¹ Instituto de Astrofísica e Ciências do Espaço, Universidade do Porto, CAUP, Rua das Estrelas, 4150-762 Porto, Portugal
 e-mail: solene.ulmer-moll@astro.up.pt

² Departamento de Física e Astronomia, Faculdade de Ciências, Universidade do Porto, Portugal

³ European Southern Observatory, Alonso de Córdova 3107, Vitacura, Santiago, Chile

⁴ Univ. Grenoble Alpes, CNRS, IPAG, 38000 Grenoble, France

Received 23 April 2018 / Accepted 10 November 2018

ABSTRACT

Context. The atmospheric absorption of the Earth is an important limiting factor for ground-based spectroscopic observations and the near-infrared and infrared regions are the most affected. Several software packages that produce a synthetic atmospheric transmission spectrum have been developed to correct for the telluric absorption; these are Molecfit, TelFit, and Transmissions Atmosphériques Personnalisées pour l’AStrophysique (TAPAS).

Aims. Our goal is to compare the correction achieved using these three telluric correction packages and the division by a telluric standard star. We want to evaluate the best method to correct near-infrared high-resolution spectra as well as the limitations of each software package and methodology.

Methods. We applied the telluric correction methods to CRIRES archival data taken in the *J* and *K* bands. We explored how the achieved correction level varies depending on the atmospheric T-P profile used in the modelling, the depth of the atmospheric lines, and the molecules creating the absorption.

Results. We found that the Molecfit and TelFit corrections lead to smaller residuals for the water lines. The standard star method corrects best the oxygen lines. The Molecfit package and the standard star method corrections result in global offsets always below 0.5% for all lines; the offset is similar with TelFit and TAPAS for the H₂O lines and around 1% for the O₂ lines. All methods and software packages result in a scatter between 3% and 7% inside the telluric lines. The use of a tailored atmospheric profile for the observatory leads to a scatter two times smaller, and the correction level improves with lower values of precipitable water vapour.

Conclusions. The synthetic transmission methods lead to an improved correction compared to the standard star method for the water lines in the *J* band with no loss of telescope time, but the oxygen lines were better corrected by the standard star method.

Key words. atmospheric effects – radiative transfer – instrumentation: spectrographs – methods: data analysis – techniques: spectroscopic

1. Introduction

In ground-based observations, the light coming from a celestial object is partly or totally absorbed by the Earth’s atmosphere, a phenomenon that is strongly wavelength dependent. Even if the position of an observatory is carefully chosen to minimize the impact of the atmosphere, there is still a need to correct for telluric absorption. In spectroscopic studies, the species present in the atmosphere imprint absorption or emission lines on top of the spectra of the target. In absorption, the telluric lines create what is called the transmission spectrum of the Earth’s atmosphere. The volume mixing ratio of the different molecules as a function of height (that can be understood in terms of density profile) present in the atmosphere and the atmospheric conditions (pressure, temperature) affect the telluric lines in their shape, depth, and position in wavelengths. High winds can shift the telluric features, Figueira et al. (2012) showed that a horizontal wind model can account for some of these shifts and is in agreement with radiosonde measurements. Thus, the transmission spectrum depends strongly on the time and location of the observations. Every molecule contributes differently to the final transmission. For example, H₂O leads to an absorption over a very wide wavelength range, spanning the optical, near-infrared,

and infrared. This absorption defines the near-infrared bands on which photometry and spectroscopy was performed for many years. The water vapour shows hourly to seasonal variations that are challenging to correct (Adelman et al. 2003; Wood 2003). O₂ absorption might be easier to correct because it provides sharp, deep, and well-defined features and the O₂ volume mixing ratio is more stable in the atmosphere. O₂ bands and individual lines in the optical have been studied for a long time (Wark & Mercer 1965; Caccin et al. 1985). When observations are done through cirrus clouds, the atmospheric transmission is not impacted. Cirrus clouds are thin clouds made of ice crystals and usually found at altitudes higher than 6 km (Wylie et al. 1994). The ice crystals transmit most of the incoming stellar light and do not introduce narrow water features in the transmission spectrum.

A correction of telluric absorption is required when the studies aim at high spectral fidelity; for example it is an essential step to characterize planetary and exoplanetary atmospheres (e.g. Bailey et al. 2007; Cotton et al. 2014; Brogi et al. 2014). Telluric correction has also been studied in the context of exoplanet search through radial velocity (RV) measurements.

Earlier on, the telluric lines started to be used as a wavelength calibration to measure precise radial velocities

E.2 Talks and Seminars

TALK

Towards exoplanetary atmospheres: new data reduction techniques for the nIR.

Location: XXVI Encontro Nacional de Astronomia e Astrofísica (ENAA), Aveiro, Portugal
Date: 2016, Sept. 09

Website: <http://gravitation.web.ua.pt/enaa2016/index2a62.html?q=node/3>

Abstract:

Exoplanetary atmospheres are one of the forefronts of exoplanet science. The measurement of exoplanet atmospheres can help break degeneracies in the mass-radius relationship for solid exoplanets allowing proper derivation of the planets properties, and may provide important clues to the origin and evolution of planets. The technological breakthrough of high-resolution spectrographs ($\Delta\lambda/\lambda = 100,000$) allow for the separation and wavelength tracking of individual molecular spectral features. This allows for the separation of the stationary telluric absorption lines from the moving planet-star spectral lines. We focus our initial investigation on extracting the atmospheric signal of brown dwarfs, which are interesting objects between giant planets and small stars. Brown dwarf targets are good candidates to begin our investigation as their larger mass induces larger radial velocity shifts to the atmospheric lines and their larger radius (and surface area) produce a stronger signal compared to smaller planets. In this talk I will discuss the ongoing work of my PhD towards extracting the signal of brown dwarf atmospheres from high-resolution nIRspectra. I will discuss the methodology and techniques developed towards extracting the spectral lines of the atmospheres and show some of our current results.

E.3 Posters

POSTER

Towards Exoplanet Atmospheres: new data reduction for the nIR

Location: IVth Azores International Advanced School in **Date:** 2016, July 17–27
Space Sciences, Horta, Faial, Azores Islands,
Portugal

Website: <http://www.iastro.pt/research/conferences/faial2016/>

Abstract:

In this poster I outline the goal of the direct subtraction technique, detailing the data preparation and correct steps needed. It shows the first results of applying the direct subtraction on our observations. The poster is provided on the next page.

POSTER

Towards Exoplanet Atmospheres: new data reduction for the nIR

Location: *XXVI Encontro Nacional de Astronomia e Astrofísica (ENAA), Aveiro, Portugal* **Date:** 2016, Sept. 09

Abstract:

I presented the same poster at ENAA as I did at the IVth Azores International Advanced School in Space Sciences.



Towards Exoplanet Atmospheres: new data reduction for the nIR

Jason J. Neal, P. Figueira, N. C. Santos, C. H. F. Melo

1) Objective

- Reduce near-Infrared CRIRES spectra with high fidelity
- Extract spectra of exoplanetary atmospheres

2) Methods

- CRIRES reduction with in-house IRAF pipeline: Data Reduction Algorithm for CRIRES Spectra (DRACS).
- Obtain models of atmospheric absorption spectra from TAPAS web-service [Bertaux *et al.* 2014, A&A, 564, A96].

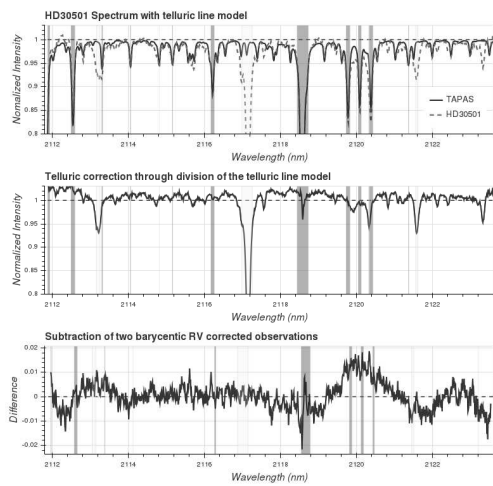
$$I_{tell}(\lambda) = 1 - \sum_{j=1}^m \text{Telluric lines} \quad (1)$$

- Wavelength calibrate the observations using the telluric absorption spectrum imprinted by the atmosphere.

$$I_{obs}(pix) = 1 - \left(\sum_{j=1}^m \text{Telluric} \times \sum_{k=1}^n \text{Stellar} \right) \quad (2)$$

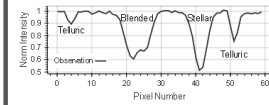
- Correct observations for telluric absorption by dividing by the same TAPAS telluric absorption models.
- Correct for Earth's barycentric motion then subtract two observations to cancel out the stellar absorption lines.

4) Results

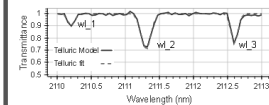


3) Calibration

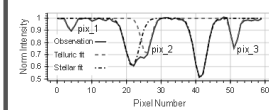
Simulated observation of 2 stellar and 3 telluric lines



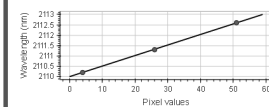
Fit Eq. 1 to telluric model to obtain the line centers in wavelength space (wl_i).



Fit Eq. 2 to the observation to obtain the telluric line centers in pixel space (pix_i).



A second order polynomial is applied to the fitted gaussian line centers wl_i and pix_i .



5) Future Work

- Model and extract the exoplanetary lines in the subtracted spectra.
- Apply these tools to 7 stars that host brown dwarf companions.

E.4 Attended Conferences and Schools

CONFERENCE

Towards Other Earths II:The star-planet connection

Location: Porto, Portugal

Date: 2014, Sept. 15–19

Website: <http://www.astro.up.pt/investigacao/conferencias/toe2014/>

Description:

The study of extrasolar planets is one of the most active areas of research of modern astronomy. The number of discoveries attests for the importance of a topic that reaches out and captivates the imagination of scientists and public alike. This conference aims at reviewing the state of the art of star-planet connection, with some focus on the detection and characterization of Earth like planets orbiting other stars. We propose to debate how the field of extrasolar planets will evolve in respect to this and how it will face the challenges of the upcoming years.

CONFERENCE

I Vietri Advanced School on Exoplanetary Science

Location: Vietri sul Mare (Salerno), Italy

Date: 2015, May 25–29

Website: <http://www.iiassvietri.it/en/asex2015.html>

Description:

The School was aimed to provide a comprehensive, state-of-the-art picture of a variety of relevant aspects of the fast-developing, highly interdisciplinary field of extrasolar planets research. The Lecture topics of the School were focused on exoplanet detection with the Radial Velocity, Photometric Transits, Gravitational Microlensing, and Direct Imaging techniques. The Lectures were delivered by four senior researchers to an audience of graduate students, Ph.D students and young post-docs.

CONFERENCE

IVth Azores International Advanced School in Space Sciences

Location: Horta, Faial, Azores Islands, Portugal **Date:** 2016, July 17–27

Website: <http://www.iastro.pt/research/conferences/faial2016/>

Description:

This International Advanced School addresses the topics at the forefront of scientific research being conducted in the fields of stellar physics and exoplanetary science.

The School covers two scientific topics that share many synergies and resources: Asteroseismology and Exoplanets. Therefore, the program aims at building opportunities for cooperation and sharing of methods that will benefit both communities. This cooperation has experienced great success in the context of past space missions such as CoRoT and Kepler. Upcoming photometry and astrometry from space, as well as complementary data from ground-based networks, will continue to foster this cooperation. Observations of bright stars and clusters in the ecliptic plane are being made by the re-purposed K2 mission, and NASA's TESS and ESA's CHEOPS missions will soon start obtaining similar data over the entire sky. ESA's PLATO mission will then build upon these successes by providing photometric light curves on a wealth of stars. Ground-based spectroscopy from the Stellar Observations Network Group (SONG) will complement the satellite data for the brightest stars in the sky, as will also be the case with the new generation of high-precision spectrographs being developed for the ESO, like the Echelle SPectrograph for Rocky Exoplanets and Stable Spectroscopic Observations (ESPRESSO).

CONFERENCE

XXVI Encontro Nacional de Astronomia e Astrofísica

Location: Aveiro, Portugal **Date:** 2016, Sept. 08–09

Website: <http://gravitation.web.ua.pt/enaa2016/index2a62.html?q=node/3>

Description:

The main goal of this national meeting is to present a general overview of the international state of the art research done in Astronomy and Astrophysics. ENAA also allows for researchers to get together and discuss scientific ideas and policies, strengthen the collaboration between national researchers and integrate young researchers in the community through the presentation of their work.

E.5 Outreach

PROOF READING

Astro Homus

Location: Porto, Portugal

Date: 2015 May

Website: <http://astrohomus.astro.up.pt/livro>

Description:

Was involved in proofreading the outreach book *Astro Homus* (Figueira et al., 2015) which highlights the people working in Astronomy. The proofreading was for the English component of the book.



A S T R O • H O M U S

P E D R O F I G U E I R A - S U S A N A N E V E S

E.6 Other

TEACHING

Monitor at the 11th, 12th, 13th Physics Summer School

Location: Faculty of Science, University of Porto, Portugal **Date:** 2015–2017

tugal

Website: <http://e-fisica.fc.up.pt/edicoes/>

Description:

Instructing and monitoring 4–5 secondary school students through activities related to planet detection and characterization. One week per year.

Na sua Edição a Escola desafia os participantes com o programa mais radical de sempre com projectos envolvendo lasers, supercondutores, nanotecnologias, física espacial, fibras ópticas, biosensores e astrofísica. Projectos que abrangem as três grandes áreas de investigação do DFA, Física, Astronomia e Engenharia Física. Assim, se tens apetência pelo conhecimento e pelo processo de investigação que permite inquirir a Natureza e testar hipóteses acerca das causas das coisas, então deixa-te arrastar pelo encantamento da experimentação e do entendimento das ideias mais profundas e abrangentes. O DFA garante uma viagem através do Universo, do microcosmo ao macrocosmo, inserindo-te num projecto que te dilatará a imaginação. Tens coragem? Aparece!

OBSERVING

HARPS-N@Telescopio Nazionale Galileo observing run

Location: La Palma, Spain

Date: 2017 Feb. 6–8

Website: <http://www.tng.iac.es/instruments/harps/>

Description:

Observing runs are an essential part of the training of any astronomer. During my PhD I had the opportunity to observe for 3 nights on HARPS-N. These were for the *TROY* project, with which some IA-Porto researchers were collaborating. These observations were to fill in the phase curve of previously detected low-mass exoplanets to further constrain their masses. These observations were used in Lillo-Box et al. (2018).

OBSERVING**ESPRESSO@VLT****Location:** Paranal, Chile**Date:** 2019 Jan. 4–10**Website:** <https://www.eso.org/sci/facilities/paranal/instruments/espresso.html>**Description:**

An observing run with ESPRESSO at Paranal was completed between 4–10 January 2019. This observed the transit of WASP-121 as part of the ESPRESSO GTO program in P102 as well as observing several transit follow up targets and targets for Radial Velocity blind searches.

E.7 Proposal

This is the original observing proposal for the CRIRES data used in this work.



EUROPEAN SOUTHERN OBSERVATORY

Organisation Européenne pour des Recherches Astronomiques dans l'Hémisphère Austral
Europäische Organisation für astronomische Forschung in der südlichen Hemisphäre

OBSERVING PROGRAMMES OFFICE • Karl-Schwarzschild-Straße 2 • D-85748 Garching bei München • e-mail: opo@eso.org • Tel.: +49-89-32 00 64 73

APPLICATION FOR OBSERVING TIME

PERIOD: **89A**

Important Notice:

By submitting this proposal, the PI takes full responsibility for the content of the proposal, in particular with regard to the names of CoIs and the agreement to act according to the ESO policy and regulations, should observing time be granted

1. Title	Category: C-7							
Uncovering the true frequency of close brown dwarf companions to Sun-like stars								
2. Abstract / Total Time Requested								
Total Amount of Time: 0 nights VM, 9.6 hours SM								
We propose to use CRIRES to validate or refute the brown dwarf candidates presented recently by Sahlmann et al. (2011). The objective is to recover the spectra of the companion, an attempt made possible in the IR by the much higher contrast (relative to the visible) between a stellar host and a brown dwarf companion. We show that it is within our capabilities to detect companions down to $80 M_{Jup}$, and thus exclude the companions in our sample from the stellar domain. This will lead to a re-evaluation of the number of brown dwarfs yielded by one of the most complete surveys up to date, and improve the statistics on the determination of the brown-dwarf desert limits. The change in frequency of brown dwarfs around main-sequence stars can go up to 45 %, from 0.66% to 0.36%, providing the most stringent constraints ever on the presence of such companions.								
3. Run Period Instrument Time Month Moon Seeing Sky Mode Type								
A	89	CRIRES	9.6h	any	n	1.2	THN	s
4. Number of nights/hours		Telescope(s)	Amount of time					
a) already awarded to this project:								
b) still required to complete this project:								
5. Special remarks:								
6. Principal Investigator:		Pedro Figueira, pedro.figueira@astro.up.pt, P, Centro de Astrofísica da Universidade do Porto						
6a. Co-investigators:								
R.	Diaz	Institut d'astrophysique de Paris,F						
J.	Sahlmann	Observatoire Astronomique de l'Universite de Geneve,CH						
N.C.	Santos	Centro de Astrofísica da Universidade do Porto,P						
I.	Bosse	Centro de Astrofísica da Universidade do Porto,P						
<i>Following CoIs moved to the end of the document ...</i>								
7. Is this proposal linked to a PhD thesis preparation? State role of PhD student in this project								

8. Description of the proposed programme

A – Scientific Rationale: The absence of brown dwarfs at orbital distances smaller than 10 AU, when compared with the abundance of both planets and stars, remains largely unexplained. In contrast with the abundance of massive planets ($M > 50 M_{\oplus}$, with $P < 10$ yr) around main-sequence hosts (14% according to Mayor et al. 2011, submitted to A&A, arXiv e-print:1109.2497) and the high-frequency of stellar binaries (60% by Duquennoy & Mayor 1991, A&A, 248 485), the very few brown dwarf detections correspond to a comparatively very small fraction: only 50 companions were detected through planetary surveys in the mass range of 13–80 M_{Jup} (e.g. Bouchy et al. 2011, A&A, 525A, 68). Marcy and Butler (2000, PASP, 112, 137) quoted a frequency of close-in brown dwarfs around main-sequence stars inferior to 0.5%, a number confirmed recently by the work of Sahlmann et al. (2011, A&A, 525, A95), who reached an upper limit of 0.6%. The work of Sahlmann et al. (2011) went further than many of its kind: it combined precise radial velocities with Hipparcos astrometry to detect low-mass companions, and increased by 20% the number of potential brown-dwarf companions. Moreover, it proposed a dividing line between the planet and stellar population based on the absence of companions in the mass range 25–45 M_{Jup} ; this feature, even though based on small-number statistics, emerges as significant for the first time.

Of the proposed companions, 10 remain candidate brown dwarfs, since their true mass could not be recovered by the combination of radial velocity measurements and astrometry. The assessment of the true nature of these objects would allow to better constrain the frequency of brown-dwarfs around main-sequence stars and improve our knowledge on the diving line between the two classes of objects. This would provide highly valuable insight into the formation mechanisms of both stars and planets, who currently lack of observational constraints in what concerns allowed mass. The confirmation of a dividing line in mass would allow to constrain these formation models, which currently produce planet populations and stellar populations that overlap (e.g. Mordasini et al 2009, A&A, 501 1139).

B – Immediate Objective: We propose to use the CRIRES spectrograph to measure the IR spectra of 7 candidate brown dwarf companions and determine if they are of stellar nature. We show that it is possible to detect an object at the mass boundary of 80 M_{Jup} ($= 0.076 M_{\odot}$, or spectral type M7–M8) in the K band due to high contrast relative to the host star, depicted in the extreme V–K color indexes (> 7.8).

Out of the 10 systems with putative brown dwarfs presented by Sahlmann et al. (2011), 6 are observable at less than airmass 1.5 from Paranal for Period 89. These are located at distances 20–50 pc which corresponds to an apparent K magnitude of 10–12 for an M8 companion. The last companion is located around HD 30501, for which an orbit was determined, locating its mass at 90 M_{Jup} . Close to the boundary limit, this object will be used as a proof of concept for our study.

The removal of 5 candidates from the current statistics would change the final frequency from $11/1650 = 0.66\%$ to $6/1650 = 0.36\%$, providing the most stringent constraints on close brown dwarf frequency ever.

Observing strategy: We will schedule two observations per star in order to obtain two different and clearly separated radial-velocities for the secondary; clearly separated means with a relative shift much larger than the width of its lines, i.e., of several km/s. Due to the close projected separation in the sky between each star and each companion ($\lesssim 0.2$ arcsec), the light of the companion will enter the CRIRES slit and be superimposed with the main spectrum.

Data reduction strategy: The observation in two different epochs will allow to disentangle the different components of the spectra. The observations will be performed in an atmospheric window in the K band in order to reduce absorption introduced by our own atmosphere (2.120–2.174 μm , for details see Barnes et al. (2008, MNRAS, 390 1258)). We will use LBLRTM (Clough et al. 2005, J. Quant. Spectrosc. Radiat. Transfer, 91, 233) forward model to correct for the telluric absorption; the main-sequence spectra will be removed by shifting the two (corrected) spectra back to the same referential and subtracting one by the other. This will cancel the stellar lines and leave a spectra with the double of the photon noise but on which the signature of an M8 star will be apparent. Our calculations, considering the difference in photon noise introduced by the subtraction of the spectra and the increased photon noise due to the primary, show that the final spectra will have a $S/N > 7$ for integration times of 30 min (see *Time Justification* box for more). This signal can be easily recovered by correlating it with a M8 binary mask derived from atmospheric models (e.g. Barman et al. 2005, ApJ, 632, 1132).

This project is particularly interesting because it will pave the way to direct detection of emission of massive planets in the IR, a domain largely unexplored. While all attempts so far resulted in non-detections (e.g. Barnes et al. 2008) we propose to approach the extreme ratios from the stellar side, a domain in which the contrast is by far more favorable.

8. Description of the proposed programme and attachments

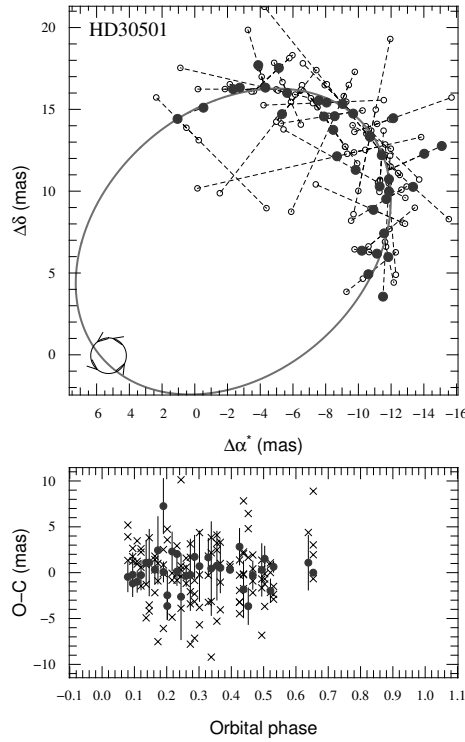


Fig. 1: Top panels: Astrometric stellar orbit of HD301501 projected on the sky. North is up and east is left. The solid red line shows the orbital solution and open circles mark the individual Hipparcos measurements. Bottom panels: OC residuals for the normal points of the orbital solution (filled blue circles) and of the standard 5-parameter model without companion (black crosses). From Sahlmann et al. (2011), for details check original reference.

9. Justification of requested observing time and observing conditions

Lunar Phase Justification: Bright targets and near-IR observations: no particular lunar phase required. Ephemerides will be used to make sure that targets lie at more than 60° from the Moon, but this will provide no stringent constraints due to the wide period in which observations are feasible.

Time Justification: (including seeing overhead) When we observe these objects we get an increased photon noise because we are collecting the photons from the parent star too. In order to calculate the true photon noise we compared the photon noise we will have with that of a single star (the companion). If we take into account that we are subtracting two stellar spectra and, assuming that the photon noise of the sum is well approximated by that of the primary, one gets:

$$\text{Noise}(B)/\text{Noise}(A) = \sqrt{2} * \sqrt{F_A/F_B} = \sqrt{2} * \sqrt{100((m_B - m_A)/5)}$$

From Hipparcos parallax one can calculate the apparent magnitude of these M dwarfs and considering as reference $m_A=7.0$ and $m_B=10.5$ we have $N(B)/N(A) = 7.09$.

This means that we reduce the S/N obtained for the spectra by this factor. For an observation with slit width of 0.4'' and NoAO (DIT=600s, NDIT=3) one will have: $52.7/7.09 = 7.43$ of S/N in the secondary. Note that a magnitude difference of 3.5 corresponds to a flux ratio of 1/25, much more favorable than those usually attempted in most direct detection campaigns. The different primary target K magnitudes lead to an adjustment to different final integration times.

9a. Telescope Justification:

CRIRES is the only available high resolution near-IR spectrograph in the southern hemisphere.

9b. Observing Mode Justification (visitor or service):

Visitor mode better suited given the proposed observing schedule.

9c. Calibration Request:

Standard Calibration

10. Report on the use of ESO facilities during the last 2 years

184.C-0639 'Characterization of the unique transiting exoplanets detected from the CoRoT space mission' (PI Bouchy)

086.C-0680, 087.C-0567, and 088.C-0679: Exploring planetary and substellar companions of L dwarfs. (PI Sahlmann)

10a. ESO Archive - Are the data requested by this proposal in the ESO Archive (<http://archive.eso.org>)? If so, explain the need for new data.

No.

10b. GTO/Public Survey Duplications:**11. Applicant's publications related to the subject of this application during the last 2 years**

Sahlmann, J.; Sgransan, D.; Queloz, D. et al., 2011, A&A, 525A, 95: "Search for brown-dwarf companions of stars"

Sahlmann, J., Lovis, C., Queloz, D., Segransan, D., 2011, A&AL, 528: HD5388 b is a 69 M_{Jup} companion instead of a planet

Díaz R F, Santerne A, Sahlmann J, et al., 2011, submitted to A&A: "The SOPHIE search for northern extrasolar planets IV. Massive companions in the planet-brown dwarf boundary"

Figueira, P.; Pepe, F.; Melo, C. H. F. et al. 2010, A&A, 511A, 55: "Radial velocities with CRIRES. Pushing precision down to 5-10 m/s"

Bouchy F, Bonomo A, Santerne S, et al., 2011, A&A, 533, 83: "SOPHIE velocimetry of Kepler transit candidates. III. KOI-423b: an 18 MJup transiting companion around an F7IV star"

12. List of targets proposed in this programme

Run	Target/Field	α (J2000)	δ (J2000)	ToT	Mag.	Diam.	Additional info	Reference star
A	HD 30501	04 45 38.5	-50 04 27.2	1.2	5.53		K band magnitude	
A	HD 4747	00 49 26.8	-23 12 44.9	1.2	5.31		K band magnitude	
A	HD 162020	17 50 38.4	-40 19 06.1	1.8	7.03		K band magnitude	
A	HD 167665	18 17 23.8	-28 17 20.3	1.2	5.04		K band magnitude	
A	HD 168443	18 20 03.9	-09 35 44.6	1.2	5.31		K band magnitude	
A	HD 202206	21 14 57.8	-20 47 21.2	1.4	6.47		K band magnitude	
A	HD 211747	22 19 15.6	+08 45 06.5	1.4	6.37		K band magnitude	

13. Scheduling requirements

This proposal involves time-critical observations, or observations to be performed at specific time intervals.

14. Instrument configuration

Period	Instrument	Run ID	Parameter	Value or list
89	CRIRES	A	no-AO	K band: 2.120-2.174 μ m

6b. Co-investigators:

...continued from box 6a.

F.	Bouchy	Institut d'astrophysique de Paris,F
G.	Hebrard	Institut d'astrophysique de Paris,F
F.	Pepe	Observatoire Astronomique de l'Universite de Geneve,CH
D.	Segransan	Observatoire Astronomique de l'Universite de Geneve,CH

Bibliography

- Adams, E. R., S. Seager, and L. Elkins-Tanton (2008). “Ocean Planet or Thick Atmosphere: On the Mass-Radius Relationship for Solid Exoplanets with Massive Atmospheres”. In: *The Astrophysical Journal* 673, pp. 1160–1164.
- Adibekyan, V. Z., S. G. Sousa, N. C. Santos, E. D. Mena, et al. (2012). “Chemical Abundances of 1111 FGK Stars from the HARPS GTO Planet Search Program - Galactic Stellar Populations and Planets”. In: *Astronomy and Astrophysics* 545, A32.
- Allard, F. (2013). “The BT-Settl Model Atmospheres for Stars, Brown Dwarfs and Planets”. In: *Proceedings of the International Astronomical Union* 8.S299. 00007, pp. 271–272.
- Allard, F., D. Homeier, and B. Freytag (2010). “Model Atmospheres From Very Low Mass Stars to Brown Dwarfs”. In: 00066. arXiv: 1011.5405 [astro-ph].
- (2012a). “Models of Very-Low-Mass Stars, Brown Dwarfs and Exoplanets”. In: *Philosophical Transactions of the Royal Society of London Series A* 370. 00280, pp. 2765–2777.
- Allard, F., D. Homeier, B. Freytag, and C. M. Sharp (2012b). “Atmospheres From Very Low-Mass Stars to Extrasolar Planets”. In: EAS Publications Series. Vol. 57. eprint: arXiv:1206.1021, pp. 3–43.
- Allard, F. and P. H. Hauschildt (1995). “Model Atmospheres for M (Sub)Dwarf Stars. 1: The Base Model Grid”. In: *The Astrophysical Journal* 445, pp. 433–450.
- Allard, F., P. H. Hauschildt, D. R. Alexander, A. Tamai, and A. Schweitzer (2001). “The Limiting Effects of Dust in Brown Dwarf Model Atmospheres”. In: *The Astrophysical Journal* 556, pp. 357–372.
- Allart, R., V. Bourrier, C. Lovis, D. Ehrenreich, et al. (2018). “Spectrally Resolved Helium Absorption from the Extended Atmosphere of a Warm Neptune-Mass Exoplanet”. In: *Science* 362.6421, p. 1384.
- Alonso, R., T. M. Brown, G. Torres, D. W. Latham, et al. (2004). “TrES-1: The Transiting Planet of a Bright K0 V Star”. In: *The Astrophysical Journal Letters* 613, pp. L153–L156.
- Andreasen, D. T., S. G. Sousa, E. Delgado Mena, N. C. Santos, M. Tsantaki, B. Rojas-Ayala, and V. Neves (2016). “Near-Infrared Spectroscopy of the Sun and HD 20010. Compiling a New Line List in the near-Infrared”. In: *Astronomy and Astrophysics* 585, A143.
- Artigau, É., D. Kouach, J.-F. Donati, R. Doyon, et al. (2014). “SPIRou: The near-Infrared Spectropolarimeter / High-Precision Velocimeter for the Canada-France-Hawaii Telescope”. In: *Proc. SPIE*. Ground-Based and Airborne Instrumentation for Astronomy V. Vol. 9147. 00047. International Society for Optics and Photonics, p. 914715.

- Artigau, É., L. Malo, R. Doyon, P. Figueira, X. Delfosse, and N. Astudillo-Defru (2018). “Optical and Near-Infrared Radial Velocity Content of M Dwarfs: Testing Models with Barnard’s Star”. In: *The Astronomical Journal* 155, p. 198.
- Asplund, M., N. Grevesse, A. J. Sauval, and P. Scott (2009). “The Chemical Composition of the Sun”. In: *Annual Review of Astronomy and Astrophysics* 47, pp. 481–522.
- Astudillo-Defru, N., X. Bonfils, X. Delfosse, D. Ségransan, et al. (2015). “The HARPS Search for Southern Extra-Solar Planets. XXXVI. Planetary Systems and Stellar Activity of the M Dwarfs GJ 3293, GJ 3341, and GJ 3543”. In: *Astronomy and Astrophysics* 575, A119.
- Bagnuolo Jr., W. G. and D. R. Gies (1991). “Tomographic Separation of Composite Spectra - The Components of the O-Star Spectroscopic Binary AO Cassiopeiae”. In: *The Astrophysical Journal* 376, pp. 266–271.
- Bailey, J., A. Simpson, and D. Crisp (2007). “Correcting Infrared Spectra for Atmospheric Transmission”. In: *Publications of the Astronomical Society of the Pacific* 119, pp. 228–236.
- Baraffe, I., G. Chabrier, T. Barman, F. Allard, and P. H. Hauschildt (2003). “Evolutionary Models for Cool Brown Dwarfs and Extrasolar Giant Planets. The Case of HD 20945”. In: *Astronomy and Astrophysics* 402.2. 00000, pp. 701–712. arXiv: astro-ph/0302293.
- Baraffe, I., D. Homeier, F. Allard, and G. Chabrier (2015). “New Evolutionary Models for Pre-Main Sequence and Main Sequence Low-Mass Stars down to the Hydrogen-Burning Limit”. In: *Astronomy and Astrophysics* 577. 00280, A42. arXiv: 1503.04107.
- Baranne, A., D. Queloz, M. Mayor, G. Adrianzyk, et al. (1996). “ELODIE: A Spectrograph for Accurate Radial Velocity Measurements.” In: *Astronomy and Astrophysics Supplement Series* 119, pp. 373–390.
- Barber, R. J., J. Tennyson, G. J. Harris, and R. N. Tolchenov (2006). “A High-Accuracy Computed Water Line List”. In: *Monthly Notices of the Royal Astronomical Society* 368.3, pp. 1087–1094.
- Barclay, T., J. Pepper, and E. V. Quintana (2018). “A Revised Exoplanet Yield from the Transiting Exoplanet Survey Satellite (TESS)”. In: *ArXiv e-prints* 1804, arXiv:1804.05050.
- Barge, P., A. Baglin, M. Auvergne, H. Rauer, et al. (2008). “Transiting Exoplanets from the CoRoT Space Mission. I. CoRoT-Exo-1b: A Low-Density Short-Period Planet around a G0V Star”. In: *Astronomy and Astrophysics* 482, pp. L17–L20.
- Barman, T. S., B. Macintosh, Q. M. Konopacky, and C. Marois (2011). “Clouds and Chemistry in the Atmosphere of Extrasolar Planet HR8799b”. In: *The Astrophysical Journal* 733, p. 65.
- Barnes, J. R., T. S. Barman, H. R. A. Jones, C. J. Leigh, A. C. Cameron, R. J. Barber, and D. J. Pinfield (2008). “HD 179949b: A Close Orbiting Extrasolar Giant Planet with a Stratosphere?” In: *Monthly Notices of the Royal Astronomical Society* 390.3, pp. 1258–1266.
- Barnes, J. W. (2007). “Effects of Orbital Eccentricity on Extrasolar Planet Transit Detectability and Light Curves”. In: *Publications of the Astronomical Society of the Pacific* 119.859, p. 986.
- Barros, S. C. C., H. Gosselin, J. Lillo-Box, D. Bayliss, et al. (2017). “Precise Masses for the Transiting Planetary System HD 106315 with HARPS”. In: *Astronomy & Astrophysics* 608, A25.
- Batista, V., J.-P. Beaulieu, D. P. Bennett, A. Gould, J.-B. Marquette, A. Fukui, and A. Bhattacharya (2015). “Confirmation of the OGLE-2005-BLG-169 Planet Signature and Its Characteristics with Lens-Source Proper Motion Detection”. In: *The Astrophysical Journal* 808, p. 170.
- Bean, J. L., E. Miller-Ricci Kempton, and D. Homeier (2010). “A Ground-Based Transmission Spectrum of the Super-Earth Exoplanet GJ 1214b”. In: *Nature* 468. 00283, pp. 669–672.

- Beaulieu, J.-P., D. P. Bennett, P. Fouqué, A. Williams, et al. (2006). "Discovery of a Cool Planet of 5.5 Earth Masses through Gravitational Microlensing". In: *Nature* 439, pp. 437–440.
- Beer (1852). "Bestimmung Der Absorption Des Rothen Lichts in Farbigen Flüssigkeiten". In: *Annalen der Physik* 162.5, pp. 78–88.
- Benedict, G. F. and T. E. Harrison (2017). "HD 202206: A Circumbinary Brown Dwarf System". In: *The Astronomical Journal* 153, p. 258.
- Bertaux, J. L., R. Lallement, S. Ferron, C. Boonne, and R. Bodichon (2014). "TAPAS, a Web-Based Service of Atmospheric Transmission Computation for Astronomy". In: *Astronomy and Astrophysics* 564, 00041, A46.
- Beuzit, J.-L., M. Feldt, K. Dohlen, D. Mouillet, et al. (2008). "SPHERE: A Planet Finder Instrument for the VLT". In: *Ground-Based and Airborne Instrumentation for Astronomy II*. Ground-Based and Airborne Instrumentation for Astronomy II. Vol. 7014. International Society for Optics and Photonics, p. 701418.
- Bevington, P. R. and D. K. Robinson (2003). *Data Reduction and Error Analysis for the Physical Sciences*. p.g. 208-212. McGraw-Hill. 320 pp.
- Binney, J. and M. Merrifield (1998). *Galactic Astronomy*.
- Bonfanti, A., S. Ortolani, and V. Nascimbeni (2016). "Age Consistency between Exoplanet Hosts and Field Stars". In: *Astronomy and Astrophysics* 585, A5.
- Borucki, W., D. G. Koch, G. Basri, N. Batalha, et al. (2011). "Characteristics of Kepler Planetary Candidates Based on the First Data Set". In: *The Astrophysical Journal* 728, p. 117.
- Borucki, W., D. Koch, G. Basri, N. Batalha, et al. (2008). "Finding Earth-Size Planets in the Habitable Zone: The Kepler Mission". In: *Exoplanets: Detection, Formation and Dynamics*. Vol. 249, pp. 17–24.
- Boss, A. P. (1997). "Giant Planet Formation by Gravitational Instability." In: *Science* 276, pp. 1836–1839.
- Bouchy, F., R. Doyon, É. Artigau, C. Melo, et al. (2017). "Near-Infrared Planet Searcher to Join HARPS on the ESO 3.6-Metre Telescope". In: *The Messenger* 169. 00000, pp. 21–27.
- Bouchy, F., F. Pepe, and D. Queloz (2001). "Fundamental Photon Noise Limit to Radial Velocity Measurements". In: *Astronomy and Astrophysics* 374.2. 00258, pp. 733–739.
- Bozza, V., L. Mancini, and A. Sozzetti, eds. (2016). *Methods of Detecting Exoplanets: 1st Advanced School on Exoplanetary Science*. Astrophysics and Space Science Library. Springer International Publishing.
- Broeg, C., A. Fortier, D. Ehrenreich, Y. Alibert, et al. (2013). "CHEOPS: A Transit Photometry Mission for ESA's Small Mission Programme". In: *European Physical Journal Web of Conferences* 47, p. 03005.
- Brogi, M., R. J. de Kok, S. Albrecht, I. A. G. Snellen, J. L. Birkby, and H. Schwarz (2016). "Rotation and Winds of Exoplanet HD 189733 b Measured with High-Dispersion Transmission Spectroscopy". In: *The Astrophysical Journal* 817.2. 00000, p. 106. arXiv: 1512.05175.
- Brogi, M., R. J. de Kok, J. L. Birkby, H. Schwarz, and I. A. G. Snellen (2014). "Carbon Monoxide and Water Vapor in the Atmosphere of the Non-Transiting Exoplanet HD 179949 B". In: *Astronomy and Astrophysics* 565. 00000, A124.
- Brogi, M., I. A. G. Snellen, R. J. de Kok, S. Albrecht, J. Birkby, and E. J. W. de Mooij (2012). "The Signature of Orbital Motion from the Dayside of the Planet τ Boötis B". In: *Nature* 486. 00000, pp. 502–504.
- Brugger, B., O. Mousis, M. Deleuil, and F. Deschamps (2017). "Constraints on Super-Earth Interiors from Stellar Abundances". In: *The Astrophysical Journal* 850, p. 93.

- Burke, C. J., F. Mullally, S. E. Thompson, J. L. Coughlin, and J. F. Rowe (2019). “Re-Evaluating Small Long-Period Confirmed Planets From Kepler”. In: *arXiv e-prints* 1901, arXiv:1901.00506.
- Burrows, A., T. Guillot, W. B. Hubbard, M. S. Marley, D. Saumon, J. I. Lunine, and D. Sudarsky (2000). “On the Radii of Close-in Giant Planets”. In: *The Astrophysical Journal Letters* 534.1, p. L97.
- Burrows, A., M. Marley, W. B. Hubbard, J. I. Lunine, et al. (1997). “A Nongray Theory of Extrasolar Giant Planets and Brown Dwarfs”. In: *The Astrophysical Journal* 491, pp. 856–875.
- Butler, R. P., G. W. Marcy, E. Williams, C. McCarthy, P. Dosanjh, and S. S. Vogt (1996a). “Attaining Doppler Precision of 3 M S-1”. In: *Publications of the Astronomical Society of the Pacific* 108, p. 500.
- Butler, R. P. and G. W. Marcy (1996b). “A Planet Orbiting 47 Ursae Majoris”. In: *The Astrophysical Journal Letters* 464, p. L153.
- Butler, R. P., G. W. Marcy, E. Williams, H. Hauser, and P. Shirts (1997). “Three New “51 Pegasi-Type” Planets”. In: *The Astrophysical Journal Letters* 474, pp. L115–L118.
- Caffau, E., H.-G. Ludwig, M. Steffen, B. Freytag, and P. Bonifacio (2011). “Solar Chemical Abundances Determined with a CO5BOLD 3D Model Atmosphere”. In: *Solar Physics* 268.2, p. 255.
- Cameron, A. C. (2012). “Extrasolar Planets: Astrophysical False Positives”. In: *Nature* 492.7427, pp. 48–50.
- Chabrier, G. and I. Baraffe (2000). “Theory of Low-Mass Stars and Substellar Objects”. In: *Annual Review of Astronomy and Astrophysics* 38.1. 00483, pp. 337–377. arXiv: astro-ph/0006383.
- Charbonneau, D., T. M. Brown, D. W. Latham, and M. Mayor (2000). “Detection of Planetary Transits Across a Sun-like Star”. In: *The Astrophysical Journal Letters* 529, pp. L45–L48.
- Charbonneau, D., T. M. Brown, R. W. Noyes, and R. L. Gilliland (2002). “Detection of an Extrasolar Planet Atmosphere*”. In: *The Astrophysical Journal* 568.1, p. 377.
- Chauvin, G., A.-M. Lagrange, C. Dumas, B. Zuckerman, et al. (2004). “A Giant Planet Candidate near a Young Brown Dwarf. Direct VLT/NACO Observations Using IR Wavefront Sensing”. In: *Astronomy and Astrophysics* 425, pp. L29–L32.
- Chen, J. and D. M. Kipping (2016). “Probabilistic Forecasting of the Masses and Radii of Other Worlds”. In: *The Astrophysical Journal* 834.1, p. 17. arXiv: 1603.08614.
- Chenciner, A. (2007). “Three Body Problem”. In: *Scholarpedia* 2.10, p. 2111.
- Ciddor, P. E. (1996). “Refractive Index of Air: New Equations for the Visible and near Infrared”. In: *Applied Optics* 35.9, pp. 1566–1573.
- Clough, S. A. and M. J. Iacono (1995). “Line-by-Line Calculation of Atmospheric Fluxes and Cooling Rates: 2. Application to Carbon Dioxide, Ozone, Methane, Nitrous Oxide and the Halocarbons”. In: *Journal of Geophysical Research: Atmospheres* 100.D8. 00002, pp. 16519–16535.
- Connes, P., M. Martic, and J. Schmitt (1996). “Demonstration of Photon-Noise Limit in Stellar Radial Velocities”. In: *Astrophysics and Space Science* 241.1, p. 61.
- Connes, P. (1985). “Absolute Astronomical Accelerometry”. In: *Astrophysics and Space Science* 110.2, pp. 211–255.
- Correia, A. C. M., S. Udry, M. Mayor, J. Laskar, et al. (2005). “The CORALIE Survey for Southern Extra-Solar Planets. XIII. A Pair of Planets around HD 202206 or a Circumbinary Planet?” In: *aap* 440. 00000, pp. 751–758.
- Correia, A. C. M. (2018). “Chaotic Dynamics in the (47171) Lempo Triple System”. In: *Icarus* 305, p. 250.

- Cotton, D. V., J. Bailey, and L. Kedziora-Chudczer (2014). “Atmospheric Modelling for the Removal of Telluric Features from Infrared Planetary Spectra”. In: *Monthly Notices of the Royal Astronomical Society* 439. 00007, pp. 387–399.
- Crepp, J. R., E. J. Gonzales, E. B. Bechter, B. T. Montet, et al. (2016). “The TRENDS High-Contrast Imaging Survey. VI. Discovery of a Mass, Age, and Metallicity Benchmark Brown Dwarf”. In: *The Astrophysical Journal* 831. 00004.
- Crossfield, I. J. M., B. Biller, J. E. Schlieder, N. R. Deacon, et al. (2014). “A Global Cloud Map of the Nearest Known Brown Dwarf”. In: *Nature* 505, pp. 654–656.
- Cumming, A., G. W. Marcy, and R. P. Butler (1999). “The Lick Planet Search: Detectability and Mass Thresholds”. In: *The Astrophysical Journal* 526, pp. 890–915.
- Czekala, I., S. M. Andrews, K. S. Mandel, D. W. Hogg, and G. M. Green (2015). “Constructing A Flexible Likelihood Function For Spectroscopic Inference”. In: *The Astrophysical Journal* 812.2. 00022, p. 128. arXiv: 1412.5177.
- Czekala, I., K. S. Mandel, S. M. Andrews, J. A. Dittmann, S. K. Ghosh, B. T. Montet, and E. R. Newton (2017). “Disentangling Time-Series Spectra with Gaussian Processes: Applications to Radial Velocity Analysis”. In: *The Astrophysical Journal* 840.1. 00002, p. 49.
- Czesla, S., T. Molle, and J. H. M. M. Schmitt (2018). “A Posteriori Noise Estimation in Variable Data Sets. With Applications to Spectra and Light Curves”. In: *Astronomy and Astrophysics* 609, A39.
- De Kok, R. J., M. Brogi, I. A. G. Snellen, J. Birkby, S. Albrecht, and E. J. de Mooij (2013). “Detection of Carbon Monoxide in the High-Resolution Day-Side Spectrum of the Exoplanet HD 189733b”. In: *Astronomy and Astrophysics* 554. 00086, A82.
- Deeg, H. (1998). “Photometric Detection of Extrasolar Planets by the Transit-Method”. In: *Brown Dwarfs and Extrasolar Planets*. Brown Dwarfs and Extrasolar Planets. Vol. 134. ASP Conference Series #134, p. 216.
- Díaz, R. F., J. M. Almenara, A. Santerne, C. Moutou, A. Lethuillier, and M. Deleuil (2014). “PASTIS: Bayesian Extrasolar Planet Validation - I. General Framework, Models, and Performance”. In: *Monthly Notices of the Royal Astronomical Society* 441, pp. 983–1004.
- Dieterich, S. B., T. J. Henry, W.-C. Jao, J. G. Winters, A. D. Hosey, A. R. Riedel, and J. P. Subasavage (2014). “The Solar Neighborhood. XXXII. The Hydrogen Burning Limit”. In: *The Astronomical Journal* 147, p. 94.
- Dorn, R. J., G. Anglada-Escude, D. Baade, P. Bristow, et al. (2014). “CRIRES+: Exploring the Cold Universe at High Spectral Resolution”. In: *The Messenger* 156, pp. 7–11.
- Duquennoy, A. and M. Mayor (1991). “Multiplicity among Solar-Type Stars in the Solar Neighbourhood. II - Distribution of the Orbital Elements in an Unbiased Sample”. In: *Astronomy and Astrophysics* 248, pp. 485–524.
- Edlén, B. (1953). “The Dispersion of Standard Air*”. In: *JOSA* 43.5, pp. 339–344.
- ESA (1997). “The HIPPARCOS and TYCHO Catalogues. Astrometric and Photometric Star Catalogues Derived from the ESA HIPPARCOS Space Astrometry Mission”. In: ESA Special Publication. Vol. 1200.
- ESO (2017). *ESO Call for Proposals - P101*.
- Esteves, L. J., E. J. W. De Mooij, and R. Jayawardhana (2013). “Optical Phase Curves of Kepler Exoplanets”. In: *The Astrophysical Journal* 772.1, p. 51.

- Ferluga, S., L. Floreano, U. Bravar, and C. Bédalo (1997). “Separating the Spectra of Binary Stars-I. A Simple Method: Secondary Reconstruction”. In: *Astronomy and Astrophysics Supplement Series* 121.1. 00012, pp. 201–209.
- Figueira, P., V. Z. Adibekyan, M. Oshagh, J. J. Neal, et al. (2016). “Radial Velocity Information Content of M Dwarf Spectra in the Near-Infrared”. In: *Astronomy and Astrophysics* 586. 00002, A101.
- Figueira, P., F. Pepe, C. H. F. Melo, N. C. Santos, et al. (2010). “Radial Velocities with CRIRES: Pushing Precision down to 5-10 m/S”. In: *Astronomy and Astrophysics* 511. 00057, A55.
- Figueira, P. and S. Neves (2015). *Astro Homus*. CAUP.
- Fischer, D. A. and J. Valenti (2005). “The Planet-Metallicity Correlation”. In: *The Astrophysical Journal* 622, pp. 1102–1117.
- Fitzpatrick, R. (2012). *An Introduction to Celestial Mechanics*.
- Fortney, J. J. and N. Nettelmann (2010). “The Interior Structure, Composition, and Evolution of Giant Planets”. In: *Space Science Reviews* 152.1-4, pp. 423–447.
- Fowler, A. M. and I. Gatley (1990). “Demonstration of an Algorithm for Read-Noise Reduction in Infrared Arrays”. In: *The Astrophysical Journal Letters* 353, p. L33.
- Fressin, F., G. Torres, D. Charbonneau, S. T. Bryson, et al. (2013). “The False Positive Rate of Kepler and the Occurrence of Planets”. In: *The Astrophysical Journal* 766, p. 81.
- Freudling, W., M. Romaniello, D. M. Bramich, P. Ballester, et al. (2013). “Automated Data Reduction Workflows for Astronomy. The ESO Reflex Environment”. In: *Astronomy and Astrophysics* 559, A96.
- Freytag, B., F. Allard, H.-G. Ludwig, D. Homeier, and M. Steffen (2010). “The Role of Convection, Overshoot, and Gravity Waves for the Transport of Dust in M Dwarf and Brown Dwarf Atmospheres”. In: *Astronomy and Astrophysics* 513, A19.
- Fulton, B. J., E. A. Petigura, A. W. Howard, H. Isaacson, et al. (2017). “The California-Kepler Survey. III. A Gap in the Radius Distribution of Small Planets”. In: arXiv: 1703.10375 [astro-ph].
- Gagné, J., J. K. Faherty, A. J. Burgasser, É. Artigau, et al. (2017). “SIMP J013656.5+093347 Is Likely a Planetary-Mass Object in the Carina-Near Moving Group”. In: *The Astrophysical Journal Letters* 841, p. L1.
- GAIA Collaboration, A. G. A. Brown, A. Vallenari, T. Prusti, et al. (2018). “Gaia Data Release 2. Summary of the Contents and Survey Properties”. In: *ArXiv e-prints*, arXiv:1804.09365.
- GAIA Collaboration, A. G. A. Brown, A. Vallenari, T. Prusti, et al. (2016). “Gaia Data Release 1. Summary of the Astrometric, Photometric, and Survey Properties”. In: *Astronomy and Astrophysics* 595, A2.
- Gaidos, E. and A. W. Mann (2014). “M Dwarf Metallicities and Giant Planet Occurrence: Ironing Out Uncertainties and Systematics”. In: *The Astrophysical Journal* 791.1, p. 54.
- Gandolfi, D., O. Barragan, J. Livingston, M. Fridlund, et al. (2018). “TESS’s First Planet: A Super-Earth Transiting the Naked-Eye Star \$\pi\$ Mensae”. In: *ArXiv e-prints* 1809, arXiv:1809.07573.
- Gao, Y., A. C. M. Correia, P. P. Eggleton, and Z. Han (2018). “Numerical Modelling of Tertiary Tides”. In: *Monthly Notices of the Royal Astronomical Society* 479.3, p. 3604.
- Gontcharov, G. A., A. A. Andronova, and O. A. Titov (2000). “New Astrometric Binaries among HIPPARCOS Stars”. In: *Astronomy and Astrophysics* 355, pp. 1164–1167.
- González, J. F. and H. Levato (2006). “Separation of Composite Spectra: The Spectroscopic Detection of an Eclipsing Binary Star”. In: *Astronomy and Astrophysics* 448, pp. 283–292.

- Goodman, J. (2009). "Thermodynamics of Atmospheric Circulation on Hot Jupiters". In: *The Astrophysical Journal* 693, pp. 1645–1649.
- Gray, D. F. (2005). *The Observation and Analysis of Stellar Photospheres*. 3rd ed. Cambridge University Press.
- Gregory, P. C. (2011). "Bayesian Re-Analysis of the Gliese 581 Exoplanet System". In: *Monthly Notices of the Royal Astronomical Society* 415, pp. 2523–2545.
- Guenther, E. (2005). "The Prospects of Searching for Planets of Brown Dwarfs with CRIRES". In: High Resolution Infrared Spectroscopy in Astronomy, pp. 487–492.
- Gullikson, K., S. Dodson-Robinson, and A. Kraus (2014). "Correcting for Telluric Absorption: Methods, Case Studies, and Release of the TelFit Code". In: *The Astronomical Journal* 148.3. 00015, p. 53.
- Hadrava, P. (1995). "Orbital Elements of Multiple Spectroscopic Stars." In: *Astronomy and Astrophysics Supplement Series* 114, p. 393.
- (2009). "Disentangling of Spectra - Theory and Practice". In: 00013. arXiv: 0909.0172 [astro-ph].
- Halbwachs, J.-L., F. Arenou, M. Mayor, S. Udry, and D. Queloz (2000). "Exploring the Brown Dwarf Desert with Hipparcos". In: *Astronomy and Astrophysics* 355. 00198, pp. 581–594.
- Hatzes, A. P. and W. D. Cochran (1992). "Spectrograph Requirements for Precise Radial Velocity Measurements". In: European Southern Observatory Conference and Workshop Proceedings. Vol. 40, p. 275.
- Hatzes, A. P. and H. Rauer (2015). "A Definition for Giant Planets Based on the Mass-Density Relationship". In: *The Astrophysical Journal Letters* 810, p. L25.
- Hauschildt, P. H., F. Allard, and E. Baron (1999). "The NextGen Model Atmosphere Grid for $3000 \leq \text{Teff} \leq 10,000$ K". In: *The Astrophysical Journal* 512. 01086, pp. 377–385.
- Hauschildt, P. H., E. Baron, and F. Allard (1997). "Parallel Implementation of the PHOENIX Generalized Stellar Atmosphere Program". In: *The Astrophysical Journal* 483, pp. 390–398.
- Helling, C. and S. Casewell (2014). "Atmospheres of Brown Dwarfs". In: *Astronomy and Astrophysics Review* 22, p. 80.
- Heng, K. and A. P. Showman (2015). "Atmospheric Dynamics of Hot Exoplanets". In: *Annual Review of Earth and Planetary Sciences* 43.1, pp. 509–540.
- Hoeijmakers, H. J., D. Ehrenreich, K. Heng, D. Kitzmann, et al. (2018). "Atomic Iron and Titanium in the Atmosphere of the Exoplanet KELT-9b". In: *Nature* 560.7719, p. 453.
- Holczer, T., T. Mazeh, G. Nachmani, D. Jontof-Hutter, et al. (2016). "Transit Timing Observations from Kepler. IX. Catalog of the Full Long-Cadence Data Set". In: *The Astrophysical Journal Supplement Series* 225, p. 9.
- Holman, M. J., D. C. Fabrycky, D. Ragozzine, E. B. Ford, et al. (2010). "Kepler-9: A System of Multiple Planets Transiting a Sun-Like Star, Confirmed by Timing Variations". In: *Science* 330, p. 51.
- Holman, M. J. and N. W. Murray (2005). "The Use of Transit Timing to Detect Terrestrial-Mass Extrasolar Planets". In: *Science* 307, pp. 1288–1291.
- Horne, K. (1986). "An Optimal Extraction Algorithm for CCD Spectroscopy". In: *Publications of the Astronomical Society of the Pacific* 98. 01548, pp. 609–617.
- Howell, S. B. (2000). *Handbook of CCD Astronomy*.
- Huang, C. X., J. Burt, A. Vanderburg, M. N. Günther, et al. (2018a). "TESS Discovery of a Transiting Super-Earth in the \$\backslash\$Pi\$\ Mensae System". In: *ArXiv e-prints* 1809, arXiv:1809.05967.

- Huang, C. X., A. Shporer, D. Dragomir, M. Fausnaugh, et al. (2018b). “Expected Yields of Planet Discoveries from the TESS Primary and Extended Missions”. In: *ArXiv e-prints* 1807, arXiv:1807.11129.
- Husser, T.-O., S. W.-. von Berg, S. Dreizler, D. Homeier, A. Reiners, T. Barman, and P. H. Hauschildt (2013). “A New Extensive Library of PHOENIX Stellar Atmospheres and Synthetic Spectra”. In: *Astronomy and Astrophysics* 553. 00243, A6. arXiv: 1303.5632.
- Jha, S., D. Charbonneau, P. M. Garnavich, D. J. Sullivan, T. Sullivan, T. M. Brown, and J. L. Tonry (2000). “Multicolor Observations of a Planetary Transit of HD 209458”. In: *The Astrophysical Journal* 540.1, p. L45.
- Kaeufl, H.-U., P. Ballester, P. Biereichel, B. Delabre, et al. (2004). “CRIRES: A High-Resolution Infrared Spectrograph for ESO’s VLT”. In: *Ground-based Instrumentation for Astronomy* 5492. 00000, p. 1218.
- Kalas, P., J. R. Graham, E. Chiang, M. P. Fitzgerald, et al. (2008). “Optical Images of an Exosolar Planet 25 Light-Years from Earth”. In: *Science* 322, p. 1345.
- Kass, R. E. and A. E. Raftery (1995). “Bayes Factors”. In: *Journal of the American Statistical Association* 90.430, pp. 773–795.
- Kerber, F., G. Nave, C. J. Sansonetti, and P. Bristow (2009). “From Laboratory to the Sky: Th–Ar Wavelength Standards for the Cryogenic Infrared Echelle Spectrograph (CRIRES)”. In: *Physica Scripta* 2009.T134. 00009, p. 014007.
- Klüter, J., U. Bastian, M. Demleitner, and J. Wambsganss (2018). “Prediction of Astrometric Microlensing Events from Gaia DR2 Proper Motions”. In: arXiv: 1807.11077 [astro-ph].
- Knutson, H. A. (2009). “Characterizing the Atmospheres of Hot Jupiters: From Spectra to Multi-Color Maps”. In: *Transiting Planets* 253, p. 255.
- Knutson, H. A., D. Charbonneau, L. E. Allen, J. J. Fortney, et al. (2007a). “A Map of the Day–Night Contrast of the Extrasolar Planet HD 189733b”. In: *Nature* 447.7141, pp. 183–186.
- Knutson, H. A., D. Charbonneau, R. W. Noyes, T. M. Brown, and R. L. Gilliland (2007b). “Using Stellar Limb-Darkening to Refine the Properties of HD 209458b”. In: *The Astrophysical Journal* 655.1, p. 564.
- Kolbl, R., G. W. Marcy, H. Isaacson, and A. W. Howard (2015). “Detection of Stars Within \sim 0.8 in of Kepler Objects of Interest”. In: *The Astronomical Journal* 149, p. 18.
- Koll, D. D. B. and D. S. Abbot (2016). “Temperature Structure and Atmospheric Circulation of Dry Tidally Locked Rocky Exoplanets”. In: *The Astrophysical Journal* 825, p. 99.
- Kostogryz, N., M. Kürster, T. Yakobchuk, Y. Lyubchik, and M. Kuznetsov (2013). “A Spectral Differential Approach to Characterizing Low-Mass Companions to Late-Type Stars”. In: *Astronomische Nachrichten* 334.7. 00000, pp. 648–660.
- Kreidberg, L. (2018). “Exoplanet Atmosphere Measurements from Transmission Spectroscopy and Other Planet Star Combined Light Observations”. In: *Handbook of Exoplanets*. Ed. by H. J. Deeg and J. A. Belmonte. Cham: Springer International Publishing, pp. 2083–2105.
- Kreidberg, L., J. L. Bean, J.-M. Désert, B. Benneke, et al. (2014). “Clouds in the Atmosphere of the Super-Earth Exoplanet GJ 1214b”. In: *Nature* 505.7481, pp. 69–72.
- Ku, H. H. (1966). *Notes on the Use of Propagation of Error Formulas*. National Bureau of Standards.
- Kubas, D., J. P. Beaulieu, D. P. Bennett, A. Cassan, et al. (2012). “A Frozen Super-Earth Orbiting a Star at the Bottom of the Main Sequence”. In: *Astronomy and Astrophysics* 540, A78.
- Kurucz, R. L. (1979). “Model Atmospheres for G, F, A, B, and O Stars”. In: *The Astrophysical Journal Supplement Series* 40, pp. 1–340.

- Kuzuhara, M., M. Tamura, T. Kudo, M. Janson, et al. (2013). “Direct Imaging of a Cold Jovian Exoplanet in Orbit around the Sun-like Star GJ 504”. In: *The Astrophysical Journal* 774, p. 11.
- Lebzelter, T., A. Seifahrt, S. Uttenthaler, S. Ramsay, et al. (2012). “CRIRES-POP. A Library of High Resolution Spectra in the near-Infrared”. In: *Astronomy and Astrophysics* 539, A109.
- Leggett, S. K., M. C. Cushing, D. Saumon, M. S. Marley, et al. (2009). “The Physical Properties of Four ~600 K T Dwarfs”. In: *The Astrophysical Journal* 695.2, p. 1517.
- Leleu, A., J. Lillo-Box, M. Sestovic, P. Robutel, et al. (2019). “Co-Orbital Exoplanets from Close Period Candidates: The TOI-178 Case”. In: *arXiv e-prints*, arXiv:1901.07250.
- Lillo-Box, J., A. Leleu, H. Parviainen, P. Figueira, et al. (2018). “The TROY Project. II. Multi-Technique Constraints on Exotrojans in Nine Planetary Systems”. In: *Astronomy and Astrophysics* 618, A42.
- Lindegren, L. and D. Dravins (2003). “The Fundamental Definition of “radial Velocity””. In: *Astronomy and Astrophysics* 401, pp. 1185–1201.
- Lissauer, J. J., G. W. Marcy, J. F. Rowe, S. T. Bryson, et al. (2012). “Almost All of Kepler’s Multiple-Planet Candidates Are Planets”. In: *The Astrophysical Journal* 750.2, p. 112.
- Lockwood, A. C., J. A. Johnson, C. F. Bender, J. S. Carr, T. Barman, A. J. W. Richert, and G. A. Blake (2014). “Near-IR Direct Detection of Water Vapor in Tau Boötis B”. In: *The Astrophysical Journal Letters* 783.2. 00038, p. L29.
- López-Morales, M., R. D. Haywood, J. L. Coughlin, L. Zeng, et al. (2016). “Kepler-21b: A Rocky Planet Around a V = 8.25 Magnitude Star”. In: *The Astronomical Journal* 152, p. 204.
- Lopez, E. D. and J. J. Fortney (2014). “Understanding the Mass-Radius Relation for Sub-Neptunes: Radius as a Proxy for Composition”. In: *The Astrophysical Journal* 792, p. 1.
- Lovis, C. and F. Pepe (2007). “A New List of Thorium and Argon Spectral Lines in the Visible”. In: *Astronomy & Astrophysics* 468.3, pp. 1115–1121.
- Ma, B. and J. Ge (2014). “Statistical Properties of Brown Dwarf Companions: Implications for Different Formation Mechanisms”. In: *Monthly Notices of the Royal Astronomical Society* 439.3, p. 2781.
- Macintosh, B. A., J. R. Graham, D. W. Palmer, R. Doyon, et al. (2008). “The Gemini Planet Imager: From Science to Design to Construction”. In: *Adaptive Optics Systems*. Adaptive Optics Systems. Vol. 7015. International Society for Optics and Photonics, p. 701518.
- Madhusudhan, N. and A. Burrows (2012). “Analytic Models for Albedos, Phase Curves, and Polarization of Reflected Light from Exoplanets”. In: *The Astrophysical Journal* 747.1, p. 25.
- Maldonado, J. and E. Villaver (2017). “Searching for Chemical Signatures of Brown Dwarf Formation”. In: *Astronomy and Astrophysics* 602, A38.
- Marcy, G. W. and R. P. Butler (1996). “A Planetary Companion to 70 Virginis”. In: *The Astrophysical Journal Letters* 464, p. L147.
- Marois, C., R. Doyon, R. Racine, D. Nadeau, et al. (2005). “Direct Exoplanet Imaging around Sun-like Stars: Beating the Speckle Noise with Innovative Imaging Techniques”. In: *Journal of the Royal Astronomical Society of Canada* 99, p. 130.
- Marois, C., B. Macintosh, T. Barman, B. Zuckerman, et al. (2008). “Direct Imaging of Multiple Planets Orbiting the Star HR 8799”. In: *Science* 322.5906, pp. 1348–1352. pmid: 19008415.
- Marois, C., B. Zuckerman, Q. M. Konopacky, B. Macintosh, and T. Barman (2010). “Images of a Fourth Planet Orbiting HR 8799”. In: *Nature* 468, pp. 1080–1083.
- Martins, J. H. C., N. C. Santos, P. Figueira, J. P. Faria, et al. (2015). “Evidence for a Spectroscopic Direct Detection of Reflected Light from 51 Pegasi B”. In: *Astronomy and Astrophysics* 576, A134.

- Martins, J. H. C., N. C. Santos, P. Figueira, and C. Melo (2016). “Reflected Light from Giant Planets in Habitable Zones: Tapping into the Power of the Cross-Correlation Function”. In: *Origins of Life and Evolution of the Biosphere* 46, pp. 487–498.
- Mathar, R. J. (2007). “Refractive Index of Humid Air in the Infrared: Model Fits”. In: *Journal of Optics A: Pure and Applied Optics* 9.5, p. 470.
- Mawet, D., P. Riaud, O. Absil, and J. Surdej (2005). “Annular Groove Phase Mask Coronagraph”. In: *The Astrophysical Journal* 633, pp. 1191–1200.
- Mayor, M., F. Pepe, D. Queloz, F. Bouchy, et al. (2003). “Setting New Standards with HARPS”. In: *The Messenger* 114, pp. 20–24.
- Mayor, M. and D. Queloz (1995). “A Jupiter-Mass Companion to a Solar-Type Star”. In: *Nature* 378.6555, pp. 355–359.
- Mazeh, T., E. L. Martin, D. Goldberg, and H. A. Smith (1997). “Detecting Faint Secondaries of Spectroscopic Binaries: HD 101177B and 149414A”. In: *Monthly Notices of the Royal Astronomical Society* 284.2. 00014, pp. 341–347.
- Mazeh, T. and S. Zucker (1994). “Todcor: A TwO-Dimensional CORrelation Technique to Analyze Stellar Spectra in Search of Faint Companions”. In: *Astrophysics and Space Science* 212.1, pp. 349–356.
- Mégevand, D., F. M. Zerbi, P. Di Marcantonio, A. Cabral, et al. (2014). “ESPRESSO: The Radial Velocity Machine for the VLT”. In: *Proc. SPIE*. Ground-Based and Airborne Instrumentation for Astronomy V. Vol. 9147, 91471H.
- Meier, R. J. (2005). “On Art and Science in Curve-Fitting Vibrational Spectra”. In: *Vibrational Spectroscopy* 39.2, pp. 266–269.
- Melo, C., N. C. Santos, W. Gieren, G. Pietrzynski, et al. (2007). “A New Neptune-Mass Planet Orbiting HD 219828”. In: *Astronomy and Astrophysics* 467, pp. 721–727.
- Ment, K., J. A. Dittmann, N. Astudillo-Defru, D. Charbonneau, et al. (2018). “A Second Planet with an Earth-like Composition Orbiting the Nearby M Dwarf LHS 1140”. In: *ArXiv e-prints* 1808, arXiv:1808.00485.
- Mordasini, C., Y. Alibert, W. Benz, and D. Naef (2009). “Extrasolar Planet Population Synthesis. II. Statistical Comparison with Observations”. In: *Astronomy and Astrophysics* 501.3, p. 1161.
- Mordasini, C., Y. Alibert, H. Klahr, and T. Henning (2012). “Characterization of Exoplanets from Their Formation. I. Models of Combined Planet Formation and Evolution”. In: *Astronomy and Astrophysics* 547, A111.
- Moulton, F. R. (1914). *An Introduction to Celestial Mechanics*.
- Moutou, C., A. Vigan, D. Mesa, S. Desidera, P. Thébault, A. Zurlo, and G. Salter (2017). “Eccentricity in Planetary Systems and the Role of Binarity - Sample Definition, Initial Results, and the System of HD 211847”. In: *Astronomy and Astrophysics* 602. 00001, A87.
- Mullally, F., S. E. Thompson, J. L. Coughlin, C. J. Burke, and J. F. Rowe (2018). “Kepler’s Earth-like Planets Should Not Be Confirmed without Independent Detection: The Case of Kepler-452b”. In: *The Astronomical Journal* 155.5, p. 210.
- Murray, C. D. and A. C. M. Correia (2010). “Keplerian Orbits and Dynamics of Exoplanets”. In: *Exoplanets*. Ed. by S. Seager. 00000. University of Arizona Press, pp. 15–23.
- Muterspaugh, M. W., B. F. Lane, S. R. Kulkarni, M. Konacki, et al. (2010). “The Phases Differential Astrometry Data Archive. V. Candidate Substellar Companions to Binary Systems”. In: *The Astronomical Journal* 140, pp. 1657–1671.

- Nemravová, J. A., P. Harmanec, M. Brož, D. Vokrouhlický, et al. (2016). “ ξ Tauri: A Unique Laboratory to Study the Dynamic Interaction in a Compact Hierarchical Quadruple System”. In: *Astronomy and Astrophysics* 594, A55.
- Nicholls, C. P., T. Lebzelter, A. Smette, B. Wolff, et al. (2017). “CRIRES-POP: A Library of High Resolution Spectra in the near-Infrared-II. Data Reduction and the Spectrum of the K Giant 10 Leonis”. In: *Astronomy and Astrophysics* 598, 00000, A79.
- Nikolov, N., D. K. Sing, N. P. Gibson, J. J. Fortney, et al. (2016). “VLT FORS2 Comparative Transmission Spectroscopy: Detection of Na in the Atmosphere of WASP-39b from the Ground”. In: *The Astrophysical Journal* 832.2, p. 191.
- Nortmann, L., E. Pallé, M. Salz, J. Sanz-Forcada, et al. (2018). “Ground-Based Detection of an Extended Helium Atmosphere in the Saturn-Mass Exoplanet WASP-69b”. In: *Science* 362, pp. 1388–1391.
- Oreshenko, M., K. Heng, and B.-O. Demory (2016). “Optical Phase Curves as Diagnostics for Aerosol Composition in Exoplanetary Atmospheres”. In: *Monthly Notices of the Royal Astronomical Society* 457.4, p. 3420.
- Passegger, V. M., A. Reiners, S. V. Jeffers, S. Wende-von Berg, et al. (2018). “The CARMENES Search for Exoplanets around M Dwarfs. Photospheric Parameters of Target Stars from High-Resolution Spectroscopy”. In: *Astronomy and Astrophysics* 615, A6.
- Passegger, V. M., S. W.-v. Berg, and A. Reiners (2016). “Fundamental M-Dwarf Parameters from High-Resolution Spectra Using PHOENIX ACES Models: I. Parameter Accuracy and Benchmark Stars”. In: *Astronomy and Astrophysics* 587, 00006, A19. arXiv: 1601.01877.
- Peck, E. R. and K. Reeder (1972). “Dispersion of Air*”. In: *JOSA* 62.8, pp. 958–962.
- Pepe, F., M. Mayor, F. Galland, D. Naef, et al. (2002). “The CORALIE Survey for Southern Extra-Solar Planets VII. Two Short-Period Saturnian Companions to HD 108147 and HD 168746”. In: *Astronomy and Astrophysics* 388, pp. 632–638.
- Pepe, F., P. Molaro, S. Cristiani, R. Rebolo, et al. (2014a). “ESPRESSO: The next European Exoplanet Hunter”. In: *Astronomische Nachrichten* 335.1, p. 8.
- Pepe, F., A. C. Cameron, D. W. Latham, E. Molinari, et al. (2013). “An Earth-Sized Planet with an Earth-like Density”. In: *Nature* 503, pp. 377–380.
- Pepe, F., D. Ehrenreich, and M. R. Meyer (2014b). “Instrumentation for the Detection and Characterization of Exoplanets”. In: *Nature* 513, pp. 358–366.
- Perryman, M. A. C. (2000). “Extra-Solar Planets”. In: *Reports on Progress in Physics* 63.8, p. 1209.
- Perryman, M. (2011). *The Exoplanet Handbook*. Cambridge University Press.
- Perryman, M., J. Hartman, G. Á. Bakos, and L. Lindegren (2014). “Astrometric Exoplanet Detection with Gaia”. In: *The Astrophysical Journal* 797.1, p. 14.
- Pilyavsky, G., S. Mahadevan, S. R. Kane, A. W. Howard, et al. (2011). “A Search for the Transit of HD 168443b: Improved Orbital Parameters and Photometry”. In: *apj* 743, 162. 00014, p. 162.
- Piskorz, D., B. Benneke, N. R. Crockett, A. C. Lockwood, et al. (2016). “Evidence for the Direct Detection of the Thermal Spectrum of the Non-Transiting Hot Gas Giant HD 88133 B”. In: *The Astrophysical Journal* 832.2, p. 131.
- Piskunov, N. E. and J. A. Valenti (2002). “New Algorithms for Reducing Cross-Dispersed Echelle Spectra”. In: *Astronomy and Astrophysics* 385.3, 00257, pp. 1095–1106.

- Plavchan, P., D. Latham, S. Gaudi, J. Crepp, et al. (2015). "Radial Velocity Prospects Current and Future: A White Paper Report Prepared by the Study Analysis Group 8 for the Exoplanet Program Analysis Group (ExoPAG)". In: *arXiv e-prints*, arXiv:1503.01770.
- Pollacco, D. L., I. Skillen, A. Collier Cameron, D. J. Christian, et al. (2006). "The WASP Project and the SuperWASP Cameras". In: *Publications of the Astronomical Society of the Pacific* 118, pp. 1407–1418.
- Pollack, J. B., O. Hubickyj, P. Bodenheimer, J. J. Lissauer, M. Podolak, and Y. Greenzweig (1996). "Formation of the Giant Planets by Concurrent Accretion of Solids and Gas". In: *Icarus* 124, pp. 62–85.
- Quarteroni, A., R. Sacco, and F. Saleri (2000). *Numerical Mathematics*. Texts in applied mathematics 37. New York: Springer. 654 pp.
- Queloz, D., F. Bouchy, C. Moutou, A. Hatzes, et al. (2009). "The CoRoT-7 Planetary System: Two Orbiting Super-Earths". In: *Astronomy & Astrophysics* 506.1, pp. 303–319.
- Quirrenbach, A., P. J. Amado, J. A. Caballero, R. Mundt, et al. (2014). "CARMENES Instrument Overview". In: *Proceedings of SPIE: Ground-Based and Airborne Instrumentation for Astronomy V*. Ground-Based and Airborne Instrumentation for Astronomy V. Vol. 9147, 91471F.
- Quirrenbach, A., P. J. Amado, I. Ribas, A. Reiners, et al. (2018). "CARMENES: High-Resolution Spectra and Precise Radial Velocities in the Red and Infrared". In: *Ground-Based and Airborne Instrumentation for Astronomy VII*. Vol. 0702, 107020W.
- Rajpurohit, A. S., F. Allard, S. Rajpurohit, R. Sharma, G. D. C. Teixeira, O. Mousis, and R. Kamlesh (2018). "Exploring the Stellar Properties of M Dwarfs with High-Resolution Spectroscopy from the Optical to the near-Infrared". In: *Astronomy and Astrophysics* 620, A180.
- Rajpurohit, A. S., C. Reylé, F. Allard, D. Homeier, M. Schultheis, M. S. Bessell, and A. C. Robin (2013). "The Effective Temperature Scale of M Dwarfs". In: *Astronomy and Astrophysics* 556, A15.
- Rajpurohit, A. S., C. Reylé, F. Allard, D. Homeier, et al. (2016). "Spectral Energy Distribution of M-Subdwarfs: A Study of Their Atmospheric Properties". In: *Astronomy and Astrophysics* 596, A33.
- Ramanathan, K. R. and B. V. R. Murthy (1953). "Daily Variation of Amount of Ozone in the Atmosphere". In: *Nature* 172.4379, p. 633.
- Ranc, C., A. Cassan, M. D. Albrow, D. Kubas, et al. (2015). "MOA-2007-BLG-197: Exploring the Brown Dwarf Desert". In: *Astronomy and Astrophysics* 580, A125.
- Rasmussen, C. E. and C. K. I. Williams (2006). *Gaussian Processes for Machine Learning*. The MIT Press.
- Rauer, H., C. Catala, C. Aerts, T. Appourchaux, et al. (2014). "The PLATO 2.0 Mission". In: *Experimental Astronomy* 38.1-2, p. 249.
- Redfield, S. (2010). "Extrasolar Planets: Fluorescent Methane Spotted". In: *Nature* 463, pp. 617–618.
- Redfield, S., M. Endl, W. D. Cochran, and L. Koesterke (2008). "Sodium Absorption from the Exoplanetary Atmosphere of HD 189733b Detected in the Optical Transmission Spectrum". In: *The Astrophysical Journal Letters* 673, p. L87.
- Reiners, A., J. L. Bean, K. F. Huber, S. Dreizler, A. Seifahrt, and S. Czesla (2010). "Detecting Planets Around Very Low Mass Stars with the Radial Velocity Method". In: *The Astrophysical Journal* 710, pp. 432–443.
- Reiners, A., M. Zechmeister, J. A. Caballero, I. Ribas, et al. (2018). "The CARMENES Search for Exoplanets around M Dwarfs. High-Resolution Optical and near-Infrared Spectroscopy of 324 Survey Stars". In: *Astronomy and Astrophysics* 612, A49.

- Ricker, G. R., J. N. Winn, R. Vanderspek, D. W. Latham, et al. (2015). “Transiting Exoplanet Survey Satellite (TESS)”. In: *Journal of Astronomical Telescopes, Instruments, and Systems* 1, p. 014003.
- Rickman, H. (2001). “Transactions of the International Astronomical Union Proceedings of the Twenty-Fourth General Assembly.” In: *Transactions of the International Astronomical Union, Series B* 24.
- Robertson, P., S. Mahadevan, M. Endl, and A. Roy (2014). “Stellar Activity Masquerading as Planets in the Habitable Zone of the M Dwarf Gliese 581”. In: *Science* 345, pp. 440–444.
- Rodler, F., C. Del Burgo, S. Witte, C. Helling, et al. (2011). “Detecting Planets around Very Cool Dwarfs at near Infrared Wavelengths with the Radial Velocity Technique”. In: *Astronomy and Astrophysics* 532, A31.
- Rodler, F., M. Lopez-Morales, and I. Ribas (2012). “Weighing the Non-Transiting Hot Jupiter τ Boo B”. In: *The Astrophysical Journal Letters* 753.1. 00077, p. L25.
- Rogers, L. A. (2015). “Most 1.6 Earth-Radius Planets Are Not Rocky”. In: *The Astrophysical Journal* 801, p. 41.
- Rothman, L., I. Gordon, Y. Babikov, A. Barbe, et al. (2013). “The HITRAN2012 Molecular Spectroscopic Database”. In: *Journal of Quantitative Spectroscopy and Radiative Transfer* 130. 01706, pp. 4–50.
- Rothman, L., I. Gordon, A. Barbe, D. Benner, et al. (2009). “The HITRAN 2008 Molecular Spectroscopic Database”. In: *Journal of Quantitative Spectroscopy and Radiative Transfer* 110.9-10. 00000, pp. 533–572.
- Sablowski, D. P. and M. Weber (2016). “Spectral Disentangling with Spectangular”. In: *Astronomy and Astrophysics*. 00000.
- Sahlmann, J., D. Segransan, D. Queloz, S. Udry, et al. (2011). “Search for Brown-Dwarf Companions of Stars”. In: *Astronomy and Astrophysics* 525. 00115, A95. arXiv: 1009.5991.
- Sallum, S., K. B. Follette, J. A. Eisner, L. M. Close, et al. (2015). “Accreting Protoplanets in the LkCa 15 Transition Disk”. In: *Nature* 527.7578, pp. 342–344.
- Sanchis-Ojeda, R., J. N. Winn, and D. C. Fabrycky (2013). “Starspots and Spin-Orbit Alignment for Kepler Cool Host Stars”. In: *Astronomische Nachrichten* 334.1-2, pp. 180–183. arXiv: 1211.2002.
- Santerne, A., J.-P. Beaulieu, B. Rojas Ayala, I. Boisse, et al. (2016a). “Spectroscopic Characterisation of Microlensing Events. Towards a New Interpretation of OGLE-2011-BLG-0417”. In: *Astronomy and Astrophysics* 595, p. L11.
- Santerne, A., B. Brugger, D. J. Armstrong, V. Adibekyan, et al. (2018). “An Earth-Sized Exoplanet with a Mercury-like Composition”. In: *Nature Astronomy* 2.5, pp. 393–400.
- Santerne, A., R. F. Díaz, C. Moutou, F. Bouchy, et al. (2012). “SOPHIE Velocimetry of Kepler Transit Candidates. VII. A False-Positive Rate of 35% for Kepler Close-in Giant Candidates”. In: *Astronomy and Astrophysics* 545, A76.
- Santerne, A., M. Endl, A. Hatzes, F. Bouchy, C. Moutou, and M. Deleuil (2011). “Radial Velocity Follow-up of CoRoT Transiting Exoplanets”. In: European Physical Journal Web of Conferences. Vol. 11. eprint: arXiv:1101.0463, p. 02001.
- Santerne, A., F. Fressin, R. F. Díaz, P. Figueira, J.-M. Almenara, and N. C. Santos (2013). “The Contribution of Secondary Eclipses as Astrophysical False Positives to Exoplanet Transit Surveys”. In: *Astronomy & Astrophysics* 557, A139.

- Santerne, A., C. Moutou, M. Tsantaki, F. Bouchy, et al. (2016b). “SOPHIE Velocimetry of Kepler Transit Candidates. XVII. The Physical Properties of Giant Exoplanets within 400 Days of Period”. In: *Astronomy and Astrophysics* 587, A64.
- Santos, N. C., V. Adibekyan, P. Figueira, D. T. Andreasen, et al. (2017). “Observational Evidence for Two Distinct Giant Planet Populations”. In: *Astronomy and Astrophysics* 603, 00001, A30.
- Santos, N. C., G. Israelian, and M. Mayor (2004). “Spectroscopic [Fe/H] for 98 Extra-Solar Planet-Host Stars. Exploring the Probability of Planet Formation”. In: *Astronomy and Astrophysics* 415, pp. 1153–1166.
- Santos, N. C., G. Israelian, M. Mayor, J. P. Bento, P. C. Almeida, S. G. Sousa, and A. Ecuvillon (2005). “Spectroscopic Metallicities for Planet-Host Stars: Extending the Samples”. In: *aap* 437, 00000, pp. 1127–1133.
- Santos, N. C., A. Santerne, J. P. Faria, J. Rey, et al. (2016). “An Extreme Planetary System around HD 219828. One Long-Period Super Jupiter to a Hot-Neptune Host Star”. In: *Astronomy and Astrophysics* 592, A13.
- Schlaufman, K. C. (2018). “Evidence of an Upper Bound on the Masses of Planets and Its Implications for Giant Planet Formation”. In: *The Astrophysical Journal* 853, p. 37.
- Schmid, H. M., D. Gisler, F. Joos, H. P. Povel, et al. (2005). “ZIMPOL/CHEOPS: A Polarimetric Imager for the Direct Detection of Extra-Solar Planets”. In: Astronomical Polarimetry: Current Status and Future Directions. Vol. 343, p. 89.
- Schneising, O., M. Buchwitz, J. P. Burrows, H. Bovensmann, P. Bergamaschi, and W. Peters (2009). “Three Years of Greenhouse Gas Column-Averaged Dry Air Mole Fractions Retrieved from Satellite - Part 2: Methane”. In: *Atmospheric Chemistry & Physics* 9.2, p. 443.
- Schwarz, G. (1978). “Estimating the Dimension of a Model”. In: *The Annals of Statistics* 6.2, pp. 461–464.
- Schwarz, H., M. Brogi, R. de Kok, J. Birkby, and I. A. G. Snellen (2015). “Evidence against a Strong Thermal Inversion in HD 209458b from High-Dispersion Spectroscopy”. In: *Astronomy and Astrophysics* 576, A111.
- Seager, S., M. Kuchner, C. A. Hier-Majumder, and B. Militzer (2007). “Mass-Radius Relationships for Solid Exoplanets”. In: *The Astrophysical Journal* 669, pp. 1279–1297.
- Seager, S. and D. D. Sasselov (2000). “Theoretical Transmission Spectra during Extrasolar Giant Planet Transits”. In: *The Astrophysical Journal* 537.2, p. 916.
- Seelmann, A. M., P. H. Hauschildt, and E. Baron (2010). “A 3D Radiative Transfer Framework . VII. Arbitrary Velocity Fields in the Eulerian Frame”. In: *Astronomy and Astrophysics* 522, A102.
- Seifahrt, A., H. U. Käufl, G. Zängl, J. L. Bean, M. J. Richter, and R. Siebenmorgen (2010). “Synthesising, Using, and Correcting for Telluric Features in High-Resolution Astronomical Spectra . A near-Infrared Case Study Using CRIRES”. In: *Astronomy and Astrophysics* 524, A11.
- Shubham, mzechmeister, and astrowright (2018). “Shbhuk/Barycorrpy: V0.2.2.1”. In:
- Simon, K. P. and E. Sturm (1994). “Disentangling of Composite Spectra”. In: *Astronomy and Astrophysics* 281, 00000, pp. 286–291.
- Sing, D. K., J. J. Fortney, N. Nikolov, H. R. Wakeford, et al. (2016). “A Continuum from Clear to Cloudy Hot-Jupiter Exoplanets without Primordial Water Depletion”. In: *Nature* 529.7584, p. 59.
- Sirbu, D., S. Thomas, R. Belikov, and E. Bendek (2017a). “Techniques for High-Contrast Imaging in Multi-Star Systems. II. Multi-Star Wavefront Control”. In: *The Astrophysical Journal* 849, p. 142.

- Sirbu, D., R. Belikov, E. Bendek, E. Holte, A. J. Riggs, and S. Shaklan (2017b). “Prospects for Exoplanet Imaging in Multi-Star Systems with Starshades”. In: Society of Photo-Optical Instrumentation Engineers (SPIE) Conference Series. Vol. 0400. eprint: arXiv:1709.00041, p. 104001D.
- Skrutskie, M. F., R. M. Cutri, R. Stiening, M. D. Weinberg, et al. (2006). “The Two Micron All Sky Survey (2MASS)”. In: *The Astronomical Journal* 131, pp. 1163–1183.
- Smette, A., H. Sana, S. Noll, H. Horst, et al. (2015). “Molecfit: A General Tool for Telluric Absorption Correction - I. Method and Application to ESO Instruments”. In: *Astronomy and Astrophysics* 576. 00067, A77.
- Snellen, I. A. G., B. R. Brandl, R. J. De Kok, M. Brogi, J. Birkby, and H. Schwarz (2014). “Fast Spin of the Young Extrasolar Planet β Pictoris B”. In: *Nature* 509. 00000, p. 63.
- Snellen, I. A. G. and A. G. A. Brown (2018). “The Mass of the Young Planet Beta Pictoris b through the Astrometric Motion of Its Host Star”. In: *Nature Astronomy*.
- Snellen, I. A. G., R. J. de Kok, and E. J. W. De Mooij (2010). “The Orbital Motion, Absolute Mass and High-Altitude Winds of Exoplanet HD209458b”. In: *Nature* 465.7301, p. 1049.
- Snellen, I. A. G., R. de Kok, J. Birkby, B. Brandl, et al. (2015). “Combining High-Dispersion Spectroscopy (HDS) with High Contrast Imaging (HCI): Probing Rocky Planets around Our Nearest Neighbors”. In: *Astronomy & Astrophysics* 576, A59. arXiv: 1503.01136.
- Soderblom, D. R. (2010). “The Ages of Stars”. In: *Annual Review of Astronomy and Astrophysics* 48. 00241, pp. 581–629.
- Sorahana, S., I. Yamamura, and H. Murakami (2013). “On the Radii of Brown Dwarfs Measured with AKARI Near-Infrared Spectroscopy”. In: *The Astrophysical Journal* 767.1, p. 77. arXiv: 1304.1259.
- Sousa, S. G., N. C. Santos, M. Mayor, S. Udry, et al. (2008). “Spectroscopic Parameters for 451 Stars in the HARPS GTO Planet Search Program. Stellar [Fe/H] and the Frequency of Exo-Neptunes”. In: *aap* 487. 00390, pp. 373–381.
- Spiegel, D. S., A. Burrows, and J. A. Milsom (2011). “The Deuterium-Burning Mass Limit for Brown Dwarfs and Giant Planets”. In: *The Astrophysical Journal* 727, p. 57.
- Starovoit, E. D. and A. E. Rodin (2017). “On the Existence of Planets around the Pulsar PSR B0329+54”. In: *Astronomy Reports* 61, pp. 948–953.
- Sterken, C. and J. Manfroid (1992). *Astronomical Photometry: A Guide*. Astrophysics and Space Science Library. Springer Netherlands.
- Stevenson, K. B., J.-M. Désert, M. R. Line, J. L. Bean, et al. (2014). “Thermal Structure of an Exoplanet Atmosphere from Phase-Resolved Emission Spectroscopy”. In: *Science* 346, pp. 838–841.
- Storer, T. (2017). “Bridging the Chasm: A Survey of Software Engineering Practice in Scientific Programming”. In: *ACM Computing Surveys* 50.
- Suzuki, D., D. P. Bennett, T. Sumi, I. A. Bond, et al. (2016). “The Exoplanet Mass-Ratio Function from the MOA-II Survey: Discovery of a Break and Likely Peak at a Neptune Mass”. In: *The Astrophysical Journal* 833, p. 145.
- Thoning, K. W., P. P. Tans, and W. D. Komhyr (1989). “Atmospheric Carbon Dioxide at Mauna Loa Observatory: 2. Analysis of the NOAA GMCC Data, 1974–1985”. In: *Journal of Geophysical Research* 94.D6, p. 8549.
- Tinetti, G., A. Vidal-Madjar, M.-C. Liang, J.-P. Beaulieu, et al. (2007). “Water Vapour in the Atmosphere of a Transiting Extrasolar Planet”. In: *Nature* 448.7150, pp. 169–171.

- Tody, D. (1993). "IRAF in the Nineties". In: *Astronomical Data Analysis Software and Systems II*. Ed. by R. J. Hanisch, R. J. V. Brissenden, and J. Barnes. Vol. 52. Astronomical Society of the Pacific Conference Series. 00000, p. 173.
- Triaud, A. (2016). "Exoplanets: Migration of Giants". In: *Nature* 537.7621, pp. 496–497.
- Tsantaki, M., S. G. Sousa, V. Z. Adibekyan, N. C. Santos, A. Mortier, and G. Israelian (2013). "Deriving Precise Parameters for Cool Solar-Type Stars. Optimizing the Iron Line List". In: *aap* 555, A150. 00077, A150.
- Udalski, A., B. Paczynski, K. Zebrun, M. Szymanski, et al. (2002). "The Optical Gravitational Lensing Experiment. Search for Planetary and Low-Luminosity Object Transits in the Galactic Disk. Results of 2001 Campaign". In: *Acta Astronomica* 52, pp. 1–37.
- Udry, S., M. Mayor, D. Naef, F. Pepe, D. Queloz, N. C. Santos, and M. Burnet (2002). "The CORALIE Survey for Southern Extra-Solar Planets: VIII. The Very Low-Mass Companions of HD 141937, HD 162020, HD 168443 and HD 202206: Brown Dwarfs or "Superplanets"?" In: *Astronomy and Astrophysics* 390.1. 00158, pp. 267–279.
- Ulmer-Moll, S., P. Figueira, J. J. Neal, N. C. Santos, and M. Bonnefoy (2018). "Telluric Correction in the Near-Infrared: Standard Star or Synthetic Transmission?" In: *arXiv e-prints*, arXiv:1811.08915.
- Vacca, W. D., M. C. Cushing, and J. T. Rayner (2003). "A Method of Correcting Near-Infrared Spectra for Telluric Absorption". In: *Publications of the Astronomical Society of the Pacific* 115.805. 00000, p. 389.
- Vanderspek, R., C. X. Huang, A. Vanderburg, G. R. Ricker, et al. (2018). "TESS Discovery of an Ultra-Short-Period Planet around the Nearby M Dwarf LHS 3844". In: *ArXiv e-prints* 1809, arXiv:1809.07242.
- Vogt, S. S., R. P. Butler, E. J. Rivera, N. Haghhipour, G. W. Henry, and M. H. Williamson (2010). "The Lick-Carnegie Exoplanet Survey: A 3.1 M \oplus Planet in the Habitable Zone of the Nearby M3V Star Gliese 581". In: *The Astrophysical Journal* 723, pp. 954–965.
- Wang, J., D. Mawet, G. Ruane, R. Hu, and B. Benneke (2017). "Observing Exoplanets with High Dispersion Coronagraphy. I. The Scientific Potential of Current and Next-Generation Large Ground and Space Telescopes". In: *The Astronomical Journal* 153, p. 183.
- Weiss, L. M., G. W. Marcy, J. F. Rowe, A. W. Howard, et al. (2013). "The Mass of KOI-94d and a Relation for Planet Radius, Mass, and Incident Flux". In: *The Astrophysical Journal* 768, p. 14.
- Wenger, M., F. Ochsenbein, D. Egret, P. Dubois, et al. (2000). "The SIMBAD Astronomical Database. The CDS Reference Database for Astronomical Objects". In: *Astronomy and Astrophysics Supplement Series* 143, pp. 9–22.
- Whitworth, A., M. R. Bate, Å. Nordlund, B. Reipurth, and H. Zinnecker (2007). "The Formation of Brown Dwarfs: Theory". In: *Protostars and Planets V*. 00087, pp. 459–476.
- Winn, J. N. (2010). "Transits and Occultations". In: *arXiv: 1001.2010 [astro-ph]*.
- Wolszczan, A. and D. A. Frail (1992). "A Planetary System around the Millisecond Pulsar PSR1257 + 12". In: *Nature* 355.6356, pp. 145–147.
- Wright, J. T. and J. D. Eastman (2014). "Barycentric Corrections at 1 Cm S-1 for Precise Doppler Velocities". In: *Publications of the Astronomical Society of the Pacific* 126.943, p. 838.
- Wright, J. T. and P. Robertson (2017). "The Third Workshop on Extremely Precise Radial Velocities: The New Instruments". In: *Research Notes of the AAS* 1.1, p. 51.

- Wyttenbach, A., D. Ehrenreich, C. Lovis, S. Udry, and F. Pepe (2015). “Spectrally Resolved Detection of Sodium in the Atmosphere of HD 189733b with the HARPS Spectrograph”. In: *Astronomy and Astrophysics* 577, A62.
- Zechmeister, M., A. Reiners, P. J. Amado, M. Azzaro, et al. (2018). “Spectrum Radial Velocity Analyser (SERVAL). High-Precision Radial Velocities and Two Alternative Spectral Indicators”. In: *Astronomy and Astrophysics* 609, A12.
- Zucker, S. and T. Mazeh (1994). “Study of Spectroscopic Binaries with TODCOR. 1: A New Two-Dimensional Correlation Algorithm to Derive the Radial Velocities of the Two Components”. In: *The Astrophysical Journal* 420, 00376, pp. 806–810.
- Zucker, S. and T. Mazeh (2001). “Analysis of the Hipparcos Observations of the Extrasolar Planets and the Brown Dwarf Candidates”. In: *The Astrophysical Journal* 562.1, 00060, p. 549.
- Zurlo, A. and M. Bonnefoy (2015). “New SPHERE Results on the Planetary System around HR8799”. In: AAS/Division for Extreme Solar Systems Abstracts. Vol. 3, p. 202.05.